Departamento de Química
Facultad de Ciencias
Universidad Autónoma de Madrid

Adsorption of organic molecules on metal surfaces and metal surfaces covered with ultrathin ionic layers: charge transfer and self-assembly

A thesis submitted for the degree of:
Doctor in Chemistry

Candidate:
Maitreyi Robledo Relaño

Supervisors:
Prof. Dr. Manuel Alcamí Pertejo y Dr. Sergio Díaz-Tendero Victoria

June, 2015

Acknowledgements

I would like to gratefully acknowledge a number of people, which have helped me a lot through the past five years that I have been a member of the Chemistry Department of the Universidad Autónoma de Madrid.
First of all I would specially like to thank my two supervisors Prof. Dr. Manuel Alcamí and Dr. Sergio Díaz-Tendero. I am very obliged to Manuel Alcamí for having accepted me in his group and given me the great opportunity to study a doctorate and to Sergio for his daily supervising and all his support. Both of them have helped me, taught me and supported me all these past five years.

In addition I would like to thank other people who made this work possible:

- Prof. Dr. Fernando Martín, for all his valuable discussions and giving me the opportunity to work with the IMDEA-Nanoscience Insitute.

- Prof. Dr. Otilia Mó and Prof. Dr. Manuel Yañez, who have always supported me from the very beginning and who had always a kind word for me.

- Prof. Dr. Gianfranco Pacchioni, for welcoming me at his group in Universitá Bicocca in Milán and helping me to take my first steps in Surface science.

- Prof. Dr. Joost VandeVondele, for inviting me to his group in the ETH in Zürich, and teaching me with patience all there is to know about AIMD and CP2K.

- Prof. Dr. Nicolás Lorente, for welcoming me at his group at the ICN2 in Barcelona and having introduced me to the field of the Transmission theory.

- Dr. Paula Abufager, for kindly teaching me all about the Transiesta and Siesta codes.

- Dr. Koen Lauwaet and all the team of the IMDEA-Institute for performing all the scanning tunneling microscope measurements of the TCNQ and TTF self-assembled monolayers on Ag(111).

I would like to thank all the members of the committee of this thesis: Dr. Amadeo L. Vazquez, Prof. Dr. Gianfranco Pacchioni, Dr. Michele Pavone, Prof. dr. Nicolás Lorente and Dr. Lourdes Vega, Prof. Dr. Manuel Yañez and Dr. María Veronica Ganduglia Pirovano.

I would also like to acknowledge all the institutions that generously founded my fellowship (FPI program), and allowed me to run the calculations (Centro de Computación Científica de la UAM and Red Española de Supercomputación).

Finally I would like to thank my father, my mother and my brother for all their truly support, always. Also thanks to all the friends that I have made the past five years, who made my laugh and have some of the better times of my life, and to Rui, who has always been there, sharing with me the ups and the downs of the last five years.

Abstract

In this thesis we present a theoretical study of the interaction between organic molecules and metal surfaces and metal surfaces previously covered with an insulating ultrathin film. To this, we have considered several organic molecules as benzene (C_6H_6), acrylonitrile (ACN), Tetracyanoquinodimethane (TCNQ) and tetrathiafulavelene (TTF). Each of these molecules shows a different behavior when they are adsorbed on a metal surface since each of them presents well-differentiated characteristics. C_6H_6 is a benchmark system for the study of molecules containing π delocalized electrons, ACN is a representative monomer widely used in the polymer industry with cyano and vinyl groups, and TCNQ and TTF are electron acceptor and donor molecules, respectively. For the substrates, we have considered the Cu(100) and the Ag(111) metal surfaces, and the Cu(100) surface previously covered with 1, 2 or 3 NaCl layers. In this way, we have studied the following adsorbed systems: C_6H_6/Cu(100); C_6H_6/*n*NaCl/Cu(100), *n* = 1, 2, 3; ACN/Cu(100); ACN/ *n*NaCl/Cu(100), *n* = 1, 2, 3; TCNQ/Ag(111); TTF/Ag(111) and TCNQ+TTF/Ag(111). While all the adsorbates of our work have been studied in a low coverage regime, TCNQ and TTF molecules have been also studied when they form self-assembled monolayers (SAMs).
For each of them, we have evaluated adsorption energies, equilibrium geometries, electronic structure and charge transfer. In addition, dynamic simulations and transmission properties have also been studied for the systems involving the ACN and C_6H_6 adsorbates, respectively.

The theoretical methods employed in this work are widely diverse, but all of them are based on the density functional theory (DFT). We have included periodic boundary conditions to simulate all the adsorbed systems, describing the correlation effects using the Generalized Gradient Approximation, in particular the PW91 functional for all the adsorbed systems and the PBE functional for the ACN/Cu(100) and ACN/*n*NaCl/Cu(100) systems.
One of the main problems in the study of organic molecules physisorbed on a metallic substrate is the prevalence of dispersive van der Waals forces, and thus the restriction

of a straightforward application of the exchange and correlation functionals in the framework of DFT. To solve it, we have employed an approach that includes dispersion forces by a semiempirical dispersion correction, only including them in the atoms of the adsorbate and the first layer of the substrate.

Our systematic study has shown interesting charge transfer phenomena, which have been quantitative and qualitatively analyzed, and whose conclusions may have an important applicability in the nano-devices and solar cells framework. In addition, the analysis of the electronic structure for each system has allowed us to evaluate the the charge transfer phenomena in terms of energy shifting and (de-)stabilization of the metallic bands and the molecular orbitals; not only through the studied Projected Density of States, but also employing Transmission theory when a voltage is applied. Furthermore, we present a new computational strategy: the combination of static and dynamic simulations. This approach should be interesting whenever studying the adsorption of complex organic molecules on different surfaces as metals, oxides, salts, etc.
Finally, the evaluation of the molecule-molecule and molecule-surface interactions provides the key aspects behind the formation of SAMs and their consequences in the observed charge transfer processes in these systems.

Resumen

En esta tesis presentamos un estudio teórico sobre la interacción entre moléculas orgánicas y superficies metálicas, así como superficies metálicas que han sido previamente recubiertas con una fina capa de un aislante. Para ello, hemos considerado diversas moléculas orgánicas como benceno (C_6H_6), acrilonitrilo (ACN), 7,7,8,8-Tetracianoquinodimetano (TCNQ) y tetratiofulvaleno (TTF). Cada una de estas moléculas muestran distintos comportamientos cuando se adsorben sobre una superficie metálica, ya que cada una de ellas presenta características bien diferenciadas. Así, el C_6H_6 es un sistema de referencia para el estudio de aquellas moléculas que contienen electrones π deslocalizados, el ACN es un monómero representativo que se usa ampliamente en la industria de los polímeros, que contiene grupos vinilo y ciano; y el TCNQ y el TTF son moléculas aceptoras o dadoras de electrones, respectivamente. En cuanto a los substratos, hemos considerado las superficies metálicas de Cu(100) y AG(100), así como la superficie de Cu(100) previamente cubierta con 1, 2 o 3 capas de NaCl. De esta manera, hemos estudiado los siguientes sistemas: C_6H_6/Cu(100); C_6H_6/*n*NaCl/Cu(100), n = 1, 2, 3; ACN/Cu(100); ACN/ *n*NaCl/Cu(100), n = 1, 2, 3; TCNQ/Ag(111); TTF/Ag(111) and TCNQ+TTF/Ag(111). Mientras que todas las moléculas han sido estudiadas en un régimen de recubrimiento bajo, el TCNQ y el TTF también han sido estudiadas cuando forman una capa auto-ensamblada.
Para cada uno de los sistemas hemos descrito energías de adsorción, geometrías de equilibrio, estructura electrónica y transferencia de carga. Además, también hemos estudiado simulaciones de dinámica y propiedades de transmisión para los sistema que implican al ACN y al benceno, respectivamente.

Los métodos teóricos que se han utilizado en este estudio son ampliamente diversos, pero todos ellos se enmarcan en la teoría del Funcional de la Densidad. Hemos incluido condiciones periódicas de contorno para similar cada uno de los sistemas y hemos

descrito los efectos de correlación electrónica utilizando la aproximación GGA, concretamente el funcional PW91 para todos los sistemas y el PBE para los sistemas de ACN/Cu(100) y ACN/*n* NaCl/Cu(100).
Uno de los principales problemas en el estudio de moléculas orgánicas adsorbidas sobre un substrato metálico es la prevalencia de fuerzas dispersivas de tipo van der Waals, y por tanto una restricción a la hora de utilizar de manera directa y única los funcionales de intercambio y correlación que proporcional la teoría del Funcional de la Densidad. Para resolverlo, hemos utilizado una aproximación que incluye fuerzas dispersivas mediante un método de corrección semiempirical, que solo incluirá estas fuerzas en los átomos de la molécula adsorbida y en la primera capa del substrato.

Nuestro estudio muestra fenómenos de transferencia electrónica muy interesantes, que hemos analizado de manera cuantitativa y cualitativa y cuyas conclusiones pueden llegar a tener un uso en nano-dispositivos y células solares. Además, el análisis de la estructura electrónica para cada uno de estos sistemas nos ha dado la posibilidad de evaluar los fenómenos de transferencia de carga mediante la estabilización (o desestabilización) y el desplazamiento de las bandas metálicas y de los orbitales moleculares; no solo mediante el estudio de la densidad de estados proyectada, si no también aplicando teoría de transmisión cuando se aplica un voltaje. Además, hemos presentado una nueva estrategia computacional basada en la combinación de estudios tanto dinámicos como estáticos. Esta manera de enfocar el problema podría ser muy interesante siempre que se quiera estudiar la adsorción de pequeñas moléculas orgánicas sobre distintas superficies como metales, óxidos, sales, etc.
Por último, la evaluación de las interacciones molécula-molécula y molécula-superficie nos ha proporcionado los aspectos clave tras la formación de monocapas auto-ensambladas y sus consecuencias en los procesos de transferencia de carga en estos sistemas.

Contents

Results

Chapter 3: C_6H_6/*n* NaCl/Cu(100)

Chapter 4: ACN/*n* NaCl/Cu(100)

Cu(100) y el efecto de una fina capa de aislante
6.2 Compuestos a partir de adición intermolecular: AIMD como herramienta para el estudio de la superficie de energía potencial del acrilonitrilo sobre Cu(100) y sobre NaCl/Cu(100)
6.3 Moléculas dadoras y aceptoras de electrones: la combinación prometedora de TCNQ y TTF sobre un substrato metálico.
6.4 Nano-dispositivos electrónicos basados en la combinación de moléculas orgánicas y sustratos metálicos: recapitulación

Publications

Chapter 1

Introduction

1.1 The historical survey of electrical conduction in organic compounds

In the beginning of the 1960's a number of organic compounds possessing electronic conductivity were found[1,2]. These compounds awoke special interest, first of all, since they were crystals, which distinguished them completely from their inorganic counterparts. Second of all, they were synthetic and therefore a full field of tuning materials was then beginning to be developed.

Backing up to the beginning of the twentieth century, a number of articles concerning the photoconductance of anthracene and its related compounds could be found in several physics journals. For instance, in 1906, Pocchettino discovered photoconduction in solid anthracene[3]. A few years later, in 1910, Byck and Bork[4] and Steubing[5] also reported similar investigations. In 1913, the spectral response of photoconduction was reported in solid anthracene by Volmer[6] and Pauli[7]. The investigations were made by irradiation with a mercury lamp. After these publications, the work in the field was halted for almost twenty years due to the shortage of reliable descriptions of the purity of their specimens and of the experimental procedures. However, after this interruption, a succession of events brought to attention again the semiconductive properties of organic compounds; some of these events were:

I) In the middle of the 1930's, Suhrmann found an attractive phenomenon, which indicated the enhancement of the photoelectrical emission of alkali metals when

a thin film, of these same metals, was deposited on an anthracene or naphthalene film[8,9].

II) In the beginning of the 1940's, Szent-Györgyi[10] studied the charge transfer in organic substances and the photoelectrical conduction effect observed in certain color proteins.

III) Photoelectrical conduction in organic dyestuffs was found by Vartanyan[11] and his coworkers in the 1950's.

IV) The possibility of electronic conduction in the simplest synthetic compounds of graphite and carbonized materials was investigates by H. Akamatu and H. Inokuchi[1] in the beginning of the 1960's. These substances are condensed polycyclic aromatic compounds, which are situated on the series of chemical structures from benzene to graphite.

Moreover, the development of experimental techniques in the 1950's made possible to progress in the observation of electronic conduction in organic solids when exposed to light. The former compounds were organic materials including aromatic compounds, dyestuffs, and complicated substances having biochemical interest[12]. Since then, a large number of synthetic compounds, which can be named after *organic semiconductors*[13] have been found.

1.2 Organic compounds with semi-conductive properties

Solids are classified into four ideal types[14]:

I) Metals: formed by the combination of the atoms of electropositive elements, with good electrical and thermal conductivity.

II) Ionic crystals: consisting on a combination of highly electropositive and highly electronegative elements with only good ionic conductivity at only high temperatures.

III) Valence crystals: with homopolar bonds throughout the crystals and with great hardness and high melting point, though poor electronic and ionic conductivity.

IV) Molecular crystals: formed by molecules that are held together by weak interactions, typically van der Waals dispersion forces.

The last example of solid, a molecular crystal, emphasizes the reason why there are meaningful difficulties encountered in finding organic materials with some electrical conductivity: the interaction between molecules is rather weak to give good electron transfer from molecule to molecule. In addition, most of the organic materials are insulators, which is why physicists have less studied the conduction properties of organic solids. However, the semiconductive materials are usually found at the borderlines of some of the former subgroups of solids. For instance, silicon is an example of borderline solid between covalent crystal and metal. Its crystal structure is similar to the diamond one, which is a prime example of covalent solid. Nevertheless, silicon presents loose covalent bonding of valence shell electrons, contributing therefore to produce a high electrical conductivity. The concept of borderline crystals refers, thus, to those solids sharing characteristics with two or more crystals types.

Organic compounds with semiconductive properties may be classified into three different groups:

I) Compounds that have a number of delocalized electrons:

Mainly found in the groups of aromatic compounds and that consist of plane molecules having relatively large size. A remarkable point in common between these compounds is that they present valence electrons (π electrons) that can freely move throughout the molecular plane. The organic semiconductors, understood as compounds with π delocalized electrons, have a basic common structure: the benzene, C_6H_6, ring, which is the prototype of all aromatic compounds.

In this molecule, the carbon atoms lie at the vertices of a regular planar hexagon and the six hydrogen atoms lie in the same plane directed radially outward from the carbons in such a way that all the valence angles are 120^o. Therefore, of the four valence electrons ($2s^2\ 2p^2$) of the carbon atom, three hybridized in the trigonal states (sp^2 hybrid atomic orbitals) so that they give rise to localized C-C and C-H bonds. Both bonds are σ-type molecular orbitals and symmetrical around the bond axis. The fourth valence electron is unhybridized. Those six electrons are π electrons as their atomic orbitals are all directed parallel to each other and extend perpendicularly to the molecular plane having ±1 component of angular momentum around the bond direction. The pairing of these neighboring electrons leads to molecular orbitals of π-type, which are asymmetrical around the bond axis. The six π electrons occupy the molecular orbitals that extends over all six carbon atoms, since the atomic orbitals overlap both of its neighbors equally, and therefore the π electrons are completely

delocalized. This delocalization implies the mobility of the π electrons giving rise to important physical properties as well as to chemical properties that define the aromatic molecules.

II) Intermolecular addition compounds:

In this subgroup the scheme would be a large molecule where the diffuse π electrons of neighboring molecules slightly overlap. A chance of finding a large molecule would be to form one, extended linearly, with carbon atoms, instead of being planar. Examples are the usual polymers. From the point of view of organic semiconductor, structures such as $(-CH=CH-)_n$ or $(=C=C=)_n$ in linear form, should be interesting because they contain π bonds. For instance, acrylonitrile (ACN) is a prime example of molecule that form these kinds of polymers. Acrylonitrile is a highly used monomer to produce polyacrylonitrile following the so-called Sohio Process[15]. The molecule consists in a vinyl group linked to a nitrile one. However, several attempts to grow polymer films on metal substrates have presented divers drawbacks. For instance, acrylamide, acrylaldehyde or acrylonitrile itself, have been used in organic solvents as methanol or butanone, with various supporting electrolytes ($NaClO_4$, KNO_3) to coat metal substrates, presenting a poor chemical stability.

III) Electron donor and acceptor organic molecules:

They are organic compounds that can form solid molecular complexes with halogens, alkali, nitrogen, sulphur, etc. In the mid-twentieth century, Mulliken[16] proposed a charge transfer mechanism to explain the interaction in the intermolecular addition compounds. Thus, aromatic hydrocarbons, for instance, can react as electron donors or acceptors in such solid complexes. They can be seen therefore as the borderline compounds between molecular and ionic crystals.

The first organic conductors were, in fact, given by linear arrays of organic molecules forming either radical ion salts or charge transfer complexes. Molecules able to accept or donate their electron depending on their affinity or on their ionization potential form typical examples of these systems. Tetracyanoquinodimethane (TCNQ) is the prototype of an acceptor molecule. This molecule, in contact with electron donors, can form the open shell anion. The single unpaired electron will be then located mainly at the cyano groups, at the lowest unoccupied π levels.

TTF (tetrathiafulvalene) is widely used as an electron donor for its molecular

simplicity, compared to other electron donors as BET-TTF, ETTDM-TTF, ETEDT-TTF[17], etc. Furthermore, due to its basic structural unit, TTF has some important properties: (1) it can be easily oxidized due to its low oxidation potential; two eleectrons are lost in succession to reach a stable structure[18]; (2) TTF can be easily modified by chemical tenability, and the oxidation potentials of TTF derivatives can be adjusted by the introduction of electron donors or electron acceptors[19] and (3) π-π overlap and the S···S interactions can help in the stabilization of organic solids formed from this molecule.

The interaction between the former molecules, TTF-TCNQ gives rise to the prototype of a charge-transfer compound where the HOMO and LUMO bands of the open shell donors and acceptors, respectively, contribute to the conduction[20]. TTF-TCNQ is a material where molecules rearrange in parallel and uniform piles with π orbitals contributing to two conduction bands in a tight binding picture. The charge transfer in the TTF-TCNQ crystal compound is of ~0.60 e^- [21,22].

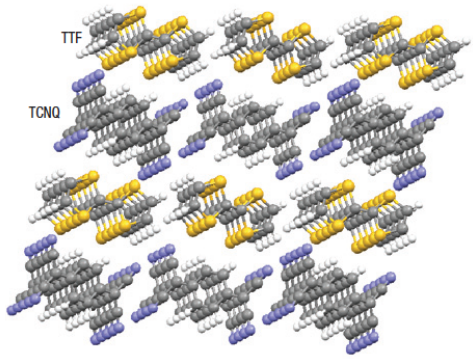

Figure 1.1: Molecular stacking of TTF-TCNQ molecules: quasi-one-dimensional, chain-like arrangement of the TTF-TCNQ molecules (Source: H. Alves, A. S. Molinari, H. Xie and A. F. Morpurgo, Nature Materials 7, 574 (2008)).

The overlap of the molecular orbitals is larger along the stack direction than between them, which makes the electron dispersion one-dimensional. In 1973 Heeger together with the Pennsylvannia group[23] found a giant conductivity peak of the order of 5 x 10^4 or 10^5 $(\Omega\ cm)^{-1}$ at 60 K just above a sharp transition towards an insulating state at lower temperature. This finding raised an especial interest in this compound and in

organic conduction altogether. The authors of this discovery even suggested that this enormous value of the conductivity could be ascribed to precursor signs of a superconductor.

However, the main dilemmas raised from the construction of organic devices is how these molecules stick together and behave when they are deposited on a substrate constituted by a different material, for instance a metal. In those cases, the molecule-metal interface and its features, completely determines the behavior of the molecular device. Therefore, there is a strong need to fully comprehend the characteristics of this region.

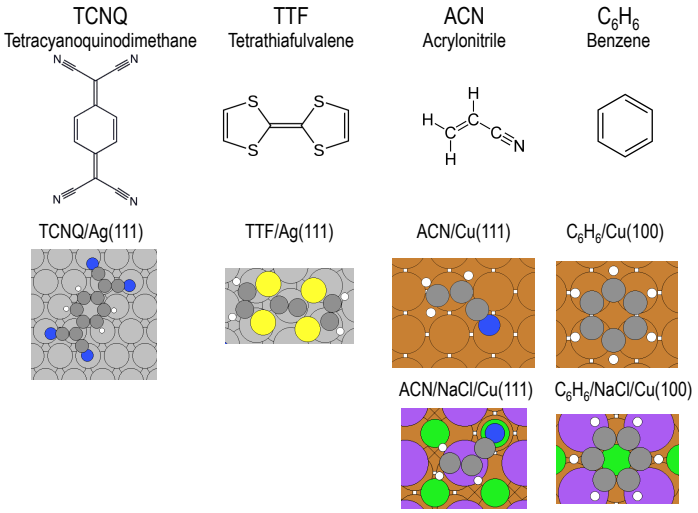

Figure 1.2: Studied molecules in this thesis (TCNQ, TTF, ACN and Benzene), as well as the substrates on which they are adsorbed (Cu, Ag and ultrathin layer of NaCl on Cu).

1.3 The molecule-metal interface at organic semiconductors

After the discovery of the organic semiconductors by Inokuchi et al.[13], they turned to the study of the charge carrier mobility in molecular single crystals. These organic semiconductors, as the Rubrene single crystals (with the highest mobility so far, 40 cm^2/Vs), have recently gained much of the attention since they present a large amount

of applications in the field of optoelectronic devices, such as light emmiting diodes (OLEDs)[24–26], organic solar cells (OSCs)[27,28] and organic field effect transistors (OFETs)[29–31]. In fact OLEDs are already used in mobile phones and are entering the commercial lighting market. On the other hand, OFETs present many applications as flexible displays and sensor systems. However, organic semiconductors present a drawback: the charge transport is often limited by their low carrier density and mobility. Thus, stable doping of the device is highly needed in order to increase this carrier density upon which is based the efficiency of many organic based devices[32].
Beyond the nowadays needs to improve these electronic devices, it is undeniable that these materials have had a huge progress and expansion as we show for instance in figure 1.3, which presents the efficiency evolution of OSCs with different solar cells technologies in the last decades.

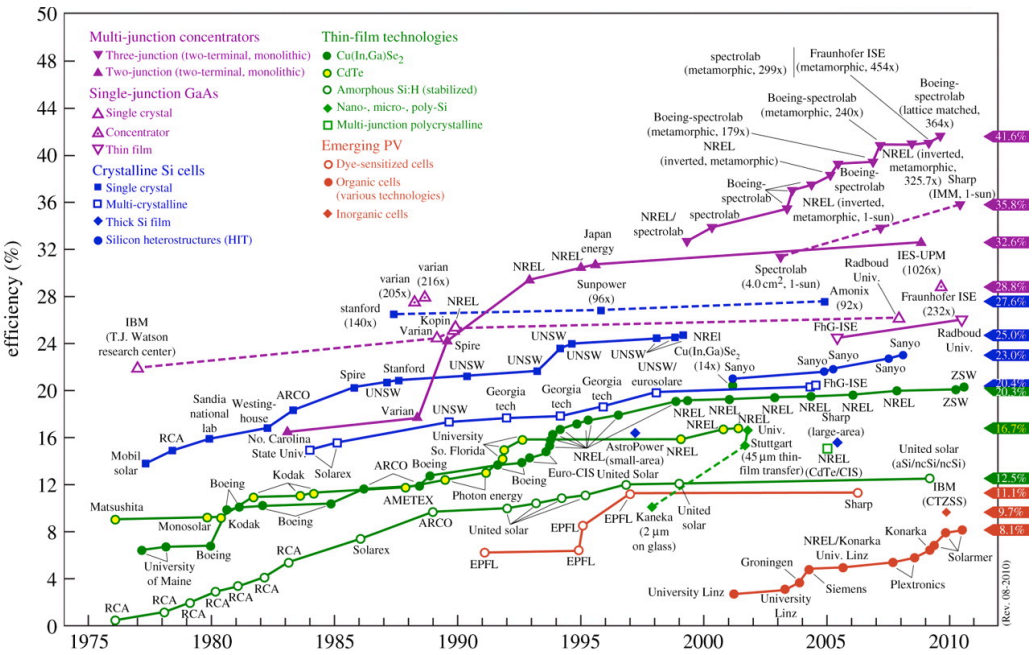

Figure 1.3: Best research solar cells efficiency (Source: L. L. Kazmerski, National Renewable Energy Laboratory (NREL), Goldem, CO).

This breakneck improvement is, beyond doubt, due to the progress and development in the science of interfaces, and the possibility to control them, and thus, a deep

understanding of the process that are taking place in between the surfaces and the adsorbates are essential in order to improve their desired abilities and to tune their properties.
These interface phenomena may be understood by investigating the direct contact between the metal and the organic semiconductor. Since the electrons fill the energy levels strictly following a Fermi-Dirac distribution, it is required that *an interface system consisting of two different materials must have a single Fermi level throughout the system when the electrons are in thermodynamic equilibrium*.

Interfaces at organic semiconductors may be divided in two subgroups:

I) Strongly interacting interfaces: new electronic states appear at the interface due to the strong electronic coupling, or even chemical bonds between the substrate and the adsorbate. These new electronic states involve an energy level alignment.
II) Weakly interacting interfaces: where no new states at the interface occur, just small modifications in the electronic structure of the metal and adsorbate can be observed.

The latter is highly significant for those processes taking place at moderate vacuum conditions or even involving solvents. In essence, to fully understand the energy level alignment and thus the applicability of organic-metal interfaces, modeling has became a fundamental tool that provides us an insight to the experimentally observed phenomena.

Two well-differentiated kingdoms treat the study of the molecule-metal interface: solid-state physics and molecular science. Both use different methods and focus on different criteria in order to describe the processes taking place in between molecules and metals. These complementary approaches are very useful for the understanding of molecule-metal interactions. Thus, as we already know, atoms in a metal stick together by a metallic bonding having the electrons delocalized over the whole structure[33]. There, the electron energy levels form continuous bands of energy, where the Fermi energy level lies within the range of one or more energy bonds, that are thus partially filled and there is no gap of energy between occupied and empty states.
On the other hand, molecules present a completely different picture: in a molecule, atoms stay together through strong molecular bonds, they do not arrange periodically,

electronic states are localized (the molecule presents discrete energy levels) and there is an energy gap between the highest occupied molecular orbital (HOMO) and the lowest unoccupied one (LUMO).
Clearing up the electronic structure of the interface is of prime interest for understanding the interaction processes and improving the performance of these devices. Thus, the interfacial issue can be divided into two aspects:

I) The energy level alignment: important for carrier injection.
II) The band bending in a thicker region: Imperative for carrier separation.

In order to understand the significance of this issue, one must start by examining the electronic structure of a single organic molecule and afterwards that for the corresponding organic solid. These organic structures will determine, together with the substrate (metal) electronic structure, the behavior of the device at the interface region. Thus, the electronic, structure of a polyatomic molecule can be described as in figure 1.4, where the effective potential well of an electron is formed by the atomic nuclei and other electrons.

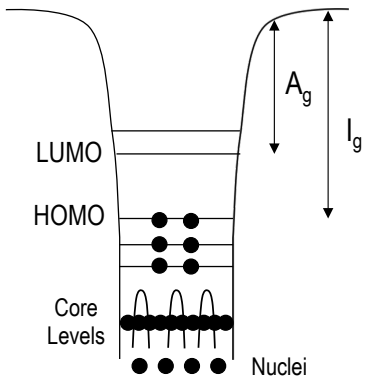

Figure 1.4: Electronic structure represented with atomic wells for a polyatomic molecule. (Source: H. Ishi et al. Adv. Mat. **1999**, 11, No. 8).

The upper part is a broad well with the atomic orbitals interacting in order to form delocalized molecular orbitals; while the deepest part of the well has atomic orbitals localized in the core levels. The horizontal fringe is the vacuum level (VL), above which the electrons can scape from the atom. On the other hand, the separations from

the HOMO and the LUMO to the VL are the gas phase ionization energy (I_g) and electron affinity (A_g) of the molecule, respectively.
On the other hand, if we have a set of organic molecules, forming an organic solid, we then face the situation depicted at figure 1.5, where molecules stick together by van der Waals dispersion forces, therefore the valence band and the conduction band are normally localized at each molecule, with thin intermolecular band widths[34,35].

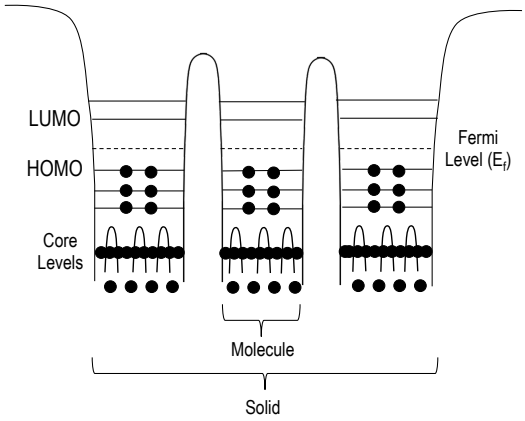

Figure 1.5: Electronic structure represented with atomic wells for an organic solid. (Source: H. Ishi et al. Adv. Mat. **1999**, 11, No. 8).

Thus, the electronic structure of a solid resemble that for a single molecule and the validity of usual bond theory (i.e. itinerant electrons) is often limited.
Over this manuscript, terms as work function (WF) or vacuum level (VL) will be continuously mentioned and discussed, hence a precise definition is needed.
The work function of the solid is defined as the energy separation between the Fermi level and the VL. When a single electron is at rest in vacuum is said to be in the VL. This VL of an electron which is at an infinite distance, VL(∞), is often taken as an invariant energy reference. However, the VL of a solid corresponds to the energy of an electron at rest just outside the solid and still being affected by this solid, V(s). The former effect of the solid on the VL(s) can be demonstrated by the dependence of the WF on the surface of a single crystal. For instance, the WF of a tungsten single crystal is 4.63, 5.25 and 4.47 eV for the (100), (110) and the (111) surfaces, respectively[36]. For a metal, the surface dipole layer determines the difference between VL(∞) and VL(s).

This surface dipole layer is formed by the tailing of the electron cloud at the surface, as shown in figure 1.6.

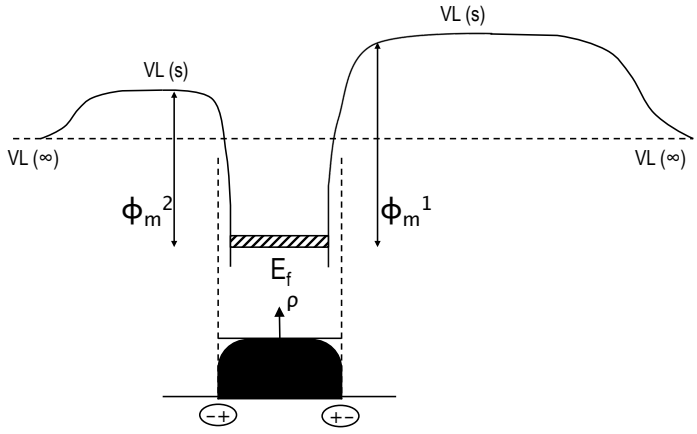

Figure 1.6: Upper part of the figure represents the potential surface for an electron in and out of the metal crystal, where E_f is the Fermi level, VL(s) is the vacuum level at the surface, VL(∞) is the vacuum level at the infinite distance and $\emptyset_m^1$ and $\emptyset_m^2$ are the work functions of different crystal surfaces. (Source: H. Ishi et al. Adv. Mat. **1999**, 11, No. 8).

The tailing of the electron cloud at the surface determines as well the different values of the WF for different surfaces.

When a metal and an organic solid are far away, they may be sharing a common VL(∞). However, when they come in contact without rearrangement of the electric charge, the organic layer is now in the region of the potential created by the surface dipole of the metal, and its energy levels rise up in order to have a common VL(s) in a narrow interfacial gap.

The dipole layer may be formed at the interface due to the charge transfer, redistribution of the electron cloud, interfacial chemical reactions, etc. The former interfacial dipole will create a brusque shift of the potential across the dipole layer leading to a shift, ΔVL, where Δ is determined by the magnitude of the dipole, as shown in figure 1.7.

The deposition and adsorption of molecules on metal surfaces create this shift of the VL[37,38] and it is called the change in the WF of the metal, $\Delta\phi$.

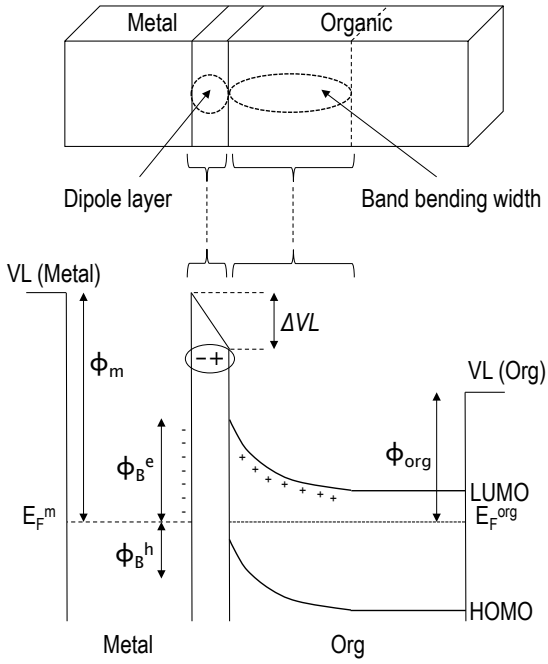

Figure 1.7: Hypothetical energy level alignment at thermal equilibrium of the electron system for the direct contact between a metal and an organic semiconductor, which are directly contacted to from an interface. Where E_f^m and E_f^{org} are the Fermi level of the metal and the organic layer, respectively, VL is the vacuum level at the surface and $\emptyset_B^h$, $\emptyset_B^e$, $\emptyset_m$, $\emptyset_{org}$ are the injection carriers for the electron and hole, and the work function for the metal and the organic semi-conductor, respectively.

1.4 Structure of the manuscript

This thesis is organized as follows:
The second part of this manuscript, chapter 2, provides the theoretical fundamentals behind the calculations carried on for this thesis. These calculations have been performed using quantum chemistry techniques (Density Functional Theory, Molecular Dynamics, etc.) employing several programs as VASP[39,40], CP2K[41-46], SIESTA[47] and TranSiesta.

In the following chapters we discuss the obtained results. Chapter 3 is devoted to the interaction between benzene and the Cu(100) surface, as well as the influence of adding an ultrathin insulating film, NaCl, in between C_6H_6 and copper. The final part of this chapter also includes the discussion of applying an electric current in between two copper leads, connected with a benzene molecule. Chapter 4 presents the interaction between the acrylonitrile monomer and the Cu(100) surface, as well as the Cu(100) surface previously covered with NaCl. However, a different perspective is offered, compared to chapter 3, by introducing a new technique: Molecular dynamics. Finally, chapter 4 is devoted to the interaction of TCNQ and TTF molecules with the Ag(111) surface. We present the interaction of low regime coverage of the surface, as well as the SAM of TCNQ, TTF and the mix of both (TCNQ+TTF) molecules. In each of these chapters, we have included a thorough discussion that corresponded to each one. Finally, chapter 5 summarizes the most relevant conclusions.

References

(1) Akamatu H.; Inokuchi H. *Proc. Third Conf. Carbon* 1959, 51.
(2) Garret C.G.B. *Semicond. NB Hannay Ed* 1959, 634.
(3) Pocchettino A. *Acad Licei Red* 1906, *15*, 355.
(4) ByckandA.; Bork H. *Ber Deut Phys. Ges* 1910, *8*, 621.
(5) Steubig. *Ber Deut Phys. Ges* 1910, *8*, 867.
(6) Volmer M. *Ann Phys.* 1913, *4*, 775.
(7) Pauli W. E. *Ann Phys.* 1913, *4*, 677.
(8) Suhrmann R. *Z Phys.* 1935, *94*, 742.
(9) Suhrmann R. *Z Phys.* 1937, *111*, 18.
(10) Szent-Györgyi A. *Nature* 1941, *148*, 157.
(11) Vartanyan A. T. *Dokl. Akad Nauk SSSR* 1950, *71*, 641.
(12) Arnold W.; Sherwood H.K. *Proceeding Natl. Acad. Sci. USA* 1957, *43*, 105.
(13) Inokuchi H. *Bull. Chem. Soc. Jpn.* 1954, *27*, 22.
(14) Seitz F. *Modern Theory of Solids*; McGraw-Hill: New York, 1940.
(15) *The Sohio Acrylonitrile Process*; American Chemical Society National Historic Chemical Landmarks, 2007.
(16) Mulliken R.S. *J. Am. Chem. Soc.* 1952, *74*, 811.
(17) Hui Jiang; Xianjin Yang; Zhenduo Cui; Yongchang Liu; Hongxiang Li; Wenping Hu; Christian Kloc. *CrystEngComm* 2014, *16*, 5968.
(18) Bendikov M.; Wudl F.; PerepichkaD.F. *Chem. Rev.* 2004, *104*, 4891–4945.
(19) Bryce M.R. *J. Mater. Chem.* 2000, *10*, 589–598.
(20) Wudl, F.; Smith, G.; Hufnagel, E. *J. Chem. Soc. Chem. Commun.* 1970, *32*, 1453.
(21) Comes R.; Shapiro S.M.; Shirane G.; Garito A.F.; Heeger J. *Phys. Rev. Lett.* 1975, *35*, 1518.
(22) Denoyer F.; Comes F.; Garito A.F.; Heeger J. *Phys. Rev. Lett.* 1975, *35*, 445.
(23) Coleman L. *Solid State Commun.* 1973, *12*, 1125.
(24) Forrest, S.R. *Chem. Rev.* 1997, *97*, 1793.
(25) Hung, L.S.; Chen, C.H. *Mater. Sci. Eng.* 2002, *39*, 143.
(26) Walzer K.; Maennig B.; Pfeiffer M.; Leo K. *Chem. Rev.* 2007, *107*, 1233.
(27) Peumans P.; Yakimov A.; Forrest S.R. *J. Appl. Phys.* 2003, *93*, 3693.
(28) Shaheen S.E.; Ginley D.S.; Jabbour G. E. *Mater. Res. Soc. Bull.* 2005, *30*, 10–52.
(29) Dimitrakopoulos C.D.; Macaro, D. J. *IBM J. Res. Dev.* 2001, *45*, 11.
(30) Dimitrakopoulos C.D.; Malenfant P.R.L. *Adv. Matter* 2002, *14*, 99.
(31) Wen Y.; Liu Y.; Guo Y.; Yu G.; Hu W. *Chem. Rev.* 2011, *111*, 3358.
(32) Gao Yu. *Mater. Sci. Eng.* 2010, *68*, 39.
(33) Ashcroft N.W.; Mermin N.D. *Solid State Physics*; Cornell University, 1976.
(34) Kao K.C.; Hwang W. *Electrical Transport in Solids*; Pergamon, Oxford, 1981.
(35) Gutman F.; Lyons L. E. *Organic Semiconductors*; Wiley, New York, 1967.
(36) Strayer R.A.; Mackie W.; Swanson L.W. *Surf. Sci.* 1973, *34*, 225.
(37) Woodruff D.P.; Delchar T.A. *Modern Techniques of Surface Science*; Cambridge University Press: Cambridge, 1986.
(38) Hoelzel J.; Schulte F.K.; Wagner H. *Solid State SUrface Physics*; Springer: Berlin, 1979.

(39)Kresse, G.; Furthmühller. *J. Phys. Rev. B* 1996, *54*, 11169.
(40)Kresse, G.; Furthmühller, J. *J. Comput. Mater. Sci.* 1996, *6*, 15.
(41) Krack M. *Theor. Chem. Acc.* 2005, *114* (1-3), 145–152.
(42) VandeVondele, J; Krack, M; Mohamed, F; Parrinello, M; Chassaing, T; Hutter, J. *J. Comput. Phys. Commun.* 2005, *167* (2), 103–128.
(43) Frigo, M; Johnson. *Proc. IEEE* 2005, *93* (2), 216–231.
(44) VandeVondele, J; Hutter, J. *J. Chem. Phys.* 2003, *118* (10), 4365–4369.
(45) Hartwigsen, C; Goedecker, S; Hutter, J. *Phys. Rev. B* 1998, *58*, 3641–3662.
(46) Lippert, G; Hutter, J; Parrinello, M. *Mol. Phys.* 1997, *92* (3), 477–487.
(47)J. M. Soler; E. Artacho;J. D. Gale; A. García; J. Junquera,P. Ordejón, and D. Sánchez-Portal, *J. Phys.: Condens. Matt.* 14, 2745-2779 (2002).

Chapter 2

Theoretical Methods

One of the most important scientific advances of the twentieth century is the development of quantum mechanics. Most important is that repeated experiments observations confirm time after time how this new theory describes with extraordinary accuracy the world we live in.

2.1 The Schrödinger Equation

Any problem we shall deal with on the electronic structure of matter is covered by solving the time-dependent Schrödinger equation. Nevertheless, for our purpose, since we are concern in the description of systems without time-dependent interactions, we are going to focus on the time-independent Schrödinger equation, meaning that the potential energy, V, does not depend on the time any more, but only on the space coordinates (x).

Starting from the time-dependent equation,

$$-\frac{\hbar}{\mathrm{i}}\frac{\partial\Psi(\mathrm{x,t})}{\partial\mathrm{t}} = -\left(\frac{\hbar}{2\mathrm{m}}\right)^2\frac{\partial^2\Psi(\mathrm{x,t})}{\partial\mathrm{x}^2} + \mathrm{V(x)}\Psi(\mathrm{x,t}) \tag{2.1}$$

We can write this equation as a product of two functions, one describing the change of the function in time, the other one describing the change in space.

$$\Psi(\mathrm{x,t}) = \mathrm{f(t)}\phi(\mathrm{x}) \tag{2.2}$$

If we derivate Eq. 2.2 as a function of t and as a function of x, namely we do partial derivates, we get

$$\frac{\partial \Psi(x,t)}{\partial t} = \frac{df(t)}{dt}\Psi(x);\ \frac{\partial^2 \Psi(x,t)}{\partial x^2} = f(t)\frac{d^2\Psi(x)}{dx^2} \tag{2.3}$$

Substituting Eq. 2.3 in Eq. 2.1

$$-\frac{\hbar}{i}\frac{df(t)}{dt}\Psi(x) = -\left(\frac{\hbar}{2m}\right)^2 f(t)\frac{d^2\Psi(x)}{dx^2} + V(x)f(t)\phi(x) \tag{2.4}$$

If we simplify this equation by dividing it by $f\phi$ we reach Eq. 2.5

$$-\frac{\hbar}{i}\frac{1}{f(t)}\frac{df(t)}{dt} = -\left(\frac{\hbar}{2m}\right)^2 \frac{1}{\phi(x)}\frac{d^2\phi(x)}{dx^2} + V(x) \tag{2.5}$$

If we take a look at the equation above, we notice how the left side of it depends only on t, and therefore the right side should depend on t as well. Nevertheless, the right side is dependent on the variable x, implying that the left side should depend on x too, what we have already seen that it is not the case. This "problem" can only be solved by assuming that both sides of Eq. 2.5 are a constant, namely E. And if we equal left side of Eq. 2.5 to E, we get:

$$\frac{df(t)}{f(t)} = -\frac{i}{\hbar}E\,dt \tag{2.6}$$

Which after integrating gives us

$$\int \frac{df(t)}{f(t)} = -\int \frac{i}{\hbar}E\,dt$$
$$\ln f(t) = -\frac{i\,t}{\hbar}E + C \tag{2.7}$$

Where C is an arbitrary integration constant. If we express Eq. 2.7 with exponentials we come to

$$f(t) = e^C e^{-iEt/\hbar} = A\,e^{-iEt/\hbar} \tag{2.8}$$

The constant A has replaced e^c. Thus, we can consider A as a factor that belongs to the function $\phi(x)$, which is multiplying $f(t)$ in Eq. 2.2, and therefore omit it.
Following, one can equal right side of Eq. 2.5 to E, and obtain

$$-\left(\frac{\hbar}{2m}\right)^2 \frac{d^2\phi(x)}{dx^2} + V(x)\phi(x) = E\phi(x) \tag{2.9}$$

Which is the so-called *time-independent Schrödinger equation* for a particle of mass m that is moving in one dimension. The constant E, we have been working with, has the same dimensions as V, the potential energy. Thus, E is postulated to be the total energy of the system.
In those cases where the potential, V, is just a function of spatial coordinates, there will be wavefunctions that look like

$$\Psi(x,t) = e^{-iEt/\hbar}\,\phi(x) \tag{2.10}$$

The wavefunction in Eq. 2.10 describes a state that is constant in energy. The exponential term makes the wavefunction be a complex equation.
However, what we can experimentally observe is the density of probability $|\Psi(x,t)|^2$. The square of this absolute value is given by the product of this quantity, $\Psi(x,t)$, by its complex conjugate, $\Psi^*(x,t)$.

$$|\Psi|^2 = \Psi\Psi^* \tag{2.11}$$

$$|\Psi(x,t)|^2 = \left[e^{-iEt/\hbar}\,\phi(x)\right]^* e^{-iEt/\hbar}\,\phi(x) = \phi^*(x)\,\phi(x) = |\phi(x)|^2 \tag{2.12}$$

To reach Eq. 2.12, E is a real number, namely $E = E^*$, which is a consequence of the hermitian hamiltonian. From the former equation we conclude that those states described by Eq. 2.10 are called *Stationary States* since their density of probability is given by $|\phi(x)|^2$ and does not depend on the time.
Eq. 2.9 can be written for an N-electron atomic or molecular system (in the Born-Oppenheimer non-relativistic approximation) as follows

$$\left[\sum_{i=1}^{N}\left(-\frac{1}{2}\nabla_i^2\right) + \sum_{i=1}^{N} v(\mathbf{r}_i) + \sum_{i<j}^{N}\frac{1}{r_{ij}}\right]\phi(x) = E\,\phi(x) \tag{2.13}$$

In which

$$v(\mathbf{r}_i) = -\sum_\alpha \frac{Z_\alpha}{\mathbf{r}_{i\alpha}} \tag{2.14}$$

Is the "external" potential acting on electron i due to the charges of nuclei, Z_α.
Eq. 2.13 can be more simply and compactly written as the well-known Eq. 2.15

$$\hat{H}\Psi = E\Psi \tag{2.15}$$

Where $\hat{H}$ is the Hamiltonian, given by Eq. 2.16, E is the electronic energy (we are considering Born-Oppenheimer approximation, which is the assumption that atomic nuclei and electronic motion in a molecule can be separated) and $\phi = \phi\,(x_1, x_2, x_3 \ldots x_N)$ is the wavefunction. The coordinates $x_1, x_2, x_3 \ldots x_N$ in the wavefunction embrace, not only space coordinates, $\mathbf{r}_i$, but also spin coordinates, s_i.
Focusing now on the Hamiltonian

$$\hat{H} = [\sum_{i=1}^{N}(-\frac{1}{2}\nabla_i^2) + \sum_{i=1}^{N} v(\mathbf{r}_i) + \sum_{i<j}^{N} \frac{1}{r_{ij}}] \tag{2.16}$$

It can be written shorter as

$$\hat{H} = \hat{T} + \hat{V}_{Ne} + \hat{V}_{ee} \tag{2.17}$$

where

$$\hat{T} = \sum_{i=1}^{N}(-\frac{1}{2}\nabla_i^2) \tag{2.18}$$

is the kinetic energy operator;

$$\hat{V}_{Ne} = \sum_{i=1}^{N} v(\mathbf{r}_i) \tag{2.19}$$

is the electron-nucleus potential energy operator and

$$\hat{V}_{ee} = \sum_{i<j}^{N} \frac{1}{r_{ij}} \tag{2.20}$$

is the repulsion energy operator.
The total energy however is given by the sum of the electronic energy E and the nucleus-nucleus repulsion energy, V_{NN}.

$$V_{NN} = \sum_{\alpha<\beta} \frac{Z_\alpha Z_\beta}{R_{\alpha\beta}} \tag{2.21}$$

There is no difference between solving Eq. 2.15 for E (the electronic energy) and adding V_{NN} afterwards, or including V_{NN} in the definition of $\hat{H}$ from the beginning.
Up to now we have described the Hamiltonian, but we have barely talked about the wavefunction. Although the electron wavefunction is a function of each of the coordinates of all N electrons, it is possible to approximate ϕ as a product of individual wavefunctions,

$$\phi = \phi_1 \phi_2 \dots \phi_N \tag{2.22}$$

Where we have neglected electron spin in our presentation, for clarity of description.
Please note that we are designating as ϕ the electronic wavefunction, whereas Ψ is the "total" time-dependent wavefunction.
The expression for the wavefunction in Eq. 2.22 is known as the *Hartree product*, and the fact of expressing ϕ as a product of individual monoelectronic functions is well motivated, as we are going to see in following sections of this chapter.
Since the Schrödinger Equation is a many-body problem, the individual monoelectronic wavefunction cannot be solved without considering, at the same time, the contribution of all others one-electron wavefunctions.

2.2 The Hartree-Fock Approximation

If we have a system, let say Ψ, which a priori may or may not satisfy Eq. 2.15, the average of measurements of the energy will be given by

$$E[\Psi] = \frac{\langle \Psi | \hat{H} | \Psi \rangle}{\langle \Psi | \Psi \rangle} \tag{2.23}$$

where

$$\langle \Psi | \hat{H} | \Psi \rangle = \int \Psi^* \hat{H} \Psi \, dx \tag{2.24}$$

Furthermore, since each particular measurement we make of the energy will give us a certain value of the Hamiltonian, we can immediately conclude that

$$E[\Psi] \geq E_0 \tag{2.25}$$

Namely, the computed energy for an initial guess wavefunction, Ψ, is an upper bound to the true ground energy, E_0. This is the so-called *Variational Principle*, and implies that full minimization of the functional $E[\Psi]$ with respect to the N-electron wavefunction gives us the true ground state and energy

$$E_0 = min\, E[\Psi] \tag{2.26}$$

Because electrons are fermions, the wavefunction must change its sign if two electrons change places with each other.
This is known as the *Antisymmetry Principle* and, unfortunately, the Hartree Product we saw in Eq. 2.22 does not satisfy it. In order to comply with this requirement the wavefunction must be defined by as a Slater determinant, which is an antisymmetrized product of N orthonormal spin orbitals $\phi_i(x)$. Each spin orbital is a product of $\phi_k(\mathbf{r})$, a spatial orbital and $\sigma(s) = \alpha(s)$ or $\beta(s)$, a spin function.

$$\Psi_{HF} = \frac{1}{\sqrt{N!}} \begin{vmatrix} \phi_1(x_1) & \phi_2(x_1) \dots & \phi_N(x_1) \\ \phi_1(x_2) & \phi_2(x_2) \dots & \phi_N(x_2) \\ \phi_1(x_N) & \phi_2(x_N) \dots & \phi_N(x_N) \end{vmatrix}$$
$$= \frac{1}{\sqrt{N!}} \det[\phi_1 \phi_2 \dots \phi_N] \tag{2.27}$$

The orthonormal orbitals, ϕ_i, that satisfy Eq. 2.27 comprise the Hartree-Fock approximation.
Since the normalization formula $\langle \Psi_{HF} | \Psi_{HF} \rangle$ is equal to 1 due to the fact that we are dealing with orthonormal orbitals, we reach the following expression

$$E_{HF} = \langle \Psi_{HF} | \hat{H} | \Psi_{HF} \rangle = \sum_{i=1}^{N} h_i + \sum_{i<j} (J_{ij} - K_{ij}) \quad (2.28)$$

where h_i describes the kinetic and potential energy of electron i

$$h_i = \int \phi_i^*(x) \left[-\frac{1}{2} \nabla_i^2 + v_i(x) \right] \phi_i(x)\, dx \quad (2.29)$$

J_{ij} is called the Coulomb integral

$$J_{ij} = \iint \phi_i(x_1) \phi_i^*(x_1) \frac{1}{r_{ij}} \phi_j^*(x_2) \phi_j(x_2)\, dx_1\, dx_2 \quad (2.30)$$

and K_{ij} is the Exchange integral

$$K_{ij} = \iint \phi_i^*(x_1)\, \phi_j(x_1) \frac{1}{r_{ij}} \phi_i(x_2) \phi_j^*(x_2)\, dx_1\, dx_2 \quad (2.31)$$

We note that in Eq. 2.28 the sum over Coulomb and Exchange integrals is over pair of states. Furthermore, if we take into account that $J_{ij} = J_{ji}$ and $K_{ij} = K_{ji}$, and that by the definition of Coulomb and Exchange integrals $J_{ii} = K_{ii}$, we can write right side of Eq. 2.28 in another way

$$\langle \Psi_{HF} | \hat{H} | \Psi_{HF} \rangle = \sum_{i=1}^{N} \frac{1}{2} h_i + \sum_{i=1}^{N} \sum_{j=1}^{N} (J_{ij} - K_{ij}) \quad (2.32)$$

Minimization of Eq. 2.32, considering orthonormalization conditions

$$\int \phi_i^*(x) \phi_j(x) dx = \delta_{ij} \quad (2.33)$$

gives us the Hartree-Fock differential equation

$$\hat{F} \phi_i(x) = \sum_{j=1}^{N} \varepsilon_{ij} \phi_j(x) \quad (2.34)$$

Where $\hat{F}$ is the Fock operator, which is given by the sum of kinetic energy, potential energy and the Coulomb-Exchange operator $\hat{g} = \hat{j} - \hat{k}$

$$\hat{F} = -\frac{1}{2}\nabla^2 + v + \hat{g} \tag{2.35}$$

here

$$\hat{j}(x_1)f(x_1) = \sum_{k=1}^{N} \int \phi_k^*(x_2)\phi_k(x_2)\ \frac{1}{r_{12}}\ f(x_1)\ dx_2 \tag{2.36}$$

and

$$\hat{k}(x_1)f(x_1) = \sum_{k=1}^{N} \int \phi_k^*(x_2)f_k(x_2)\ \frac{1}{r_{12}}\ \phi(x_1)\ dx_2 \tag{2.37}$$

with f (x_1) being an arbitrary function.
The matrix ε_{ij} in Eq. 2.34 consists of a set of Lagrange multipliers, which satisfy the constraints of Eq. 2.33. Also ε_{ij} is Hermitian and therefore

$$\varepsilon_{ji}^* = \varepsilon_{ij} \tag{2.38}$$

If we now multiply Eq. 2.34 by ϕ_i^* and integrate, we obtain the *Orbital Energies*.

$$\varepsilon_{ii} = \int \phi_i^*(x)\ \hat{F}\ \phi_i(x)\ dx = h_i + \sum_{j=1}^{N}\left(J_{ij} - K_{ij}\right) \tag{2.39}$$

If we now sum over i and compare Eq. 2.39 with Eq. 2.32, we reach

$$E_{HF} = \sum_{i=1}^{N} \varepsilon_i - V_{ee} \tag{2.40}$$

where V_{ee} is the total electron-electron repulsion energy

$$\begin{aligned} V_{ee} &= \int \Psi_{HF}^*(x)\left[\sum_{i<j}\frac{1}{r_{ij}}\right]\Psi_{HF}(x)dx \\ &= \frac{1}{2}\sum_{i=1}^{N}\sum_{j=1}^{N}(J_{ij} - K_{ij}) \end{aligned} \tag{2.41}$$

Solution of Eq. 2.34 must proceed iteratively since the orbitals ϕ_i that solve the problem are included in the Fock operator. Therefore, the Hartree-Fock method is a *Self-Consistent Field* method.

Summarizing what we have seen up to now, Hartree-Fock provides an exact description of electron exchange. Namely, Hartree-Fock wavefunction has exactly the same features as the true solutions of the full Schrödinger equation when the coordinates of two or more electrons are exchanged. In fact, if it would be possible to use an infinitely large basis set, the calculated energy for N electrons is known as the Hartree-Fock limit. Nevertheless, this will not be the true electron wavefunction since the HF Method is not able to describe correctly how electrons influence other electrons. That is to say, the HF Method does not deal with electron correlations. We discuss in the next section how to take into account the electron correlation, but before we get into it, we shall explain the Restricted Hartree-Fock (RHF) and the Unrestricted Hartree-Fock (UHF) Methods, since we are dealing in our present work with closed and open electron shell systems.
Let's imagine we have a set of n spatial orbitals ($\phi_1, \phi_2 \ldots \phi_n$), so they will form 2n spin orbitals since each spatial orbital can be multiplied by an α or a β spin function; and therefore we get

$$\phi_i = \phi_i(\mathbf{r})\,\alpha(s)$$
$$\overline{\phi}_i = \phi_i(\mathbf{r})\,\beta(s) \qquad (2.42)$$

These are the so-called *Restricted Spin Orbitals* and they give rise to a restricted determinant. In the former one can have a spatial orbital ϕ_i being occupied either by a single electron (α or β spin) or by two electrons (α and β spin).
A closed shell configuration is given by a doubly occupied spatial orbital. On the other hand an open shell configuration refers to singly occupied spatial orbitals.
In the RHF theory electrons are forced to occupy the same spatial orbital irrespective of being α or β: This constraint has the advantage of giving rise to a determinant, formed by a set of $\{\phi_i\}$, that is eigenfunction of S^2 (see below). The disadvantage is that this constraint ignores the correlation between two electrons with α and β spins occupying the same spatial orbital.
On the other hand, the UHF theory has no restrictions on the spatial nature of the orbitals and the set of spin orbitals has the form

$$\phi_i = \phi_i(\mathbf{r})\,\alpha(s)$$
$$\phi'_i = \phi'_i(\mathbf{r})\,\beta(s) \qquad (2.43)$$

Eq. (2.42) implies that α spin electrons are represented by a set of spatial orbitals, $\{\phi_i\}$, while β spin electrons will be given a different set, $\{\phi_i'\}$. However, UHF theory gives an unrestricted wavefunction that is not eigenfunction of S^2.
To illustrate this point, let's consider a closed shell specie with $1s^2$ electronic configuration. Whose wavefunction, following RHF theory, is given by

$$\Psi = \frac{1}{\sqrt{2}}\{\phi_1(1)\alpha(1)\ \phi_1(2)\beta(2) - \phi_1(1)\beta(1)\ \phi_1(2)\alpha(2)\} \tag{2.44}$$

The operator $\hat{S}^2$ can be written as

$$\hat{S}^2 = \hat{S}_-\hat{S}_+ + \hat{S}_z + \hat{S}_z^2 \tag{2.45}$$

Since there are two electrons in the system

$$\hat{S}_+ = \hat{S}_{+,1} + \hat{S}_{+,2} \tag{2.46}$$

$$\hat{S}_+\Psi = \hat{S}_{+,1}\Psi + \hat{S}_{+,2}\Psi \tag{2.47}$$

We have

$$\hat{S}_{+,1}\Psi = \frac{1}{\sqrt{2}}[0 - \phi_1(1)\alpha(1)\phi_1(1)\alpha(2)]$$
$$\hat{S}_{+,2}\Psi = \frac{1}{\sqrt{2}}[\phi_1(1)\alpha(1)\phi_2(2)\alpha(2) - 0] \tag{2.48}$$

$$\hat{S}_{+,1} + \hat{S}_{+,2} = 0 \tag{2.49}$$
$$\hat{S}_z\Psi = \left(\hat{S}_{z,1} + \hat{S}_{z,2}\right)\Psi = 0 \tag{2.50}$$
$$\hat{S}_z^2\Psi = \hat{S}_z\hat{S}_z\Psi = 0 \tag{2.51}$$
$$\hat{S}^2\Psi = 0 \tag{2.52}$$

This means that the multiplicity state is $2 \text{ x } 0 + 1 = 1$, i.e. singlet state. And therefore, the above two electron wavefunction is an eigenfunction of $\hat{S}^2$.

Let's now consider a $1s^2 2s^1$ electronic configuration with doublet spin multiplicity. If $1s\alpha$, $1s\beta$ and $2s\alpha$ spin orbitals are chosen to appear in Ψ, the Fock operator becomes (using Eq. 2.39)

$$\hat{F} = h + J_{1s\alpha} + J_{1s\beta} + J_{2s\alpha} - [K_{1s\alpha} + K_{1s\beta} + K_{2s\alpha}] \quad (2.53)$$

This operator, when acting on a α-spin orbital gives us

$$\hat{F} = h\phi_{j\alpha} + [J_{1s\alpha} + J_{1s\beta} + J_{2s\alpha}]\phi_{j\alpha} - [K_{1s\alpha} + K_{1s\beta} + K_{2s\alpha}]\phi_{j\alpha} \quad (2.54)$$

Where $\phi_{j\alpha}$ is a α spin orbital. In contrast, when acting on a β spin orbital $\phi_{j\beta}$

$$\hat{F} = h\phi_{j\beta} + \left[J_{1s\alpha} + J_{1s\beta} + J_{2s\alpha}\right]\phi_{j\beta} - K_{1s\beta}\phi_{j\beta} \quad (2.55)$$

Equations 2.54 and 2.55 show that the spin orbital of α and β spins do not experience the same exchange potential and therefore $1s\alpha$ and $1s\beta$ are solutions of two different Fock equations.
Consequently, they have different energies and are not spatially identical. Such determinant $\|1s_\alpha\ 1s'_\beta\ 2s_\alpha\|$ is not a pure doublet spin eigenfunction, as we previously explained.

2.3 Electron Correlation Energy

The electron correlation energy is the difference between the Hartree-Fock limit and the exact ground state energy. The exact wavefunction of a system of many interacting electrons is not a single determinant, as the Hartree-Fock method proposes. In fact, many advanced quantum chemical approaches aim to improve the Hartree-Fock method including this electron correlation energy adding a combination of a few determinants, these are the so-called *Multiconfigurational Methods*; on the other hand, others try to include using many-body perturbation techniques.
Correlation energy tends to remain constant for atomic and molecular changes that do not involve any change on the type and number of chemical bonds, but when these

bonds do change the correlation energy magnitude can vary from 20 or 30 to thousands of kilocalories per mol. It is therefore a term of the total energy of the system that one must take with the utmost care.

2.4 Electron Density

The electron density for a given state is defined as the number of electrons per unit volume of the mentioned state. We will designate it from now on as $\rho(\mathbf{r})$, and it can be expressed as

$$\rho(\mathbf{r}_1) = N \int \dots \int |\Psi(x_1, x_2, \dots, x_N)|^2 \, ds_1 \, dx_2 \dots dx_N \tag{2.55}$$

This is a nonnegative simple function of three variables, x, y and z integrating to the total number of electrons

$$\int \rho(\mathbf{r}) dr = N \tag{2.57}$$

We now that electrons are indistinguishable, so somehow the wavefunction Ψ contains more information than we can actually even use. In fact the only thing we directly observe is the electron density, which gives us the total number of electrons within a volume element. In the following sections we show how a whole theory can be built based just on this function (i.e. Eq. 2.57): the Density Functional Theory.

2.5 Density Functional Theory

2.5.1 Thomas-Fermi Model

The history of Density Functional Theory (DFT) begins in the 1920's, when Thomas and Fermi suggested describing atoms as uniformly distributed electrons, namely negatively charged clouds. These authors realized that the distribution of electrons in

atoms could be approximated through statistics considerations. This is an enormous simplification of the many-body problem that presents the Schrödinger Equation, since they proposed that the total energy of the system could be presented as a functional of the electron density.

L. H. Thomas[1] stated that: "Electrons are distributed uniformly in the six-dimensional phase space for the motion of an electron at the rate of two for each h^3 of volume", and that there is an effective potential field that "is itself determined by the nuclear charge and this distribution of electrons".

In order to derive Thomas-Fermi formulae, we will begin by considering the division of space into many small cubes or cells, each one of side l and therefore volume $\Delta V = l^3$. Each of these cells contains a fixed number of electrons, ΔN. This number may differ between different cells. Last, but not least we assume the electrons of each cell behave as independent fermions at 0 K.

On the other hand, the energy levels of a particle in a three-dimensional infinite well are given by

$$E(n_x, n_y, n_z) = \frac{h^2}{8ml^2}\left(n_x^2 + n_y^2 + n_z^2\right) = \frac{h^2}{8ml^2}R^2 \tag{2.58}$$

where the radius, R, of the sphere in the space (n_x, n_y, n_z) covering all occupied states, determines the maximum energy of electrons, which is known as *Fermi Energy*.

The number of energy levels within this maximum value at 0 K is given by

$$N_f = \frac{1}{2^3}\frac{4\pi R^3}{3} = \frac{\pi}{6}\left(\frac{8ml^2}{h^2}\right)^{\frac{3}{2}} \tag{2.59}$$

The number of energy levels between E and $E + dE$ is consequently

$$\begin{aligned} g(E)dE &= N_f(E + dE) - N_f(E) \\ &= \frac{\pi}{4}\left(\frac{8ml^2}{h^2}\right)^{\frac{3}{2}} E^{\frac{1}{2}}\, dE \end{aligned} \tag{2.60}$$

where $g(E)$ is the *Density of States* at energy E.

We will now define the Fermi-Dirac distribution, which is the probability for the state with energy E, to be occupied.
The Fermi-Dirac distribution is necessary in order to compute the total energy of the cell with ΔN electrons, and is given by the formula

$$f(E) = \frac{1}{1+e^{(E-E_f)/kT}} \tag{2.61}$$

where E_f is the already mentioned Fermi Energy.

Eq. 2.61 reduces, at 0 K, to a step function:

$$f(E) = \begin{matrix} 1, & E < E_f \\ 0, & E > E_f \end{matrix} \tag{2.62}$$

i.e. those states with energy smaller than E_f are occupied and those with energy greater than E_f are empty.
If we sum all the contributions from the different energy states, we will obtain the total energy of the electrons in this cell

$$\begin{aligned} \Delta E &= 2 \int E\, f(E) g(E) dE \\ &= 4\pi \left(\frac{2m}{h^2}\right)^{\frac{3}{2}} l^3 \int_0^{E_f} E^{\frac{3}{2}}\, dE \\ &= \frac{8\pi}{5} \left(\frac{2m}{h^2}\right)^{\frac{3}{2}} l^3\, E_f^{5/2} \end{aligned} \tag{2.63}$$

The factor 2 in Eq. 2.63 is due to the fact that each energy level is doubly occupied by an α and a β spin electrons.

The Fermi energy, E_f, can be related with the number of electrons in the cell, ΔN,

$$\begin{aligned} \Delta N &= 2 \int f(E) g(E) dE \\ &= \frac{8\pi}{3} \left(\frac{2m}{h^2}\right)^{\frac{3}{2}} l^3\, E_f^{3/2} \end{aligned} \tag{2.64}$$

Eliminating E_f from Eq. 2.63 by Eq. 2.64 one obtains

$$\Delta E = \frac{3}{5}\Delta N\, E_f$$
$$= \frac{3h^2}{10m}\left(\frac{3}{8\pi}\right)^{\frac{2}{3}} l^3 \left(\frac{\Delta N}{l^3}\right)^{\frac{5}{3}} \quad (2.65)$$

Eq. 2.65 is a relation between total kinetic energy and the electron density for each cell in the space.

$$\rho = \frac{\Delta N}{l^3} = \frac{\Delta N}{\Delta V} \quad (2.66)$$

Adding the contribution from all cells, one obtains the total kinetic energy (in atomic units):

$$T_{TF}[\rho] = C_f \int \rho^{\frac{5}{3}}(\mathbf{r})\, d\mathbf{r}$$
$$C_f = \frac{3}{10}(3\pi^2) = 2.871 \quad (2.67)$$

This is the well-known Thomas-Fermi kinetic energy functional. So for kinetic energy they got creative by considering a homogeneous electron gas, daring afterwards to apply it to electrons in atoms.

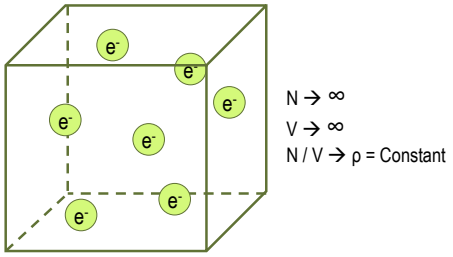

Figure 2.1: Cube of side l and volume V, containing a certain number of electrons, N. Representing the homogeneous electron gas of the Thomas-Fermi model.

But, what about the other terms in the total energy formula (i.e. nucleus-nucleus attraction and electron-electron repulsion)? For these terms they considered next formulae. First, for nucleus-electron attraction:

$$V_{TF}[\rho] = -\int V(\mathbf{r})\ \rho(\mathbf{r})\, d\mathbf{r} = -Z\int \frac{\rho(\mathbf{r})}{\mathbf{r}}\, d\mathbf{r} \tag{2.68}$$

where $V(\mathbf{r})$ is the potential of atomic nuclei. Further, for electron-electron repulsion they used classical energy, which includes self-interaction

$$J_{TF}[\rho] = \frac{1}{2}\iint \frac{\rho(\mathbf{r}_1)\rho(\mathbf{r}_2)}{|\mathbf{r}_1-\mathbf{r}_2|}\, d\mathbf{r}_1\, d\mathbf{r}_2 \tag{2.69}$$

Therefore, if we neglect the exchange and correlation terms, thus only taking into account the classical electrostatic energies (i.e. electron-nucleus attraction and electron-electron repulsion) we get to an energy formula for an atom in terms of electron density,

$$E_{TF}[\rho] = C_f\int \rho^{\frac{5}{3}}(\mathbf{r})\, d\mathbf{r}\ - Z\int \frac{\rho(\mathbf{r})}{\mathbf{r}}\, d\mathbf{r} + \frac{1}{2}\iint \frac{\rho(\mathbf{r}_1)\rho(\mathbf{r}_2)}{|\mathbf{r}_1-\mathbf{r}_2|}\, d\mathbf{r}_1\, d\mathbf{r}_2 \tag{2.70}$$

which is known as the *Energy Functional of the Thomas-Fermi theory of atoms*.
The simplicity of the Thomas-Fermi model goes hand-in-hands with many defects. For instance, no molecular binding is predicted in the method; furthermore, it is only exact for the free electron gas and therefore the accuracy for atoms is not higher as that with other methods.
However, Hohenberg and Kohn published the paper that meant the landmark for a change in the situation, since they gave rise to the theorems that showed how for ground states the Thomas-Fermi model may be seen as an approximation to an exact theory: The Density Functional Theory.

2.5.2 The Hohenberg-Kohn Theorem

The entire field of Density Functional Theory rests on two fundamental mathematical theorems proposed by Kohn and Hohenberg and a derivation of a set of equations by Kohn and Sham in the middle 1960's.

The minimization of the energy functional, $E[\Psi]$,

$$E[\Psi] = \frac{\langle \Psi | \hat{H} | \Psi \rangle}{\langle \Psi | \Psi \rangle} \tag{2.71}$$

give us both ground state energy and wavefunction of a system described a Hamiltonian (Eq. 2.16). But we still need $v(\mathbf{r})$, the external potential and N, the number of electrons in the system, in order to define the whole nuclear frame and electronic properties of our system.

The first Hohenberg-Kohn (H-K) theorem uses the electron density $\rho(\mathbf{r})$ to put in place of N and $v(\mathbf{r})$. It states: "The external potential $v(\mathbf{r})$is determined, within a trivial additive constant, by the electron density $\rho(\mathbf{r})$. Since ρ gives us the number of electrons, $\rho(\mathbf{r})$ provides us with the ground state wavefunction and all other electronic properties".
To proof this theorem, all one needs to apply is the *Minimum Energy Principle* to the ground state. The electron density $\rho(\mathbf{r})$ of a non-degenerated ground state N-electron system determines N (Eq. 2.57) and $v(\mathbf{r})$, and hence all properties.
Let's suppose two external potentials, v and v', in such a way that both of them give the same ρ for its ground state, but having two different Hamiltonians, H and H', and wavefunctions, Ψ and Ψ', repectively. Using the Variational Principle

$$E[\Psi] \geq E_0 \tag{2.72}$$

and taking Ψ' as a trial function for the $\hat{H}$ problem, one gets to

$$\begin{aligned} E_0 < \langle \Psi' | \hat{H} | \Psi' \rangle &= \langle \Psi' | \hat{H}' | \Psi' \rangle + \langle \Psi' | \hat{H} - \hat{H}' | \Psi' \rangle \\ &= E_0' + \int \rho(\mathbf{r}) \, [v'(\mathbf{r}) - v(\mathbf{r})] \, d\mathbf{r} \end{aligned} \tag{2.73}$$

where E_0 and E_0' are the ground state energies for H and H', respectively.
Taking now Ψ as a trial function for the $\hat{H}'$ problem and following a similar procedure, one gets to

$$\begin{aligned} E_0' < \langle \Psi | \hat{H}' | \Psi \rangle &= \langle \Psi | \hat{H} | \Psi \rangle + \langle \Psi | \hat{H}' - \hat{H} | \Psi \rangle \\ &= E_0 + \int \rho(\mathbf{r}) \, [v(\mathbf{r}) - v'(\mathbf{r})] \, d\mathbf{r} \end{aligned} \tag{2.74}$$

If we now sum equations 2.73 and 2.74 we obtain $E_0 + E_0' < E_0' + E_0$, which is obviously a contradiction. The former tells us that there cannot be two different external potentials giving us the same electron density, ρ, for their ground states. Therefore, ρ determines N and v, and thus all properties for the ground state, namely the kinetic energy $T[\rho]$, the potential energy $V[\rho]$ and the total energy $E[\rho]$.

In place of Eq. 2.70 we would have

$$E_v[\rho] = T[\rho] + V_{Ne}[\rho] + V_{ee}[\rho] \\ = \int \rho(\mathbf{r})v(\mathbf{r})dr + F_{HK}[\rho] \quad (2.75)$$

where we have substituted E for E_v in order to state its dependence on v, the external potential.

The H-K theorem actually states that if N interacting electrons move in an external potential, the ground state density minimizes the former functional, $E_v[\rho]$, where F_{HK} is a universal functional of ρ (i.e. it is defined independently of the external potential, $v(\mathbf{r})$)

$$F_{HK}[\rho] = T[\rho] + V_{ee}[\rho] \quad (2.76)$$

In Eq. 2.76 we may write

$$V_{ee}[\rho] = J[\rho] + \text{non classical term} \quad (2.77)$$

where $J[\rho]$ is the classical repulsion (Eq.2.69) and the non classical term is the major part of the exchange-correlation energy.
This theorem states that there is a one-to-one mapping between the ground state wavefunction and the ground state electron density.

Another way to interpret Hohenberg and Kohn's result is to say that the ground state electron density uniquely determines all properties, including the energy and the wavefunction of the ground state.
This result is extremely important since we will be able now to solve the Schrödinger equation by finding a function of three spatial variables, the electron density, rather

than a function of 3N variables, the wavefunction. In the former statement, by "solving the Schrödinger equation" we mean, finding the ground state energy.

The second Hohenberg-Kohn theorem defines an important property of the functional: *The electron density that minimizes the energy of the overall functional is the true electron density corresponding to the full solution of the Schrödinger equation*.
The second H-K theorem gives us the energy Variational Principle, which can be quoted as: "For a trial density $\tilde{\rho}(r)$, such that $\tilde{\rho}(r) \geq 0$ and $\int \tilde{\rho}(r)\ d\mathbf{r} = N$,

$$E_0 \leq E_v[\tilde{\rho}] \tag{2.78}$$

where $E_v[\tilde{\rho}(\mathbf{r})]$ is the energy functional" of Eq. 2.75.
To prove this theorem we may recall the previous one that states that $\tilde{\rho}$ determines its own $\tilde{v}$, $\tilde{H}$ and $\tilde{\Psi}$. Thus,

$$\begin{aligned}\langle \tilde{\Psi} | \tilde{H} | \tilde{\Psi} \rangle &= \int \tilde{\rho}(r) v(r) dr + F_{HK}[\tilde{\rho}] \\ &= E_v[\tilde{\rho}] \geq E_v[\rho]\end{aligned} \tag{2.79}$$

Assuming differentiability of $E_v[\rho]$, the Variational Principle of Eq. 2.78 requires that the ground state density satisfy the stationary principle.

$$\delta\{E_v[\rho] - \mu[\int \rho(\mathbf{r})\ d\mathbf{r} - N]\} = 0 \tag{2.80}$$

which gives us the Euler-Lagrange equation (i.e. the differential equation whose solutions are the functions for a stationary functional)

$$\mu = \frac{\delta E_v[\rho]}{\delta \rho(\mathbf{r})} = v(\mathbf{r}) + \frac{\delta F_{HK}[\rho]}{\delta \rho(\mathbf{r})} \tag{2.81}$$

where μ is a Lagrange multiplier associated to the constraint of Eq. 2.57 and the physical meaning of "chemical potential". If we were able to find the exact $F_{HK}[\rho]$, Eq. 2.80 would be an exact equation for the ground state electron density. Thus, Eq. 2.81 is the fundamental formula of the Density Functional theory.

2.5.3 The Kohn-Sham Equations

Kohn and Sham derived a set of differential equations in order to make possible to find $\rho(\mathbf{r})$. For this purpose, they separated $F_{HK}[\rho]$ in three terms, so that the functional of Equations 2.70 and 2.75 becomes

$$E[\rho] = T_S[\rho] + \frac{1}{2}\iint \frac{\rho(\mathbf{r})\rho'(\mathbf{r})}{|\mathbf{r}-\mathbf{r}'|}\,d\mathbf{r}\,d\mathbf{r}' + E_{XC}[\rho] + \int \rho(\mathbf{r})v(\mathbf{r})\,d\mathbf{r} \tag{2.82}$$

where E_{XC} is the non-classical term we previously mentioned and $T_S[\rho]$ is defined as the kinetic energy of a non-interacting electron gas with density $\rho(\mathbf{r})$; be aware that this is not the kinetic energy of the real system.

$$T_S[\rho] = -\frac{1}{2}\sum_i^N \int \Psi_i^*(\mathbf{r})\nabla^2\Psi_i(\mathbf{r})\,d\mathbf{r} \tag{2.83}$$

Eq. 2.83 is a special case of

$$T = -\frac{1}{2}\sum_i^N n_i \int \Psi_i^*(\mathbf{r})\nabla^2\Psi_i(\mathbf{r})d\mathbf{r} \tag{2.84}$$

having $n_i = 1$ for N orbitals and $n_i = 0$ for the rest. Furthermore, the electron density is given by

$$\rho(\mathbf{r}) = \sum_i^N \sum_s |\Psi_i(\mathbf{r}, s)|^2 \tag{2.85}$$

where the former conditions have also been imposed giving

$$\rho(\mathbf{r}) = \sum_i^N n_i \sum_s |\Psi_i(\mathbf{r}, s)|^2 \tag{2.86}$$

Thus, we can rewrite Eq. 2.81 in terms of an effective potential, $v_{eff}(\mathbf{r})$

$$\mu = v_{eff}(\mathbf{r}) + \frac{\delta T_s[\rho]}{\delta\rho(\mathbf{r})} \tag{2.87}$$

where

$$v_{eff}(\mathbf{r}) = v(\mathbf{r}) + \frac{\delta J[\rho]}{\delta \rho(\mathbf{r})} + \frac{\delta E_{XC}[\rho]}{\delta \rho(\mathbf{r})} = v(r) + \int \frac{\rho(\mathbf{r}')}{|\mathbf{r}-\mathbf{r}'|} d\mathbf{r}' + V_{XC} \quad (2.88)$$

and

$$V_{XC} = \frac{\delta E_{XC}[\rho]}{\delta \rho(\mathbf{r})} \quad (2.89)$$

The non-classical term $E_{XC}[\rho]$ is the so-called exchange-correlation energy. It contains the difference between T and T_S, which is expected to be small, and the non-classical part of v_{ee}. For a given $v_{eff}(\mathbf{r})$ one obtains $\rho(\mathbf{r})$ that satisfies Eq. 2.87 by solving the N one-electron equation that follows

$$\left(-\frac{1}{2}\nabla_i^2 + v_{eff}(\mathbf{r}) - \varepsilon_i\right)\Psi_i(\mathbf{r}) = 0 \quad (2.90)$$

which should be solved self-consistently with Eq. 2.85 due to the dependence of $v_{eff}(\mathbf{r})$ on $\rho(\mathbf{r})$.
Equations 2.85 and 2.88-2.90 are the Kohn-Sham equations, and provide an exact method for finding the ground state energy of an interacting system, if the form of $E_{XC}[\rho]$ is known. The main problem of this method is that the exact exchange-correlation energy is not known and its exact value has been calculated only for a few simple models.
As the particles in the Kohn-Sham system are non-interacting fermions, the Kohn-Sham wavefunction is a single Slater determinant constructed from a set of orbitals that are the lowest energy solutions to the eigenvalue Kohn-Sham equation. These orbitals are called the Kohn-Sham orbitals.

2.6 Periodicity and Reciprocal Space

The need of describing periodic infinite systems (i.e. bulks and surfaces) takes us away from the confortable three-dimensional real space, where positions are defined, and bring us into what is known as the reciprocal space, where momenta are construed. The

concepts associated with this former term are fundamental to much of the solid state physics.
Solving the Schrödinger equation when the electrons feel a periodic potential requires a special treatment, which will be explained in the following sections.

2.6.1 The Bloch's Theorem and the Brillouin Zone

In order to present the Bloch's Theorem, key issue for the following explanations, let us introduce the translation operator T_R that commutes with the Hamiltonian. Indeed, the kinetic energy is translationally invariant, and if the potential is periodic, then we have:

$$\begin{aligned}[T_R, V]f(r) &= T_R\, V(r)f(r) - V(r)\, T_R\, f(r) \\ &= V(r+R)f(r+R) - V(r)f(r+R) = 0\end{aligned} \tag{2.91}$$

On the other hand we can also show that $[T_R, T_{R'}] = 0$. Thus, the Hamiltonian and all the translation operators of the crystal commute with each other. They posses therefore, a common set of eigenstates. Let now search for the eigenstates of the translation operator T_R.
For a general function satisfying the boundary condition of the problem, one can write, after expanding the eigenstate on a plane wave basis, the eigenvalue equation as follows:

$$T_R\, f(\mathbf{r}) = T_R \sum_q C_q e^{i\,\mathbf{q}.\mathbf{r}} e^{i\,\mathbf{q}.\mathbf{R}} = t_R \sum_q C_q e^{i\,\mathbf{q}.\mathbf{r}} \tag{2.92}$$

where t_R is the eigenvalue. The above equality is true only if $e^{i\,\mathbf{q}.\mathbf{r}}$ is a constant: $\mathbf{q}.\mathbf{R} = 2\pi n + \text{constant} \Rightarrow \mathbf{q} = \mathbf{k} + \mathbf{G}$, where k is an arbitrary vector and $\mathbf{G}$ is a reciprocal lattice vector: $\mathbf{G}.\mathbf{R} = 2\pi n$. The eigenvalue is therefore $t_r = e^{i\,\mathbf{k}.\mathbf{R}}$ and the eigenvector could be any plane wave of momentum $\mathbf{k} + \mathbf{G}$. The eigenvalue t_R is degenerate with respect to $\mathbf{k} + \mathbf{G}$, and the associated eigenvector can be written as:

$$f_k(r) = \sum_{\mathbf{G}} C_{k+G} e^{i(\mathbf{k}+\mathbf{G}).\mathbf{r}} = e^{i\,\mathbf{k}.\mathbf{r}} \sum_G C_{k+G} e^{i\,\mathbf{G}.\mathbf{r}} = e^{i\,\mathbf{k}.\mathbf{r}}\, u_k(\mathbf{r}) \tag{2.93}$$

The arbitrary vector $\mathbf{k}$ labels thus different eigenvalues and eigenstates of translation operators. Furthermore, the above function also represents the eigenstates of all possible translation operators of the lattice.
Note that the infinite sum over all possible momenta $\mathbf{q}$ is now reduced to a discrete (still infinite) sum over the reciprocal lattice vectors, $\mathbf{G}$, and that is a great simplification in the problem.
We can also notice that all states corresponding to $\mathbf{k}$ and any $\mathbf{k} + \boldsymbol{G}$ are equal, i.e. the function f_k is periodic in the reciprocal space, $f_k = f_{k+G}, \forall G$.
Due to the previously mentioned commutation relation, f_k is also eigenstates of $\widehat{H}$. To obtain its coefficient C_{k+G}, we just need to insert this wavefunction into the Schrödinger equation.
The Hamiltonian matrix must therefore be diagonalized in the space of all plane waves of momentum $\mathbf{k} + \mathbf{G}$ for any vector $\mathbf{k}$ chosen in the first Brillouin zone. Indeed the periodicity of f_k in the reciprocal space implies that it is sufficient to chose the arbitrary vector $\mathbf{k}$ in the first Brillouin zone (see below the definition).
Let's finally state the Bloch's theorem: The eigenstate f_k of a periodic Hamiltonian can be written as a product of a periodic function with a plane wave of momentum $\mathbf{k}$ restricted to be in the first Brillouin zone, $f_k(\mathbf{r}) = u_k(r)e^{i\,\mathbf{k}.\mathbf{r}}$ (with u_k periodic in $\mathbf{k}$ and $\mathbf{r}$); furthermore, $f_k(\mathbf{r} + \mathbf{R}) = e^{i\,\mathbf{k}.\mathbf{r}} f_k(\mathbf{r})$.
Different boundary conditions apply for ψ (in $H\psi = E\psi$, the Schrödinger's equation) of a crucial, therefore the basis set must satisfy these conditions. Thus, while for a molecule, basis functions must go to zero at infinite, for an infinite crystal the basis must satisfy the boundary conditions.

The "crystal potential", $V(\mathbf{r})$, is a periodic function:

$$V(\mathbf{r} + \mathbf{R}) = V(\mathbf{r}) \tag{2.94}$$

Making use of the Fourier decomposition, we can describe it as:

$$V(\mathbf{r}) = \sum_G \widehat{V}_G e^{i\,\mathbf{G}.\mathbf{r}} \tag{2.95}$$

where

$$\widehat{V}_G = \int_{cell} V(\mathbf{r}) e^{-i\,\mathbf{G}.\mathbf{r}}\, dr/\Omega \tag{2.96}$$

G's are reciprocal lattice vectors defined by $\mathbf{G}.\mathbf{R} = 2\pi n$, **R**'s are translational vectors of the crystal lattice and Ω is the unit cell volume.
If $\{R_1, R_2, R_3\}$ is the basis of the primitive cell, then the reciprocal lattice vectors are defined by: $G_i . R_i = 2\pi\,\delta_{ij}$ or more explicitly $G_1 = 2\pi\,(R_2 \times R_3)/\Omega$ *with* $\Omega = R_1.(R_2 \times R_3)$ and so on.
The boundary conditions satisfied by the wavefunctions come from Bloch's theorem:

For every eigenfunction ψ*, there exists a vector* $\boldsymbol{k}$ *such that:* $\psi_k(\boldsymbol{r}) = e^{i\,\boldsymbol{k}.\boldsymbol{r}}\, u_k(\boldsymbol{r})$ *where* $u_k(\boldsymbol{r})$ *is a periodic function*.

We see therefore that ψ is not periodic, and thus, to solve the eigenvalue problem, one may take any basis set satisfying the above theorem. One simple choice would be the plane waves:

$$\emptyset_k(r) = e^{i\,\mathbf{k}.\mathbf{r}}/\sqrt{\Omega} \tag{2.97}$$

which are eigenstates when $V(r) = 0$
The eigenvalue equation in this basis would be

$$\sum_q \left[H_{kq} - ES_{kq}\right] C_q = 0;\ \forall \mathbf{k} \tag{2.98}$$

But since

$$S_{kq} = \delta_{k,q} \text{ and } H_{kq} = \delta_{k,q}\ k^2/2m + \widehat{V}_{k-q} \tag{2.99}$$

we have that $\mathbf{k} - \mathbf{q} = \mathbf{G}$ must be a reciprocal lattice vector.
The final solution for each **k** are therefore (this is another statement of the Bloch's theorem):

$$\psi_k(r) = \sum_G C_{k+G} e^{i\,k+G.r}/\sqrt{\Omega} \tag{2.100}$$

and now ψ_k is periodic in the reciprocal space:

$$\psi_k(r) = \psi_{k+G}(r) \tag{2.101}$$

The number of obtained eigenvalues is equal to the number of chosen basis functions. The eigenvalues and eigenstates for each **k** will also be labeled by an integer λ, which is called the band index ($\lambda = 1$ corresponds to the first band, $\lambda = 2$ to the second one, etc.). The form of the Schrödinger equation in the plane-wave basis is:

$$\left[(k+G)^2/2m + \widehat{V}_0 - E_{k+G}\right]C_{k+G} + \sum_{G' \neq G} \widehat{V}_{G-G'} C_{G+G'} = 0 \tag{2.102}$$

We define the shape of the unit cell that is repeated in space, the supercell, by lattice vectors, $\mathbf{a}_1, \mathbf{a}_2$ and $\mathbf{a}_3$. If we solve the Schrödinger equation for this periodic system, the solution must satisfy the Bloch's theorem (Eq. 2.93) where $u_k(\mathbf{r})$ is periodic in space and has the same periodicity of the supercell; that is:

$$u_k(\mathbf{r} + n_1\mathbf{a}_1 + n_2\mathbf{a}_2 + n_3\mathbf{a}_3) = u_k(\mathbf{r}) \tag{2.103}$$

for any integers n_1, n_2 and n_3.

Just as positions can be defined in the real space in terms of the lattice vectors $\mathbf{a}_1, \mathbf{a}_2$ and $\mathbf{a}_3$, it is useful to define three vectors that define positions in the reciprocal space. These vectors are called the reciprocal lattice vectors $\mathbf{b}_1, \mathbf{b}_2$ and $\mathbf{b}_3$ and are defined such that

$$\mathbf{a}_i \,.\, \mathbf{b}_j = 2\pi\delta_{ij} \tag{2.104}$$

The three-dimensional shape defined by the reciprocal lattice vectors is not always the same as the shape of the reciprocal lattice vectors; for instance, in the FCC (Face Centered Cubic) primitive cell. We can form this structure by filling the space with cubes of size length **a** that have atoms at the corners of each cube and also in the center of each face of each cube. One can define a supercell for a FCC material using the same cube of side length "**a**" of a simple cubic material and placing atoms at (0,0,0), (0, a/2,0), (a/2, 0, a/2) and (a/2,a/2,0).
The primitive cell for the FCC metal can be defined by connecting the atom at the origin in the structure defined above with three atoms in the cube faces adjacent to the atom. That is we define cell vectors:

$$\mathbf{a}_1 = a\left(\frac{1}{2}, \frac{1}{2}, 0\right)$$
$$\mathbf{a}_2 = a\left(0, \frac{1}{2}, \frac{1}{2}\right)$$
$$\mathbf{a}_3 = a\left(\frac{1}{2}, 0, \frac{1}{2}\right) \quad (2.105)$$

These vectors define the FCC lattice if we place atoms at the positions:
$\mathbf{r} = n_1\mathbf{a}_1 + n_2\mathbf{a}_2 + n_3\mathbf{a}_3$ for all integers n_1, n_2 and n_3. This situation is illustrated in figure 2.2.

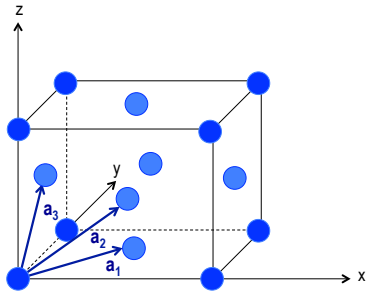

Figure 2.2: Illustration of the cell vectors of an FCC metal.

The reciprocal vectors for the FCC material will be:

$$\mathbf{b}_1 = \frac{2\pi}{a}(1,1,-1)$$
$$\mathbf{b}_2 = \frac{2\pi}{a}(-1,1,1,)$$
$$\mathbf{b}_3 = \frac{2\pi}{a}(1,-1,1) \quad (2.106)$$

where the length of the reciprocal lattice vectors are inversely related to the reciprocal of the length of the real space lattice vectors. Views of these lattice vectors in real and reciprocal space are shown in figure 2.3.

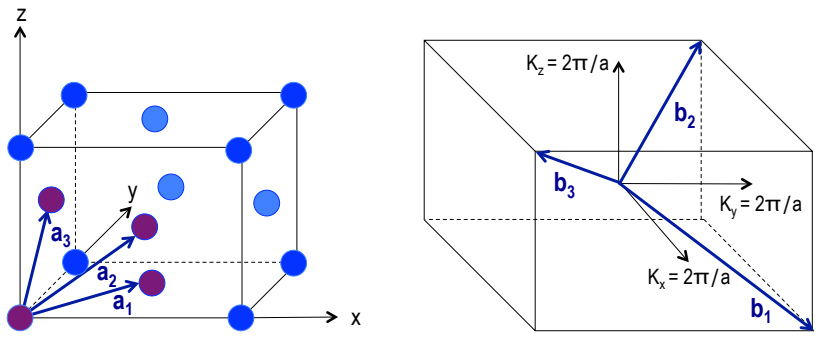

Figure 2.3: View of the Real space (left) and the Reciprocal space (right) lattice vectors for the FCC primitive cell.

A primitive cell is the supercell that contains the minimum number of atoms necessary to fully define a periodic material with infinite extent. A more general way of thinking about the primitive cell is that it is a cell that is minimal in terms of volume but still contains all the information we need. This concept can be made more precise by considering the so-called Wigner-Seitz cell. The former can be defined for reciprocal lattice vectors just as easily as it can be for real space vectors. Stated in words a Wigner-Seitz cell about a lattice point, is the region in space that is closest to that lattice point than to any other lattice point. While the definition may not be easy to visualize at first glance, it is actually quite easy to determine, as shown in fig 2.4.
Take any two points in space and draw a straight line joining them. Then draw a plane that perpendicularly bisects the line joining these two points. All of the points on one side of the perpendicular bisector are by definition closer to the point on the same side of the perpendicular bisector than to the other point. A lattice is an array of points. In the most general case, it is a three dimensional array of points.

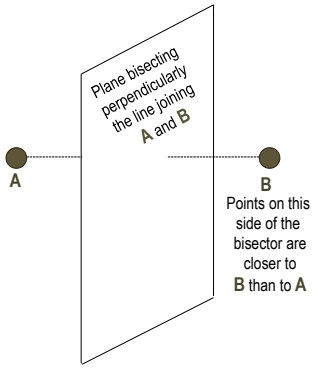

Figure 2.4: Illustration for the comprehension of the Wigner-Seitz cell construction

To identify the region in space closest to a single lattice point than to any other lattice point, we merely extend the approach we have adopted above. As first step we identify all of the nearest neighbors. Perpendicular bisectors are drawn to each of the lines. Once these steps

are completed, it will be possible to identify the innermost region bounded by these perpendicular bisectors. That innermost region then consists of all of the points in space that are closest to the lattice point in that region than to any other lattice point. This region bounded by the perpendicular bisectors, is then the Wigner-Seitz (WS) cell about that lattice point. The procedure described above is shown in figure 2.5.

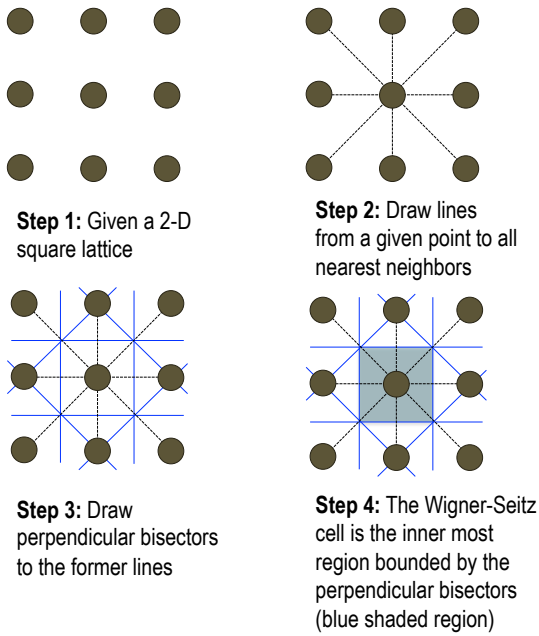

Figure 2.5: Procedure to identify the Wigner-Seitz cell about a lattice point in a 2-dimensional square lattice.

It is necessary to introduce now, due to its relevance in solid-state physics, the term "Brillouin zone (BZ)", previously mentioned as we explained the Bloch's theorem, and more specifically the "First BZ". The first BZ is defined as the WS primitive cell about a lattice point in reciprocal space. In other words, to identify the first BZ for a lattice, we first draw the reciprocal lattice corresponding to the given lattice, and then identify the WS cell about a point in that reciprocal lattice. This specific WS cell is then the first BZ corresponding to the original real space lattice. Further BZ's have greater significance in terms of the electronic properties of the materials. To identify the second, third and higher BZ's we extend the procedure we have followed thus far.

The second BZ is identified as the region in reciprocal space that extends beyond the nearest (first) Bragg plane in all directions but not beyond the very next (second) Bragg plane in each of those directions.
Here, "Bragg plane" refers to those planes bisecting lines joining a reciprocal lattice point, chosen as the origin, to all of the other points in the reciprocal lattice, and are not restricted to just lines joining the reciprocal lattice point to its nearest neighbors. The first BZ is thus the region bounded by the nearest collection of Braggs planes around a reciprocal lattice point.

Generalizing further, the n^{th} BZ is all of the point between the $(n-1)^{th}$ Bragg plane and the n^{th} Bragg plane in all directions.

The BZ plays a central role in the band theory of materials. Several points in the BZ with special significance are given individual names. The most important of these is the point where $\boldsymbol{k} = 0$; this location in $\boldsymbol{k}$ space is called the Gamma, Γ, point.

2.6.2 From Plane Waves to Electron Density

The Kohn-Sham potential of a periodic system exhibits the same periodicity as the direct lattice, and the Kohn-Sham orbitals can be written in general Bloch form (Eq. 2.93), where **k**, the quantum number associated with the crystal momentum, is a vector in the first BZ, and the functions $u_j(\mathbf{r}+\mathbf{k})$ have the periodicity of the direct lattice, as we have already explained.

$$u_j(\mathbf{r}+\mathbf{k}) = u_j(\mathbf{r}+\mathbf{L},\mathbf{k}) \tag{2.107}$$

where **L** are the direct lattice vectors connecting equivalent points in consecutive cells.

The periodic functions are now expanded in the plane wave basis:

$$u_j(\mathbf{r},k) = \frac{1}{\sqrt{\Omega}}\sum_G C_j(\mathbf{G},k)\exp\,[i\,\mathbf{G}.\mathbf{r}] \tag{2.108}$$

where the normalization is simply given by $\frac{1}{\sqrt{\Omega}}$, and Ω is the volume of the periodic cell. The band index j runs over all states and the states have an occupation number $f_j(\mathbf{k})$ associated with them, which is a relative weight.

Plane waves are defined as:

$$f_G^{PW} = N \exp[i\,\mathbf{G}.\mathbf{r}] \tag{2.109}$$

and the Kohn-Sham orbitals are:

$$\emptyset_j(r,k) = \frac{1}{\sqrt{\Omega}} \sum_G C_j(\mathbf{G},k) \exp[i\,(\mathbf{G}+\mathbf{k}).\mathbf{r}] \tag{2.110}$$

where $C_j(\mathbf{G},k)$ are complex numbers. With this expansion the charge density can also be expanded into a plane wave basis

$$\begin{aligned} n(r) &= \frac{1}{\sqrt{\Omega}} \sum_j \int f_j(\mathbf{k}) \sum_{G,G'} C_j^*(\mathbf{G}',\mathbf{k}) C_j(\mathbf{G},\mathbf{k}) \exp[\,i(\mathbf{G}+\mathbf{k}).r]\ dk \\ &= \sum_G n(\mathbf{G}) \exp[i\mathbf{G}.\mathbf{r}] \end{aligned} \tag{2.111}$$

where the sum over $\mathbf{G}$ in Eq. 2.111 extends over twice the range given by the wavefunction expansion. Thus, while for atomic orbital basis sets the number of functions needed to describe the density grows quadratically with the size of the system, there is only a linear dependence for plane waves. This is one of the main advantages of plane waves.

2.6.3 Cutoffs and K-points

In actual calculations, the infinite sum over $\mathbf{G}$ vectors and cells has to be truncated. Furthermore, one has to approximate the integral over the Brillouin zone by a finite sum over a set of K-points,

$$\int_{BZ} dk \rightarrow \sum_k w_k \tag{2.112}$$

where w_k are the weights of these integration points.

The truncation of the plane wave basis rests on the fact that the Kohn-Sham potential, $V^{KS}(\mathbf{G})$, converges rapidly with increasing modulus of $\mathbf{G}$ vectors with a kinetic energy lower than a given maximum cutoff

$$1/2\ |k+G|^2\ \leq E_{cut} \tag{2.113}$$

The precision of the calculation within the approximation of Density Functional Theory is controlled by a single parameter, namely the plane wave energy cutoff, E_{cut}. The number of plane waves for a given cutoff depends on the unit cell and the Kpoint(s). An estimate for the size of the basis at the center of the BZ is:

$$N_{PW} = \frac{1}{2\pi^2}\,\Omega\,E_{cut}^{3/2} \tag{2.114}$$

where E_{cut} and Ω are given in atomic units; Hartree and $(Bohr)^3$, respectively .

2.6.4 Pseudopotentials

In order to minimize the size of the plane wave basis necessary for calculation involving many atoms, the core electrons have to be replaced by pseudopotentials (PP). The replacement of chemically inactive electrons by PP is a common method used in many of electronic structure calculations. The inert core electrons are eliminated within the frozen-core approximation, being considered, together with the nuclei, as rigid non-polarizable ion-cores. All electrostatic and quantum-mechanical interactions of the valence electrons with the cores, such as nuclear Coulomb attraction screened by the core electrons, Pauli repulsion, and exchange and correlation between core and valence electrons are taken into account by using angular momentum-dependent pseudopotentials. These should reproduce the true potential and valence orbitals outside a chosen core region but remain much weaker and smoother inside. The valence electrons are then described by smooth pseudo orbitals, which play the same role as the true orbitals, but avoid the nodal structure near the nuclei that keeps the core

and valence states orthogonal in an all-electron framework. Thus, pseudopotentials replace electronic degrees of freedom in the Hamiltonian by an effective potential. They lead to a reduction of the number of electrons in the system and thereby allow for faster calculations or the treatment of larger simulations.

Most important, in the framework of plane wave basis, pseudopotentials allow for a considerable reduction of the basis set size for the following reasons:

I) Valence states are smoother than core states already at the level of an all-electron calculation and therefore need fewer basis functions for an accurate description.

II) The pseudized valence wave functions are nodeless functions and thus, allow for an additional reduction of the basis.

In the framework of using pseudopotentials, instead of exact potentials, we find the Projector-Augmented-Wave (PAW) Method[2]: which is the method we have used in order to carry on all the calculations presented in this manuscript.

The PAW transformation theory consists on transforming a physical wavefunction $\psi(r)$ onto an auxiliary wavefunction $\tilde{\psi}(r)$:

$$\tilde{\psi}(r) = \hat{U}\,\psi(r) \tag{2.115}$$

with the goal in mind that we can represent these smooth auxiliary wavefunctions in a plane wave expansion.
The procedure is as follows: we first define an auxiliary wave function, $\tilde{\psi}_n(r)$, and a transformation operator $\hat{T} = \hat{U}^{-1}$, such that

$$\psi_n(r) = \hat{T}\,\tilde{\psi}(r) \Leftrightarrow \tilde{\psi}_n(r) = \hat{U}\,\psi_n(r) \tag{2.116}$$

and thus, it maps the auxiliary wave functions $\tilde{\psi}_n(r)$ onto true wavefunctions $\psi_n(r)$.
Afterwards, the total energy must be expressed by auxiliary wavefunctions:

$$E = E[\psi_n(r)] = E[\hat{T}\,\tilde{\psi}(r)] \tag{2.117}$$

and the Schrödinger-like equation for auxiliary functions

$$\frac{\partial E}{\partial \tilde{\psi}_n^*(r)} = (T^+ H T - T^+ T \epsilon_n)\tilde{\psi}_n(r) = 0 \tag{2.118}$$

where the expectation values are

$$\langle A \rangle = \sum_n \langle \psi_n | A | \psi_n \rangle = \sum_n \langle \tilde{\psi}_n | T^+ A T | \tilde{\psi}_n \rangle \tag{2.119}$$

and thus, we have to find a transformation $\hat{T}$ so, that the auxiliary wave functions are well behaved. The requirements for a suitable transformation operator are:

I) The relevant wave functions shall be transformed onto numerically convenient auxiliary wave functions

$$\tilde{\psi}_n(\mathbf{r}) = \sum_{\mathbf{G}} e^{i\,\mathbf{G}.\mathbf{r}}\, \tilde{\psi}_n(\mathbf{G}) \tag{2.120}$$

II) Linear (algebraic operations)
III) Local (no interaction between sites)

$$T = 1 + \sum_R S_R \tag{2.121}$$

In order to define the proper T operator, we have to define a complete set of initial and final states for the transformation

$$\forall i, |\phi_i\rangle = T|\tilde{\phi}_i\rangle \tag{2.122}$$

The final states should be all-electron valence partial waves $|\phi_i\rangle = \mathbf{R}, l, m, \alpha$, in such a way that we are able to solve the Schrödinger equation for the all-electron atomic potential for a set of energies.
Furthermore, the initial states must be auxiliary partial waves, $|\tilde{\phi}_i\rangle$, such as true and auxiliary wave functions are pairwise identical outside some augmentation radius r_c.

$$\tilde{\phi}_i(\mathbf{r}) = \phi_i(\mathbf{r}), \quad |\mathbf{r} - \mathbf{R}| > r_c \tag{2.123}$$

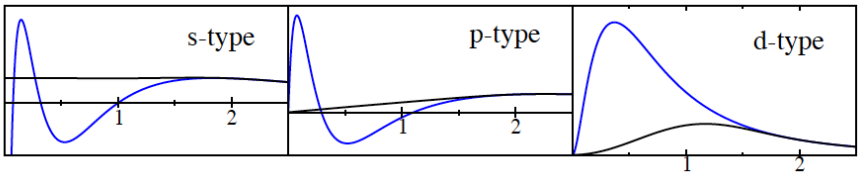

Figure 2.6: Auxiliary partial waves in their s-, p- and d-type.

Following, one must find a closed expression for the transformation operator (Eq. 2.121) and derive

$$
\begin{aligned}
&|\phi_i\rangle = S_{R_i}|\tilde{\phi}_i\rangle \\
&\quad \Rightarrow S|\tilde{\phi}_i\rangle = |\phi_i\rangle - |\tilde{\phi}_i\rangle = \sum_j [\,|\phi_j\rangle - |\tilde{\phi}_j\rangle]\,\langle \tilde{P}_j|\tilde{\phi}_i\rangle \\
&\quad \Rightarrow T = 1 + \sum_j [\,|\phi_j\rangle - |\tilde{\phi}_j\rangle]\langle \tilde{P}_j| \qquad (2.124)
\end{aligned}
$$

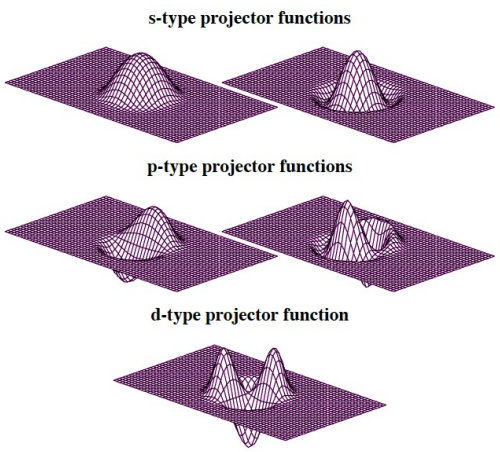

Thus, the projector function, $\langle \tilde{P}_j|$, must be localized within its own augmentation region and obey the bi-orthogonality condition.

.

Figure 2.7: Projectors functions of s-, p- and d-types. (Source: P. E. Blöchl, "Projected-Augmented Wave Method: An Introduction"; Technische Universität Clausthal, Germany; http://www.pt.tu-clausthal.de/atp/)

Finally, the reconstruction of the true wave functions is done using the transformation operator (Eq. 2.124) and thus, the all-electron wavefunction obtains the form:

$$|\psi_n\rangle = |\tilde{\psi}_n\rangle + \sum_j [\,|\phi_j\rangle - |\tilde{\phi}_j\rangle]\,\langle \tilde{P}_j|\tilde{\phi}_i\rangle \qquad (2.125)$$

In summary the PAW Method makes the following approximations:

I) Frozen-core approximation.

II) Truncate plane wave expansion
III) Truncate partial plane wave expansion

In comparison with pseudopotentials, where the energy is given as a Taylor expansion, PAW calculates this expression exactly, while the Pseudopotentials methods truncates the expansion after the linear term, and as a consequence a charge transferability problem appears.
PAW creates pseudopotentials that adjust to instantaneous electronic structure.
Furthermore, if we compare the PAW method with the Ultrasoft Pseudopotentials one, the later needs a plane wave cutoff for the density equivalent to that of norm-conserving Pseudopotentials, and thus support grids are required. On the other hand, PAW uses one-center expansions with radial grids and a smooth compensation density, in such a way that that require lower cutoff for the density.

2.7 Electron transmission through molecules and molecular interfaces

In the latest years the Scanning Tunneling Microscope (STM) has generated great interest due to all possibilities presented by this powerful tool to force chemical reactions. Thus, STM does not only allow us to visualize direct images of the electronic structure of adsorbed molecules on surfaces. In fact, there are many research groups that, in the last decades, have employed STM to induce vibrational or electronic excitations, achieving different phenomena of the adsorbates placed at the surface. Therefore, STM can be considered as a way to control chemical reaction on the nanoscale.

In this manuscript, we present several results based on both functionalities of the former engine, i.e. provide real-space images of the adsorbates on the surface and induce chemical reactions processes. In order to fully understand the theory lying underneath an Scanning Tunneling Microscope we will begin by explaining the standard electron transfer theory and arrive to the Landauer formula, relating the electrical resistance of a quantum conductor to the scattering properties of the conductor.

2.7.1 Standard electron transfer theory

We will focus on the non-adiabatic electron transfer, where the electron transfer rate, k_{et}, is given (under the Condon approximation) by the golden rule based expression

$$k_{et} = \frac{2\pi}{\hbar}|V_{DA}|^2 F \tag{2.126}$$

where V_{DA} is the coupling between the donor (D) and the acceptor (A) electronic states and where F is the thermally averaged and Franck Condon (FC) weighted density of nuclear states.

$$\begin{aligned} F &= F(E_{AD}) \\ &= \sum_{\upsilon_D}\sum_{\upsilon_A} P_{th}(\varepsilon_D(\upsilon_D))\,|\langle\upsilon_D|\upsilon_A\rangle|^2\;\delta(\varepsilon_A(\upsilon_A) - \varepsilon_D(\upsilon_D) + E_{AD}) \end{aligned} \tag{2.127}$$

In Eq. (2.127) υ_D and υ_A denote the donor and acceptor nuclear states, P_{th} is the Boltzman distribution over donor states, $\varepsilon_D(\upsilon_D)$ and $\varepsilon_A(\upsilon_A)$ are nuclear energies above the corresponding electronic origin and E_{AD} is the electronic energy gap between the donor and acceptor states.

If the donor (say) is replaced by an electrode, we have to sum over all occupied electrode states

$$\begin{aligned} |V_{DA}|^2 F &\Rightarrow \sum_k f(\varepsilon_k) - e\Phi\;|V_{kA}|^2 \\ &= \int d\varepsilon\;\; f(\varepsilon)\;\; F(\varepsilon - e\Phi)\;\sum_k \delta(\varepsilon - \varepsilon_k)|V_{kA}|^2 \end{aligned} \tag{2.128}$$

where

$$f(\varepsilon) = \frac{1}{1+e^{\varepsilon/k_B\Theta}} \tag{2.129}$$

is the Fermi-Dirac distribution function with ε measured relative to the electron chemical potential μ in the electrode, and Φ, which determines the position of the acceptor level relative to μ is the *overpotential*. Defining

$$\sum_k \delta(\varepsilon - \varepsilon_k)|V_{kA}|^2 \equiv\; |V(\varepsilon)|^2 \tag{2.130}$$

the electron transfer rate takes the form

$$k_{et} = \frac{2\pi}{\hbar}\int d\varepsilon \ \frac{e^{-(\lambda - e\Phi + \varepsilon)^2/4\lambda k_B \Theta}}{\sqrt{4\pi\lambda k_B \Theta}} \ |V(\varepsilon)|^2 \ f(\varepsilon) \tag{2.131}$$

where the reorganization energy term in Eq. 2.131 is associated with the change in the redox state of the molecular species only. The nominal change in the "oxidation state" of the macroscopic electrode does not affect the polarization of the surrounding solvent because the transferred electron or hole does not stay localized.
As expected for a tunneling process, the rate is found to decrease exponentially with the donor-acceptor distance

$$k_{et} = k_0 e^{-\beta' R_{DA}} \tag{2.132}$$

where β' is the range parameter that characterizes the distance dependence od the electron transfer rare. The smallest value for β' are found in highly conjugated organic bridges for which β' is in the range of 0.2-0.6 Å[3–8].

On the other hand, for a bridge assisted transfer between a molecule and an electrode, Eq. 2.131 applies with $|V(\varepsilon)|^2$ given by

$$|V(\varepsilon)|^2 = \left(\frac{V_B}{\Delta E_B}\right)^{2N} \sum_k \delta(\varepsilon - \varepsilon_k) \left|\frac{V_{1k} V_{NA}}{V_B}\right|^2 \tag{2.132}$$

where we have assume for simplicity that the donor level $|D\rangle$ is coupled only to bridge state $|1\rangle$ and that the acceptor level $|A\rangle$ is coupled only to bridge level $|N\rangle$.

2.7.2 Transmission between conducting leads

Equations 2.126, 2.131 and 2.132 (together with 2.131) are expressions for the *rate* of electron transfer between donor and acceptor molecules or between a molecule and a metal electrode. While the primary observable in "standard" charge transfer processes

involving molecular donors and/or acceptors is a transient quantity, in metal-molecule-metal (MMM) junctions we focus on the *steady state* current through the junction for a given applied voltage between the two metal ends.

Consider first a simple model for a metal-insulator-metal (MIM) system, where the insulator is represented by a continuum characterized by its dielectric constant[9], ε. For specificity we will assume that the electrode surfaces are infinite parallel planes perpendicular to the x direction. In this case the transmission problem is essentially 1-dimensional and depends only on the incident particle velocity in the x direction, $v_x = \sqrt{2E_x/m}$. In the Bretzel-Kramers-Brillouin (BKB) approximations the transmission probability is given by

$$T(E_x) = \exp\left[-\frac{4\pi}{\hbar}\int_{s_1}^{s_2}[2m(U_B(x) - E_x)]^{1/2}\,dx\right] \tag{2.133}$$

where $U_B(x)$ is the barrier potential that determines the turning points s_1 and s_2, and m is the mass of the tunneling particle. The tunneling flux is given by $T(E_x)\,n(E_x)\,\sqrt{2E_x/m}$, where $n(E_x)$ is the density per unit volume of electron of energy E_x in the x direction. $n(E_x)$ is obtained by integrating the Fermi-Dirac function with respect to E_y and E_z. When a potential Φ is applied so that the right electrode (say) is positively biased, the net current density is obtained in the form[9]

$$J = \int_0^\infty dE_x\ T(E_x)\,\xi(E_x) \tag{2.134}$$

where

$$\begin{aligned}\xi(E_x) &= \frac{2m^2e}{(2\pi\hbar)^3}\int_{-\infty}^{\infty}dv_y\int_{-\infty}^{\infty}dv_z\ [f(E) - f(E + e\Phi)] \\ &= \frac{4\pi me}{(2\pi\hbar)^3}\int_0^\infty dE_r\ [f(E) - f(E + e\Phi)]\end{aligned} \tag{2.135}$$

and where $E_r = E - E_x = (1/2)m\left(v_y^2 + v_z^2\right)$ is the energy in the direction perpendicular to x. In obtaining this result it is assumed that the electrodes are chemically identical. At zero temperature and when $\Phi \to 0$, then $f(E) - f(E + e\Phi) =$

$e\Phi\ \delta(E - E_F)$. Eqs. 2.134 and 2.135 then lead to an expression for the conductivity per unit length

$$\sigma_x = \frac{4\pi m e^2}{(2\pi\hbar)^3} \int_0^{E_F} dE_x T(E_x) \tag{2.136}$$

For finite Φ these expression provide a framework for predicting the current-voltage characteristics of the junction; explicit approximate expressions were given by Simmons[9].

The dependence on Φ arises partly from the structure of Eqs. 2.134 and 2.135, for instance, at zero temperature

$$J = \frac{4\pi m e^2}{(2\pi\hbar)^3} \left[e\Phi \int_0^{E_F - e\Phi} dE_x T(E_x) + \int_{E_F - e\Phi}^{E_F} dE_x (E_F - E_x)\, T(E_x) \right] \tag{2.137}$$

but mainly from the voltage dependence, T. The simplest model for metal-vacuum-metal barrier between identical electrodes without an external field is a rectangular barrier of height above the Fermi energy given by the metal workfunction. When a uniform electric field imposed between the two metals a linear potential drop from E_F on one electrode to $E_F - e\Phi$ on the other is often assumed. In addition the image potential experienced by the electron between the two metals will considerably modify the potential barrier. For a point charge e, located at position x between two conducting parallel plates that are separated by a distance d, the image potential is

$$V_I = \left(-\frac{e^2}{4\pi\varepsilon} \right) \left[\frac{1}{2x} + \sum_{n=1}^{\infty} \left\{ \frac{nd}{[(nd)^2 - x^2]} - \frac{1}{nd} \right\} \right] \tag{2.138}$$

where ε is the dielectric constant of the spacer. For $x = d/2$, middle point between the electrodes, this becomes

$$V_I = -\frac{e^2 \ln 2}{2\pi\varepsilon d} \tag{2.139}$$

This negative contribution to the electron's energy reduces the potential barrier, and has been invoked to explain a lower barrier than expected as observed in STM experiments[10,11]. However, some points should be kept in mind, for instance classical results (Eq. 2.138) fail close to the metal surface where quantum mechanical and

atomic size effects change both the position of the reference image plane and the functional form of the image potential.
The planar geometry implied by the assumption that transmission depends only on the energy of the motion parallel to the tunneling direction, as well as the explicit form of Eq. 2.133 are not valid for a typical STM configuration that involves a tip on one side and a structured surface on the other. To account for these structures Tersoff and Hamman[12] have applied the Bardeen's formalism[13], which is a perturbative approach to tunneling in arbitrary geometries. The Bardeen's formula for the tunneling current is

$$I = \frac{4\pi e}{\hbar}\sum_{l,r}\left[f(E_l)\left(1 - f(E_r + e\Phi)\right) - \left(1 - f(E_l)\right)f(E_r + e\Phi)\right]|M_{lr}|^2\delta(E_l - E_r)$$
$$= \frac{2\pi e}{\hbar}\sum_{l,r}[f(E_l) - f(E_r + e\Phi)]|M_{lr}|^2\delta(E_l - E_r) \quad (2.140)$$

where

$$M_{lr} = \frac{\hbar^2}{2m}\int d\mathbf{S}\cdot(\psi_l^*\nabla\psi_r - \psi_l\nabla\psi_r^*) \quad (2.141)$$

is the transition matrix element for the tunneling process, which is just the Golden rule rate expression (multiplied by the electron charge e), with M playing the role of coupling. In Eq. 2.141 ψ_l and ψ_r are electronic eigenstates of the negatively biased (left) and positively biased (right) electrodes, respectively, Φ is the bias potential and the integral is over any surface separating the two electrodes and lying entirely in the barrier region. Furthermore, the wavefunction in Eq. 2.141 are eigenfunctions of Hamiltonians that describe each electrode in the absence of the other, this is, electrodes interfaced with an infinite spacer medium. Therefore, these functions decay exponentially in the space between the two electrodes.
For $\Phi \to 0$ Eq. 2.140 yields the conduction

$$g \equiv \frac{I}{\Phi} = \frac{4\pi e^2}{\hbar}\sum_{l,r}|M_{lr}|^2\,\delta(E_l - E_F)\delta(E_r - E_F) \quad (2.142)$$

Tersoff and Hamman have used substrate wavefunctions that correspond to a corrugated surface of a generic metal while the tip is represented by spherical *s* orbitals centered about the center r_0 of the tip curvature.
In this case they found that

$$I \propto \sum_V |\psi_V(r_0)|^2 \, \delta(E_V - E_F) \tag{2.143}$$

The right hand side of the former equation (2.143) is the local density of states (LDOS) of the metal. This result is useful for analysis of spatial variation of the tunneling current on a given metal surface, as we will see in following chapters of this manuscript.

2.7.3 The Landauer Formula

Landauer[14,15] presented a more accurate representation of the conduction and the current-voltage characteristic of a given junction that what we have seen in Eqs. 2.133 - 2.136 and 2.140 - 2.142.

At first, Landauer determined the conductance for a system of two 1-dimensional leads connecting two macroscopic electrodes via a scattering object or a barrier characterized by a transmission function $T(E)$, at zero temperature and as the limit $\Phi \to 0$

$$g = \frac{e^2}{\pi\hbar} \, T(E_F) \tag{2.144}$$

The former result is obtained after computing the total unidirectional current carried in an ideal lead by electrons in the energy range $(0, E) = \left(0, \frac{\hbar^2 k_E^2}{2m}\right)$.
In a 1-dimensional system of length L the density of electrons, including spin, with wavevectors in the range between k and $k + dk$ is $n(k)dK = 2\left(\frac{1}{L}\right)\left(\frac{L}{2\pi}\right) f(E_k)dk = f(E_k)dk/\pi$.

The corresponding velocity is $v = \hbar k/m$. Thus

$$\begin{aligned} I(E) &= e \int_0^{k_E} dk v(k) n(k) \\ &= e \int_0^{k_E} dk \, (\hbar k/m) \, f(E_k)/\pi = \frac{e}{\pi\hbar} \int_0^E dE' f(E') \end{aligned} \tag{2.145}$$

At zero temperature, the net current carried under bias Φ is

$$I = \frac{e}{\pi\hbar}\int_0^\infty dE\ (f(E) - f(E + e\Phi)) \ \rightarrow \frac{e^2}{\pi\hbar}\Phi \tag{2.146}$$

Thus the conductance of an ideal 1-dimensional lead is $\frac{I}{\Phi} = \frac{e^2}{\pi\hbar} == (12.9K\Omega)^{-1}$.

More generally, the current for a voltage difference Φ between the electrodes is given by

$$I = \int_0^\infty dE\ [f(E) - f(E + e\Phi)]\frac{g(E)}{e} \tag{2.147}$$

where

$$g(E) = \frac{e^2}{\pi\hbar}\sum_{i,j} T_{ij}(E) \tag{2.148}$$

The former equation is the Landauer formula, where $g(E)$ is the electrical conductance, $\frac{e^2}{\pi\hbar}$ is the conductance quantum and T_{ij} are the transmission eigenvalues. In essence, the Landauer formula is a simple expression that gives us the transmission probability of an electron when propagating with an energy that is equal to the chemical potential of the conducting leads.

2.7.4 Green's functions formalism

Green's functions are relatively easy to be solved and calculated, compared to a direct numerical solution of the Schrödinger equation. In particular, a very efficient recursive method is available for obtaining the Green's functions necessary for the evaluation of the transmission coefficients in the Landauer-Büttiker formalism.

2.7.4.1 Basic ideas of Green's functions

In quantum physics, the single-particle Green's function operator of a system described by a Hamiltonian can be defined as the solutions to the operator equation

$$\left[\widehat{\mathrm{E}} - \widehat{\mathrm{H}}\right]\widehat{\mathrm{G}}(\mathrm{E}) = 1 \tag{2.149}$$

where $\widehat{\mathrm{G}}(\mathrm{E})$ is the Green's operator. A formal solution to this equation would be given by $\widehat{\mathrm{G}}(\mathrm{E}) = (\mathrm{E} - \widehat{\mathrm{H}})^{-1}$. However, the former solution is not well defined for values of E corresponding to the eigenvalues of the Hamiltonian. This can be appreciated when going to the position-spin representation of Eq. (2.149)

$$[\mathrm{E} - \mathrm{H}(\mathbf{x})]\, \mathrm{G}(\mathbf{x}, \mathbf{x}', \mathrm{E}) = \delta(\mathbf{x} - \mathbf{x}') \tag{2.150}$$

The vector x contains both the position and spin variables $\mathrm{x} = (\mathbf{r}, \sigma)$, and the function

$$\mathrm{G}(\mathbf{x}, \mathbf{x}', \mathrm{E}) = \left\langle \mathrm{x}\middle|\widehat{\mathrm{G}}(\mathrm{E})\middle|\mathrm{x}'\right\rangle \tag{2.151}$$

is called the Green's function of the system.

From Eq. (2.150) it can be seen that the Green's function can be considered as a wavefunction at $\mathbf{r}$ resulting form a unit excitation at $\mathbf{r}'$. But on the other hand, G can also be considered as the source of such excitation. Both solutions satisfy Eq. (2.150), but they correspond the different boundary conditions: if H would be the Hamiltonian for a particle moving in a constant potential, then the first solution would correspond to an outgoing wave form the point $\mathbf{r}'$, while the second solution would be an incoming wave. We can add an infinitesimal imaginary variable, in order to incorporate such boundary conditions into the Green's function:

$$\mathrm{G}^{\pm}(\mathbf{x}, \mathbf{x}', \mathrm{E}) = \lim_{\eta \to 0^+} \mathrm{G}(\mathbf{x}, \mathbf{x}', \mathrm{E} \pm \mathrm{i}\eta) \tag{2.152}$$

where the functions $\mathrm{G}^{\pm}$ satisfy

$$[\mathrm{E} \pm \mathrm{i}\eta - \mathrm{H}(\mathbf{x})]\mathrm{G}^{\pm}(\mathbf{x}, \mathbf{x}', \mathrm{E}) = \delta(\mathbf{x} - \mathbf{x}') \tag{2.153}$$

The functions G^+ and G^- are called the advanced and retarded Green's function, respectively.
In the operator language, the retarded and advanced Green's functions operators are defined uniquely for all real values of E by the relation

$$\widehat{G}^{\pm}(E) = \lim_{\eta \to 0^+} \frac{1}{E \pm i\eta - \widehat{H}}, \tag{2.154}$$

From Eq. (2.154) we can conclude that the advanced Green's function corresponds to the hermitian conjugate of the retarded one, i.e., $G^- = (G^+)^\dagger \equiv G^\dagger$.

2.7.4.2 Transmission coefficients and the Green's functions

In the Landauer-Büttiker formalism, presented in section 2.7.3, a central device is connected to perfect leads, and its current-voltage characteristics can be expressed in terms of transmission coefficients between those leads. These transmission coefficients can be related to the Green's functions of the central device.
In a tight-binding representation of the system, the transmission coefficient between leads p and q is given by

$$T_{pq} = \mathrm{Tr}\left[\Gamma_p G_{pq} \Gamma_q G_{pq}^\dagger\right] \tag{2.155}$$

where G_{pq} is a submatrix of the Green's function G of the whole system. It contains only the elements of G between sites in the central device that connect to leads p and q: in particular, if $\mathcal{P}_{p(q)}$ is a projection operator onto the sites of the central device to which lead p(q) is connected , then

$$G_{pq} = \mathcal{P}_p G \mathcal{P}_q \tag{2.156}$$

The matrix Γ_p in Eq.(2.155) is the so-called broadening function of lead p. It is given in terms of what is known as the self-energy Σ_p of the lead:

$$\Gamma_p = i(\Sigma_p - \Sigma_p^\dagger) \tag{2.157}$$

This self-energy is related to elements of the Green's functions between sites at the surface of the lead.

2.8 Molecular Dynamics

Classical molecular dynamics, using what we can call "predefined potentials" is a powerful tool to investigate the time evolution of many-body condensed matter systems. The former "predefined potentials" can be either based on empirical data or independent electronic structure calculations. The first question we may ask ourselves is how to describe the interatomic interactions. Molecular dynamics, in its most traditional route determines these potentials in advance. Thus, typically the full interaction is broken up into two-body, three-body contributions, long-range and short-range terms, etc.

Ab initio molecular dynamics (AIMD) greatly extended the traditional molecular dynamics and the electronic structure methods. The basic idea of AIMD is to compute the forces acting on the nuclei from electronic structure calculations that are performed "on-the-fly" as the molecular dynamics trajectory is generated. In this way the electronic variables are considered as active degrees of freedom and therefore given a suitable approximate solution of the many-electron problem, also "chemically complex" systems can be handled by molecular dynamics.

However, although its advantages, a price has to be payed for putting molecular dynamics on *ab initio* ground: the correlation lengths and relaxation times that are accessible are much smaller than what is affordable via standard molecular dynamics. Moreover, standard molecular dynamics presents another interesting feature, which is the "experimental aspect of playing with the potential". Thus, tracing back the properties of a given system and comparing it to a physical picture is much harder in AIMD.

In order to reach the AIMD in the framework of the Born-Oppenheimer approximation, we will start by deriving classical molecular dynamics. Our starting point will be thus, the non-relativistic quantum-mechanics as formalized via the time-dependent Schrödinger equation.

$$i\hbar\frac{\partial}{\partial t}\Phi(\{\mathbf{r}_i\};\{\mathbf{R}_I\};t) = \hat{H}\Phi(\{\mathbf{r}_i\};\{\mathbf{R}_I\};t) \tag{2.158}$$

where $\{\mathbf{r}_i\}$ and $\{R_I\}$ are the electronic and nuclear degrees of freedom, respectively., and $\hat{H}$ is the standard Hamiltonian. Thus, only the bare electron-electron, electron-nuclear and nuclear-nuclear Coulomb interactions are taken into account.
We will derive classical molecular dynamics separating nuclear and electronic contributions to the total wavefunction $\Phi(\{\mathbf{r}_i\};\{\mathbf{R}_I\};t)$. The simplest form is a product ansatz

$$\Phi(\{\mathbf{r}_i\};\{\mathbf{R}_I\};t) \approx \psi(\{\mathbf{r}_i\};t)\ \chi(\{\mathbf{R}_I\};t)\ \exp\left[\frac{i}{\hbar}\int_{t_0}^{t} dt'\ \widetilde{E}_e(t')\right] \tag{2.159}$$

Where $\widetilde{E}_e$ is a phase factor, introduced at this stage in order to simplify the final equation.

$$\widetilde{E}_e = \int d\mathbf{r}d\mathbf{R}\ \psi^*(\{\mathbf{r}_i\};t)\ \chi^*(\{\mathbf{R}_I\};t)\ \hat{H}_e\ \psi(\{\mathbf{r}_i\};t)\ \chi(\{\mathbf{R}_I\};t) \tag{2.160}$$

Note that this product ansatz (excluding the phase factor) differs form the Born-Oppenheimer ansatz for separating the fast and slow variables

$$\phi_{BO}(\{\mathbf{r}_i\};\{\mathbf{R}_I\};t) = \sum_{k=0}^{\infty}\widetilde{\psi}_k(\{\mathbf{r}_i\},\{\mathbf{R}_I\})\tilde{\chi}_k(\{\mathbf{R}_I\},t) \tag{2.161}$$

Inserting Eq. (2.159) in Eq. (2.158) yields (after multiplying from the left by $\langle\psi|$ and $\langle\chi|$ and imposing energy conservation $\frac{d\langle\hat{H}\rangle}{dt} \equiv 0$) the following relations

$$i\hbar\frac{\partial\psi}{\partial t} = -\sum_i\frac{\hbar^2}{2m_e}\nabla_i^2\psi + \{\int d\mathbf{R}\ \chi^*(\{\mathbf{R}_I\};t)V_{n-e}(\{\mathbf{r}_i\},\{\mathbf{R}_I\})\ \chi(\{\mathbf{R}_I\},t)\} \tag{2.162}$$

$$i\hbar\frac{\partial\chi}{\partial t} = -\sum_i\frac{\hbar^2}{2M_I}\nabla_i^2\chi + \left\{\int d\mathbf{r}\ \psi^*(\{\mathbf{r}_i\};t)\hat{H}_e(\{\mathbf{r}_i\},\{\mathbf{R}_I\})\ \psi(\{\mathbf{r}_i\},t)\right\}\chi \tag{2.163}$$

The former set of coupled equations defines the basis of the time-dependent self-consistent field (TDSCF) method.
The former is the simplest possible separation of electronic and nuclear variables.

The next step in the derivation of classical molecular dynamics is to approximate the nuclei as classical particles. In order to extract classical mechanics form quantum mechanics we will start with rewriting the corresponding wavefunction

$$\chi(\{\mathbf{R}_I\};t) = A(\{\mathbf{R}_I\};t)\exp[iS(\{\mathbf{R}_I\};t)/\hbar] \tag{2.164}$$

in terms of an amplitude factor, A, and a phase factor, S, which are both considered to be real and $A > 0$ in this polar representation. After transforming the nuclear wavefunction in Eq. (2.163) and after separating the real and the imaginary parts, the TDSCF equation for the nucleiis exactly re-expressed in terms of the new variables A and S.

$$\frac{\partial S}{dt} + \sum_I \frac{1}{2M_I}(\nabla_I S)^2 + \int d\mathbf{r}\ \psi^*\,\hat{H}_e\,\psi = \hbar^2 \sum_I \frac{1}{2M_I}\frac{\nabla_I^2 A}{A} \tag{2.165}$$

$$\frac{\partial A}{dt} + \sum_I \frac{1}{M_I}(\nabla_I A)(\nabla_I S) + \sum_I \frac{1}{2M_I} A\left(\nabla_I^2 S\right) = 0 \tag{2.166}$$

Eqs. (2.165-66) are the so-called "quantum fluid dynamical representation" and they can be used to solved the time-dependent Schrödinger equation.

In the relation for S, Eq. (2.165), we see how this equation contains one term that depends on $\hbar$, a contribution that vanishes if the limit is taken as $\hbar \to 0$.

$$\frac{\partial S}{dt} + \sum_I \frac{1}{2M_I}(\nabla_I S)^2 + \int d\mathbf{r}\ \psi^*\,\hat{H}_e\,\psi = 0 \tag{2.167}$$

The resulting equation is isomorphic with equations of motion in the Hamilton-Jacobi formulation

$$\frac{\partial S}{dt} + \hat{H}(\{\mathbf{R}_I\},\{\nabla_I S\}) = 0 \tag{2.168}$$

of classical mechanics with the classical Hamilton function

$$\hat{H}(\{\mathbf{R}_I\},\{\mathbf{P}_I\}) = T(\{\mathbf{P}_I\}) + V(\{\mathbf{R}_I\}) \tag{2.169}$$

defined in terms of coordinates, $\{\mathbf{R}_I\}$ and their conjugated momenta $\{\mathbf{P}_I\}$. With the help of the connecting transformation

$$\mathbf{P}_I \equiv \nabla_I S \tag{2.170}$$

the Newtonian equation of motion $\dot{\mathbf{P}}_I - \nabla_I V(\{\mathbf{R}_I\})$ corresponding to Eq. (2.167) can be read off

$$\frac{d\mathbf{P}_I}{dt} = -\nabla_I \int d\mathbf{r}\, \psi^* \hat{H}_e \psi \tag{2.171}$$

or

$$M_I \ddot{\mathbf{R}}_I(t) = -\nabla_I \int d\mathbf{r}\ \psi^* \hat{H}_e \psi \tag{2.174}$$

$$= -\nabla_I V_e^E(\{\mathbf{R}_I(t)\}) \tag{2.175}$$

Thus, the nuclei move according to classical mechanics in an effective potential V_e^E due to the electrons. This potential is a function only of the nuclear positions at time t as a result of averaging $\hat{H}_e$ over the electronic degrees of freedom, i.e. computing its quantum expectation value $\langle\psi|\hat{H}_e|\psi\rangle$, while keeping the nuclear positions fixed at their instantaneous values $\{\mathbf{R}_I(t)\}$.

However, the nuclear wavefunction still occurs in the TDSCF equation for electronic degrees of freedom and has to be replaced by the positions of the nuclei for consistency.
In this case the classical reduction can be achieved simply by replacing the nuclear density $|\chi(\{R_I\};t)|^2$ in Eq. (2.162) in the limit $\hbar \to 0$ by a product of delta functions $\Pi_I \delta(R_I - R_I(t))$ centered at the instantaneous positions $\{\mathbf{R}_I(t)\}$ of the classical nuclei as given by Eq. (2.174).

This classical limit yields to a time-dependent wave equation for the electrons

$$i\hbar \frac{\partial \psi}{\partial t} = -\sum_i \frac{\hbar^2}{2m_e} \nabla_i^2 \psi + V_{n-e}(\{\mathbf{r}_i\}, \{\mathbf{R}_I(t)\})\psi$$

$$= \hat{H}_e(\{\mathbf{r}_i\}, \{\mathbf{R}_I(t)\})\ \psi(\{\mathbf{r}_i\}, \{\mathbf{R}_I(t)\}) \tag{2.176}$$

We observe now how $\widehat{H}_e$ and ψ depend parametrically on the classical nuclear positions $\{\mathbf{R}_I(t)\}$ at time t through $V_{n-e}(\{\mathbf{r}_i\},\{\mathbf{R}_I(t)\})$. Thus, there is a feedback between classical and quantum degrees of freedom.
The former approach, shown in Eqs. (2.174) and (2.176) is called "Ehrenfest molecular dynamics", in honor to Ehrenfest, who was the first to address how the Newtonian classical dynamics can be derived from Schrödinger's wave equation.

2.8.1 Born-Oppenheimer Molecular Dynamics

Another approach to include the electronic structure, and the one that we have used to carry on our dynamical study, is to straightforwardly solve the *static* electronic structure problem in each molecular dynamics step, given by the set of *fixed* nuclear positions at that instance of time. Therefore, the electronic structure is solved as a *time-independent* quantum problem, i.e. propagating the nuclei via classical molecular dynamics.
Thus, the time-dependence of the electronic structure is a consequence of nuclear motion, and not intrinsic as in the Ehrenfest molecular dynamics.

The resulting Born-Oppenheimer molecular dynamics method is defined by

$$M_I\ddot{\mathbf{R}}_I(t) = -\nabla_I \min_{\psi_0}\{\langle\psi_0|\widehat{H}_e|\psi_0\rangle\} \tag{2.177}$$

$$E_0\psi_0 = \widehat{H}_e\psi_0 \tag{2.178}$$

for the electronic ground state. The main difference with the Ehrenfest method is that the minimum of $\langle\widehat{H}_e\rangle$ has to be reached in each Born-Oppenheimer molecular dynamics step according to Eq. (2.177).

For the Hartree-Fock case, Eqs. (2.177) and (2.178) would be

$$M_I\ddot{\mathbf{R}}_I(t) = -\nabla_I \min_{\{\psi_i\}}\{\langle\psi_0|\widehat{H}_e^{HF}|\psi_0\rangle\} \tag{2.179}$$

$$0 = -\hat{H}_e^{HF}\psi_i + \sum_j \Lambda_{ij}\psi_j \quad (2.180)$$

A similar set of equations would be obtained if Hohenberg-Kohn-Sham density functional theory were used, where $\hat{H}_e^{HF}$ has to be replaced by $\hat{H}_e^{KS}$ the Kohn-Sham effective one-particle Hamiltonian.

2.9 Correlation exchange functionals

Density Functional Theory would be an exact approach to electronic calculations if only we knew the exact exchange-correlation functional. Therefore, several functionals have been developed along the years in order to give the most accurate and precise result for the system of interest.

A first approach is the Local Density Approximation (LDA), in which the exchange-correlation term, $E_{XC}[\rho]$, is approximated by the exchange-correlation energy of an electron in an homogeneous electron gas of the same density, $\rho(\mathbf{r})$. The correlation energy is determined by Quantum Montecarlo calculations as Ceperly and Alder[16] did to very high accuracy; and others (Vosko, Wilk and Nusair, "VWN" and Perdew and Wang, "PW") fitted these numerical results to analytical models in ρ.

Since this method is based in a homogeneous electron gas, where ρ changes smoothly with the position, we find the need of a more precise method that gives us another functional for describing the exchange-correlation term. We reach this way to the so-called Generalized Gradient Approximation (GGA)[17,18], which calls for an improvement in the description of the variation of ρ with the position. This method performs this idea by including the gradients of ρ. Furthermore, this method is based in separating both correlation and exchange terms in such a way that they are independently calculated. It is a *semilocal* approximation to the exchange-correlation energy as a functional of the density and its gradient to fulfill a maximum number of exact relations,

$$E_{XC}^{GGA}[\rho^{\alpha}\ .\rho^{\beta}] = \int dr\, f\left(\rho^{\alpha}(r), \rho^{\beta}(r), \nabla\rho^{\alpha}(r), \nabla\rho^{\beta}(r)\right) \quad (2.181)$$

and the exchange correlation potential is given by

$$V_{xc}[n(r)] = \frac{\partial E_{xc}[\rho]}{\partial \rho(r)} - \nabla . \frac{\partial E_{xc}[\rho]}{\partial(\nabla\rho(r))} \quad (2.182)$$

The gradient of the density, ρ, is usually determined *numerically*.
In this framework, we find the Perdew Wang 91 (PW91) functional and the 1996 functional of Perdew, Burke and Ernzerhof (PBE)[19, 20]. The Perdew-Wang 1991 functional is a purely ab initio functional, which fulfills almost all scaling relations except high density limit of uniform scaling. The exchange energy is given by

$$E_x^{PW91}[\rho] = -\int dr\, \rho\, \frac{3k_F}{4\pi}\, \frac{1+0.1965\, s \sinh^{-1}(7.796s)+(0.274-0.151e^{-100s^2})s^2}{1+0.1964s \sinh^{-1}(7.796s)+0.004s^4} \quad (2.183)$$

and the correlation energy

$$E_c^{PW91}[\rho] = \int dr\, \rho(\varepsilon_c(r_s, \zeta) + H(t, r_s, \zeta)) \quad (2.184)$$

with $k_F = (3\pi^2 n)^{1/3}$, $s = {|\nabla\rho|}/{2k_F\,\rho}$, $t = {|\nabla\rho|}/{2gk_s\,\rho}$, $k_s = (4k_F/\pi)^{1/2}$ and $g = \left[(1+\zeta)^{2/3} + (1-\zeta)^{2/3}\right]/2$.

The Perdew-Burke-Erzenhof 1996 (PBE) functional introduces a simplification of the derivation of PW91. The exchange energy is given by

$$E_x^{PBE}(\rho, |\nabla\rho|) = \int_r dr\, \rho \varepsilon_x^{LDA}(\rho) F_x^{PBE}(s) \quad (2.185)$$

where $F_x^{PBE}(s) = 1 + k - \frac{k}{1+\frac{\mu s^2}{k}}$, and $\mu = \beta\left(\frac{\pi^2}{3}\right)$.

The correlation energy is then given by

$$E_x^{PBE}(\rho, |\nabla\rho|) = \int_r dr\, \rho[\varepsilon_{xc}^{LDA}(\rho) + H_c^{PBE}(r_s, \eta, t) \quad (2.186)$$

where $H_c^{PBE}(r_s,\eta,t) = \gamma\emptyset^3 \ln\left[1+\frac{\beta}{\gamma}t^2\left(\frac{1+At^2}{1+At^2+A^2t^4}\right)\right]$, $A(r_s,\eta) = \frac{\beta}{\gamma}\frac{1}{e^{-\varepsilon_c^{LDA}/\gamma\emptyset^3}-1}$, $\emptyset(\eta) = \frac{1}{2}\left[(1+\eta)^{2/3}+(1-\eta)^{2/3}\right]$, $\gamma = \frac{1-\ln 2}{\pi^2}$, $r_s = \left[\frac{3}{4\pi\rho}\right]^{1/3}$, which is the local Wigner-Seit radius, and $\beta \approx 0.066725$, comes from the generalized gradient expansion for the correlation.

In this work, we have used the PW91 and the PBE functionals; in order to include the van der Waals interactions, we have added to the obtained energies a dispersion term as explained in chapter 3.

2.10 Analysis tools

In this last section of chapter 2, we present different analysis tools, which have been used during our study. In particular, the Bader charge analysis method, and the calculation of the Projected Density of States and the work function calculated are explained.

2.10.1 Bader charge Analysis

Richard Bader developed an intuitive way of dividing molecules into atoms called The Quantum Theory of Atoms in Molecules (QTAIM)[21,22]. His definition of an atom is purely based on the electronic charge density. Bader uses what are called the zero flux surfaces to divide atoms. They are a 2-D surface on which the charge density is a minimum perpendicular to the surface. Typically in molecular systems, the charge density reaches a minimum between atoms and this is a natural place to separate atoms from each other.

Bader's theory of atoms in molecules is often useful for charge analysis. For instance, the charge enclosed within the Bader volume is a good approximation to the total electronic charge of an atom.

The group of Henkelman[23-25] developed a computational method fro portioning the charge density grid into Bader volumes (see figure 2.8)

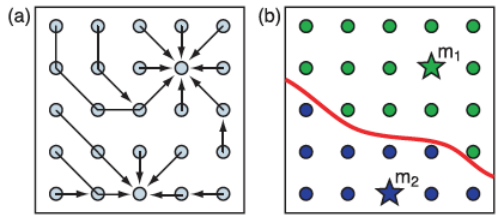

Figure 2.8: Steepest ascent paths (a) on a charge density grid to find the Bader volumes. Ascent trajectories are constrained to the grid points, moving at each step to the neighboring grid point towards which the charge density gradient is maximized. Each trajectory either terminates at a new charge density maximum, m_i, or at a grid point which has already been assigned. After all grid points are assigned (b), the set of points that terminate at each maximum (green to m_1 and blue to m_2) constitute the Bader volume. The Bader surfaces (red curved line) separate the volumes. (Source: W. Tang *et al.* J. Phys. Condens. Matter 21 (2009) 084204)

This is an efficient method that scales linearly with the number of grid points. The portioning algorithm follows steepest ascent paths along the charge density gradient from grid point to grid point until a charge density maximum is reached. As the algorithm assigns grid points to charge density maxima, subsequent paths are determined when they reach previously assigned grid points. Finally, numerical integration of the density in each volume provides the charge around each atom. This grid based approach gives the algorithm an efficiency that allows us to perform a charge analysis of large grids generated from plane waves density functional theory calculations.

2.10.2 Projected Density of States

In solid-state physics the Density of States (DOS) of a system describes the number of states per interval of energy, at each energy level, that are available to be occupied. Unlike atoms or molecules (in gas phase) the density distributions are not discrete.
The density of states is defined as

$$n(\varepsilon) = \sum_j \langle \psi_j | \psi_j \rangle \delta(\varepsilon - \varepsilon_j) \qquad (2.187)$$

where ε_n is the eigenvalue of the eigenstate ψ_n.
Inserting a complete orthonormal basis, this can be written as

$$N(\varepsilon) = \sum_i n_i(\varepsilon), \qquad n_i(\varepsilon) = \sum_j \langle\psi_j|i\rangle\langle i|\psi_j\rangle\, \delta(\varepsilon - \varepsilon_j) \tag{2.188}$$

$$N(\varepsilon) = \int dr\, n(r,\varepsilon), \qquad n(r,\varepsilon) = \sum_j \langle\psi_j|r\rangle\langle r|\psi_j\rangle\, \delta(\varepsilon - \varepsilon_j) \tag{2.189}$$

using that $1 = \sum_i |i\rangle\langle i|$ and $1 = \int dr\, |r\rangle\langle r|$.
$n_i(\varepsilon)$ is called the projected density of states (PDOS), and $N(r,\varepsilon)$ the local density of states (LDOS). If we integrate the energy of the LDOS and multiply it by a Fermi distribution, we obtain the electron density

$$\int d\varepsilon\, n_F(\varepsilon) N(r,\varepsilon) = \rho(r) \tag{2.190}$$

On the other hand, summing the PDOS over i gives the spectral weight of orbital i.
The construction of the PDOS requires the projection of the Kohn-Sham eigenstates $|\psi_n\rangle$ onto a set of orthonormal states $|\psi_{\bar{n}}\rangle$.

$$\rho_{\bar{n}} = \sum_n |\langle\psi_{\bar{n}}|\psi_n\rangle|^2 \delta(\varepsilon - \varepsilon_n) \tag{2.191}$$

The all electron overlaps $\langle\psi_{\bar{n}}|\psi_n\rangle$ can be calculated with the PAW formalism from the pseudo wavefunctions $|\tilde{\psi}\rangle$ and their projector overlaps by

$$\langle\psi_{\bar{n}}|\psi_n\rangle = \langle\tilde{\psi}_{\bar{n}}|\tilde{\psi}_n\rangle + \sum_a \sum_{i_1 i_2} \langle\tilde{\psi}_{\bar{n}}|\tilde{p}^a_{i_1}\rangle\, \Delta S^a_{i_1 i_2}\, P^a_{n\, i_2} \tag{2.192}$$

where $\Delta S^a_{i_1 i_2} = \langle\phi^a_{i_1}|\phi^a_{i_2}\rangle - \langle\tilde{\phi}^a_{i_1}|\tilde{\phi}^a_{i_2}\rangle$ is the overlap metric, $\phi^a_{i_1}$, $\tilde{\phi}^a_{i_1}$, and $\tilde{p}^a_{i_1}$ are the partial waves, pseudo partial waves and projector functions of atom a respectively, and $P^a_{n\, i_2} = \langle\tilde{p}^a_i|\tilde{\psi}_n\rangle$.
If one choses the state $|\psi_{\bar{n}}\rangle$ as eigenstate of a different reference Kohn-Sham system, with the projector overlaps $\overline{P}^a_{\bar{n}\, i}$, the PDOS relative to these states can be calculates by

$$\langle\psi_{\bar{n}}|\psi_n\rangle = \langle\tilde{\psi}_{\bar{n}}|\tilde{\psi}_n\rangle + \sum_a \sum_{i_1 i_2} \overline{P}^{a*}_{\bar{n} i_1}\, \Delta S^a_{i_1 i_2}\, P^a_{n\, i_2} \tag{2.193}$$

2.10.3 Work Function

The work function, ϕ, is the energy required to remove an electron from the highest filled level in the Fermi distribution of a solid, so that it is stationary at a point in a field-free zone just outside the solid, at absolute zero.
The work function for a given surface is defined by the difference

$$\phi = -e\chi - E_f \tag{2.194}$$

where $-e$ is the charge of an electron, χ is the electrostatic potential in the vacuum nearby the surface, and E_f is the Fermi level (electrochemical potential) inside the material. The term $-e\chi$ represents the energy of an electron at rest in the vacuum nearby the surface, and the meaning of $-E_f$ is the work required to remove an electron from the material to a state at rest in the vacuum nearby the surface.

Figure 2.9 represents the local potential (averaged in the coordinate parallel to the surface) as a function of the vertical distance for one of the systems of our study, C_6H_6/Cu(100). We observe four initial oscillations corresponding to the four Cu layers of the substrate. The red solid line depicts the whole adsorbed system, and therefore a fifth oscillation is observed at the height where the benzene molecule is adsorbed. The Fermi level is shown with a black dotted line. The potential stops fluctuating at the vacuum level and outside the surface shows the Coulomb tail (image potential). The distance between the Fermi level and the potential in the vacuum level is the work function of the system.

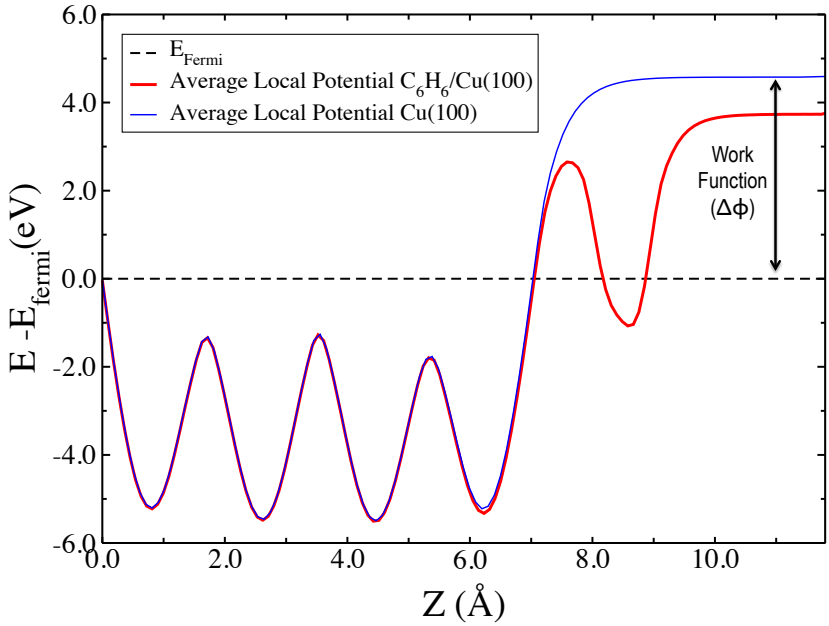

Figure 2.9: Total local potential for the complete adsorbed system C_6H_6/Cu(100) (red solid line), for the bare metal Cu(100) surface (blue solid line). Black dotted line represents the Fermi level for the complete adsorbed system.

References

(1) Thomas L.H. *Proc Camb. Phil SOc* 1927, *33*, 542.
(2) Blöchl, P. E. *Phys. Rev. B* 1994, *50*, 17953–17979.
(3) Sautet P.; Dunphy J.C.; Ogletree D.F. et al. *Surf. Sci.* 1994, *315*, 127.
(4) Sautet P.; Joachim C. *Chem. Phys. Lett.* 1921, *185*, 23.
(5) Sautet P.; Joachim C. *Chem. Phys.* 1989, *135*, 99.
(6) Chavy C.; Joachim C.; Altibeli A. *Chem. Phys. Lett.* 1993, *214*, 569.
(7) Doumergue P.; Pizzagalli L.; Joachim C., et al. *Phys. Rev. B* 1999, *59*, 15910.
(8) Joachim C.; Gimzewski J.K. *Eur. Lett.* 1993, *214*, 569.
(9) Simmons J.G. *J. Appl. Phys.* 1963, *34*, 1793.
(10) Lang N.D. *Phys. Rev. B* 1987, *36*, 8173.
(11) Lang N.D. *Phys. Rev. B* 1988, *37*, 10395.
(12) Tersoff J.; Hamman D.R. *Phys. Rev. B* 1985, *805*, 5031.
(13) Bardeen J. *Phys. Rev. Lett.* 1961, *6*, 57.
(14) Landauer R. *IBM J. Res. Dev.* 1957, *1*, 223.
(15) Landauer R. *Phil Mag* 1970, *21*, 863**.**
(16) Ceperley D. M. and Alder B.J., *Phys. Rev. Lett.* 1980, 45, 566.
(17) Perdew J. P.; Chevary J. A.; Vosko S. H.; Jackson K. A.; Pederson M. R.; Singh D. J.; Fiolhais C. *Phys. Rev. B* 1992 *46*, 6671
(18) Perdew J. P.; Chevary J. A.; Vosko S. H.; Jackson K. A.; Pederson M. R.; Singh D. J.; Fiolhais C. *Phys. Rev. B* 1993 *48*, 4978
(19) Perdew J. P.; Burke K.; Ernzerhof M. *Phys. Rev. Lett.* 1996 *77*, 3865-68
(20) Perdew J. P.; Burke K.; Ernzerhof M. *Phys. Rev. Lett.* 1997 78, 1396
(21) Bader R. F. W. *Chemical Reviews* 1991 *91*, 893
(22) Bader R. F. W. *Atoms in Molecules: A Quantum Theory* (Oxford University Press, USA, 1994)
(23) Tang W.; Sanville E.; Henkelman G.; *Journal of physics: Condensed Matter* 2009 *21*, 084204
(24) Sanville E.; Kenny S. D.; Smith R.; Henkelman G. *Journal of Computational Chemistry* 2007 *28*, 899
(25) Henkelman G.; Arnaldsson A.; Jonsson H. *Computational Materials Science* 2006 *36*, 354

Results

Chapter 3

C_6H_6/n NaCl/Cu(100)

3.1 Introduction

In the first chapter of this manuscript, we explained how the organic compounds with semiconductive properties can be classified into three different groups. Among those, we already mentioned the compounds where a number of delocalized electrons provide the semiconductive properties. These compounds are normally aromatic molecules with delocalized π valence electrons. In this framework, benzene can be considered as a benchmark molecule due to its short size and its representative structure.
Moreover, adsorption of organic molecules is an easy and excellent way of modifying the properties of metal surfaces.
Already at the prehistoric time they were used (in the form of fats) to cover bronze tools; and in the meantime it constitutes a multibillion-dollar industry that imparts tailored characteristics to metal surfaces.

Nowadays, the most common molecules used in organic-based electronic devices [1] combine π delocalized electrons (aromatic compounds) with other functional groups (alcohol, carboxyl, cyano, etc.) as in TCNQ[2,3], PTCDA[4–9] or azobenzene derivatives[10,11], all of them containing benzene rings on their structure. Therefore, understanding the adsorption of benzene on a metal surface is a prime step in order to get an overall idea of this kind of interactions.

On the other hand, many different metals are used as metallic substrates for further

deposition of organic molecules; however the specific interest aroused towards a noble metal as copper has grown due to the crucial role that this metal plays in hydrogen catalysis and cracking reactions. An example of the latter is the dissociation of benzene on Cu(001) into smaller fragments caused by the tunneling current during an STM study[12]. However, copper is a noble metal with a full *d* band and therefore, quite inert, thus leading to a weak interaction when benzene adsorbs on it[13,14]. Thus, when we study such a benchmark system as C_6H_6/Cu(100), we may not only evaluate the rearrangement of the molecule upon adsorption, but also the electronic structure at the interface between benzene and the metal surface; The mismatch of the electronic levels at the interface of the adsorbate and the substrate determines the charge transfer (electrons that can be injected from the latter to the former) limiting the interaction between the organic molecule and the metal substrate.
In this chapter we thoroughly discuss the kind of interaction between C_6H_6 and Cu(100), see sections 3.2 and 3.3.

In this thesis we also explore the effects of adding an insulating thin film, in particular atomic monolayers of NaCl, in between the organic molecule and the metal surface. The former will presumably decouple benzene from the copper surface[15] electronically and therefore will provide a best position to study the inner features of the isolated benzene, as e.g. its unperturbed molecular orbitals. The electronic properties of the molecule cannot be studied otherwise since the direct adsorption of benzene on the metal surface implies the broadening of the molecular orbitals.
In short, we want to explore the effects of including one, two and three atomic layers of NaCl on the metal surface prior to the benzene adsorption. Thus, this chapter focuses on the first subgroup of organic compounds with semiconductive properties, presenting for this aim the benchmark system C_6H_6 interacting with Cu(100). As an "add-on" we have also thoroughly explored the effects of including an insulating film, NaCl.

3.2 The importance of properly accounting for van der Waals (vdW) dispersion forces

We have already stated how the interface geometry in the hybrid inorganic-organic systems plays a crucial role in the determination of their electronic properties and

therefore a proper description of its structure and stability is essential for controlling the function and quality of future electronic devices.

A reliable prediction of the equilibrium structure for hybrid inorganic-organic systems represents a great challenge to the state-of-the-art theoretical methods due to the interplay of covalent interactions, electron transfer processes, van der Waals interactions and Pauli repulsion forces. Specifically, vdW interactions are fundamental in determining the structure and stability of organic molecules interacting with solid surfaces[16–18]. Indeed, the theoretical description of the interaction between benzene and copper possesses particular difficulties, because the prevalence of dispersive vdW forces restricts the applicability of semilocal exchange and correlation (xc) functionals in the framework of Density Functional Theory. High-level theories that include non-local vdW interaction by constructions are still barely tractable for large systems, as surface-adsorbed molecules. Therefore, computationally inexpensive semiempirical dispersion correction schemes to semilocal DFT (DFT-D) represent an appealing alternative.

Within this approach, vdW interactions are considered approximately by adding a pairwise interatomic C_6R^{-6} term to the Becke's power-series ansatz (the term of the DFT energy)[19].

$$E_{DFT-D} = E_{KS-DFT} + E_{disp.} \tag{3.1}$$

where E_{KS-DFT} is the usual self-consistent Kohn-Sham energy as obtained from the chosen density functional and $E_{disp.}$ is an empirical dispersion correction given by

$$E_{disp.} = -s_6 \sum_{i=1}^{N_{at}-1} \sum_{j=i+1}^{N_{at}} \frac{C_6^{ij}}{R_{ij}^6} f_{dmp}(R_{ij}) \tag{3.2}$$

where N_{at} is the number of atoms in the system, C_6^{ij} denotes the dispersion coefficient for atom pair ij, s_6 is a global scaling factor that only depends on the density functional used, and R_{ij} is an interatomic distance. In order to avoid near-singularities for small R, a damping function f_{dmp} must be used, which is given by

$$f_{dmp}(R_{ij}) = \frac{1}{1+e^{-d(R_{ij}/R_r-1)}} \tag{3.3}$$

where R_r is the sum of atomic vdW radii.

However, though it has been proven to give accurate results for a range of molecular systems[20] applying DFT-D approach to organic molecules adsorbed at metal surfaces is limited and uncertain. This uncertainty mainly concerns the fact that it is not clear how the results are affected by the neglected dispersive interaction between the adsorbate and more distant substrate atoms, i.e. the screening of the vdW forces between the molecule and the inner metal atoms due to the intermediate atomic layers. Therefore the neglect of the electronic screening at the metal surface leads to a sizeable overbinding. Moreover, those molecules which also interact covalently with the substrate atoms, exhibit molecule-substrate distances so short that the uncertainties in the damping function of the dispersion term combines in an uncontrolled way with deficiencies of the employed semilocal xc functional.

In order to properly include vdW dispersion forces we have evaluated the performance of this method in the first system of our study (C_6H_6/Cu(100)) as follows (see figure 3.1 and table 3.1):

I) "With vdW": we have included the contribution of the dispersion forces in the whole system (i.e. all atoms of the adsorbate and the substrate).
II) "Partial vdW": dispersion forces have been only considered in the atoms of the adsorbate and the first layer of the metallic substrate (for those cases where NaCl is included, all insulating film atoms were also treated with vdW dispersion forces).
III) "Without vdW": dispersion forces have been excluded completely from the total energy of the system.

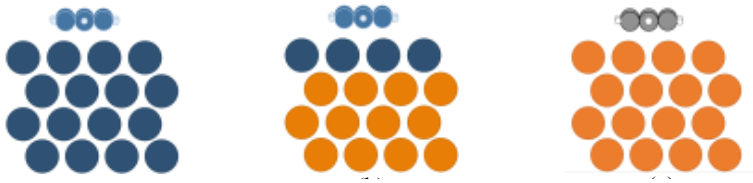

(a)

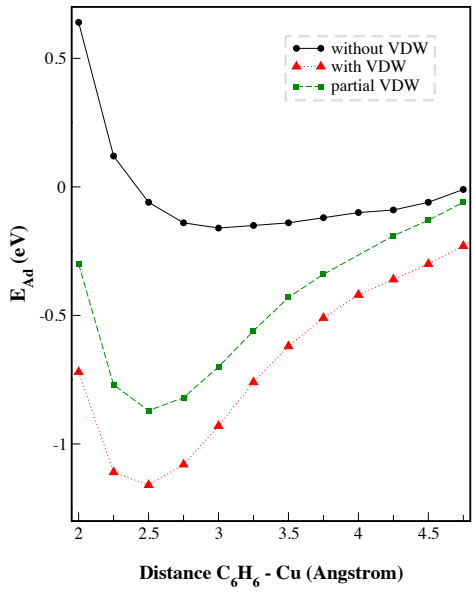

(b)

Figure 3.1: (a) The three different approaches have been evaluated to include van der Waals forces in the C_6H_6/Cu(100) system: top-left "With vdW", top-center "Partial vdW" and top-right "Without vdW". Atoms in blue represent those accounting for vdW dispersion forces. (b) Scan in the coordinate normal to the surface with the molecule interacting on the Hollow adsorption site employing the three approaches.

Table 3.1 shows the three considered approaches for evaluating the interaction between C_6H_6 and the metal substrate on a hollow site (which is in fact the most stable adsorption site) [14]. Adsorption energies and interaction distances shown in the table are quite different, and show the importance of a correct use of the Grimme correction.

Procedure	Hollow site-C_6H_6/Cu(100) E_{Ad} (eV)	$d_{C_6H_6-Cu}$ (Å)
"With vdW"	-1.38	2.16
"Partial vdW"	-1.02	2.26
"Without vdW"	-0.23	3.12

Table 3.1: Interaction energy and distance obtained after geometry optimization of the C_6H_6/Cu(100) (Hollow site) at the three different implementation procedures employed to apply vdW forces: "Without vdW", "Partial vdW" and "With vdW". Initial geometries have been taken from the most favorable distance previously found in the scan calculations.

Table 3.2 shows a detailed comparison between the results obtained employing "With vdW" and "Without vdW" for the two systems: C_6H_6/Cu(100) and C_6H_6/1NaCl/Cu(100). The following findings show how the neglect of the vdW dispersion forces leads mainly to a misinterpretation of the adsorption distances, resulting in significant differences in the interaction energies, equilibrium distances, work function and charge transfer.

System	E_{Ad} (eV)	$d_{C_6H_6-Surf.}$(Å)	ΔΦ (eV)	q_{Bader}
C_6H_6/Cu(100) "Partial vdW"	-1.02	2.26	3.74	-0.22
C_6H_6/Cu(100) "Without vdW"	-0.23	3.12	4.16	0.00
C_6H_6/1NaCl/Cu(100) "Partial vdW"	-0.75	3.21	3.84	-0.02
C_6H_6/1NaCl/Cu(100) "Without vdW"	-0.02	3.43	3.93	0.00

Table 3.2: Interaction energy and distances, work function and charge transfer for the C_6H_6/Cu(100) and C_6H_6/1NaCl/Cu(100) systems "With vdW" and the former "Without vdW".

3.3 C_6H_6/Cu(100)

We have already exposed how the adsorption of aromatic molecules at transition-metal surfaces is important for fundamental and applied surface science studies. Thus, the adsorption of such a benchmark system as benzene on Cu(100) has already been explored by several groups. In this sense, those previous studies have shown how not including vdW dispersion forces would lead to an underestimation of the adsorption energy; for instance Toyoda and coworkers[21] found huge energetic differences between their theoretical study, carried out within the Generalized Gradient Approximation (GGA), and the experimental values ($E_{C6H6/Cu}$ (GGA) = -0.05 eV; $E_{C6H6/Cu}$ (Exp.) = -0.58 eV). Other works [10] have shown as well discrepancies and overestimations of binding energies when dispersion forces were included in the whole metal slab, due to the already described screening effect of the metal.

In view of this situation, we found necessary to properly describe the interaction of such a representative aromatic molecule with a metal surface; and thus, study the features relative to equilibrium distances, charge transfer and electronic structure, when the adsorption energies where close to an exact description.

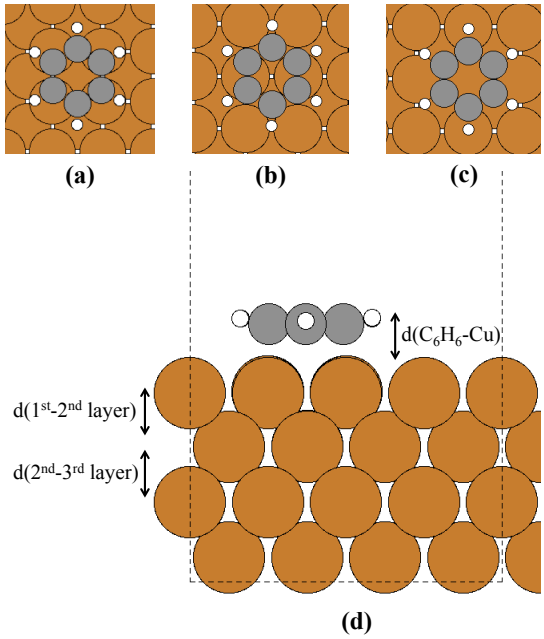

Our first step was then to explore all possible adsorption sites on the Cu(100) surface. The former presents three main locations, known as: hollow, top and bridge. These adsorption sites are shown in figure 3.2.

Figure 3.2: Benzene adsorption sites on the Cu(100) surface: **(a)** Hollow, **(b)** Bridge and **(c)**Top. Schematic overview of the distances in the system **(d)**.

According to previous works on C_6H_6/Cu(100)[14] the hollow site presents the most favorable location for benzene adsorption. Given that, we first performed a scan in the z axes (figure 3.1(b)), with the C_6H_6 molecule on top of a hollow site. The scan shown in Fig. 3.1(b), which has been already mentioned as part of the discussion on how to apply the vdW dispersion forces, also seeks to provide the equilibrium distance between benzene and the metal surface ($d_{C6H6\text{-}Cu[hollow]}$ = 2.26 Å), in order to perform a further scan in the xy angle (plane parallel to the surface), with the aim of finding the most favorable orientation of the molecule on the surface. This second scan is shown in figure 3.3.

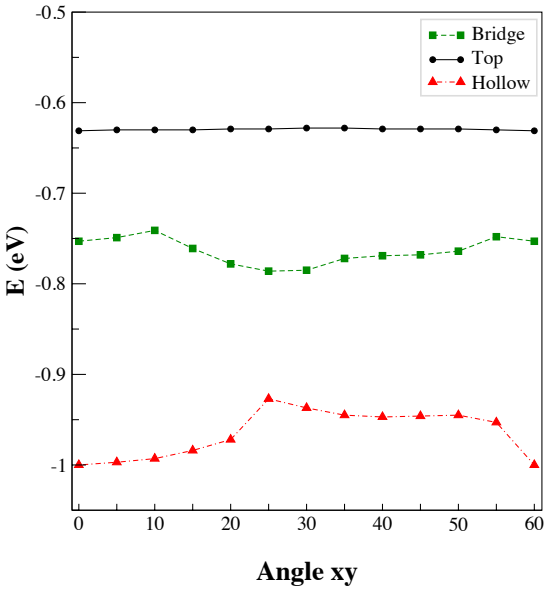

Figure 3.3: Scan in the xy angle (plane parallel to the surface) for the three adsorption sites on the Cu(100) surface.

We have rotated the C_6H_6 molecule from its initial position (as shown in Fig.3.1) 60°, due to its D_{6h} symmetry. While C_6H_6 will stand on its 0° orientation for the hollow and the top sites, it will rather rotate 25° when it is adsorbed on a bridge site of the Cu(100) surface. However, relative energies between one or another orientation of the hydrogen atoms do not differ much ($\Delta E \approx 0.05$ eV); Thus, revealing a soft potential energy surface (PES).

With both scans we have got a flavor of a) the need of including vdW dispersion forces

in the so-called "Partial vdW" way, b) the orientation of the molecule on the surface, and c) the soft PES, we have evaluated the adsorption energies and optimized geometries of C_6H_6 on Cu(100) when adsorbed on the three main adsorption sites (bridge, Hollow and Top).
To this, we define the adsorption energy, E_{Ad} as:

$$E_{Ad} = E_{C_6H_6/Cu(100)} - [E_{C_6H_6} + E_{Cu(100)}] \quad (3.4)$$

where $E_{C_6H_6/Cu(100)}$, $E_{C_6H_6}$ and $E_{Cu(100)}$ are the electronic energies obtained for the complete adsorbed system, the isolated molecule and the bare metal surface, respectively. Thus, negative values of the adsorption energy imply bounded systems; the smaller the value, the energetically stronger molecule-surface bonding.

Table 3.3 shows the results for the optimization and the adsorption energies at the hollow, bridge and top sites with a 1x1x1 K-mesh and the E_{Ad} after single point energy (SPE) calculations with a 4x4x1 K-mesh, over geometries previously obtained.

Adsorption site	$d_{C_6H_6-Cu}$ (Å)	C_6H_6/Cu(100) 1x1x1 K-mesh xy-angle (Degrees)	E_{ad} (eV)	4x4x1 K-mesh E_{ad} (eV)
Hollow	2.26	0	-1.14	-1.02
Bridge	2.57	25	-0.90	-0.85
Top	2.90	0	-0.96	-0.75

Table 3.3: Optimization results of C_6H_6-Cu(100) at the Hollow, Bridge and Top sites with a 1x1x1 K-mesh, adsorption energies with a 1x1x1K-mesh and with 4x4x1 K-mesh over the geometries previously obtained. In all the calculations the "Partial vdW" procedure was employed to include dispersion forces. Initial geometries in the optimization have been taken from the most favorable adsorption distances and angles previously obtained in both scans.

The adsorption of benzene on the metallic substrate induces an elongation of the C-C bond in the carbon ring from 1.39 Å for the optimized C_6H_6 in gas phase, to 1.41/1.42 Å, for the molecule on the hollow site and 1.39/1.40 Å on the top and bridge sites.
The greater breadth of the C-C bond at the hollow site can be explained in terms of the

adsorption energy which, being the largest one, brings the C_6H_6 molecule closer to the surface, breaking its D_{6h} symmetry, and leading in essence to a greater disruption of the π-π C_6H_6 bonding.
It is also remarkable the slight geometrical distortion that C_6H_6 adsorption induces on the metal surface. Changes in the interlayer distances have been summarized in Table 3.4.

	C_6H_6/Cu(100)	
Adsorption site	$d_{1^{st}-2^{nd}\ Cu\ layer}$ (Å)	$d_{2^{nd}-3^{rd}\ Cu\ layer}$ (Å)
Hollow	1.846	1.740
Bridge	1.834	1.770
Top	1.831	1.767
Cu(100)	1.829	1.765

Table 3.4: Optimized distances between the first and second layers, $d_{1^{st}-2^{nd}\ Cu\ layer}$, and the second and third layers, $d_{2^{nd}-3^{rd}\ Cu\ layer}$ in the Hollow, Bridge and Top C_6H_6-Cu(100) systems and in the clean Cu(100) metal slab obtained with a 1x1x1 K-mesh. The third and fourth layers have been fixed and their positions are thus not allowed to be relaxed.

The copper atoms lying immediately beneath the adsorbate are raised up towards the benzene molecule 0.072 Å (hollow), 0.037 Å (bridge) and 0.016 Å (top).; accordingly with the obtained energies: the hollow site shows the highest adsorption energy and the largest distortion of the copper layers, while the top site presents the weakest binding energy and the smallest distortion of the atoms in the surface.
We have studied as well the charge transfer from the metallic surface to the C_6H_6 LUMO orbital, performing a Bader analysis[22,23]. The charge transfer between the substrate and the adsorbate is almost negligible for all cases; being the final charge on the molecule -0.223 e^- (hollow), -0.013 e^- (bridge) and -0.002 e^- (top). These small values confirm that the interaction between benzene and Cu(100) is predominantly due to the dispersion forces: there is a weak overlap of electron orbitals between the adsorbate and the substrate surface, and therefore vdW interactions are the only force that binds the molecule to the surface. This situation is usually referred as physisorption. On the other hand, in the chemisorption case, the covalent or ionic bonding dominates and the effect of vdW interactions on the overall system can be neglected.

Furthermore, the small charge transfer from the metal to the molecule also explains the minor geometrical distortions of both the substrate and the adsorbate upon adsorption.

Charge transfer has been also explored from a qualitative point of view, within a 3D representation of the induced charge density difference. The former is defined as:

$$\rho_{Ad} = \rho_{C_6H_6/Cu(100)} - [\rho_{C_6H_6} + \rho_{Cu(100)}] \quad (3.5)$$

where $\rho_{C_6H_6/Cu(100)}$, $\rho_{C_6H_6}$ and $\rho_{Cu(100)}$ are the electron densities of the complete adsorbed system, the isolated benzene molecule and the bare metal surface, respectively (keeping the geometry after absorption).
Figure 3.4 shows the induced charge density difference for C_6H_6/Cu(100) hollow system; where red and blue isovalues refer to charge accumulation and depletion, respectively.
We observe changes in the electron density in between the adsorbate and the substrate. The density is reduced in the π orbitals of benzene and the Cu atoms lying beneath, and it is augmented in the molecule/surface interface. The rise in charge density is the responsible of the interaction between benzene and the Cu(100) surface.

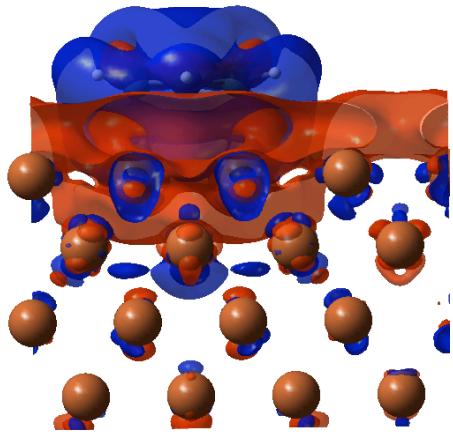

Figure 3.4: Lateral view of the induced charge density difference for the C_6H_6/Cu(100) hollow system. The isovalue for the surface is 5.10^{-5} a.u; red and blue isovalues depict charge accumulation and depletion, respectively.

We have as well studied the electronic structure by evaluating the change in the workfunction, upon adsorption, and the Projected Density of States (PDOS). Figure 3.5 depicts the PDOS for the most favorable position (i.e. C_6H_6/Cu(100) hollow).

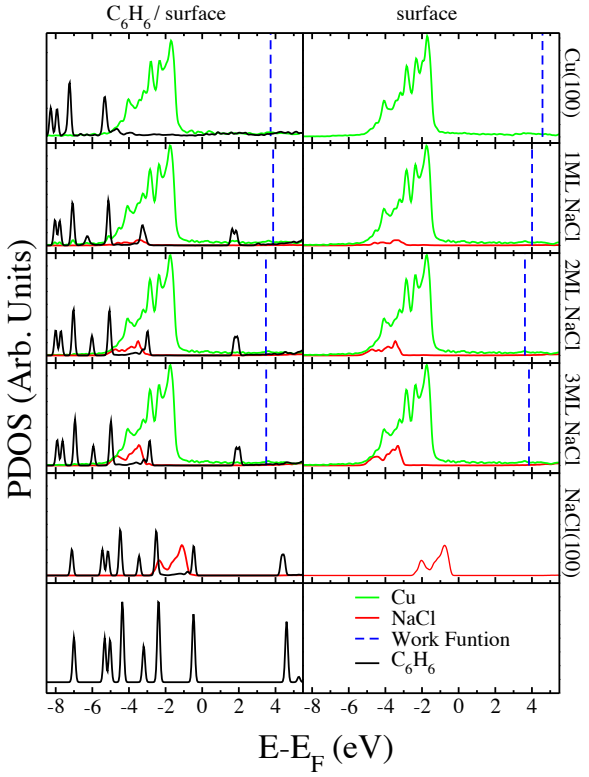

Figure 3.5: Density of states projected on the Cu, NaCl and C_6H_6 atoms for the studied systems: right column surface, left column molecule adsorbed on the surface. Bottom graph corresponds to the isolated molecule (for reference). Energy referred to the Fermi level. Work function is also given.

The computed workfunction for the clean Cu(100) surface is 4.57 eV and for the C_6H_6/Cu(100) hollow system is 3.74 eV. We observe that the Fermi level is located in the gap that appears in the projected bulk band structure. The molecule-metal interaction is reflected in the shift of the orbitals with respect to gas phase and mainly in their broadening. The charge transfer is seen in the mixing of the LUMO with the metal states.

3.4 NaCl/Cu(100)

In this section, we present the results obtained for the optimized geometry and the electronic structure for 1, 2 and 3 monolayers of NaCl, deposited on the Cu(100) surface.

Our first challenge was to fit the NaCl overlayer on the Cu(100) unit cell: the lattice constant of an isolated NaCl monolayer is 5.55 Å[24], which does not match the Cu(100) lattice constant (3.64 Å). In this isolated monolayer, Na^+ and Cl^- ions are in a flat configuration. In order to achieve a lattice matching between the Cu(100) surface and the NaCl layer, a biaxial compression of 1.77% has to be imposed, thus getting a final lattice parameter of 5.45 Å. This compression represents a NaCl:Cu matching of 2:3 along the x and y directions (parallel to the surface plane), as shown in figure 3.6. In this way the surface unit cell is set to contain 2 NaCl pairs.

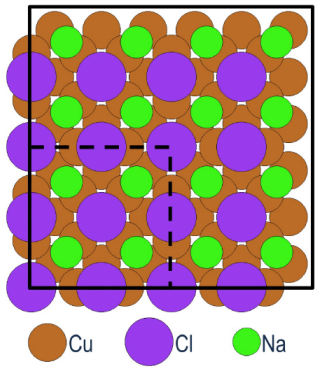

Figure 3.6: Structure of one NaCl monolayer on Cu(100). Large purple and small green open circles represent Cl^- and Na^+ ions, respectively. On the Cu(100) surface there are three inequivalent sites for Cl^- ions: Top, Bridge and Hollow sites, depending on the Cu atom lying beneath; while Na^+ ions are all placed in equivalent positions. Dashed line shows the unit cell with the 2:3 mismatching in NaCl:Cu. Full line show the unit cell employed for studying adsorption of benzene molecules.

However and despite the good lattice match, experimental results[25] have shown how the growth is incommensurate and the orientation alignment is not perfect, as can be deduced from the Moiré pattern shown in figure 3.7.

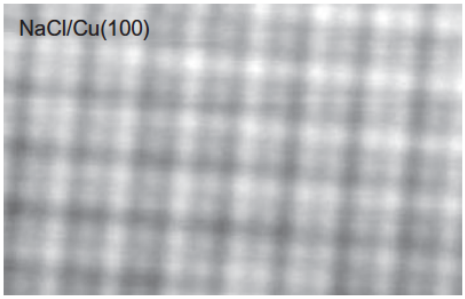

Figure 3.7: Atomically resolved doubled layer of NaCl on Cu(100). The growth is incommensurate and the atomic corrugation exhibits a Moiré pattern. (Source: J. Repp and G. Meyer "Atomic and Molecular Manipulation" Edited by Andrew J. Mayne and Gérald Dujardin, Institut des Sciences Moléculaires d'Orsay CNRS, UMR 8214, Bâtiment 210; Université de Paris-Sud 11, Orsay F-91405, France)

However, the mere possibility of a 2:3 lattice matching makes DFT simulations affordable for this system. The energy cost to match an isolated monolayer with the Cu(100) surface is 0.009 eV per NaCl pair[24]. This small energy advocates that even a small NaCl-Cu interaction would be enough to compensate the growth of the NaCl layer.

The structure is built up by placing one Cl atom on a top site of the copper surface and thus, leading to three different inequivalent Cl positions (i.e. Cl_{Top}, Cl_{Bridge} and Cl_{Hollow}) and one type of Na position. The second NaCl layer was added in such a way that the assemblage in the NaCl bulk was kept, i.e. a Na atom was placed on top of Cl and vice versa. In this second NaCl overlayer we find thus three inequivalent Na locations (i.e. Na_{Top}, Na_{Bridge} and Na_{Hollow}) and one type of Cl positions. The subscript in the notation corresponds to the adsorption site of the metal just below each ion.

While the isolated NaCl bulk shows a planar rearrangement of its ions at each layer, the interaction of a NaCl monolayer with a Cu slab induces a crumpling surface, where the Na^+ and the Cl^- ions are not longer at the same height.

		n ML-NaCl/Cu(100)		
n	Atom	1ML	2ML	3ML
1st layer	Cl_{Top}	2.609	2.666	2.676
	Cl_{Bridge}	2.953	2.748	2.769
	Cl_{Hollow}	2.692	2.702	2.721
	Na	2.588	2.707	2.652
2nd layer	Na_{Top}	-	5.492	5.586
	Na_{Bridge}	-	5.532	5.617
	Na_{Hollow}	-	5.478	5.569
	Cl	-	5.608	5.514
3rd layer	Cl_{Top}	-	-	8.449
	Cl_{Bridge}	-	-	8.475
	Cl_{Hollow}	-	-	8.438
	Na	-	-	8.312

Table 3.5: Distances (in Å) between each inequivalent atom of the 1st, 2nd and 3rd NaCl layers and the Cu surface.

Table 3.5 summarizes the obtained distances after optimization of each inequivalent ion to the outermost Cu layer. The most noteworthy effect is the decrease of the crumpling surface, i.e. the Na^+ and the Cl^- ions positions get flatter as more overlayers are added to the structure, and thus, the meaningful corrugation observed for the first NaCl layer decreases up to the third layer.

Furthermore, we have also observed that upon deposition of the NaCl overlayers, the copper atoms in the interface get slightly compressed (≈ 0.01- 0.04 Å). The geometrical distortion of the copper surface is smaller when the number of NaCl monolayers increases.

We have also analyzed the PDOS for the three structures (i.e. 1NaCl/Cu(100), 2NaCl/Cu(100) and 3NaCl/Cu(100)), as shown in figure 3.5. We observe that the position of the projected metal band-gap is not affected with the number of NaCl layers, while the PDOS of the NaCl itself do change their position with respect to the bare NaCl bulk. They stabilize upon adsorption on the metallic substrate.

On the other hand, the work function is reduced with respect to the metal surface (ϕ = 4.57, 4.00, 3.62 and 3.84 for 0, 1, 2 and 3 monolayers of NaCl, respectively).

3.5 C_6H_6/n NaCl/Cu(100)

In this section we present the results obtained for the complete adsorbed system C_6H_6/n NaCl/Cu(100), where n = 1, 2 or 3 monolayers of NaCl.

Our first step was to clarify all possible adsorption sites for the benzene molecule on the three different surfaces. As explained before, 1NaCl/Cu(100) and 3NaCl/Cu(100) present equivalent surfaces with Na^+ and Cl^- ions arranged in the same manner; thus, there are four inequivalent sites for the Cl^- ions on the first and third NaCl overlayers: Cl_{Top}, Cl_{Hollow} and Cl_{Bridge}, and one Na^+ position; other four for the second NaCl layer: Na_{Top}, Na_{Hollow} and Na_{Bridge} and one Cl^- position. Besides these adsorption sites, we have also checked intermediate positions in between Cl_{Bridge} and Cl_{Top} sites (H_{BT}) and in between Cl_{Hollow} and Cl_{Bridge} sites (H_{HB}), for the first NaCl monolayer. All these structures are shown in figure 3.8.

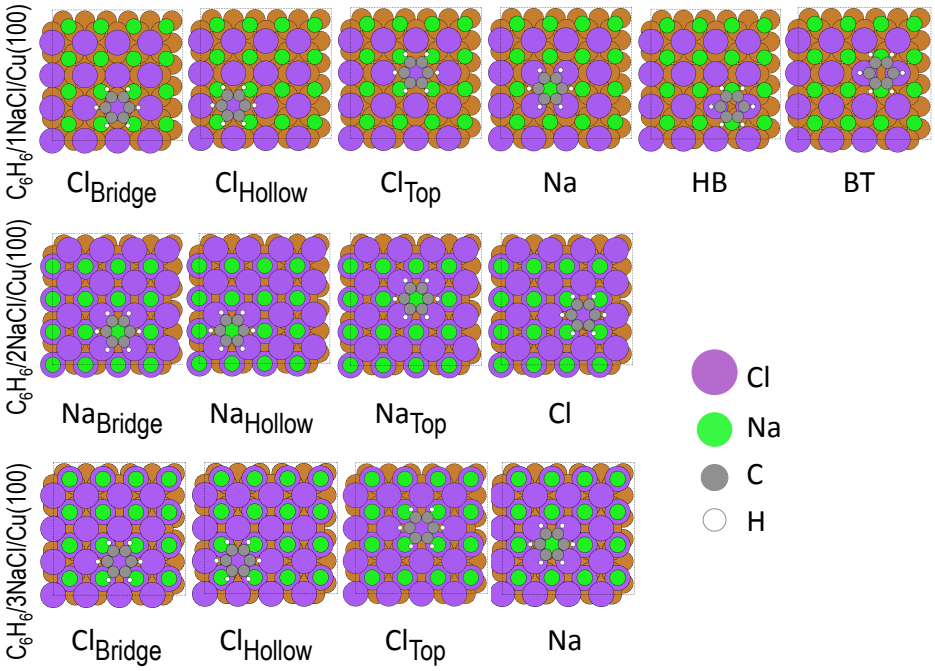

Figure 3.8: Top view for all the studied adsorption sites on the C_6H_6/n NaCl/Cu(100) surface (n= 1, 2 and 3 NaCl monolayers).

Adsorption energies and distances for all the former structures are shown in figure 3.9 and table 3.6.

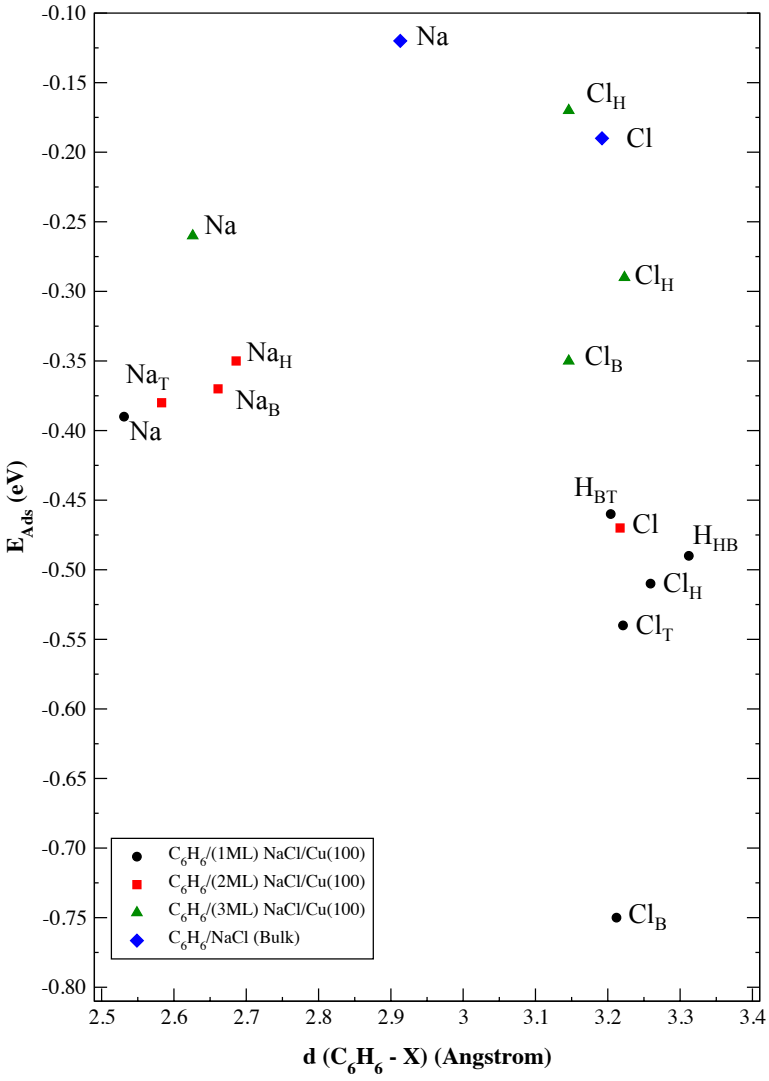

Figure 3.9: Adsorption energies and distances for the most stable geometries in C_6H_6/n ML NaCl/Cu(100).

	C_6H_6/nML-NaCl/Cu(100)		
	Ads. site	Ead (eV)	$d_{C_6H_6-X}$ (Å)
C_6H_6/1ML-NaCl/Cu(100)	Cl_{Top}	-0.54	3.221
	Cl_{Bridge}	-0.75	3.212
	Cl_{Hollow}	-0.49	3.312
	Na	-0.39	2.531
C_6H_6/2ML-NaCl/Cu(100)	Na_{Top}	-0.38	2.583
	Na_{Bridge}	-0.37	2.661
	Na_{Hollow}	-0.35	2.686
	Cl	-0.47	3.217
C_6H_6/3ML-NaCl/Cu(100)	Cl_{Top}	-0.29	3.146
	Cl_{Bridge}	-0.35	3.223
	Cl_{Hollow}	-0.17	3.146
	Na	-0.26	2.626
C_6H_6/NaCl	Cl	-0.19	3.192
	Na	-0.12	2.913

Table 3.6: Adsorption energies (E_{ad} in eV) and equilibrium distances ($d_{C_6H_6-X}$ in Å) for all inequivalent sites between benzene and the ion immediately beneath (X may be either Cl^- or Na^+ depending on the system).

The results in figure 3.9 show that:

The distance between the benzene and the ion of the insulating film, immediately below the adsorbate, is always shorter when the C_6H_6 ring is placed on top of a Na^+ than when it is on top of a Cl^-, regardless the number of NaCl layers in the system. This behavior may be explained in terms of the Cl^- and the Na^+ radius: the former is larger than the latter, thus pushing the benzene ring farther away. Furthermore, the Cl^- ions immediately interacting with the C_6H_6 molecule undergo a larger surface reconstruction (i.e. displacement compared to the other ions of its layer). In fact, the Cl^- interacting with the molecule is 0.73, 0.40 and 0.42 Å below the rest of the ions belonging to its layer, for 1, 2 and 3 NaCl monolayers, respectively. This behavior illustrates that not only the radius of the ion is affecting the C_6H_6-ion distance, but also the electron densities of both are playing an important role: the π electronic cloud of C_6H_6 is pushing the Cl^- ion towards the surface due to repulsion between both

electronic densities.

The computed adsorption energies decrease with the number of NaCl monolayers (see figure 3.9). Benzene molecule has to interact with the metallic substrate through the insulating film. We have already explained how the overlap of the molecular orbitals of benzene with the surface bands is barely inexistent, and how this fact leads to a weak adsorption, already at the C_6H_6/Cu(100) system. This applies a fortiori to the fact that adding the insulating film makes the C_6H_6 orbitals to decouple from the metallic substrate, decreasing thus the adsorption energies.

For all systems, the most stable adsorption site always involves a Cl^- ion in contact with the adsorbate. At this point is relevant to consider the interaction of a single Cl^- or Na^+ ion with benzene in the gas phase. Interaction of these ions with aromatic *p* structures in the gas phase has been widely studied (see refs.[26–28,28–32]). These studies reveal that interaction above the center of the benzene ring for Na^+ is of the order of 25 kcal/mol[26,29–34] and with a large electrostatic component[32,34] while for Cl^- the interaction is repulsive (a minimum above the ring is located with an interaction energy of +0.9 kcal/mol[34]). Indeed interaction with Cl^- becomes attractive only when electron-withdrawing substituents are considered, as in perfluorbenzene (C_6F_6)[27–30,34]. These results strongly differ with our findings that the preferred interaction is in the Cl_B position. A deeper analysis reveals that, when a flat NaCl layer without metal substrate is considered, the interaction energy is practically zero or positive (red triangles in figure 3.9). It is the presence of the metal and the distortion of the NaCl layer upon adsorption the responsible of a strong polarization of the Cl^- ions and the creation of local atomic dipoles. When these atomic dipoles are created, the part of the Cl^- ions facing the surface is electron deficient and attracts the electronic cloud of benzene.

Figure 3.10 shows the lateral views of the induced charge density difference after adsorption of C_6H_6. It evidences the decoupling of the molecule from the metallic substrate: there is a charge depletion of the electron density immediately beneath the benzene molecule and in-between the former and the NaCl surface. The molecule-metal decoupling is clearly observed, since no remaining electron density between them is appreciated. As clearly seen in figure 3.10, the π electronic cloud of benzene is polarized towards the Cl^- and an accumulation of electron density immediately beneath the molecule is observed. Figure 3.10 also shows that part of the charge recovered by Cl^- is accumulated between the ion and the metal atom underneath (Cu or Na); This accumulation of charge is coherent with the displacement of the Cl^- ion interacting with the molecule out of the NaCl plane.

When the benzene molecule is adsorbed on the surface and interacting with the Cl^- ion, the repulsion between the π electronic cloud of benzene and the electrons of the chlorine ion makes the former to displace towards the inner side of the surface. Since the Cl^- ion has now been displaced, there is a negative charge "hollow" where the ion was previously placed. In order to fill this hole, and to keep the electrostatic equilibrium, the π electronic cloud of benzene moves towards the hollow, i.e. it gets polarized (see figure 3.10 for 1NaCl/Cu(100)).
The picture for 2 and 3 NaCl monolayers is somewhat more complex since these 2nd and 3rd monolayers try to compensate this charge deficiency caused by the displacement of the Cl^- ion and the polarization of the π electronic cloud of C_6H_6.

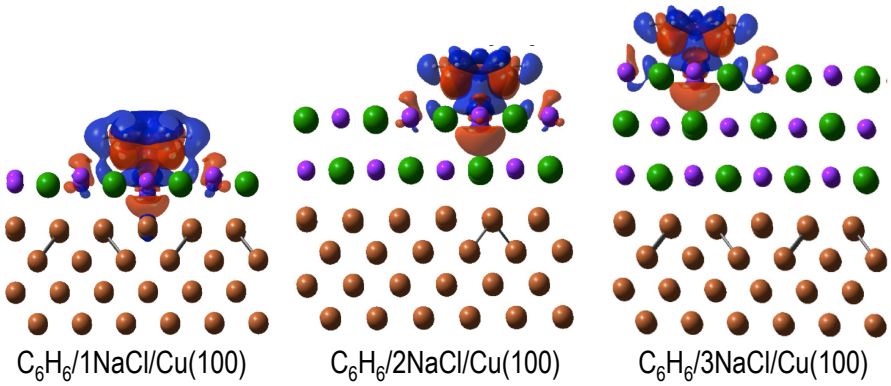

Figure 3.10: Side view of the induced charge density difference for the C_6H_6/n NaCl/Cu(100) system. The isovalue for the surface is 5.10^{-5} a.u; red and blue isovalues depict charge accumulation and depletion, respectively.

A further analysis of the adsorption energies is shown in figure 3.11. Here we have compared the adsorption energies of the complete adsorbed system, i.e. C_6H_6/n NaCl/Cu(100), where n = 0, 1, 2 and 3 NaCl layers, with the adsorption energies for 1, 2 and 3 NaCl monolayers, with and without metal substrate, assuming a flat configuration of the NaCl ions (i.e. before optimization). We have thus compared the relevance of a) the presence of the metallic slab, and b) the crumpling NaCl surface to the total computed adsorption energies.
From this analysis we conclude that both of them contribute to the stabilization of the C_6H_6 molecule adsorption in ≈0.3-0.5 eV each.

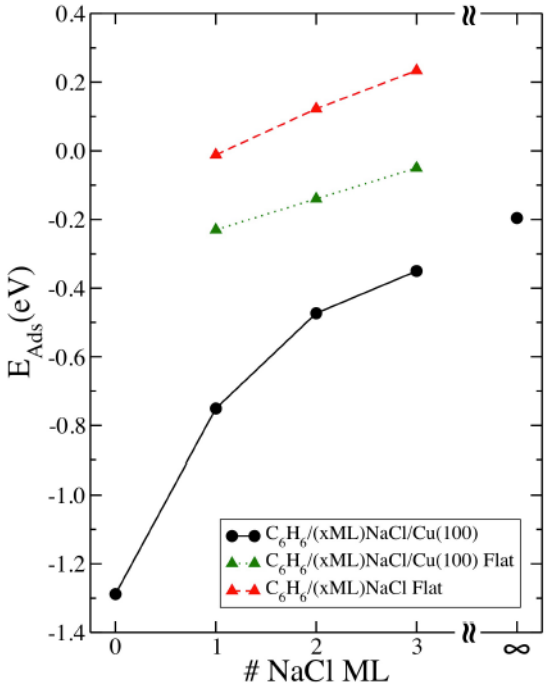

Figure 3.11: Adsorption energy in the favorable position for C_6H_6/n NaCl/Cu(100). In the adsorption energy we have considered three cases: flat NaCl geometry without metal substrate (triangles dashed red line), flat NaCl geometry with metal substrate (triangles with dotted lines) and the geometry after optimization with metal substrate (circles with full lines). ∞ indicates NaCl bulk, without metal substrate

As we did for the C_6H_6/Cu(100) system, charge transfer has been also studied from a quantitative (q_{Bader}) point of view. As initially expected, due to the addition of the insulating film, the benzene molecule decouples from the surface and we do not observe charge transfer from the metallic surface to the organic molecule. Figure 3.12 shows how saturation in the transferred charge is already reached when 1 NaCl layer is present in the structure.

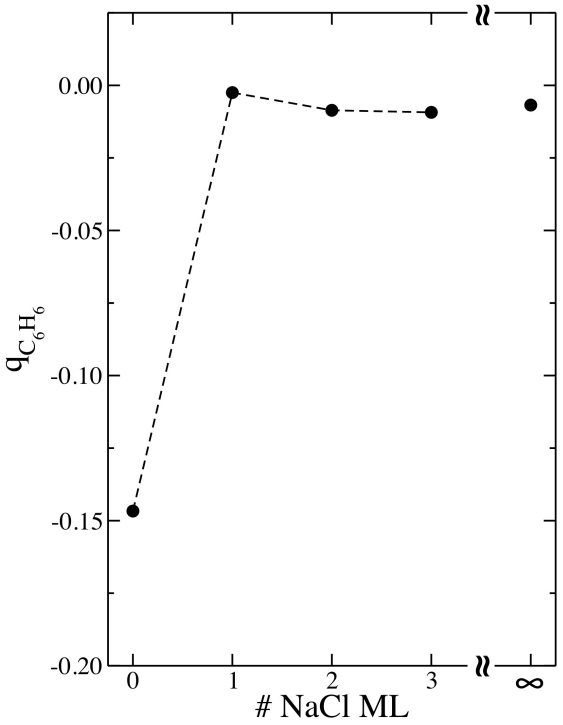

Figure 3.12: Charge transfer in the favorable position for C_6H_6/nNaCl/Cu(100). ∞ indicates NaCl bulk, without metal substrate.

Finally, we have evaluated the electronic structure of these systems through the PDOS and the changes in the workfunction. These results are shown in figure 3.5; they underline the weak interaction between he adsorbate and the substrate. This conclusion is drawn from the slight shift of the C_6H_6 molecule orbitals at the C_6H_6/n NaCl/Cu(100) system with respect to the gas phase ones; only the HOMO stabilizes and moves to lower energies, though mainly due to the decrease of the workfunction as more NaCl layers are added (ϕ = 3.84, 3.48 and 3.49 eV for 1, 2 and 3 monolayers of NaCl, respectively).

3.6 C_6H_6/NaCl Bulk

Up to now, we have seen how the insulating film disrupts the, already quite weak, interaction between benzene and the copper slab. A limit situation, where a large

number of NaCl layers are added to the substrate, can be envisaged by studying the C_6H_6/NaCl bulk system. Thus, we have first computed the bare NaCl surface. To this, we included four atomic layers and allowed relaxation of the first two layers. In the geometry optimization we observed that the Cl^- ions in the first layer are 0.134 Å above the Na^+ ions, while in the second layer Cl^- ions are found 0.053 Å below the Na^+ ones.

We have afterwards explored the two main adsorption sites on the NaCl surface (i.e. on top of Na^+ and on top of Cl^-). Adsorption energies and distances for both sites are given in table 6. The interaction energy is lower than in the case of C_6H_6/1NaCl/Cu(100) and C_6H_6/2NaCl/Cu(100), but of the same order as in C_6H_6/3NaCl/Cu(100).

On the other hand, equilibrium distances in the NaCl bulk are similar than in the *n* NaCl/Cu(100) adsorbed system: benzene is closer to the Na^+ ions than to the Cl^- ones. Also in the same manner than for *n* NaCl/Cu(100), when the molecule interacts with Cl^-, the ion is pushed towards the bulk (0.312 Å), however when the molecule is placed on top of Na^+, the ion is raised towards the molecule, out of the surface (0.266 Å).

The charge transfer analysis (see figure 3.12) is similar once again to that obtained for the C_6H_6/n NaCl/Cu(100) system: the charge transfer from the metallic surface to the benzene molecule disappears in the presence of the NaCl layers; this applies a fortiori when no metallic substrate is present, and thus no charge is transferred from the substrate to the adsorbate. Furthermore, the induced charge density, shown in figure 3.13, reveals a similar picture as the C_6H_6/3NaCl/Cu(100) system; i.e. the molecule is decoupled from the substrate. This is observed in the electron density depletion in the middle part between the adsorbate and the substrate.

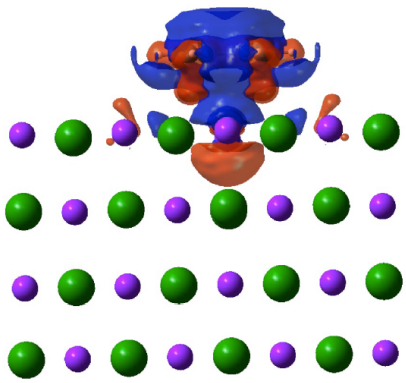

Figure 3.13: Side view of the induced charge density difference for the C_6H_6/NaCl bulk system. The isovalue for the surface is 5.10^{-5} a.u; red and blue isovalues depict charge accumulation and depletion, respectively.

The analysis of the electronic structure reveals, through the PDOS, a shift with respect to those cases where the metallic substrate was included. This fact occurs due to the larger workfunction in the NaCl as insulator (ϕ = 6.03 eV). The low interaction between the molecule and the substrate is shown in the PDOS (figure 3.5), which is quite similar to the molecule in gas phase.

3.7 Events affecting the change in the Workfunction

Figure 3.14 represents the work function as a function of the number of NaCl monolayers for the cases with and without molecular adsorption.

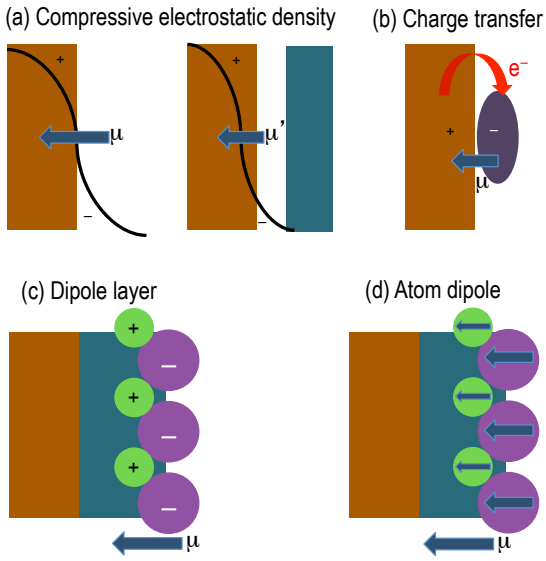

Figure 3.14: Schematic representation of the different effects that modify the local dipole on the surface and thus change the work function.

As a general trend, we observed reduction in the work function with the presence of the NaCl and with the adsorption of the molecule. Changes in the local dipole of the surface, upon adsorption of the molecule and due to the presence of NaCl layers, modify the work function. Four different effects contribute to change the dipole (see

schemes in Figure 14 a–d):

a) The electron density of the surface is pushed towards the bulk due to the presence of the molecule and the NaCl layer; the compressive electrostatic density modifies the local dipole thus reducing the work function with respect to the bare metal surface[35].

b) In the metal–molecule interface, a dipole is created due the charge transfer between the surface and the molecule. This dipole also modifies the work function with respect to the bare surface: if electrons are transferred to the molecule the work function is increased.

c) In the geometry optimization we have observed that the Na^+ and Cl^- ions are placed at different heights; this results in a layer of positive charges and a layer of negative charges at different heights, i.e. a dipole layer. The potential of this dipole layer also changes the work function with respect to the metal surface; [36] depending on the relative position of the positive and negative ions, the work function is increased or reduced.

d) The atoms in the ionic layer (Na^+ and Cl^-) are polarized due to the potential created by the dipole layer (c). In particular, Cl^- is quite polarizable and thus, a layer of atomic dipoles appears on the surface. The potential created by these atomic dipoles also modifies the work function[36].

Therefore, the combination of these factors influences in the changes observed in the work function, upon adsorption of NaCl layers and benzene. Our simulations are thus in agreement with the experimental measurements of work function reduction in NaCl films on metal surfaces[37–39].

3.8 STM as a tool for inducing chemical reactions: Benzene dehydrogenation

In chapter 2 of this manuscript, we described the STM as a powerful tool, not only for visualizing direct images of the electronic structures of molecules, but also for inducing chemical reactions in a controlled way[40,41]. These chemical reactions are induced after the vibrational and/or electronic excitation, caused at the adsorbates by the inelastic electron scattering. Thus, the advent of single molecule manipulation has permitted the control of matter at the atomic scale[42,43].

In the following sections, we present the study of the benzene molecule, placed in between two copper semi-infinite leads. Through these copper leads, a finite potential will be applied, affecting thus the benzene molecule.

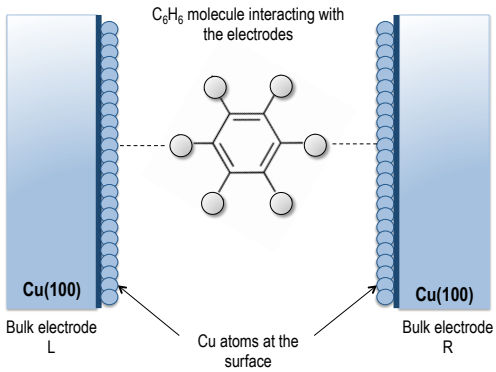

Fig 3.15: Left and right copper electrodes and the C_6H_6 molecule. The Cu atoms at the electrode surface will bind to the Hydrogen atoms of the Benzene molecule. The electric current will flow from left to right, presumably breaking the C-H bond of the C_6H_6 molecule.

The manipulation of C_6H_6 on Cu(100) with the STM leads to the dissociations of the benzene molecule into smaller fragments[40]. In fact, it has been shown C-H bond cleavage, leading to C_6H_5 (phenyl) and C_6H_4 (benzyne) molecules, chemisorbed on the Cu(100) surface[44,45]. The formation of other fragments is unlikely due to the large fragmentation barrier or their STM constant-current image would not present the experimental C_{2v} symmetry[12].

The loss of the first hydrogen atom gives rise to the phenyl species. The former is achieved after the benzene molecule makes a transition from its planar configuration to a stand-up one, when it has already lost its H atom. This transition is performed in such a way that the molecule lifts up, with one of the carbon atoms facing a copper one, while the hydrogen, which is detaching, moves towards a hollow site of the metallic substrate [44]. Figure 3.16 depicts this process.

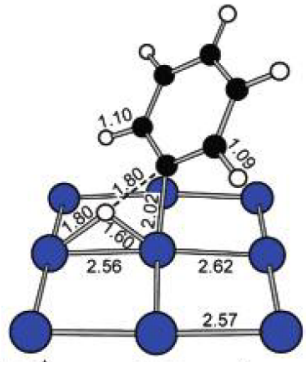

Figure 3.16: Geometrical structure of the transition state between C_6H_6 and C_6H_5, with bonding distances in Å. (Source: H. Lesnard, M-L. Bocquet, N. Lorente, JACS 129, 4298 (2007))

Although benzene dehydrogenation, under STM, has been widely studied, we considered that there is still a task missing: understanding what happens in the molecular orbitals while this current was tunneling from one metallic lead to the other, and moreover, if the analysis of the atomic forces and the changes taking place on them, could serve as a direct and easy way of controlling and determining the C-H bond breaking.

Thus, we here present the study of benzene molecule, trapped in between two copper electrodes. An increasing voltage is then applied between the two semi-infinite leads. This current will produce changes in the electronic structure and in the atomic forces acting on the benzene molecule. Here, we show that the analysis of the atomic forces allows us to predict the dehydrogenation of the benzene molecule.

3.9 Benzene between two copper electrodes

Our first goal is to build up a copper electrode, large enough in order to contain the benzene molecule. We have already thoroughly discussed how the benzene molecule adsorbs on a copper surface: it stands parallel to it. However, previous works on the dehydrogenation of benzene, under an STM current [44] found that the C_6H_6 molecule losses a hydrogen atom and gives rise to the phenyl species tilting towards a top site of the Cu(100) surface. In a second step, the hydrogen atoms, which is no longer attached

to the benzene molecule, stands adsorbed on a hollow site of the metallic surface. Thus, in our simulations the benzene molecule is placed in a vertical position (i.e. perpendicular to the surface plane) and thus, a 3x3 Cu atoms unit cell would properly represent the C_6H_6/Cu-electrodes situation, avoiding as well the interaction between vicinity unit cells in the x and y directions (parallel to the surfaces).
Figure 3.17 shows a schematic representation of the copper electrodes. Black bricks and balls represent the atoms of the right and left electrodes; Light blue bricks and balls represent atoms of the surface. The interlayer distance at the electrodes has been set to the copper bulk lattice constant; while the distance between surface layers has been optimized, being 1.857 Å for the 4th and 5th layers and 1.837 Å fro the 5th and 6th ones. The distance between the right and the left copper electrodes has been set to 8 Å according to the benzene length (≈ 4.3 Å), the bonding distance between the phenyl moiety and the copper surface (≈ 2.0 Å)[44] and the bonding distance of the detached hydrogen atom with the copper surface (≈ 1.5 Å)[44].

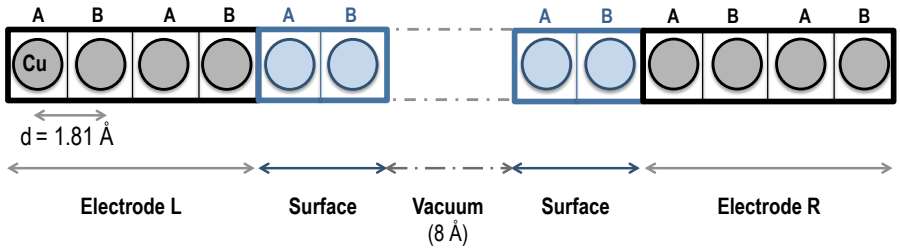

Figure 3.17: Schematic representation of the left and right copper electrodes, the surface layers and the vacuum space shaping the full scattering region. Interlayer distance for the bulk electrodes and vacuum space are shown in angstroms. "A" and "B" letters denote the material stacking.

Once we have constructed the copper electrodes, we test which adsorption site is more favorable for a "standing-up" benzene molecule. The purpose of this analysis is to obtain the most stable configuration of C_6H_6 and not perform any further optimization during the whole study. Thus, we analyze the C-H fragmentation or any other bond breakings by just computing the changes on the atomic forces.
With this goal in mind we have optimized the C_6H_6/Cu(100) system, with its molecular plane perpendicular to the metallic surface, and with one of its hydrogen atoms facing a hollow or a top site (see figure 3.18). Both configurations are almost degenerated in

energy, being the hollow site inconspicuously more stable (0.02 eV).

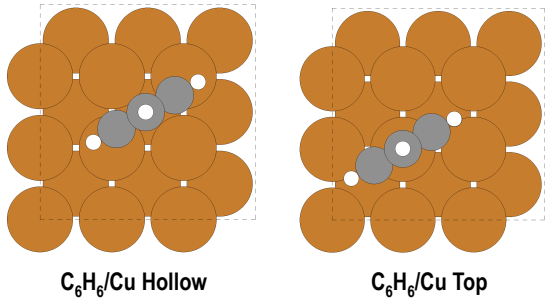

Figure 3.18: Left and right side of the figure show vertical benzenes adsorbed on a Cu(100) surface on a hollow and a top site, respectively. Dark orange, grey and white spheres denote copper, carbon and hydrogen atoms.

Afterwards, we have optimized, with the VASP code, a representative part of the full unit cell, as shown in figure 3.19; i.e. in this first approach to the final optimization, we have only depicted essential layers in order to get a picture of the arrangement of the benzene molecule inside the two copper leads.
The resulting geometry shows a perpendicular benzene molecule facing both copper surfaces at a hollow and a top site.

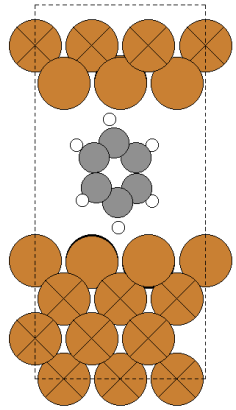

Figure 3.19: Optimized unit cell, where the bulk electrodes have been represented by 4 Cu layers and 2 layers have been optimized as the surface of the electrode.

After the initial optimization with VASP, a second optimization has been performed with the SIESTA code, not including so far any voltage to the sample. To our surprise, there were substantial differences between bot results: while the molecule was completely perpendicular to the surface after the VASP geometry optimization, it was slightly laying down after the SIESTA geometry optimization (see figure 3.20).

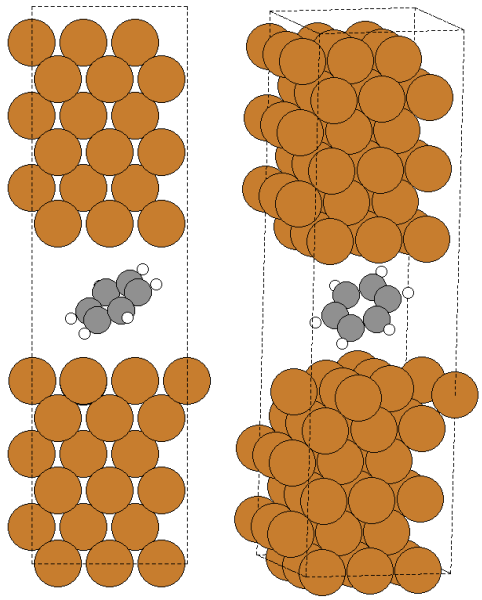

Figure 3.20: Side and slightly turned views of the full scattering region, containing as well the benzene molecule, after the geometry optimization with VASP. The molecule is confronted with the surface through two hydrogen atoms, one facing a hollow site and the other one a top site.

This last arrangement of the benzene molecule is far from being a bug or a failure of the optimization process of the SIESTA code; On the contrary, it seems more reasonable than the first approach reached by the VASP optimization. We have to take into consideration that VASP code would go for a search just of local minima, due to its gradients approach to locate a minimum; thus, the first input geometry will highly determine the final optimized structure. According to this, and since the initial geometry was that where the benzene was perfectly perpendicular to the surface plane, it is not surprising that the output geometry closely mimics the input one. Moreover and as we have seen in previous paragraphs, the benzene molecule adsorbs parallel to

the copper surface; furthermore, previous works show how the dehydrogenation of the first hydrogen atom of the benzene molecule occurs in such a way that the molecule first faces a top site copper atom with one of its H units and afterwards this H unit dehydrogenates staying trapped on a hollow site. If we combine both events, we get the last geometry optimization, where benzene confronts both surfaces with one hydrogen atom each; one facing a hollow site and the other one a top site, while the molecule slightly leans towards a parallel arrangement in order to maximize the π interaction of its orbitals with the metallic surfaces.
Once the optimal geometry, for zero voltage, is found, we start to apply an increasing voltage to the sample and study the effect of the former by analyzing the change in the atomic forces on the carbon and hydrogen atoms.

3.9.1 Different features as function of the voltage: atomic forces, transmission, current and charge density difference

Atomic forces on each pair of C-H atoms has been evaluated as a function of the applied voltage. To this, we have analyzed the effects of the voltage from 0 V to 1.4 V (previous experimental studies[44] determined that the dehydrogenation of the first hydrogen atom occurs at 1.8 V). Figure 3.21 shows the results for this analysis.

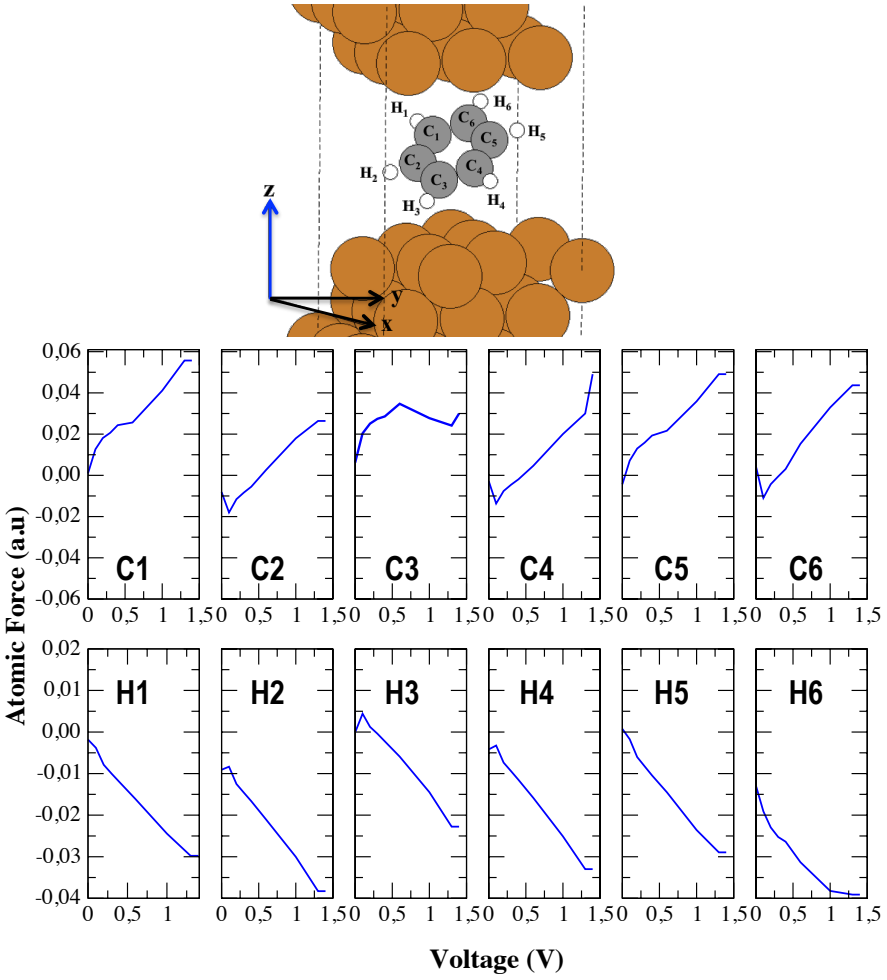

Figure 3.21: Atomic forces in the z axes, in a.u, as a function of the voltage, in Volts. First row represent the carbon atoms and the second row the hydrogen atoms. The list of atoms is indicated in the upper image.

We can conclude that carbon and hydrogen atoms are moving in opposite directions: carbon atoms are being attracted by the upper copper electrode while the hydrogen atoms are displacing towards the lower metallic lead. This situation forces the molecule to a boat-like configuration, where carbon atoms labeled as 1, 5 and 6, and

hydrogen atoms labeled as 2, 3 and 4, undergo the largest attraction to their closer copper electrode. If we represent these forces, applied on each atom and scaled for each value, we can get a better idea on the effects caused by the voltage on the organic molecule. Figure 3.22 brings face to face the forces at one of the lowest tested values for the voltage (0.2 V) and the largest one (1.4 V).

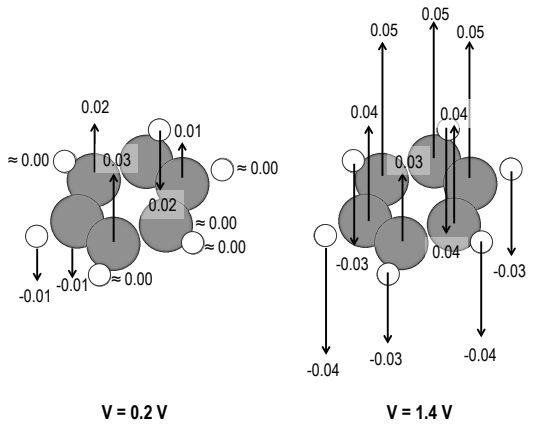

Figure 3.22: Atomic forces on the z axes, for C and H atoms for 0.2 and 1.4 Volts. Values, in a.u, are shown in the image next to the corresponding force vector.

We have evaluated as well the transmission as a function of the voltage. As we have already explained in chapter 2, the transmission reflects the probability of an electron to cross through the conductor; thus, the transmission probability is closely related to the shape and features of the Density of states, since electrons will transmit though available channels (i.e. bands). Therefore, the information extracted from the transmission diagrams will guide us about the behavior of the DOS.
Our first approach was to study the transmission in the zero voltage scattering region and compare it to the DOS to verify the relation between both. Figure 3.23 shows the transmission probability and the DOS for the C_6H_6/Cu-electrode system, when no voltage is applied.

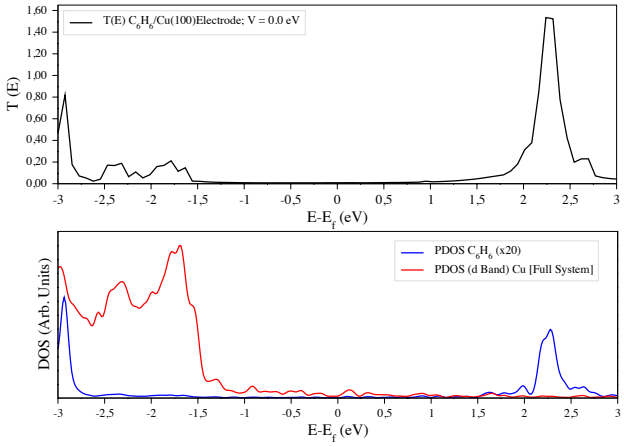

Figure 3.23: Transmission probability, T(E) and Density of States, DOS (Arb. Units), as a function of the energy, E-E_f (eV), for the C_6H_6/Cu-electrode system at V = 0.0 V. DOS show the PDOS for the C_6H_6 molecule in solid blue line and the *d* band of the Cu electrodes in solid red line.

Following, we have analyzed the transmission for the scattering region at different values of the voltage; the results are shown in figure 3.24.

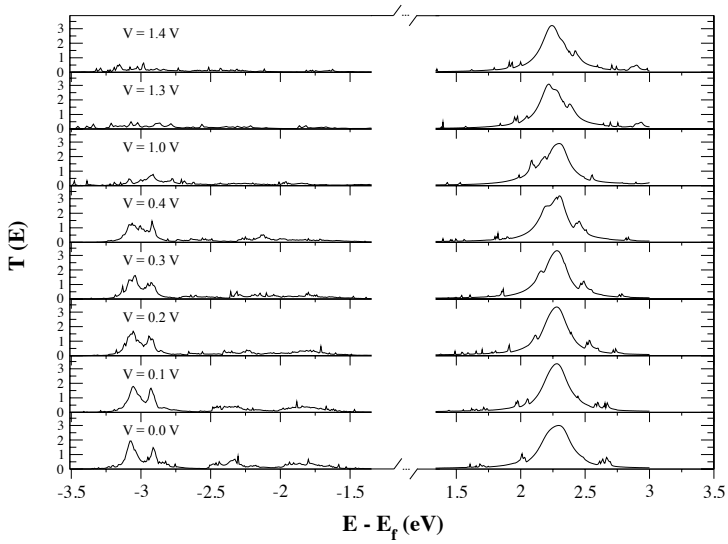

Figure 3.24: Transmission probability, T(E), as a function of the energy, E-E_f (eV), for 0.0 V to 1.4 V.

We observe how the HOMO band continuously disappears as the voltage applied to the sample increases, until we have almost no electronic band left at 1.4 V. However, the LUMO stays changeless. This event might be due to the hybridization of the *d* band of the copper outmost layer with the HOMO of the benzene molecule. Thus, the electronic structure of the molecule is changing upon increasing voltage. However, the gap between the HOMO and the LUMO of the benzene molecule is too large and no big changes are observed in the molecule.
On the other hand, if we analyze the current as a function of the voltage (see figure 3.25) we observe how the system behaves as a semi-conductor (This means that its conductivity falls in between that of a conductor material and an insulator one). Modern electronics are based on this kind of materials. An strictly definition of a semiconductor states that, for this kind of systems, the band gap is sufficiently small to allow electrons in the filled band bellow it to jump into the upper empty band by thermal excitation. For semiconductor materials, its conductivity increases with an increase of the temperature, which is the opposite behavior observed in pure metals. This means that the conductivity may be increased by pumping energy to the system.

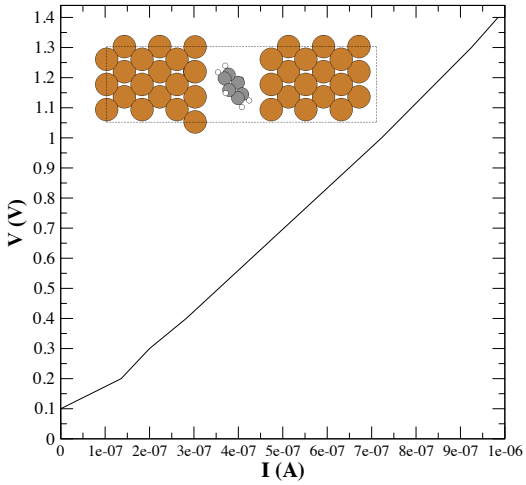

Figure 3.25: Current, I in Amperes, as a function of the voltage, V in Volts.

In a semiconductor the current conduction occurs through the movement of electrons, leaving behind the so-called “holes”, which leads to charge carriers. This is, in

semiconductors charge is not carried exclusively by the electrons, but also holes carry charge.
Voltage-Induced charge density difference, has been computed as

$$\Delta\rho = \rho(C_6H_6/\text{Cu Electrodes};\ V_i) - \rho(C_6H_6/\text{Cu Electrodes};\ V_o) \quad (3.6)$$

where $\rho(C_6H_6/\text{Cu Electrodes};\ V_i)$ is the density of the of the system at the applied voltage (in this case 1.0 V), and $\rho(C_6H_6/\text{Cu Electrodes};\ V_o)$ is the density of the system at zero voltage.
Figure 3.26 shows the charge density difference for an applied voltage of 1.0 V. We observe how charge depletion on the carbon atoms as well as on hydrogen atoms labeled 2, 3 and 4; while there is a charge accumulation on the hydrogen atoms labeled as 1, 5 and 6.

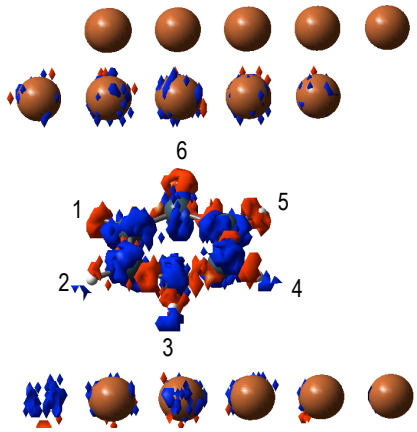

Figure 3.26: Induced charge density difference for C_6H_6/Cu electrode at 1.0 V. Red and blue lobes denote charge accumulation and depletion respectively. Isovalues have been set to ± 2.10^{-5} a.u.

As we have seen before, carbon atoms 1, 5 and 6 undergo the largest atomic forces values in the positive direction of the z axes. Hydrogen atoms bonded to the former carbon are those presenting charge accumulation. On the other hand, H atoms 2, 3 and 4, which are closer to the lower copper electrode (to which they feel attracted) present charge depletion. Thus, the forces on the atoms are the consequence of the electronic structure changes with the applied voltage.

3.10 Computational details for the C_6H_6/*n* NaCl/Cu(100) and the C_6H_6/Cu-electrodes systems

The aim of this section is to provide detailed and concrete specifics concerning the computational methods employed to calculate all the results presented in this chapter. Calculations for the C_6H_6/Cu(100) and C_6H_6/*n* NaCl/Cu(100) systems were carried out using Density Functional Theory (DFT) including periodic boundary conditions (PBC) and using the Vienna Ab initio Simulation Package (VASP)[46–49]. The exchange and correlation effects have been described using the Generalized Gradient Approximation, in particular employing the Perdew-Wang 91 functional (GGA-PW91)[50,51].The interaction of the electrons with the atoms has been taken into account within the projector augmented wave method (PAW pseudo-potentials) [52,53]. The electron density has been described employing a plane wave basis set expanded up to a kinetic energy cutoff of 400 eV.

The metal surfaces were modeled by a slab consisting of four atomic layers, separated by a vacuum space of 10 in the coordinate perpendicular to the surface, z. The adsorption of benzene has been considered in all cases, in a low coverage regime, within a unit cell of (4 x 4) Cu atoms in the direction parallel to the surface (xy coordinates). Geometries have been optimized sampling the Brillouin zone with a **Γ**–centered Monkhorst–Pack of 1x1x1 K-mesh. Final electronic energies have been computed employing the previously optimized geometries by single point energy calculations using a **Γ**–centered Monkhorst-Pack of 4x4x1 K-mesh. Both samplings of the Brillouin zone include a Methfessel–Paxton smearing of 0.2 eV. The geometries of the studied systems were optimized by relaxing all atoms of the adsorbate, C_6H_6, in the three spatial directions (xyz), all atoms of the insulating films, NaCl, in the z direction and the first two layers of the metal slab, Cu, in the z direction as well. The layer spacing of the two lower Cu layers was taken from the optimized lattice constant parameter (a_o = 3.365 Å). All these coordinates were optimized until all forces were smaller than 0.001 eV $Å^{-1}$. The electronic self-consistent convergence was set in an energy difference of 10^{-5} eV with respect to the previous cycle.

Dispersion forces, which have been already explained at the beginning of this chapter, have been included via the DFT-D2 Method of Grimme[19].

Calculations for the C_6H_6/Cu-electrodes system were carried out using the SIESTA and TranSiesta codes [54]. In a first step calculation, we have used DFT in order to optimize the Cu(100) electrode using PBC. The exchange and correlation effects have been

described using the Generalized Gradient Approximation, in particular employing the Perdew, Burke and Ernzerhof functional [55,56]. In this first calculation, the TSHS file will be generated, containing all the information necessary for the calculation of the electrodes, it is the Hamiltonian matrix. Geometries have been optimized sampling the Brillouin zone with a **Γ**–centered Monkhorst–Pack of 11x11x7 K-mesh. The plane wave cutoff has been set to 300 Ry.

In a second step, we have as well performed DFT calculation, though this time for the whole scattering region, i.e. both electrodes separated at the desired distance of 8 Å. The aim of this second step is to relax the geometry of the scattering region, mostly the surface layers of the electrodes. In this step we add the vacuum region, the right electrode and two copper layers to each of the electrodes (which will be relaxed during the calculation), getting to the system showed in figure 20. Finally, in a third step, we have calculated the transmission through a TranSiesta simulation calculation. The lowest and highest energy values for the transmission function were -10.00 and 10.00 eV, respectively, with a number of energy points between them of 200.

Chapter 4

ACN/*n* NaCl/Cu(100)

4.1 Introduction

Polymer structures, in which the unit structure is a molecule with diffuse π electrons form another subgroup of organic compounds with semiconductive properties. In this context, we have studied the adsorption of the acrylonitrile monomer (ACN) on different substrates.

Acrylonitrile (vinyl cyanide), CH_2=CHCN, which is mainly produced by the reaction of propylene and ammonia, is one of the most important monomers of the polymer industry. Its polymer, polyacrylonitrile, has an important meaning in the preparation of synthetic fibers. ACN is a very reactive substance due to the presence of both double C=C bond and electron-accepting nitrile group. Generally, ACN reacts by the nitrile group or by the double bond. Both reactions can also occur simultaneously[57]. The polymerization of the carbon-carbon double bond is the most important reaction. On the other hand, the reactions of the nitrile group include hydration/hydrolysis, reactions with olefins and alcohols, and reactions with aldehydes and methylol compounds [58].

Recently, polyacrylonitrile has become the most important precursor for the manufacture of carbon fibers, which are fundamental materials for advanced composites. There are also many possibilities for the development of new materials based on polyacrylonitrile because of its relatively low production cost, the high reactivity of its nitrile group and its ability to combine with other monomers and polymers.

The aim of our study is to examine the properties of acrylonitrile monomer adsorbed on a metal surface; this would be a first step in order to consider this scene as possible growing media of the polymer. The presence of polymer films on various surfaces as metals, glasses or even other polymers, can modify the initial properties of the substrate. These modifications can be used to prepare brand new materials with likely applications in the highly ambitious fields of electronics and catalysis.

In recent years the field of surface preparation techniques has grown due to the success of film deposition on anodes[59,60]. However, various monomers as acrylonitrile, acrylamide or acrylaldehyde, in organic solvents as methanol and butanone, with various supporting electrolytes ($NaClO_4$, KNO_3) have presented several drawbacks. For instance, films were not completely coated, since for many cases the chemical stability was rather poor.

Several theoretical studies have been carried out with the aim of shading some light on those not fully understood processes of metal coating. In the case of acrylonitrile molecule (ACN) interacting with a copper surface, Geskin *et al.*[61] described such interaction as a coordination of the molecule to two copper atoms with both vinyl and nitrile groups. Furthermore, Fredriksson *et al.*[62] reported a theoretical and experimental study on the interaction of several transition metals with ACN. Among nickel, copper and zinc they concluded that only Ni and Cu substrates could support the formation of a well-growth polyacrylonitrile film. Their theory was drawn upon the formation of π bonds between the organic molecule and the Ni and Cu atoms. Bureau *et al.*[63] studied the neutral complex of the saturated methacrylonitrile monomer with a Ni cluster representing the Ni(111) surface thus, trying to simulate the grafted polymer. In their study they showed the presence of a bound state for this system and hence the possibility of the polymer end-on chemisorption. However, these DFT studies were based upon modeling the surface via different sized metal clusters, and therefore they were missing some crucial effects, only available by performing Periodic Boundary Conditions (PBC) simulations. Some of these missed features are the interactions between vicinity ACN molecules or the influence on the adsorption energy of several copper layers in the slab. In order to enhance previous studies, we have modeled the Cu(100) surface employing PBC's. It is indeed well known both theoretically[64] and experimentally[65] that the chemisorption energy of an adsorbate can notably change with the size of the transition metal cluster. In this way, using PBC on a metal slab gives us a more accurate description of the adsorption energies on the metal surface.

A more recent theoretical study[66] was based on the study of the structure and vibrations

of the ACN molecule adsorbed on a Cu(100) surface, showing a good agreement with previous experimental results[67]. In this work, we extend the previous works by a combination of both static and dynamic DFT studies of the adsorption of a single ACN molecule on a Cu(100) surface. We have included van der Waals (vdW) dispersion forces in our geometry optimization and adsorption energies calculations, as we previously did for the adsorbed system C_6H_6/*n* NaCl/Cu(100) (see chapter 3) via the DFT+D2 Method of Grimme[19], since the inclusion of these weak dispersion forces is mandatory in order to properly describe the interactions between organic molecules and transition metals[68].

Not only structural rearrangement upon adsorption, characterization of the interaction, electronic structure and charge transfer have been tasks of our interest, but also the study of these systems from a dynamical point of view. Thus, we have also evaluated the stability of ACN adsorbed on Cu(100) when different temperatures and conditions are imposed, by means of an Ab Initio DFT molecular dynamics study.

We have studied as well the effect of adding 1, 2 and 3 NaCl atomiclayers to the copper substrate prior to the adsorption of the ACN molecule. This interaction has been also addressed evaluating different properties (structure, charge transfer, stability when increasing the temperature, etc). The desired target is to study the influence of the insulating films in the interaction and charge transfer process from the metal to the adsorbate (which has been achieved by the static DFT study) and the impact of these NaCl overlayers on the chemisorption and stability of the ACN molecule (evaluated with the ab initio DFT molecular dynamics study).

4.2 Structure and adsorption properties of ACN/*n*NaCl/Cu(100); *n* = 0, 1, 2 and 3 ML

The most stable conformations of ACN adsorbed on the Cu(100) metal surface have been considered after a previous study[66] (Figure 4.1): in the most stable geometry, the ACN molecule attaches to the bare metal surface via a σ bond between the lone pair electrons of the N atom and via the π bond of the C=C (this structure has been designated as σNπCC). In a second structure the ACN is attached to the surface through two π bonds of the molecule: C=C and C≡N (named as πCCπCN). These two

stable structures are connected through two transitions states (TS1 and TS2). TS1 results from the molecular rotation around π_{CN} anchorage and TS2 around the π_{CC} one.
As we previously did for the C_6H_6/n NaCl/Cu(100) system, our first step towards understanding the features and behavior of the ACN/*n* NaCl/Cu(100) systems is the construction of the NaCl/Cu(100) surface. For this purpose, we have proceeded in the same manner as explained in section 3.2.
Once the substrate is built up, we have considered several configurations of the ACN molecule when adsorbed on the NaCl/Cu(100) surface.
After geometry optimizations, we have obtained seven possible structures for each (*n* ML)NaCl/Cu(100) surface (see Figure 4.1). The nomenclature of these isomers follow in the same vein as for ACN/Cu(100); for instance, structure ACN/NaCl/Cu(100) σNNaπCl_{Top} presents a sigma bond between the ending nitrogen atom of the ACN molecule and a Na^+ ion of the surface; and the C=C π bond interacts with a Cl^- ion placed on the Top site of the surface. Table 4.1 summarizes the relative energies of these structures as obtained with PBE and PW91 functionals.

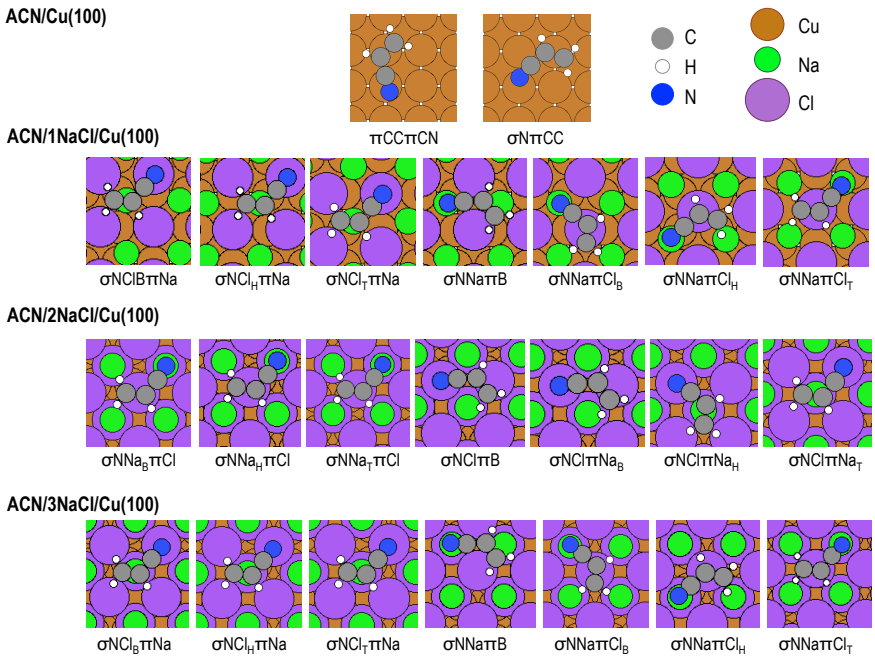

Figure 4.1: All the studied molecular arrangement of ACN on the surface, for ACN/Cu(100) and ACN/*n* NaCl/Cu(100).

	Isomer	ΔE (eV) PW91	PBE
ACN/1NaCl/Cu(100)	σNCl$_B$πNa *	0.14	0.16
	σNCl$_H$πNa	0.18	0.19
	σNCl$_T$πNa	0.12	0.14
	σNNaπB *	0.00	0.00
	σNNaπCl$_B$	0.17	0.17
	σNNaπCl$_H$	0.12	0.11
	σNNaπCl$_T$	0.12	0.12
ACN/2NaCl/Cu(100)	σNNa$_B$πCl	0.02	0.01
	σNNa$_H$πCl *	0.01	0.02
	σNNa$_T$πCl	0.02	0.02
	σNClπB	0.18	0.18
	σNClπNa$_B$ *	0.00	0.00
	σNClπNa$_H$	0.04	0.04
	σNClπNa$_T$	0.02	0.01
ACN/3NaCl/Cu(100)	σNCl$_B$πNa	0.18	0.15
	σNCl$_H$πNa	0.19	0.18
	σNCl$_T$πNa	0.17	0.20
	σNNaπB *	0.00	0.00
	σNNaπCl$_B$	0.15	0.16
	σNNaπCl$_H$ *	0.11	0.12
	σNNaπCl$_T$	0.09	0.13

Both functionals predict the same structure as the most stable one. The most stable minimum for the ACN/1NaCl/Cu(100) system is the σNNaπBridge structure, in which the molecule interacts with the surface via a direct σ bond between the N atom and a Na^+ ion of the surface and with its C=C central double bond over a bridge position (between Na and Cl). In the case of the ACN/2NaCl/Cu(100) system, the most stable configuration is the σNClπNa$_{Bridge}$, where the molecule interacts with the second NaCl overlayer through a σ bond between the N ending atom and Cl^- ion of the surface and the π bond of the C=C moiety and a Na^+ ion on the Bridge site of the surface. Finally, for ACN/3NaCl/Cu(100), the most stable isomer is given by the σNNaπBridge structure as we observed to occur for the ACN/1NaCl/Cu(100) system.

Table 4.1. Relative energies, in eV, for all the studied ACN/xNaCl/Cu(100)structures. Selected structures for analysis are denoted with (*).

The former is an expectable result since for both systems (ACN/1NaCl/Cu and ACN/3NaCl/Cu) the ACN molecule faces the same arrangement of the ions in their outer NaCl overlayer.

We found as well that all the considered conformations of ACN on the insulating film surface are almost degenerated (ΔE ≤ 0.2 eV); in particular, the ACN/2NaCl/Cu(100)

systems shows a remarkable degeneracy for six of the seven studied structures ($\Delta E \leq$ 0.04 eV).

In the following we present a further analysis for each ACN/*n* NaCl/Cu(100) system; to this, we have chosen the most stable conformation and another minimum. In our procedure, we have not used the adsorption energy as a criterion to choose the second minimum, since all the structures can be considered degenerated one from the others, as explained above. Thus, we have considered it more interesting to select the second structure upon those that implied a more drastic bond cleavage breaking, of the molecule from the surface (see table 4.1 and figure 4.1). This arrangement implies a deeper analysis of the potential energy surface (PES) and therefore a larger amount of information.

The adsorption energy of ACN adsorbed on Cu(100) and on NaCl/Cu(100) is given by:

$$E_{Ad} = E_{ACN/n\ NaCl/Cu} - [E_{ACN} + E_{n\ NaCl/Cu(100)}] \quad (4.1)$$

where n = 0, 1, 2 or 3 monolayers of NaCl and $E_{ACN/n\ NaCl/Cu}$ is the total energy of the molecule adsorbed on the surface, E_{ACN} is the energy of the isolated molecule in gas phase and $E_{n\ NaCl/Cu(100)}$ is the energy of the bare surface. By this, negative values of the adsorption energy imply energetically favorable adsorption of the adsorbate on the substrate.
Adsorption energies, with PBE and PW91, as a function of the number of NaCl layers for the two selected structures are given in figure 4.2.

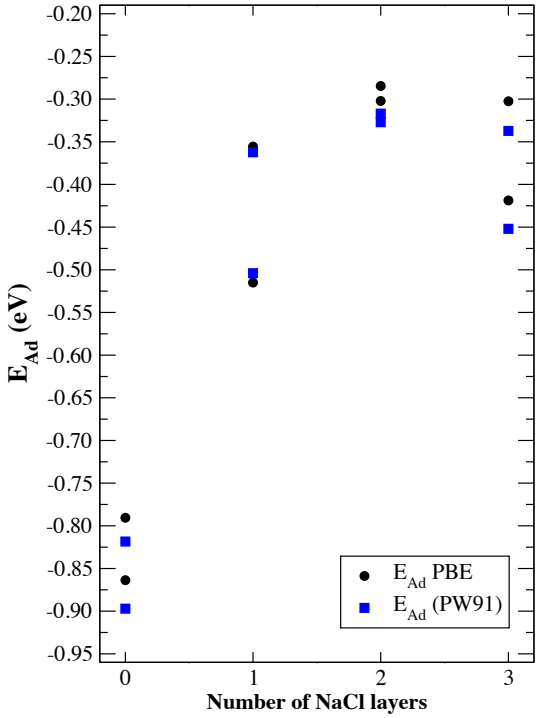

Figure 4.2: Adsorption energies, in eV, for the two considered conformations as a function of the number of NaCl layers.

Larger interaction energies are observed for ACN on Cu(100): the E_{Ad} of the most stable structure (σNπCC) is -0.897 eV (PW91), -0.864 eV (PBE); and -0.818 eV (PW91) and -0.790 eV (PBE) for the second most stable one (πCCπCN). Furthermore, the adsorption energies decrease as more NaCl layers are added, due to the decoupling of the molecule from the metallic substrate and therefore, decrease of the interaction strength between the ACN molecule and the copper slab. Furthermore, we can conclude that the system reaches saturation when more than 2NaCl layers are present in the adsorbed system.

On the other hand, we have also studied the charge transfer from surface to the organic molecule. We have found a low charge transfer from the copper surface to the adsorbate in the ACN/Cu(100) system: the ACN molecule takes 0.36 electrons from the metal surface (σNπCC) and 0.31 electrons (πCCπCN). This charge transfer is much lower when the insulating films are added to the structure: 0.020 electrons for

ACN/1NaCl/Cu(100), 0.025 electrons for ACN/2NaCl/Cu(100) and 0.010 electrons for ACN/3NaCl/Cu(100).
A further qualitative analysis of the charge transfer has been carried out by computing the induced charge density difference, $\rho_{induced}$, defined as in Eq. 3.5.

Figure 4.3 shows the cross sectional views of the induced charge density difference for the most stable structures as well as for the second set of chosen conformations. In the case of ACN/Cu(100) we observe changes in the charge density difference caused by the adsorption of the ACN molecule.

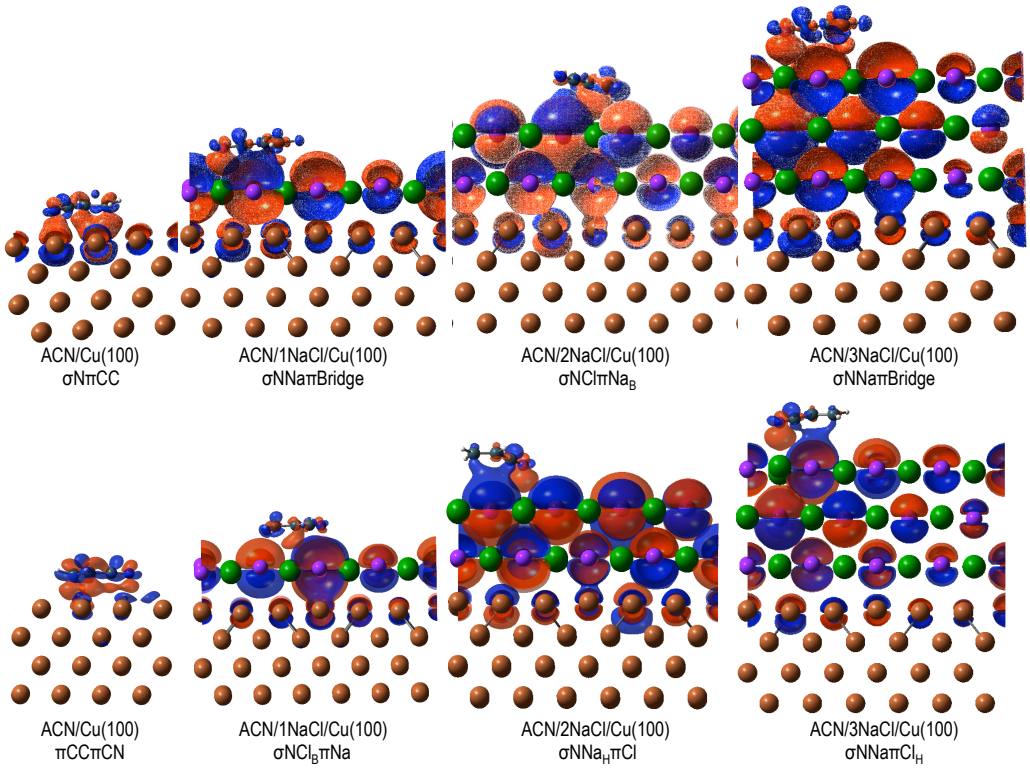

Figure 4.3: Cross sectional view of the induced charge density difference for the most stable isomers and the second set of selected geometries for ACN/Cu(100) and ACN/*n* NaCl/Cu(100). Red density maps correspond to charge accumulation, while blue ones correspond to charge depletion. Isovalues for the charge density maps have been set to 0.001 a.u for the ACN/Cu(100) systems and to 0.0001 a.u for the ACN/ *n* NaCl/Cu(100) ones.

There is charge accumulation between the adsorbate and the metal surface indicating that copper is transferring electrons to the ACN molecule. The rise in charge density is the responsible for the interaction between ACN and the copper surface, and hence, it is visible the bond formation between the molecule and the substrate.

In the σNπCC structure we clearly appreciate the two bonds (σN→Cu and πCC→Cu) and in the πCCπCN the interaction between the π cloud with the metal surface.
For the ACN/*n* NaCl/Cu systems, we observe charge accumulation between the molecule and the surface, and strong polarization of the chlorine atoms induced by the interaction.
In the most stable structure of ACN/1NaCl/Cu and ACN/3NaCl/Cu, the N atom is directly interacting with a Na^+ ion, giving rise to charge accumulation between them. Due to this bonding, the molecule leans towards the surface, making the dipole of the molecule (which goes in the direction of the N atom) to point towards the surface; thus, the molecular dipole polarizes the atoms on the surface, mainly the Cl^- ions nearby. Furthermore, the charge accumulation in between the N atom of the ACN molecule and the Na^+ ion of the outer most layer, induces further polarization of the other ions surrounding the adsorption site.
For the most stable structure of ACN/2NaCl/Cu we have a different picture: the N atom interacts with a Cl^- ion, presenting a depletion of charge in the interface between them. The former charge depletion induces the molecule to slightly lift up from the surface, and thus the molecular dipole moment points out from the substrate, on the contrary to what we observed to happen for ACN/1NaCl/Cu and ACN/3NaCl/Cu. Thus, the striking behavior of the ACN/2NaCl/Cu(100) system, which was previously noted from its adsorption energy (lower adsorption energy than ACN/3NaCl/Cu(100)) and its charge transfer from the substrate to the adsorbate (the ACN molecule is more negatively charged after the adsorption in the ACN/2NaCl/Cu system than in the ACN/1NaCl/Cu one), is also confirmed in the induced charge density map.
The same behavior can be observed for the second set of chosen structures: the direct interaction between a N atom and a Na^+ ion, lean the molecule toward the surface as a charge accumulation is being formed in between both of them; while the direct interaction between the N tom and a Cl^- ion makes the molecular dipole moment to point out of the surface, slightly lifting the molecule out of the former.

	ϕ (eV)	
	PBE	PW91
Cu(100)	4.52	4.57
ACN/Cu(100) σNπCC	4.17	4.21
ACN/Cu (100) πCCπCN	4.21	4.27
1NaCl/Cu(100)	4.02	4.00
ACN/1NaCl/Cu(100) σNNaπB	3.85	3.89
ACN/1NaCl/Cu (100) $\sigma NCl_B\pi Na$	3.94	3.96
2NaCl/Cu(100)	3.60	3.61
ACN/2NaCl/Cu(100) $\sigma NCl\pi Na_B$	3.65	3.70
ACN/2NaCl/Cu(100) $\sigma NNa_H\pi Cl$	3.46	3.44
3NaCl/Cu(100)	3.71	3.83
ACN/3NaCl/Cu(100) σNNaπB	3.61	3.78
ACN/3NaCl/Cu(100) $\sigma NNa\pi Cl_H$	3.86	3.75

Table 4.2: Work function, in eV, with PBE and PW91 functionals, for the bare surfaces and the adsorbed systems for the most stable isomers and the second set of minima for each ACN/x NaCl/Cu(100) system.

We have analyzed the change in the work function ($\Delta\phi$), after the adsorption of the ACN molecule, with both functionals (PBE and PW91) and for the two minima selected for all the systems (see Table 4.2 and figure 4.4). We observe that, for the most stable minima, the work function decreases upon molecular adsorption, except for ACN/2NaCl/Cu, where the work function increases compared to the bare surface. This behavior may be explained in terms of the molecular orientation on the surface: The

ACN molecule is adsorbed parallel to the surface (ACN/Cu σNπCC) or with its dipole moment pointing towards the surface (ACN/1NaCl/Cu σNNaπBridge and ACN/3NaCl/Cu σNNaπBridge), leaving in both situations a charge accumulation in between the molecule and the surface. However a different picture is observed when the dipole moment of the molecule points out of the surface (ACN/2NaCl/Cu σNClπNaBridge), leaving in this case a charge depletion in between the N atom and the NaCl outer most layer. The charge depletion involves an increase of the work function of ACN/2NaCl/Cu σNClπNaBridge, which makes the former system not follow the trend observed for all others. On the other hand, for the second selected structure of ACN/2NaCl/Cu ($\sigma NNa_H\pi Cl$), and since the N atom is directly facing a Na ion, we observe a charge accumulation and therefore it does decrease its work function upon molecular adsorption. Thus, the charge accumulation (created, for instance at the N-Na sigma bonds) influences on the geometry of the molecule (i.e. how it is adsorbed on the surface); the charge accumulation in between the molecule and the surface polarizes the surrounding atoms and ions and determines the direction of the molecular dipole moment. These three aspects (i.e. charge accumulation or depletion in the molecule-surface interface, molecular dipole moment direction and the polarization of the surface atoms and ions) determine the change of the work function of the system.

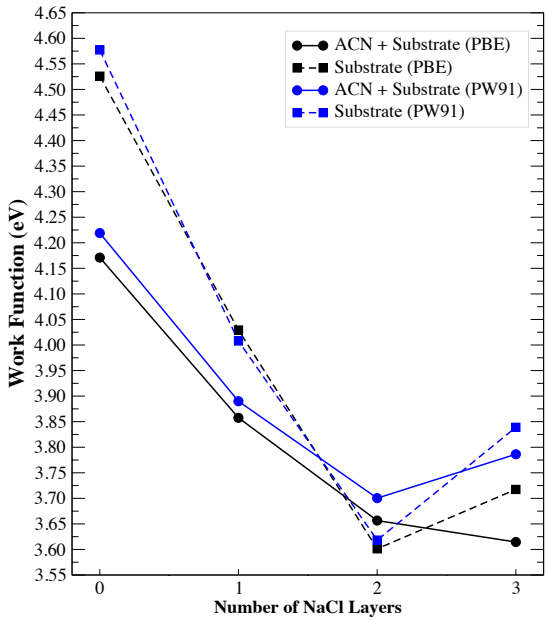

Figure 4.4: Work function of the ACN/*n* NaCl/Cu(100) adsorbed systems, in eV, as a function of the number of NaCl layers.

4.3 Exploring the potential energy surface of ACN/*n* NaCl/Cu(100); *n* = 0, 1, 2 and 3 ML

In theoretical chemistry, and in particular in condensed matter physics, a frequent problem is the identification of the lowest energy path. Such a path is often referred as the "Minimum Energy Path" (MEP). The MEP defines a "reaction coordinate", which allows us to study changes in conformations and energy barriers. Many different methods have been presented for finding stable structures and saddle points along the reaction path, for instance the so-called "Chain-of-states methods", where several images (or "states", or "replica") of the system are connected together to trace out a path. In this framework the "Nudged Elastic Band method" (NEB)[69] is used to find the reaction pathways when the initial and final states (or geometries) are known. The NEB method works by linearly interpolating a set of images between the known initial and final states, and then minimizes the energy of this string of images. Thus, each of the former images corresponds to a specific configuration of the atoms in their pathway from the initial to the final states. Once the energy of this string is minimized, the true MEP is revealed. An example of how the NEB method works is shown in figure 4.5. Figure 4.5 (a) shows the energy convergence of each replica, or state, along the 200 convergence steps. At the end of the process all images are converged, giving rise to the true MEP. Figure 4.5 (b) depicts the energetic profile built from the previous information. In the same manner, we observe how the first convergence cycles give us high energetic profiles, which do not match the reliable situation, and how it continuously adjust to achieve the final optimized MEP.

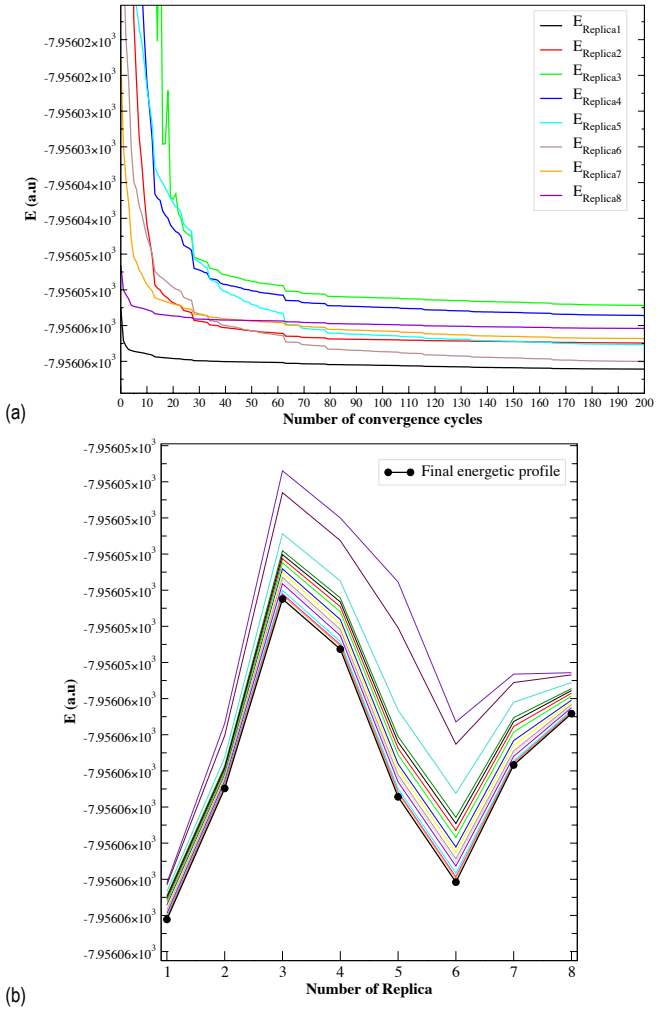

Figure 4.5: (a) Energy convergence for each replica along the 200 convergence cycles and (b) energy convergence for the replica's energetic profile, for the ACN/1NaCl/Cu(100) systems. In fig. 9 (b), solid black line shows the converged energetic profile (final one).

In this section we present the study of the potential energy surface of the ACN/*n* NaCl/Cu(100) adsorbed systems, using the NEB method. The purpose of this study is to obtain further information of the behavior of the ACN adsorption on the different surfaces, and a static picture of the potential energy surface of each system, prior to the molecular dynamics simulations.

In the NEB simulations, three different optimized geometries have been given as starting, transition and ending points. For the starting and ending geometries we have used the most stable configurations and the second set of chosen structures, respectively. On the other hand, for the transition geometries we have used (a) for ACN/Cu(100) σNπCC and πCCπCN structures, the TS1 and TS2 transition states found in a previous work[66] and (b) for the ACN/*n* NaCl/Cu(100) systems, a guess hand-built geometry. These structures have been built in the following way:

I) ACN/1NaCl/Cu(100): The σNNaπBridge and the σNCl$_B$πNa starting and ending geometries have been connected by an intermediate configuration where we have rotated the molecule 90^o, followed by a smooth displacement in the x direction.

II) ACN/2NaCl/Cu(100): The σNClπNa$_B$ and the σNNaπCl starting and ending geometries have been connected by an intermediate structure reached after a 45^o rotation and a slight displacement of the ACN molecule in the y direction.

III) ACN/3NaCl/Cu(100): Finally, the σNNaπBridge and the σNNaπCl$_H$ starting and ending geometries have been connected by a intermediate guess geometry built from the rotation of the molecule, less than 45^o, around the N atom.

Figure 4.6 shows the final results for the NEB calculation.

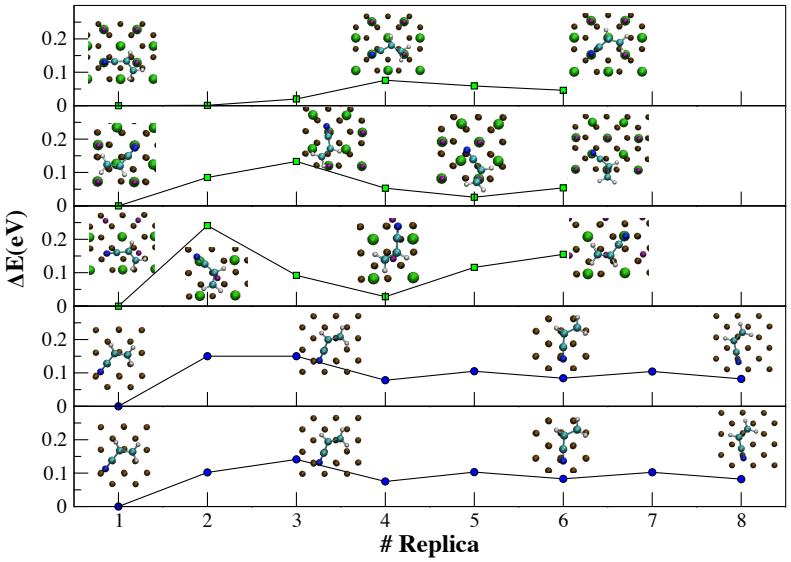

Figure 4.6: Final energetic profiles, studied through a Nudged Elastic Band calculation, connecting the most stable minimum of each structure with the second chosen minimum.

The reaction path going from ACN/Cu(100) σNπCC to ACN/Cu(100) πCCπCN, through TS1 has been evaluated by eight replica. In this MEP we observe two minima (Replica 1 and 8) and the transition geometry (Replica 4). Furthermore, another minimum and transition state, at replica 5 and 7 respectively, were found. The minimum in replica 5 shows the ACN molecule attached to the surface via a sigma N bond and one of the carbon atoms of the central C=C double bond. This minimum is slightly more stable that the πCCπCN structure (ΔE = 0.008 eV).
The reaction path going from σNπCC to πCCπCN through TS2, also envisaged by eight replica, shows as well these two new structures observed in the previous NEB: the minimum at replica number 5 and the transition state at replica number 7.
Moreover, we have studied the change in the bond lengths of C=C, C-C and C≡N for both NEB calculations during the reaction path. The C=C central double bond undergoes the main bond length changes ($\Delta d_{C=C}$ = ±0.03 Å), in agreement with previous results on the charge transfer, where we observed that the charge was mainly gathered in between the metal surface and the C=C cleavage.
For the ACN/*n* NaCl/Cu(100) systems, we have as well performed NEB calculations, from which distil information about the nature of the interaction of ACN with the NaCl/Cu(100) surface. In this case, we have evaluated eight replica for the ACN/1NaCl/Cu system and six replica for the ACN/2NaCl/Cu and ACN/3NaCl/Cu ones; due to the larger decoupling of the surface, six replica is enough in order to give a complete overview of the potential energy surface. Also the changes in the bond distances, along the reaction path described by the NEB, have been envisaged.

The ACN molecule, adsorbed on the 1NaCl/Cu(100) system, does not undergo any significant distortion; The ACN molecule achieves the transition from one minimum to the other by rotating around the C=C clevage, though the bond distances do not differ at each replica step ($\Delta d_{C=C}$ = ±0.01 Å) and therefore, the ACN molecule is almost not affected or influenced by the surface. If we compare these results to those obtained for ACN/Cu(100), where bond lengths changed upon the reaction path, we conclude that the molecule, when adsorbed on 1NaCl/Cu(100), is decoupled from the metal surface, thus, it is not influenced by copper and it moves freely over the insulating film influenced only by weak van der Waals dispersion forces. On the other hand, the NaCl monolayer undergoes a noticeable surface reconstruction along the NEB path, Cl-Cu and Na-Cu distances change 0.20 Å and 0.07 Å, respectively, while the most outer Cu layers do not change their position in the cartesian z direction upon

adsorption and displacement of the ACN molecule. The change in the bond distances between the molecule and the surface has also been studied. In the $\sigma NCl\pi Na_B$ structure, we observe a remarkable change in its initial position (0.10 Å), during the transition of the molecule from one minimum to the other. The former behavior is a consequence of its location, i.e. beneath the C=C central bond, around which the molecule performs its rotation.
Geometry changes along the MEP are due to the type of interaction, i.e. as the molecular dipole changes, the ions on the surface (Na^+ and Cl^-) change their position.

Figure 4.6 shows as well the energetic profile for ACN/2NaCl/Cu(100). The ACN molecule achieves the transition from one minimum to the other by rotating around the C=C bond. The change in the bond distance has also been studied in order to understand to which extension does the surface affect and disrupts the C=C double bond as well as other main atom links in the molecule. Thus, the surface does not undergo a huge distortion in its initial arrangement of the Na^+ and Cl^- ions. We observe a remarkable change in the initial position (0.10 Å) of the Na^+ ion lying immediately beneath the ACN molecule, in the $\sigma NCl\pi Na_B$ structure, during the transition of the molecule from one minimum to the other. The former behavior is a consequence of its location, i.e. beneath the C=C central bond, around which the molecule performs its rotation.

Finally, for the ACN/3NaCl/Cu(100) system, the transition geometry between both minima implies a rotation of the molecule around the N atom. Figure 4.6 shows us the low energy barrier in between the two minima and the soft potential energy surface that the molecule has to go across to move from the σNNaπBridge configuration to the $\sigma NNa\pi Cl_H$ one. Furthermore, none of the ACN bonds change their length during the NEB path, and thus, the molecule is barely affected by the surface since it is completely decouple from it. Moreover, the distances between Na-Cl, Na-Cu and Cl-Cu atoms of the surface barely change in comparison to the initial structure: changes are in the range of 0.01 Å.

4.4 Ab initio Molecular Dynamics simulations for ACN/*n* NaCl/Cu(100), n = 0, 1, 2 and 3 ML

In this section we present the results obtained for the ab initio Molecular Dynamics (AIMD) simulations. Dynamic simulations on surfaces is an innovative topic, as well as a computational expensive technique, which in the future will allow us to study different aspects (self-assembly of molecules depending on the temperature, reactivity, etc.) that we have not yet been able to treat.

We have considered as initial geometries for the simulations all the structures presented above (i.e. the most stable geometry and the second set of chosen structures for ACN/*n* NaCl/Cu(100), *n* = 0, 1, 2 and 3ML, and the transition states connecting the ACN/Cu (100) σNπCC and πCCπCN structures).

The determining factor in the initial conditions for the simulations is the temperature; thus, for each starting geometry, several temperatures have been tested. For those systems where no insulating film is present, the temperatures of the simulations have been set to 1100 K, 600 K and room temperature (300 K). Our choice for such a high temperature, 1100 K, was to give the largest amount of energy possible to the molecule and try to observe it go through the energetic barrier connecting stable structures: from ACN/Cu(100) σNπCC to πCCπCN. This temperature has been chosen after taking into account the melting point of copper (1357 K). We have afterwards considered reducing the temperature by half the initial one, i.e. ≈ 600 K, in order to analyze the behavior of ACN when half the energy was provided. On the other hand, we found interesting as well setting the initial temperature to 300 K, since our calculations could be directly compared with experimental ones.

Same procedure has been followed for those systems where the insulating film is present on the structure, except for the fact that the melting point of NaCl is 1074 K and therefore the temperatures at which we have started the simulations have been set to 1000 K, 500 K and 300 K.

Finally, we have considered a fourth situation: as an initial temperature condition, we have imposed the largest one (1100 K for ACN/Cu(100) and 1000 K for ACN/*n* NaCl/Cu(100)) and we have fixed the coordinates of the substrate; only allowing the molecule to move freely over the surface. This approach gave us the importance of the surface reconstruction in the path followed by the ACN molecule.

In our AIMD simulations, we are using a canonical ensemble: It is a statistical ensemble representing a probability distribution of microscopic states of the system, in

which the number of particles and the volume of each system in the ensemble remain constant, and the ensemble has a well-defined temperature (Ensemble NVT).
A variety of thermostat methods are available to add and remove energy from the boundaries of a molecular dynamic system, approximating thus the canonical ensemble. In our case we have used the CSVR (Canonical Sampling through Velocity Rescaling)[70], which is an algorithm to rescale the velocity of particles in molecular dynamic simulations. The CSVR thermostat is an extension of the Berendsen[71] one, in which a proper force is added in order to enforce the correct distribution for the kinetic energy.
Due to the weak adsorption energies and the decoupling of the molecule when the insulating film is added to the adsorbed system, ACN will desorb from the surface for most of the cases presented here; thus, we give thorough detail on the desorption times of the molecule as a function of the temperature imposed to the system. We have considered desorption of the molecule for vertical distances larger than 4 Å between the C=C double bond of the molecule and the surface.
Following we present the main features of AIMD simulation, for each studied system:

I) ACN/Cu(100):
For this system, we have observed that the temperature highly influences the behavior of the metal surface; at 1100 K and at 600 K the surface reconstruction is remarkable and the Cu slab loses its initial periodicity, as shown in figure 4.7. When starting the simulations from the most stable structure for ACN/Cu(100), σNπCC, only at 1100 K transition to one of the other structures (TS2) is observed. However, when we run the dynamics at 1100 K but keeping the Cu slab frozen, the ACN molecule undergoes a completely different path: the N atom does not float over the neighbor hollow site, as in the two previous trajectories, but it remains next to the Cu atom to which it is initially attached. Thus, the surface reconstruction has a large influence on the path followed by the adsorbate. At 600 K the molecule remains attached to the surface during all the simulation time (≈1000 fs). Finally, running the dynamics at 300 K shows how the energy given at this temperature is not enough to make the ACN overtake the energetic barrier connecting the σNπCC configuration with the πCCπCN one: the ACN molecule does not detach from its initial point of cleavage during the whole simulation time (≈ 1200 fs).

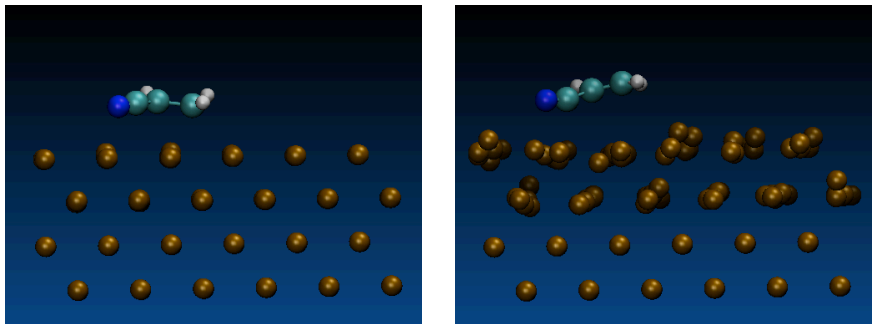

ACN/Cu(100) σNπCC (1100 K) t = 0 fs ACN/Cu(100) σNπCC (1100 K) t = 605 fs

Figure 4.7: Simulation for ACN/Cu(100) σNπCC (1100 K) at time of simulation 0 fs and 605 fs. The two outermost copper layers, which are allowed to relax in the Cartesian coordinates along the dynamics, show the loss of periodicity of the copper slab at this temperature.

Starting the simulation from the second most stable structure (πCCπCN) showed as well that at 1100 K the surface reconstruction is too large in order to keep the ACN molecule adsorbed on the surface. In this process, the molecule breaks it πCN cleavage to the metal slab after 85 fs of simulation and starts to "float" randomly over the neighbor sites of the surface. On the other hand, the other moiety that kept the molecule attached to the surface, the πCC bond, changes its type of interaction, leading to a C-Cu sigma bond. Thus, although the high temperature provided, the transition to the other minimum (σNπCC) is not observed, neither in this case, in the simulation time of ≈ 800 fs. For the trajectory at 1100 K keeping the slab frozen, we observe that the molecule is randomly floating over the surface during the first 800 fs of simulation and finally it stands up and desorbs from the surface. The path followed by the molecule is completely different to that observed at 1100 K allowing the Cu slab to relax. Figure 4.7 shows these differences. Thus, once again the surface reconstruction highly influences and determines how the ACN molecule is going to move over the substrate.

At 600 K we observe a similar behavior as at 1100K, up to 300 fs of simulation; latter the molecule moves upwards the slab leaving the central C=C double bond on top of a hollow site.

Finally, at room temperature (300 K) we observe how the ACN molecule does not detach, but it performs the transition to the σNπCC adsorption site at the simulation time of 950 fs. For those trajectories tested starting from the transition states (i.e. TS1

and TS2), we observed how high temperatures involve the melting of the Cu slab, losing its periodicity, despite the ACN molecule does not desorb form the metallic surface; on the other hand, lower temperatures involve the molecule "floating" over the surface, not reaching any stable and long-lasting configuration.
Thus, for the adsorbed system ACN/Cu(100) the ACN molecule remains attached to the copper slab for almost all trajectories (only at 1100 K, and due to surface reconstruction, the molecule desorbs from the surface and leaves further than 4 Å away from the slab).

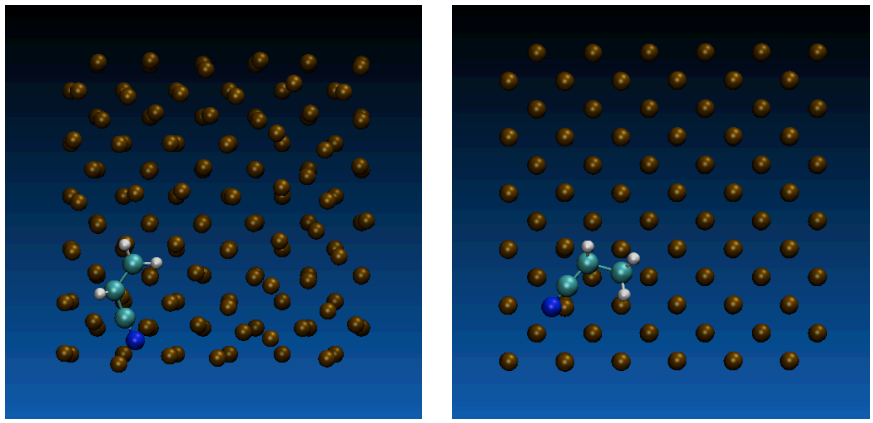

Figure 4.8: ACN/Cu piCCpiCN at 1100 K relaxing the copper cartesian coordinates, left side of the figure, and at 1100K, keeping all slab coordinates fixed, right side of the figure. For both cases the frame was taken at the simulation time of 635 fs.

II) ACN/*n* NaCl/Cu(100), *n* = 1, 2 and 3ML
The static calculations have shown that the ACN/*n* NaCl/Cu(100) systems present a weaker molecular adsorption, due to the presence of the ionic film. For all ACN/*n* NaCl/Cu(100) systems, several trajectories have been computed as well starting from the most stable minima and from the second set of chosen structures. For ACN/1NaCl/Cu(100) σNNaπBridge at 1000 K and 500 K, the ACN molecule desorbs from the surface (after 110 fs and 180 fs, respectively), as shown in figure 4.9.

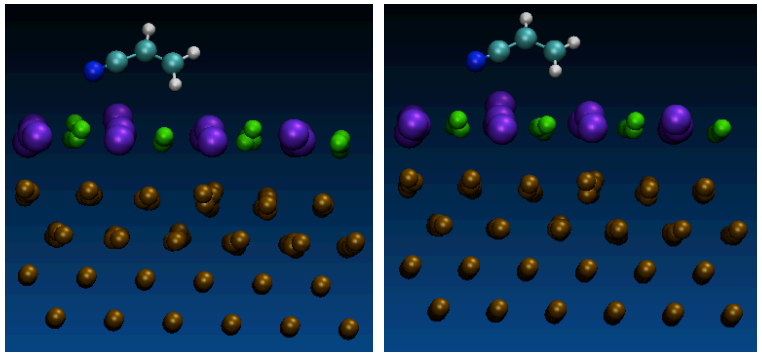

ACN/1NaCl/Cu(100) σNNaπBridge
(1000 K)
t = 110 fs

ACN/1NaCl/Cu(100) σNNaπBridge
(500 K)
t = 180 fs

Figure 4.9: Desorption of ACNfor ACN/1NaCl/Cu(100) σNNaπBridge at 1000 K and 500 K.

At 1000 K, keeping the surface frozen, despite the high temperature, there is no surface reconstruction that incites the molecule to desorb. On the other hand, at 300 K the molecule performs the transition from one minimum to the other (see figure 4.10), executing much slower movements compared to the higher temperature simulations and finally, it desorbs from the surface at the simulation time of 730 fs.

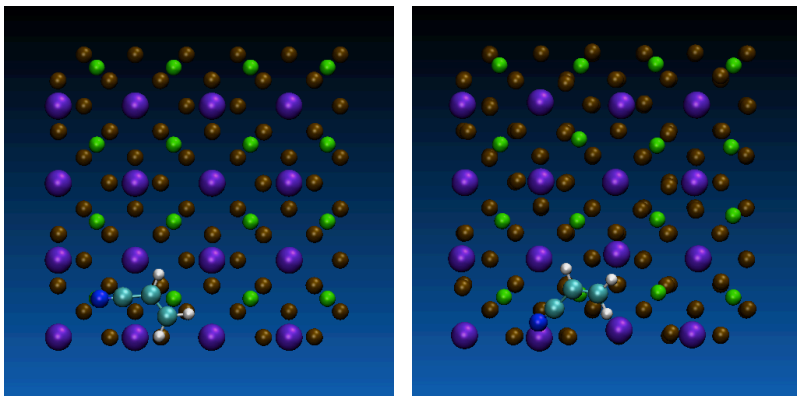

ACN/1NaCl/Cu(100) σNNaπBridge
(300 K)
t = 0 fs

ACN/1NaCl/Cu(100) σNNaπBridge
(300 K)
t = 325 fs

Figure 4.10: Left side of the image: ACN/1NaCl/Cu(100) σNNaπBridge, which is the initial geometry for the simulation; Right side of the image, ACN/1NaCl/Cu(100) σNCl$_B$πNa, which is the second chosen structure.

The simulations for ACN/1NaCl/Cu(100) σNCl$_B$πNa showed molecular desorption from the substrate for all considered temperatures (300 K, 500 K and 1000 K) at 152 fs, 114 fs and 82 fs, respectively. Therefore, no transition is observed from one minimum to the other either at 1000 K, at 500 K or at 300 K; in fact, the NaCl overlayer loses its periodicity and melts, while the molecule completely desorbs from the metallic substrate. Furthermore, this behavior highlights the fact that increasing the temperature accelerates desorption of the molecule from the substrate. When the slab is kept frozen, at 1000K, the ACN molecule follows a completely different path compared to the previous trajectories: it remains parallel to the surface and it does not desorb from it. Figure 4.11 shows the differences between the simulations carried out at 1000 K and at 1000 K keeping the slab coordinates fixed. The surface reconstruction showed in the left image results in a larger distortion of the substrate reducing the interaction and finally leading to molecular desorption.

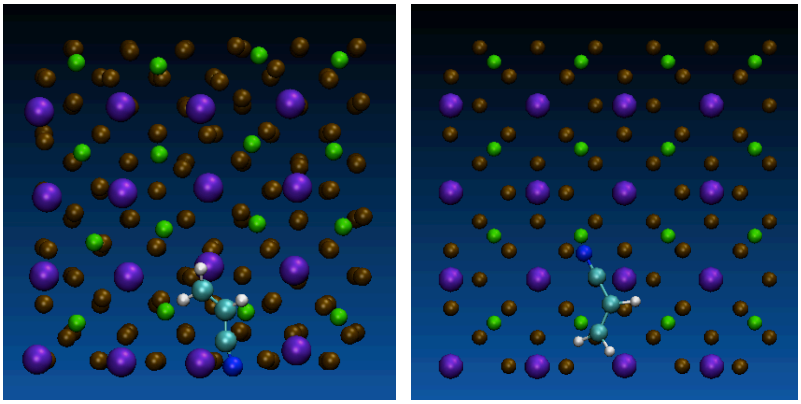

Figure 4.11: Comparisson between ACN/1NaCl/Cu(100) σNCl$_B$πNa at 1000 K and at 1000 K, keeping fixed the slab coordinates.

For ACN/2NaCl/Cu(100) σNClπNa$_B$ we observe that the molecule desorbs from the surface for all the studied temperatures (i.e 1000 K, 500 K and 300K) at the simulation time of 235, 270 and 420 fs, respectively; thus lower temperatures imply larger desorption times. Furthermore, the path followed by the molecule at 500 K and at 300

K is similar to the path at 1000 K, despite the large surface reconstruction presented at 1000 K, as shown in figure 4.12.

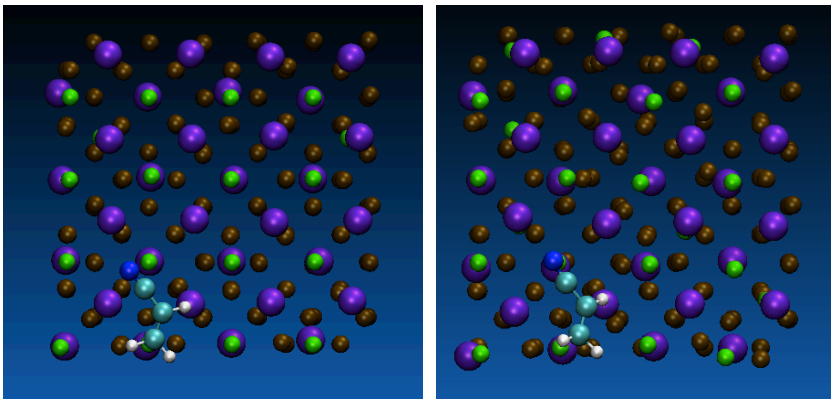

Figure 4.12: Comparisson between ACN/2NaCl/Cu(100) σNClπNa$_B$ at 330 K and at 1000 K, where the surface reconstruction is evident, though the molecule follows the same path as at lower temperature.

At 1000 K, keeping the slab coordinates fixed, the ACN follows a completely different pathway compared to former trajectories: the N atom does not move towards the nearest Na ion, but it is the C=C double bond the one leading the molecule displacement towards the lower part of the slab and finally desorbing from the surface in 335 fs. Thus, we can conclude that the relaxation of the ions of the first NaCl overlayer, in the x and y directions, determines the dynamics of the ACN molecule, though, due to the high decoupling of the molecule from the surface, even keeping the surface fixed, the molecule desorbs from it.

For ACN/2NaCl/Cu(100) σNNa$_H$πCl, the molecule desorbs from the surface acquiring a "stand-up" position at the firsts steps of the dynamics, for all the temperatures of our study (140 fs for 1000 K, 144 fs for 500 K and 150 fs for 300 K). Even for 1000 K and a fixed slab, where no influence of the surface reconstruction is present, the molecule desorbs from the surface at 141 fs. Figure 4.13 shows how the ACN molecule lifts up

at 300 K and at 1000 K, and how this process occurs before at the largest temperature, due to the large amount of energy given to the molecule.

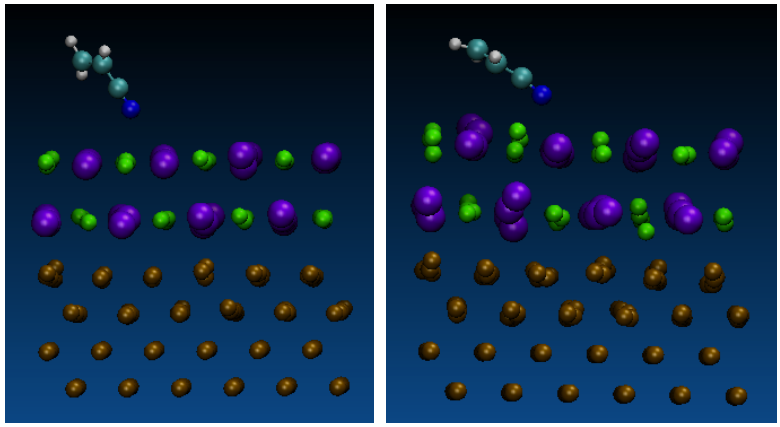

Figure 4.13: ACN/2NaCl/Cu(100) σNNa$_H$πCl at room temperature, left side, and at 1000 K, right side of the image. Desorption is accelerated due to the rise in temperature.

For ACN/3NaCl/Cu(100) σNNaπBridge, the ACN molecule desorbs from the surface at the time of simulation of 500, 370, 170 and 680 fs for 300, 500, 1000 and 1000 K keeping the slab coordinates fixed, respectively. The large time needed for the desorption of the ACN molecule at 300 K may be explained in terms of the surface reconstruction along the simulation: the molecule adjusts to it during the dynamics following the ups and downs of the Cu atoms. Figure 4.14 shows desorption of ACN at 300 K; the surface reconstruction is less remarkable than in the previous simulations and, though adsorption energies are smaller, the distortion of the slab affects to a lesser extent the desorption of the molecule.

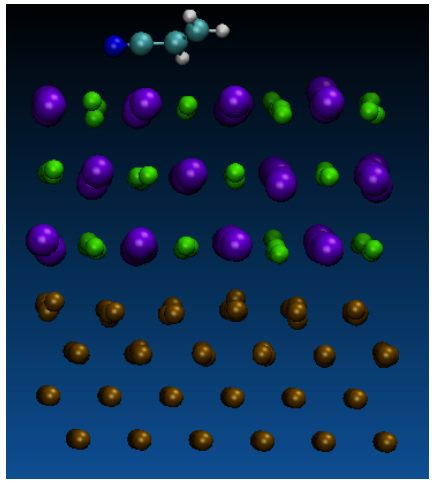

Figure 4.14: Desorption of ACN for ACN/3NaCl/Cu(100) σNNaπBridge at room temperature.

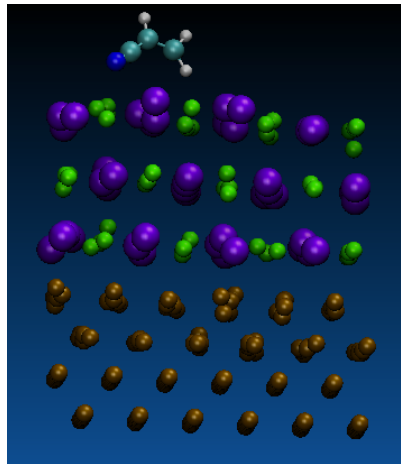

Figure 4.15: ACN somersaulting over the surface and desorbing from it, for ACN/3NaCl/Cu(100) σNNaπCl$_H$.

Finally, for ACN/3NaCl/Cu(100) $\sigma NN a \pi Cl_H$ (figure 4.15) the molecule desorbs from the surface at the first steps of our simulations, for all temperatures (350 fs for 1000 K and the Cu slab fixed, 100 fs for 1000 K, 115 fs for 500 K and 130 fs for 300 K), evidencing the large decoupling of the molecule for this system. The molecules somersaults while maintaining its initial N-Na cleavage, until desorption is reached.

From the ab initio molecular dynamics simulations we can conclude that the behavior of the ACN molecule follows two different aspects:

I) Fixed slab vs. relaxation of the surface atoms: The relaxation of the surface atoms highly influences the path followed by the molecule. In most cases this surface reconstruction is responsible for the molecular desorption.

II) Influence of the insulating film: ACN remains adsorbed to the Cu surface even in the simulations started from structures far from the most stable one. On the other hand, when the insulating film is added to the metal surface, the ACN molecule decouples from the former since adsorption energies significantly decrease, and the molecule desorbs from the surface even at low temperatures.

Figure 4.16 shows the desorption time of the ACN molecule as a function of the temperature, for the ACN/*n* NaCl/Cu(100) systems. Black solid lines represent the most stable configurations, while red solid ones show the second set of chosen structures. At sight of figure 4.16, we can conclude that:

I) The most stable configurations are distinguished by larger desorption times compared to the second set of chosen structures.

II) The system reaches saturation already when two NaCl layers are added.

III) The desorption time decreases when the temperature increases.

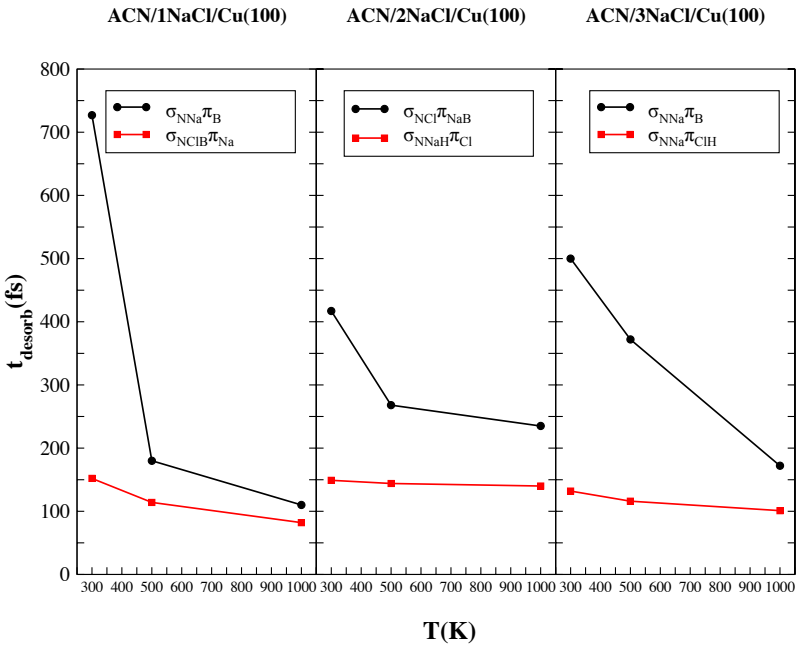

Figure 4.16: Desorption time, in fs, of the ACN molecule, as a function of the temperature, in K for the ACN/*n* NaCl/Cu(100), *n* = 1, 2 and 3 ML. Black solid lines indicate the most stable structure for each adsorbed system; red solid ones represent the second set of structures for each system.

4.5 Computational details for the ACN/*n*NaCl/Cu(100) system

Finally, we present the details of the computational methods used in this chapter. For the static part of our work periodic density functional calculations were performed using the Vienna ab initio simulation package (VASP)[46,47]. The exchange and correlation effects have been described by using the Generalized Gradient Approximation (GGA)[50,51] and employing two different functionals: The Perdew Wang 91 (PW91) functional and the 1996 functional of Perdew, Burke and Ernzerhof (PBE)[55,56]. Both functionals have been used to calculate geometry optimizations and single point energy (SPE) calculations, in order to give a comparative perspective between both. The adsorption of such an organic molecule as acrylonitrile customarily

needs to account for dispersion forces, as it occurred with C_6H_6/n NaCl/Cu(100); we have thus applied the DFT-D2 method of Grimme[19] in the same manner as explained in the previous chapter.

We have as well computed the charge transfer after the adsorption of the ACN molecule on the surface (both on Cu(100) and *n*NaCl/Cu(100)) by using the Quantum Theory of Atoms in Molecules (QTAIM) by R. Bader[22,23] as implemented by Henkelman et al.[72–74].

The Projected Augmented Wavefunctions (PAW) have been expanded in a plane wave basis set up to a kinetic energy cutoff of 400 eV. The metal surfaces were modeled by a slab consisting of four atomic layers, separated by a vacuum space of 10 Å in the coordinate z, perpendicular to the surface.

The adsorption of ACN has been considered in all cases, in a low coverage regime, within a unit cell of (4 x 4) Cu atoms in the direction parallel to the surface (x and y coordinates). Geometries have been optimized sampling the Brillouin zone (BZ) with a Γ-centered Monkhorst-Pack of 1x1x1 K-Mesh. Final electronic energies have been then computed employing the optimized geometries by single point energy calculations using a Γ-centered Monkhorst-Pack of 4x4x1 K-Mesh.

A Methfessel - Paxton smearing, which is the best procedure for a metal relaxation, of 0.2 eV have been used for the sampling of the BZ during the geometry optimization, while the SPE calculations have been carried out using a Gaussian smearing of 0.1 eV, which smears out the Fermi level so more of the k-points will be effectively located on the Fermi surface.

The geometries of the studied systems were optimized by relaxing all atoms of the adsorbate (acrylonitrile), in the three spatial directions and all atoms of the insulating films, NaCl, and the first layer of the metal slab, Cu, in the direction perpendicular to the surface. The layer spacing of the two lower Cu layers was taken form the optimized lattice constant parameter (a_o = 3.365 Å), while the third and fourth layers were allowed to relax in a first geometry optimization of the Cu(100) slab, and subsequently fixing the third Cu layer during the optimization of the whole system containing the adsorbate. All these coordinates were optimized until all forces were smaller than 0.001 eV $Å^{-1}$. The electronic self-consistent convergence was set in an energy difference of 10^{-5} eV with respect to the previous cycle.

Two different sets of calculations have been carried out using the CP2K package[75–80]: Nudged Elastic Band (NEB) calculations and ab initio molecular dynamics (AIMD). The former will give us the thorough study of the Potential Energy Surface (PES),

while the latter will show us the stability of the adsorbate upon the inclusion of temperature in the system.

For the NEB calculations we have used 3 input geometries, as explained in section 3.11. The initial geometries for the start and end configurations have been taken from the optimized structures obtained by the VASP code and have been reoptimized during the NEB calculation with the CP2K program. During the optimization the adsorbate, ACN, the first Cu layer and the insulating film, NaCl, were allowed to relax in the spatial coordinates. However, a first step to connect the results of both program packages and maintain the continuity of our study was to perform an energy convergence calculation of the copper unit cell. The lack of use of K-points in the CP2K code implies the necessity of enlarging the unit cell in order to simulate the mirror image that is achieved by using K-points. Thus, we arrived to the conclusion that the VASP 4x4x4 Cu slab was successfully modeled by a 6x6x4 Cu slab when using the CP2K code. We have used the Quickstep method, which is based on the Gaussian and plane waves method (GPW). Central in this approach is a dual basis of atom centered Gaussian orbitals and plane waves (regular grids). The former is used to represent the wave functions and the Kohn-Sham Matrix, whereas the latter is used to represent the electronic density. For the plane waves we have used 5 multigrids with an energy cutoff of 500 eV. Furthermore, a DZVP basis set has been employed for the Gaussian functions as well as the PBE functional. The electronic self-consistent convergence was set in an energy difference of 10^{-7} eV with respect to the previous cycle. A total number of 100 molecular orbitals have been added for each spin while the Fermi-Dirac method has been employed for the smearing of the function. For all the calculations carried out with the CP2K code we have also considered dispersion forces, as we did for our previous Geometry optimization and SPE calculations with the VASP code, by adding a semi-empirical potential in the framework of the DFT-D2 Method of Grimme.

For the Molecular dynamics calculations and in addition to the former theoretical methods details, we have used a canonical (NVT) ensemble with a time step of 0.5 fs, which showed to give well-behaved energy conservation results. A Canonical Sampling through Velocity Rescaling (CSVR) thermostat has been used, which is an algorithm to rescale the velocity of particles in molecular dynamic simulations. The thermostat suppresses fluctuations of the kinetic energy, so it does not strictly follow the canonical ensemble, though in practice, the amount it deviates from canonical is quite small.

Chapter 5

TCNQ+TTF/Ag(111)

5.1 Self-assembly of molecules on surfaces

In this chapter, we present the third and last subgroup of organic compounds with semiconductive properties: electron donors and acceptors molecules that can form, for instance, solid molecular systems.
In this context, TCNQ (Tetracyanoquinodimethane) and TTF (tetrathiafulvalene) are widely known and studied molecules, due to their large ability to accept and donate electrons, respectively.
In the two previous chapters, we presented isolated molecules as adsorbates; thus, we were dealing with low regime coverage of the substrate. However, in this chapter we introduce a new perspective: Self-assembled monolayers (SAMs).
Self-assembly (SA) is a process in which molecules, polymers, colloids, etc. organize themselves into ordered systems without human intervention: just mixing the components and the forces of nature will spontaneously assemble them into a favorable structure.
In nanotechnology, SA covers several molecular structures as self-assembled monolayers[81,82] amphilic fibers[83,84], nano-particles[85] and nanorods[86]. The term "assembly" is defined as the process of "fitting together of manufactured parts into a complete machine, structure or unit of machine". In this definition, the keywords are "parts" and "fitting together", which give us a more precise idea of how "assembly" reflects the fact that some discrete pieces come together into some kind of spatial ordering. Thus, a more proper definition of self-assembly would be: the spontaneous

formation of *organized* structures from many *discrete* components that interact with one another directly by electrostatic repulsions[87] or indirectly, by environmental ones[88]. The term "organized" distinguishes SA from other processes as precipitation, since it refers to some form of spatial and temporal ordering. We can go further into the description of self-assembled structures by dividing them into two subgroups:

I) Equilibrium self-assembled structures: They are characterized by a maximum in the system's entropy and no systematic energy flows.

II) Dynamic self-assembled structures: they are non-equilibrium structures. They depend on an external energy supply. An example of this kind of structures is the self-assembly of some proteins called helicase, which acquire a well-organized structure after the replication of DNA, energetically driven by the hydrolysis of deoxyribonucleotidetriphosphate precursors[89].

In this work, we have focused on the first subgroup, equilibrium self-assembled structures. In this chapter we will first present a thorough study of each molecule (i.e. TCNQ and TTF) individually self-assembled on a metallic substrate: Ag(111); and afterwards, we will considered the self-assembled structures reached by the mix of both molecules in different stoichiometric proportions. The interaction between the SA organic molecules and the metallic substrate has been treated, as in previous cases, including vdW forces. Once more, they are essential if we want to describe the interaction between the molecules and the Ag surface, and beyond that, they are indispensable in order to properly ascribe for the intramolecular interactions between the molecules constituting the SA monolayer. Thus, our results are divided into three main sections:

I) Self-assembled TCNQ adsorbed on Ag(111): TCNQ/Ag(111).

II) Self-assembled TTF adsorbed on Ag(111): TTF/Ag(111).

III) The mix of both molecules, self-assembled on Ag(111): TCNQ+TTF/Ag(111).

5.2 Scanning Tunneling Microscope

All theoretical calculations presented here are reinforced with a solid background of experimental studies carried out with a Scanning Tunneling Microscope (STM), at IMDEA-Nanoscience Institute (Madrid, Spain). One of the main motivations for this

chapter of the thesis was to explain the experimental findings, in particular the observed self-assembled patterns and the charge transfer processes.
The STM was invented by Binning and Rohrer, and implemented by Binning, Rohrer, Gerber and Weibel[90,91]. A probe tip, usually made of W or a Pt-Ir alloy, is attached to a piezodrive, consisting of three perpendicular piezoelectric transducers: x piezo, y piezo and z piezo. These piezo electric transducers contract upon a voltage. During the process of scanning the sample, the electron wavefunctions in the tip overlap electron wavefunctions in the sample surface. A finite tunneling conductance is then generated. By applying a bias voltage between the tip and the sample, a tunneling current is generated. Figure 5.1 shows an scheme of a STM.

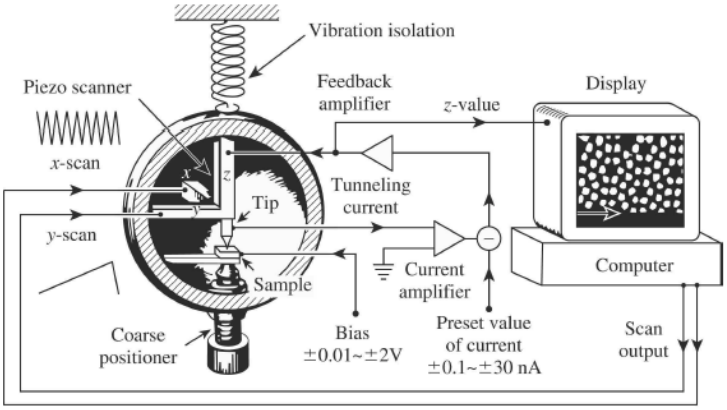

Figure 5.1: The scanning tunneling microscope: The scanning waveforms, applying on the x and y piezos, make the tip raster scan on the sample surface. A bias voltage is applied between the sample and the tip to induce a tunneling current. The z piezo is controlled by a feedback system to maintain the tunneling current constant. The voltage on the z piezo represents the local height of the topography. (Source: C. Julian Chen "Introduction to Scanning Tunneling Microscope" Department of Applied Physics and Applied Mathematics, Columbia University, New York; Oxford University Press)

The most widely used convention of the polarity of bias voltage is that the tip is virtually grounded. The bias voltage, V, is the sample voltage. If $V > 0$, the electrons tunnel from the occupied states of the tip into the empty states of the sample. If $V < 0$, the electrons tunnel from the occupied states of the sample into the tip.
The tunneling current is converted to a voltage by the current amplifier, which is then

compared to a reference value. The difference is amplified to drive the z piezo.
The phase of the amplifier is chosen to provide a negative feedback: if the absolute value of the tunneling current is larger than the reference value, then the voltage applied to the z piezo tends to withdraw the tip from the sample surface, and vice versa. Thus, an equilibrium z position is established. As the tip scans over the xy pane, a two-dimensions array of equilibrium z positions, representing a contour plot of the equal tunneling-current surface, is obtained, displayed and stored in the computer memory. The topography of the surface is finally displayed on the computer screen, as shown in figure 5.2.

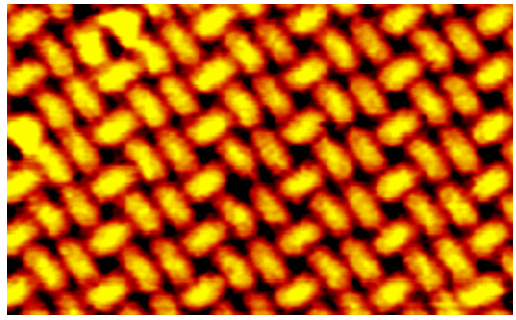

Figure 5.2: STM image of TCNQ SAM adsorbed on a Ag(111) surface. (Obtained by the experimental group at the IMDEA-Nanoscience Institute).

There two modes of proceeding when measuring a sample with an STM: constant height and constant current modes. The former concerns the measure of the current when a constant height of the tip is involved, while the later refers to measuring the height of the tip while the current is kept constant.
The height variation in constant current mode comes from the tip topography variation and thus, contrast on the image is due to variations in the charge density. In constant height mode, both height and voltage are kept constant while the current changes (in order to keep constant voltage); the image is therefore made of current changes over the surface, which can be related to charge density.
In addition, the STM can be also used to study the electronic structure by measuring the current as a function of the applied voltage (I *vs.* V). The derivative of this curve provides the density of states (the so-called dI/dV curve). This technique is called Scanning Tunneling Spectroscopy (STS).

5.3 TCNQ/Ag(111)

We will start presenting our results for the deposition of Tetracyanoquinodimethane (TCNQ) molecules on the Ag(111) surface. TCNQ has recently focused a growing attention from the scientist community due to its great properties as prototype of π acceptor molecule. It presents as well a strong tendency to bond to transition metal atoms[92], due to its electrophilic character[93]. Thus, TCNQ is the perfect candidate to be used in the formation of charge transfer compounds, as a *p*-dopant in organic semiconductors[94] and in nano-electronic metal/organic devices.
Figure 5.3 shows the molecular structure of TCNQ: it is a four cyanocarbon relative to para-quinone.

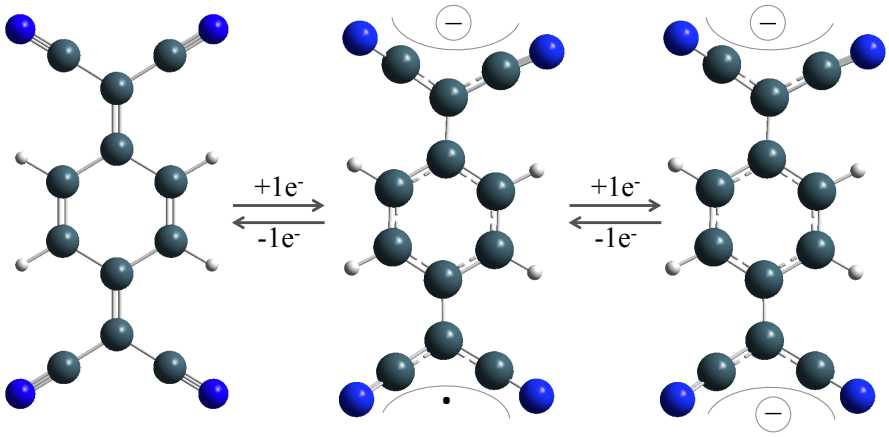

Figure 5.3: Chemical structures for TCNQ, $TCNQ^{-}$ and $TCNQ^{2-}$. In its neutral form the central benzene ring is not aromatic; the uptake of at least one electron aromatizes the central ring. Besides, the C=C double bond, connecting the carbon ring with the cyano groups, becomes a single C-C bond, enhancing the conformational freedom. Blue, grey and white atoms are nitrogen, carbon and hydrogen ones.

5.3.1 Experimental structure (STM) *vs.* Theoretical models for TCNQ/Ag(111)

Figures 5.4 (a) and (b) show the experimental STM images of self-assembled TCNQ

molecules on a Ag(111) surface. TCNQ molecules rearrange in these two different patterns when they are deposited on the metallic substrate.

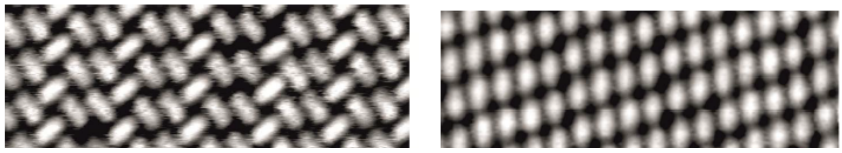

(a) TCNQ/Ag(111) Zipper phase (b) TCNQ/Ag(111) Lineal phase

Figure 5.4: (a) STM image of TCNQ/Ag(111), with the TCNQ molecules rearranged in a "zipper" structure. (b) STM image of TCNQ/Ag(111), with the TCNQ molecules creating well-ordered lineal structures. (Obtained by the experimental group at the IMDEA-Nanoscience Institute).

Figure 5.4(a) shows a self-assembled monolayer of TCNQ molecules deposited on the Ag(111) surface. In this case, TCNQ molecules interweave together giving rise to the Zipper phase, where the pattern shows how two consecutive TCNQ rows follow the same direction and rearrangement, while a third row of molecules is rotated almost 90^{o} respect to the other previous two rows. Figure 5.4(b) shows a different picture: TCNQ molecules have been deposited on the Ag(111) surface and molecules are well-ordered in parallel rows.
STM experimental images are crucial in order to perform a theoretical study; otherwise the number of possible structures and rearrangements of the organic molecules on the metallic surface is a nonstarter fact to deal with. Not only we need to know in advance the appearance of the self-assembled organic monolayer, but also how the molecule itself is oriented with respect to the high symmetry directions of the Ag(111) surface.

In a first step, independently to the STM measurements, we have performed a theoretical study of a single TCNQ molecule adsorbed on the Ag(111) surface. Thus, we explored the Ag(111) surface in pursuit of the most stable configuration. To this, we have performed a scan in the z-axes coordinate (perpendicular to the surface plane) by single point energy calculations, keeping the TCNQ molecule flat. Since TCNQ molecule is well known to bend on metallic surfaces (i.e. to bond its N atoms to the metal ones), these calculations were used to get a first idea of the binding distance between TCNQ and the silver surface. The results for this scan are shown in figure 5.5.

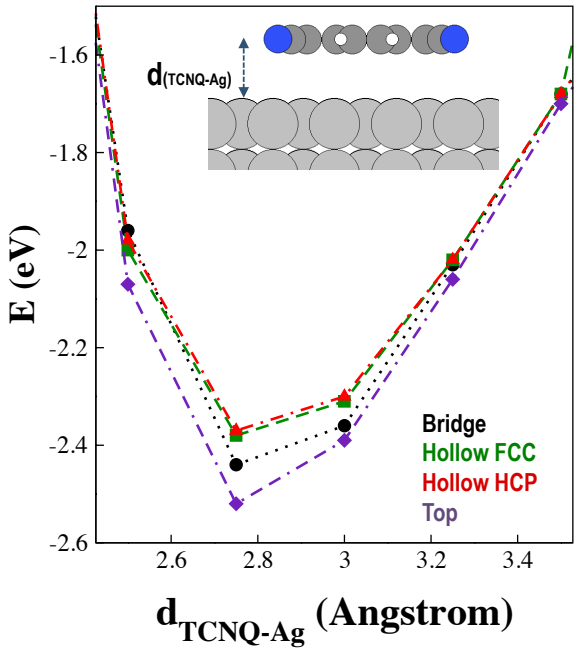

Figure 5.5: Scan in the z axes for a single TCNQ molecule (in a flat configuration) on the four high symmetry adsorption sites of the Ag(111) surface.

The most stable adsorption site for TCNQ on the Ag(111) surface is the top position, where the central benzene ring of the organic molecule is placed on top of a Ag atom. Nitrogen atoms of the TCNQ molecules are placed in an effective manner on top of Ag atoms as well, such as to maximize the contact between the molecule and the metal substrate and to achieve the maximum charge transfer from the latter to the former. Figure 5.6 shows top and side views of this structure, as well as the molecule-metal distance after a further optimization. The adsorption energy obtained, after optimization, for this structure is -3.42 eV. The optimized structure shows how the TCNQ molecule is bent towards the surface, i.e. the TCNQ molecule has taken charge from the Ag substrate, changing its initial C=C bond to a single one, which enhances the conformational freedom (see also figure 5.3).

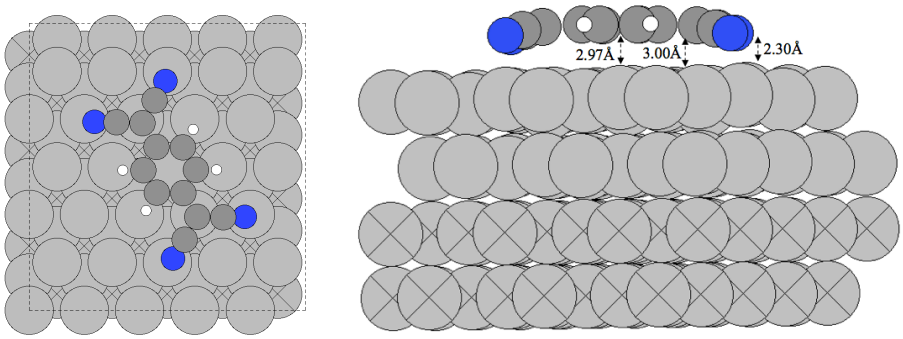

Figure 5.6: Top (left) and side (right) views of TCNQ/Ag(111) adsorbed on a top position. The bending of the TCNQ molecule is shown at sight of the equilibrium distance of the right side image.

We now know the more stable configuration of one isolated TCNQ molecule on the Ag(111) surface and we expect then that a self-assembled monolayer would behave in a similar way if the interaction between the molecules does not influence the self-assembly process. However, we also know that all high symmetry adsorption sites present similar, almost degenerate, adsorption energies for the adsorbed system and in addition, we do not now a priori how the molecule-molecule interaction can change the structure in the SAM. Thus, the experimental measurements have been used to guide the simulations. In fact, experimental values for the orientation of the self-assembled monolayer bring us to a final unit cell where TCNQ molecules will rather stick together through hydrogen bonds than to search for the most stable adsorption site, for both the Zipper and the Lineal phases. Figures 5.7 and 5.8 show the optimized unit cells for the two observed phases. The theoretical unit cell size agrees perfectly the experimental values.

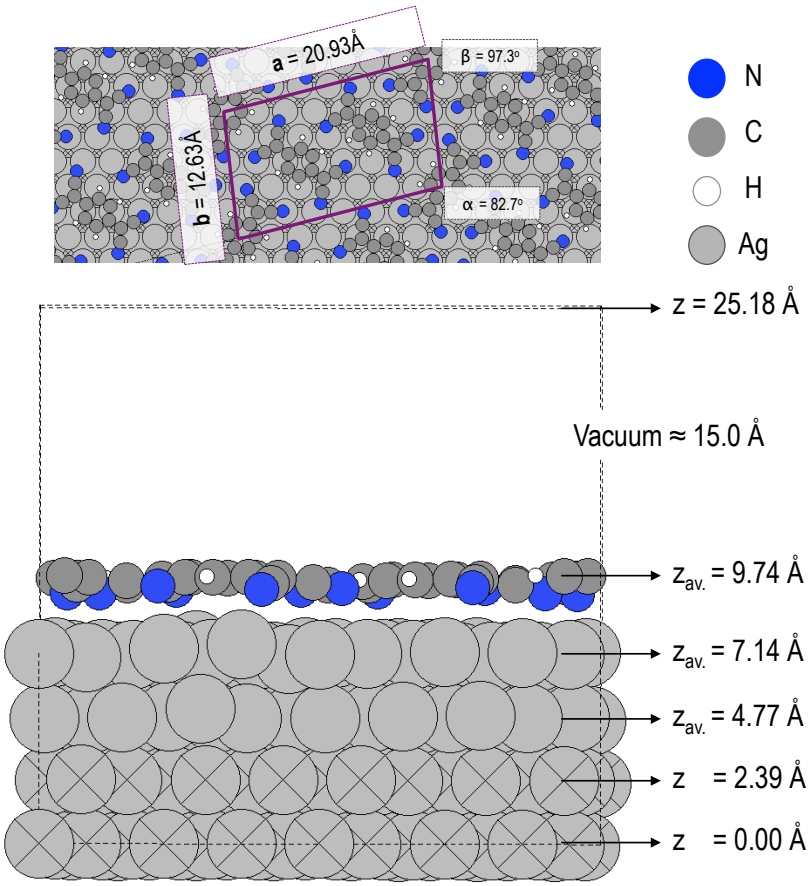

Figure 5.7: Top and side views of the TCNQ/Ag(111) Zipper phase. In the top view the unit cell has been delimited by purple solid lines and the axes (a and b) length is shown, as well as the α and β angles of the unit cell. In the side view the average location of each Ag layer is shown. Silver atoms that are crossed out are those that are not relax during the optimization. The unit cell contains 144 Ag Atoms.

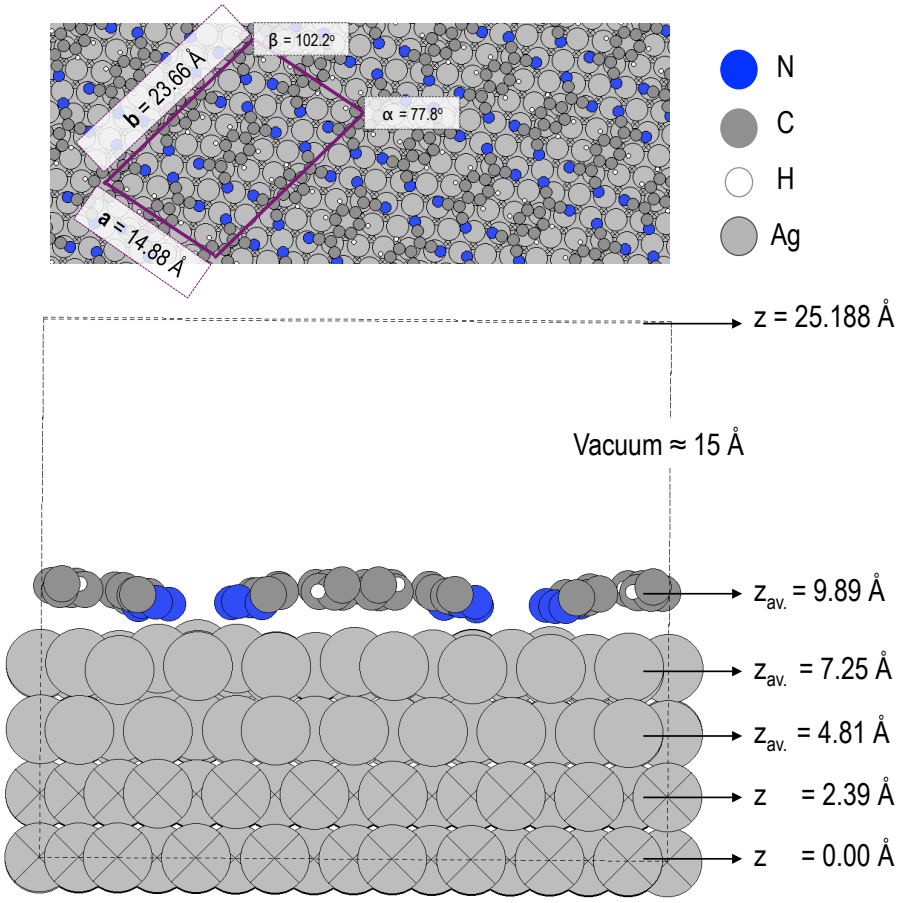

Figure 5.8: Top and side views of the TCNQ/Ag(111) Lineal phase. In the top view the unit cell has been delimited by purple solid lines and the axes (a and b) length is shown, as well as the α and β angles of the unit cell. In the side view the average location of each Ag layer is shown . Silver atoms that are crossed out are those that are not relax during the optimization. The unit cell contains 192 Ag Atoms.

5.3.2 Structure and adsorption properties of TCNQ/Ag(111)

Figures 5.7 and 5.8 show two patterns of self-assembled monolayers of TCNQ adsorbed on the Ag(111) surface: the zipper and the lineal phase, respectively. As

measured in the STM experiments (figure 5.4) in the zipper phase, each unit cell contains 3 molecules (i.e. two TCNQ molecules in the center of the unit cell and a third one at the corners); for the lineal phase 4 molecules constitute the unit cell (i.e. one in the center, two molecules in two different edges and one on the corner).
Adsorption energies per molecule were computed as shown in equation 5.1:

$$E_{Ad} = \frac{E_{TCNQ/Ag(111)} - [E_{Ag} + (n * E_{TCNQ\ "flat"})]}{n} \quad (5.1)$$

where $E_{TCNQ/Ag(111)}$ is the energy of the complete adsorbed system, E_{Ag} is the energy of the bare metal surface, $E_{TCNQ\ "flat"}$ is the energy of one TCNQ molecule in the gas phase (where it remains in a planar, "flat", configuration) and n is the number of TCNQ molecules on the unit cell. Thus, negative values for E_{Ad} mean adsorbed systems.
Adsorption energies are very similar for both models: -3.39 eV/molecule (Zipper phase) and -3.06 eV/molecule (Lineal phase). Already at sight of theses results, comparing them with previous systems as benzene on copper or ACN on copper, we observe the large interaction between this electron acceptor, TCNQ, and the metallic surface, Ag. This large interaction is due to the final optimized geometry of TCNQ adsorbed on the metal surface: the TCNQ bents towards the Ag surface, with its higher atoms located at ~2.90 Å and the lower ones (the nitrogen atoms at the edges) at ~2.30 Å, above the surface. The closer position of the nitrogen atoms shows the covalent-like interaction between the former and the metallic substrate. The optimized geometries for the TCNQ molecules contained in the SAM are similar to the optimized geometry of the isolated TCNQ molecule adsorbed on Ag(111), i.e. in both cases the molecule is bent towards the molecule. As a consequence, adsorption energies of the TCNQ SAM adsorbed on Ag(111) and the isolated molecule on Ag(111) are very similar.
Furthermore, the zipper and the lineal models present one or two of their TCNQ molecules on a top position (the most favorable one), respectively, while the others stand on a hollow HCC and FCC sites. In the gas phase, TCNQ presents an angle for the NC-C-CN moiety of 117.5°; however, this angle decreases for the TCNQ molecule on a top position for the Zipper phase (114.0°), and presents alternated differences for the hollow FCC and hollow HCC positions (112 °/120 ° and 116 °/119 °, respectively), depending on how the C-CN subunit has to elongate in order to reach a silver atom. For the Lineal phase, both TCNQ molecules placed on a top position decrease their

NC-C-CN angles to 115 º, while the ones standing on the bridge site at the larger and the shorter edges present almost no changes (117 º and 118 º, respectively).
Not only a direct bonding between nitrogen and silver atoms is taking place, but also N···H intermolecular bonding between adjacent molecules, as might been seen in the STM images (see figure 5.4 a and b).
Furthermore, The Ag(111) surface undergoes a remarkable surface reconstruction, mostly at those points where it directly interacts with an atom of the TCNQ molecules. Thus, for the Zipper phase the Ag atoms lying beneath the N ones lift up 0.11 Å, while the metallic atoms underneath the carbon ring go down to 0.04 Å, with respect to the metal bulk atoms positions. For the lineal phase, similar behavior is found: N atoms lift up 0.20 Å the silver ones, while the carbon rings push the atoms of the surface 0.01 Å.
We have also analyzed the charge transfer after adsorption of the organic monolayer by means of a Bader analysis and by studying the induced charge density difference, computed as previously explained (see eq. 3.5). The charge transferred form the Ag substrate to each TCNQ molecule is 1.15 e^- for both phases, which contrasts with the neutrality of TCNQ on Au(111)[92] but not so much with TCNQ on Cu(111)[95], where each TCNQ molecule takes almost 1.5 e^- from the surface. Visualization of the charge transfer is given by the induced charge density difference (figure 5.9).
Figure 5.9 shows the induced charge density difference for the Zipper and Lineal phases from a top and a side views. There is a clear charge accumulation in between the nitrogen atoms and the silver ones lying beneath. This charge accumulation evidences the N-Ag bond formation and confirms the charge transfer observed by the Bader analysis. There is a strong intrinsic molecular dipole in the TCNQ/Ag(111) interface, due to the geometrical distortions in the molecule (with respect to its gas-phase structure) and due to the charge transfer. This effect is clearly rather visible for the monolayer structure (figures 5.7 and 5.8). The Ag surface is thus polarized as a consequence of this charge accumulation in the interface.

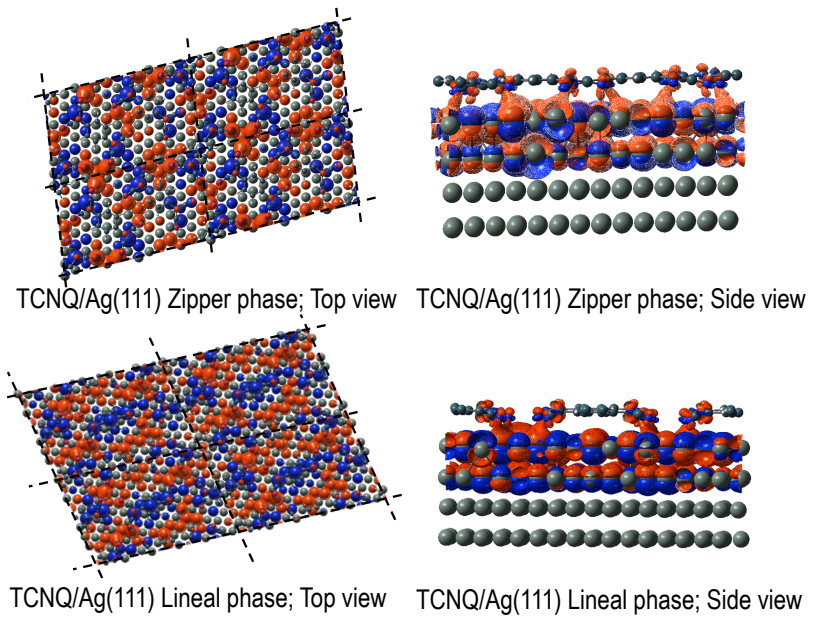

Figure 5.9: Top and side views of the induced charge density difference for the Zipper and the Lineal phases of TCNQ/Ag(111). The isovalue has been set to 0.2 a.u; red and blue isovalues represent charge accumulation and depletion areas, respectively.

The electronic structure and the change in the work function upon adsorption has also been analyzed for the two studied TCNQ/Ag(111) models. The Projected Density of States (PDOS) for both TCNQ/Ag(111) models are shown in figure 5.10.

The relative position of the Fermi level with respect to the molecular levels and the change in the molecular orbitals position upon adsorption, will be thoroughly analyzed at the end of this chapter, comparing them with the TTF/Ag(111) and the TCNQ+TTF/Ag(111) adsorbed systems.

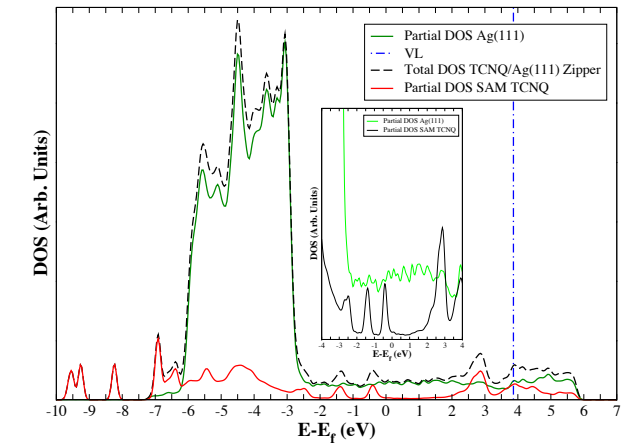

(a) PDOS TCNQ/Ag(111) Zipper phase

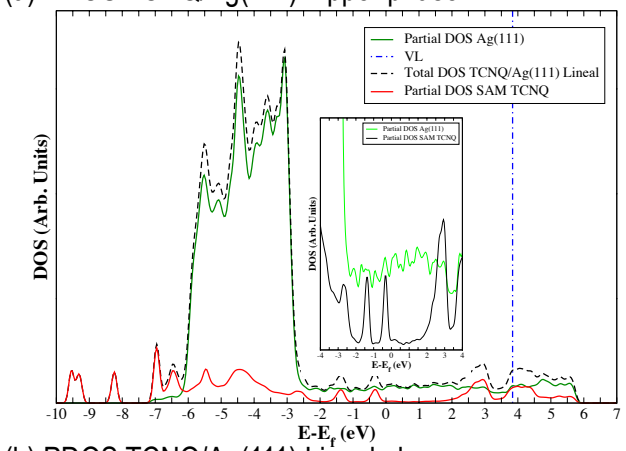

(b) PDOS TCNQ/Ag(111) Lineal phase

Figure 5.10: Partial Density of States, in Arbitrary units, for (a) TCNQ/Ag(111) Zipper phase and (b) TCNQ/Ag(111) Lineal phase, as a function of the energy, E-E_f in eV. PDOS for the Ag substrate and the TCNQ (SAM) are shown in solid green and red lines, respectively; the total DOS and the vacuum level are shown in black dotted and blue dotted lines, respectively. Each graph shows an insight of the PDOS in the energy range of -4, +4 eV, where the PDOS of TCNQ SAM and Ag surface have been depicted in black and light green solid lines, respectively.

The computed work function for the bare Ag(111) surface is 4.54 eV, in good agreement with experimental results(ϕ = 4.46 eV)[96]. The work function of the metal surface increases upon adsorption of the self-assembled organic layer, being 4.98 eV

for the Zipper phase and 4.95 eV for the Lineal phase.
The Integer Charge Transfer model (ICT)[97] describes interfaces that are characterized by a negligible hybridization of the π-electronic molecular orbitals and substrate wavefunctions. In this model, the energy of a negative integer charge transfer state, E_{ICT-}, is defined as the energy gained when one electron is added to the molecule producing a fully relaxed state (both geometrical and electronic relaxations are included as well as the screening from the substrate). Figure 5.11 illustrates the case where $\phi_{SUB} < E_{ICT-}$, that is, the work function of the substrate is smaller than the energy of the negative integer charge state of the π-conjugated organic material. When bringing the organic material in contact with the substrate, electrons flow from the substrate to the organic material at the interface. As this flows continues, the organic molecules (i.e. TCNQ) become more negatively charged, and the substrate becomes more positively charged, creating a potential (dipole) at the interface that up-shifts the vacuum level. The potential continues to grow until equilibrium is reached, where ϕ_{SUB} together with the potential energy Δ at the interface is equal to E_{ICT-}. At this point no energy is gained by transferring electrons to the molecules. With this model, we easily explain the increase of the work function of Ag(111) upon adsorption of TCNQ.

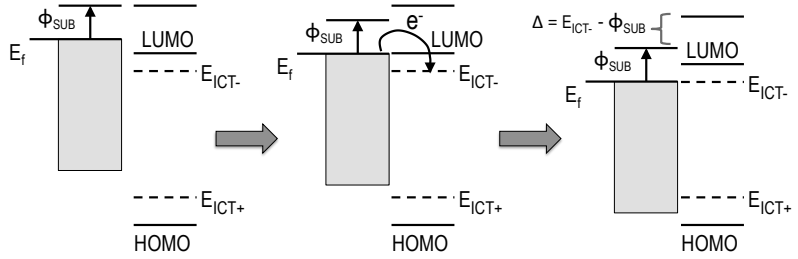

Figure 5.11: Schematic illustration of the evolution of the energy-level alignment when a π-conjugated organic molecule is adsorbed on a substrate and $\phi_{SUB} < E_{ICT-}$.

5.4 TTF/Ag(111)

In this section, we present the features of a SAM of tetrathiofulvalene (TTF) adsorbed

on a Ag(111) surface. This heterocyclic compound is widely used as an electron donor in the development of molecular electronics. In the adsorption on metal surface, for instance on a Cu(100) surface[98], the formation of self-assembled chains of TTF was observed; the TTF molecules were tilted along the chain interacting between them by means of vdW dispersion forces. Adsorption of a single molecule of TTF has also been studied for other metal surfaces as Au(111), Ag(111) and Cu(111), from a theoretical point of view (DFT)[99]. Hofmann et al.[99] encouraged using TTF as a way to reduce the metal work function.
Figure 5.12 shows the molecular structure of TTF: it is related to the hydrocarbon fulvalene $(C_5H_4)_2$ by the replacement of four CH groups with sulfur atoms.

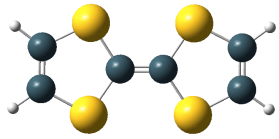

Figure 5.12: TTF molecule in the gas phase. Yellow, grey and white spheres represent sulphur, carbon and hydrogen atoms, respectively.

5.4.1 Experimental structure (STM) *vs.* Theoretical models for TTF/Ag(111)

Figures 5.13 (a) and (b) show the experimental STM images for the SAM of TTF on Ag(111) when the sample is annealed at 35º and at 53º. We observe that different temperatures give rise to different rearrangement of the molecules on the surface.

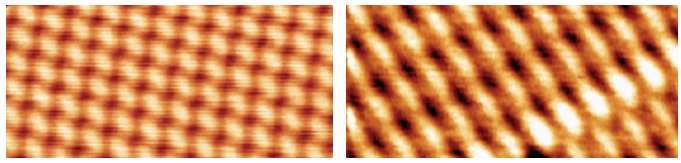

(a) TTF/Ag(111) Annealed at 35º (b) TTF/Ag(111) Annealed at 53º

Figure 5.13: (a) TTF/Ag(111) annealed at 35º, molecules are rearranged forming some kind of diamond structures. (b) TTF/Ag(111) annealed at 53º, molecules show a rectangular order. (Obtained by the experimental group at the IMDEA-Nanoscience Institute).

Before going into the details about the experimentally measured unit cells and how to represent them by a theoretical model, we have studied an isolated TTF molecule on the Ag(111) surface. Figure 5.14 shows a scan in the z axes (normal to the surface plane), of a flat TTF molecule interacting with the Ag surface (i.e. no optimizations of the molecule, neither the surface, were performed during the scan). This procedure is analogous to that followed for TCNQ/Ag(111). The main goal of this scan is to explore the potential energy surface of the metallic substrate with a TTF molecule adsorbed on it at different distances. This calculation will give us a first idea of the most stable adsorption sites on the surface. At sight of the obtained results, the most stable adsorption site is the top high symmetry site of the Ag surface. This means that the central C=C bond of the TTF molecule is placed on top of a Ag atom, while the four sulphur atoms lye just above some other four silver atoms; thus this position maximizes the contact between all the atoms of the molecule with silver atoms of the surface.

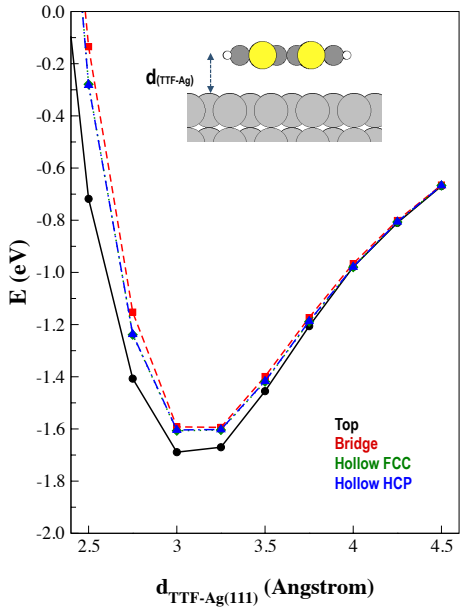

Figure 5.14: Scan in the z axes for a single TTF molecule (in a flat configuration) on the four high symmetry adsorption sites of the Ag(111) surface.

As we proceeded with the isolated TCNQ molecule adsorbed on the Ag(111) surface, we have performed an optimization of the most stable adsorption site configuration.

Thus, for the top site the TTF molecule presents an adsorption energy of -1.87 eV and its optimized geometry reveals a flatter configuration compared to the isolated adsorbed TCNQ: the carbons at the edges of the molecule, the carbon atoms at the center and the sulphur atoms are at 3.05 Å, 3.14 Å and 2.96 Å, respectively. Figure 5.15 shows the optimized geometry for the isolated TTF molecule adsorbed on a top site of the Ag(111) surface.

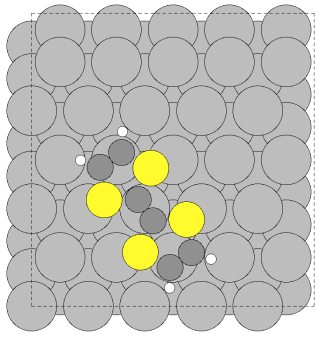

Figure 5.15: TTF/Ag(111) adsorbed on a top position.

As can been seen in the STM images, molecules on the TTF/Ag(111) 35^{o} model have a "banana" shape. Such asymmetry could stem from a slight tilt of the molecule with respect to the surface plane. This kind of tilt has been previously proposed by other groups for TTF adsorbed on Au(111)[100]; On main difference is that, in our case, the asymmetry observed is much bigger than the one observed by them. On the other hand, for the TTF/Ag 53^{o} model, experimentalists observed molecular islands with a rectangular order. They attribute this aspect to islands with the long axis of the TTF molecules oriented along one of the high symmetry directions of the Ag(111) surface.
After considering the orientation of the molecules on the Ag surface and studying the experimental lengths for the unit cells, we arrive to the following two theoretical models for TTF/Ag(111) for simulating the patterns observed after annealing at 35^{o} and at 53^{o} (figures 5.16 and 5.17). As for the TCNQ/Ag(111) patterns, the sizes of the theoretical unit cells for TTF/Ag(111) fit perfectly the sizes of the experimental unit cells.

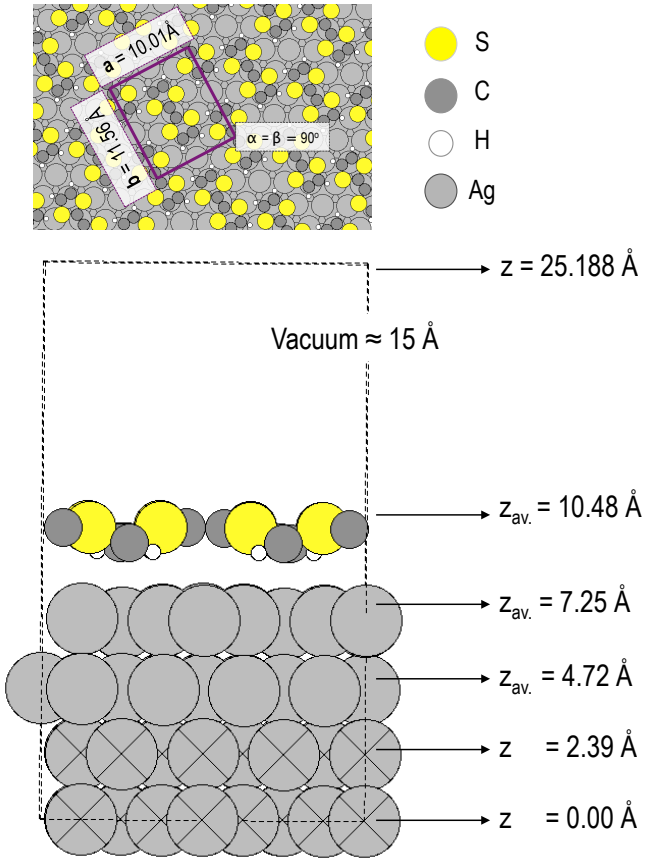

Figure 5.16: Top and side views of the TTF/Ag(111) annealed at 35°. In the top view the unit cell has been delimited by purple solid lines and the axes (a and b) length is shown, as well as the α and β angles of the unit cell. In the side view the average location of each Ag layer is shown. Silver atoms that are crossed out are those that are not relax during the optimization. The unit cell contains 64 Ag Atoms.

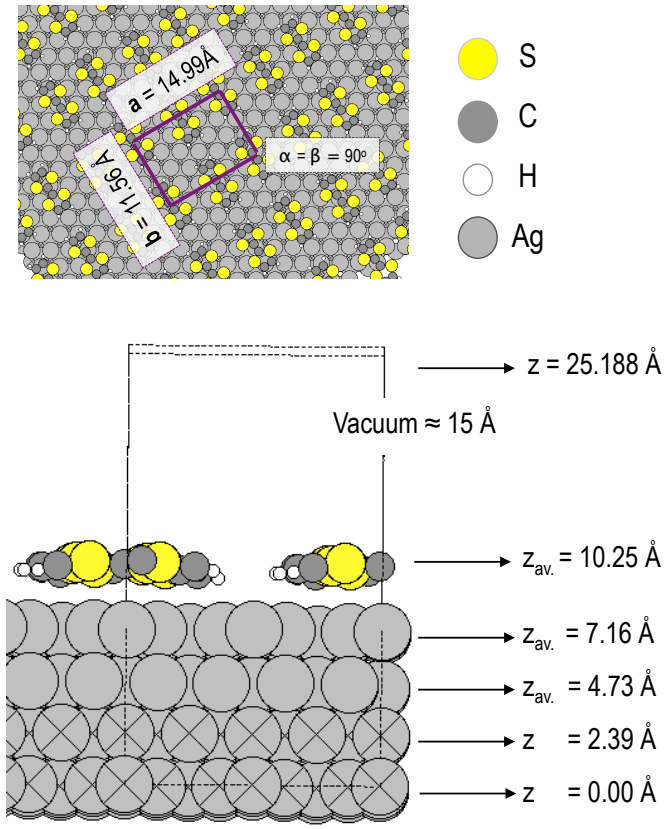

Figure 5.17: Top and side views of the TTF/Ag(111) annealed at 53º. In the top view the unit cell has been delimited by purple solid lines and the axes (a and b) length is shown, as well as the α and β angles of the unit cell. In the side view the average location of each Ag layer is shown. Silver atoms that are crossed out are those that are not relax during the optimization. The unit cell contains 96 Ag Atoms.

5.4.2 Structure and adsorption properties of TTF/Ag(111)

Figures 5.16 and 5.17 show the TTF SAM adsorbed on the Ag(111) surface for the 35º and the 53º models, respectively. In the 35º model, each unit cell contains two

molecules (i.e. one TTF in the center of the cell and another one on the edges); for the 53° model two molecules constitute as well the unit cell, except that, while one of them is at the edges, the other one is on the corner of the unit cell. In both models, TTF molecules are always oriented following one of the high symmetry axes of the Ag(111) surface, agreeing the obtained results for the most stable structure of an isolated TTF molecule adsorbed on Ag(111).
Adsorption energies per molecule were computed as:

$$E_{Ad} = \frac{E_{TTF/Ag(111)} - [E_{Ag} + (n * E_{TTF\ "flat"})]}{n} \quad (5.2)$$

where $E_{TTF/Ag(111)}$ is the energy of the complete adsorbed system, E_{Ag} is the energy of the bare metal surface, $E_{TTF\ "flat"}$ is the energy of one TTF molecule in the gas phase and n is the number of TTF molecules on the unit cell. Thus, negative values for E_{Ad} mean adsorbed systems.
Adsorption energies for the TTF/Ag(111) 35° and 53° models are -1.42 eV/molecule and -1.75 eV/molecule, respectively, which is comparable with the computed adsorption energy of the isolated TTF molecule adsorbed on Ag(111). The low adsorption energy, compared to the TCNQ/Ag(111) models, is mainly due to the presence of sulphur atoms, instead of nitrogen ones. The latter give the molecule an electron acceptor character while the formers make the TTF molecule be a donor one. Thus, it is more favorable for a metal surface to donate electrons to the molecular layer, than to take electrons from it. Moreover, the interaction of the cyano groups, $-C\equiv N\rightarrow Ag$, at the TCNQ/Ag(111) systems is stronger from the one observed between sulphur atoms and Ag ones.
The energetic difference between both models corresponds to the different assembly of the molecules: in the 53° model, TTF molecules are more distanced ones from the others and in a planar configuration, while in the 35° model molecules stay closer and their sulphur atoms are slightly tilted up respect to the molecular plane. In fact, for the 35° model the C=C end bond, the C=C central bond and the sulphur atoms stay at a distance from the surface of 3.36 Å, 3.28 Å and 2.93 Å, respectively, while for the 53° model this values are 3.00 Å, 3.15 Å and 3.00 Å, respectively, revealing the flatter configuration of the TTF molecules at the TTF/Ag(111) 53° model. However, the larger adsorption energy of the TTF/Ag(111) 53° model is mainly due to the shorter interface distance, i.e. distance between the whole SAM of TTF and the first overlayer

of Ag (see figures 5.16 and 5.17).

The general trend observed for the surface reconstruction is that the TTF molecules move the Ag atoms in a different way depending on the kind of interaction with the different atoms of the molecule; however, if we analyze molecule by molecule, we observe that, for the TTF/Ag(111) 35^{o} model sulphur atoms lift the silver atoms lying beneath them 0.07 Å, while the central C=C bond push them 0.01 Å. For the TTF/Ag(111) 53^{o} model these numbers are 0.03 Å (impact of the sulphur atoms) and 0.09 Å (impact of the C=C central bond).

Charge transfer has also been studied from a quantitative perspective, as in former cases, by means of a Bader analysis: for the TTF/Ag(111) 35^{o} model, we have observed that both TTF molecules (i.e. the TTF placed at the corner of the unit cell and the TTF on the edge) donate to the surface the small amount of 0.011 e^{-}; However, the TTF/Ag(111) 53^{o} model shows two different values: the TTF on the corner donates 0.073 e^{-} and the TTF on the edge donates 0.056 e^{-} to the Ag surface. Thus, the silver substrate is taking 0.022 e^{-} from the SAM, at the TTF/Ag(111) 35^{o} model; while it takes 0.129 e^{-} at the TTF/Ag(111) 53^{o} model in each unit cell. In any case, it is clear that the amount of charge that TTF is capable of donating to the metallic substrate is almost negligible. This absence of a proper charge transfer between the adsorbate and the substrate (or vice versa) is one of the source of the smaller adsorption energy compared to the TCNQ/Ag(111) adsorbed systems.

Charge transfer from a qualitative perspective, i.e. the induced charge density difference, is shown in figure 5.18. There is charge depletion (blue lobes) in between the TTF molecules and the surface (for both models). On the other hand, the Ag surface is polarized as a consequence of the interaction with the molecules (mainly due to dispersion forces).

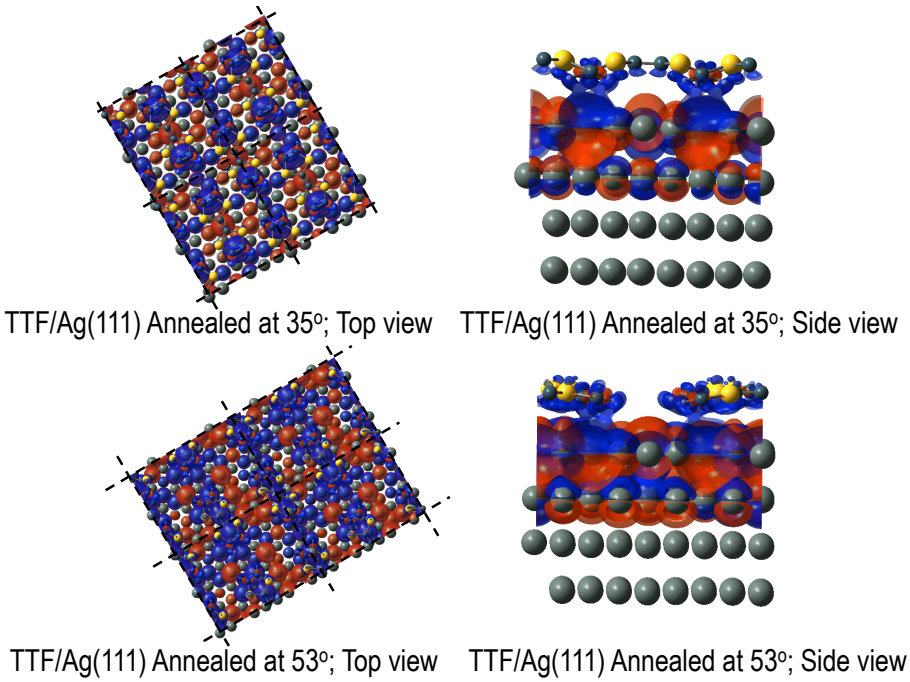

Figure 5.18: Top and side views of the induced charge density difference for the 35° and the 53° phases of TTF/Ag(111). The isovalue has been set to 0.0003 a.u; red and blue isovalues represent charge accumulation and depletion areas, respectively.

The study of the electronic structure has been envisaged by considering the PDOS and the change in the work function; the results for both models are shown in figure 5.19 (a) and (b).

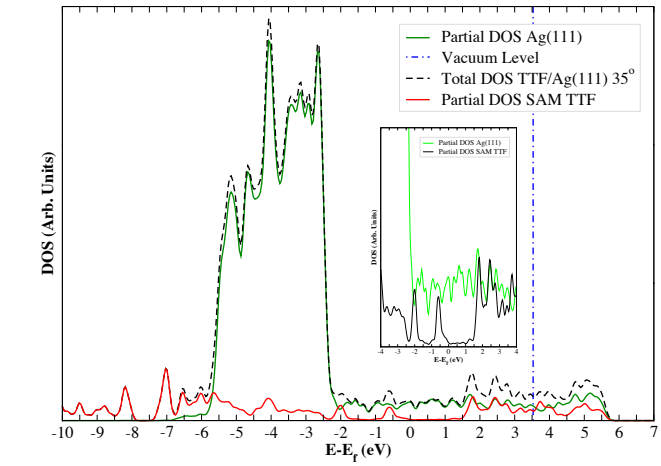

(a) PDOS TTF/Ag(111) Annealed at 35°

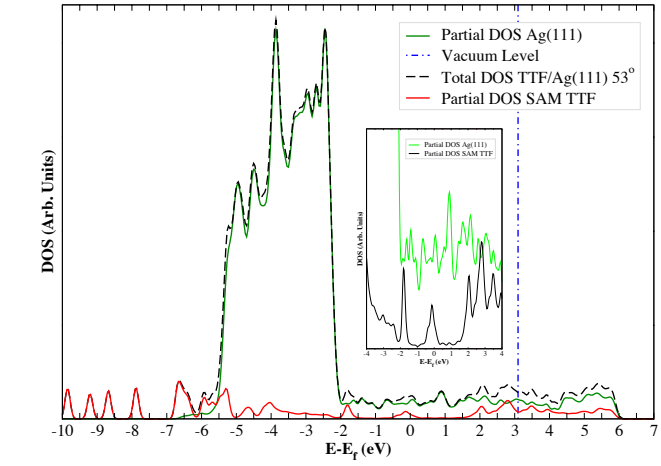

(b) PDOS TTF/Ag(111) Annealed at 53°

Figure 5.19: Partial Density of States, Arbitrary units, for (a) TTF/Ag(111) 35° model and (b) TTF/Ag(111) 53° model, as a function of the energy, E-E$_f$, in eV. PDOS for the Ag substrate and the TTF. Self-assembled monolayer (SAM) are shown in solid green and red lines, respectively; the total DOS and the vacuum level are shown in black dotted and blue dotted lines, respectively. Each graph shows an insight of the PDOS in the energy range of -4, +4 eV, where the PDOS of TTF SAM and Ag surface have been depicted in black and light green solid lines, respectively.

When the TTF SAM is adsorbed on the metallic substrate, the work function decreases from 4.54 eV, in the bare metal surface, to 3.96 eV for TTF/Ag(111) 35° and 3.75 eV for TTF/Ag(111) 53°.The workfunction of a metal depends on the bulk chemical potential and the electrostatic potential across the metal surface. Weakly physisorbed atoms or molecules at the surface will not affect the bulk chemical potential, but the electrostatic potential across the metal surface will. Thus, although the lack of covalent bonds in the adsorbed systems TTF/Ag(111), the resulting physisorbed monolayer should affect the metal surface dipole potential energy, and hence decrease the workfunction of the organic/Ag system. Recent calculations combined with UPS measurements[101], confirmed that the presence of a physisorbed species leads to a shortening of the electron-density tail at the metal surface, which reduces the metal-surface dipole potential energy, and the work function is the decreased. This is known as the "push-back effect"[97]. This effect is shown in figure 5.20, which illustrates the case where $\phi_{SUB} > E_{ICT+}$, where E_{ICT+} is the energy of a positive integer charge-transfer state, defined as the energy required to take away one electron from the molecule producing a fully relaxed state.

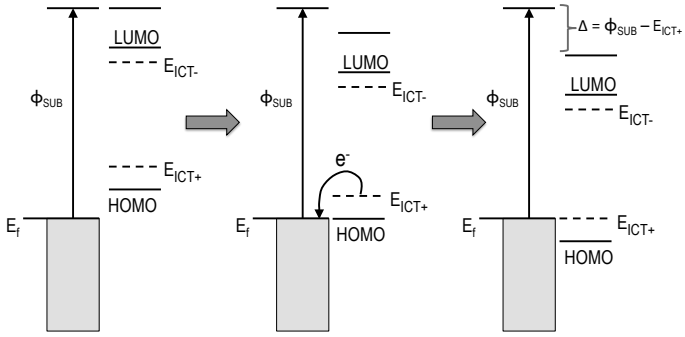

Figure 5.20: Schematic illustration of the evolution of the energy-level alignment when a π-conjugated organic molecule is adsorbed on a substrate and $\phi_{SUB} > E_{ICT+}$.

It shows the case where the work function of the substrate is larger than the energy of the positive integer charge state of the π-conjugated organic material. When bringing the organic material in contact with the substrate, electrons will spontaneously flow from the organic material into the substrate. Thus, the organic molecules become increasingly positively charged while the substrate becomes increasingly negatively charged, creating a local dipole that reduces the work function.

5.5 TCNQ+TTF/Ag(111)

Molecular charge transfer complexes are based on the interaction between two molecular species, namely donor and acceptor. The electron donor has small ionization energy, while the counterpart acceptor molecule has a large electronegativity or electron affinity. When donor and acceptor interact, the charge is redistributed among the compound. The donor species oxidizes by the loss of charge and the acceptor is reduced by the gain of it. TTF-TCNQ is the prototype of the charge transfer compound, where their HOMO and LUMO bands, respectively, contribute to the conduction. Indeed, TTF-TCNQ compound gained interest when the group of Coleman[107] reported of a large conductivity peak of the order of 5.10^4-10^5 $(\Omega\ cm)^{-1}$ at 60 K just above the transition towards the insulating state at lower temperature. This giant conductivity value is about the copper conductivity at room temperature with a hundred times less carriers per unit cell. The authors then ascribed this behavior to an incipient superconductor.
TTF-TCNQ as a crystal with 1:1 ratio, is a material comprising uniform segregated and parallel stacks with π orbitals contributing to two conduction bands in a tight binding picture[102]. In this picture, the overlap of the molecular orbitals, being largest along the stack direction and much weaker between them, makes the electron dispersion one-dimensional. The overlapping of π molecular orbitals leads to the formation of bands in the organic crystal, whose properties differ significantly from metallic bands. The density of free charge carriers is lower than in the case of a metal[103].
The metallicity of the compound is due to:

I) The formation of bands through the π overlapping of the molecular components.
II) The partial occupation of these bands at the Fermi level.

The molecular packing maximizes the overlapping integral and, consequently, the amount of charge that can be delocalized along the stacks. The free carriers are generated in both π-stacked rows due to charge transfer between TTF and TCNQ. This charge transfer is then delocalized along the **b** direction of the crystal (see figure 5.21) resulting in a one-dimensional electron dispersion as it has been described both theoretically[104,105] and experimentally[106]. In a deeper analysis, the formation of the organic crystal results from anisotropic non-covalent interactions between TTF and TCNQ. TTF-TCNQ crystallizes in a monoclinic structure built up from homologous stacks of TTF and TCNQ. The molecules overlap within the rows in a “ring double

bond" fashion along direction **b**, as shown in figure 5.21. The **a** direction of the crystal corresponds to the alternating rows of TTF cations and TCNQ anions, stabilized by hydrogen bonds[108].

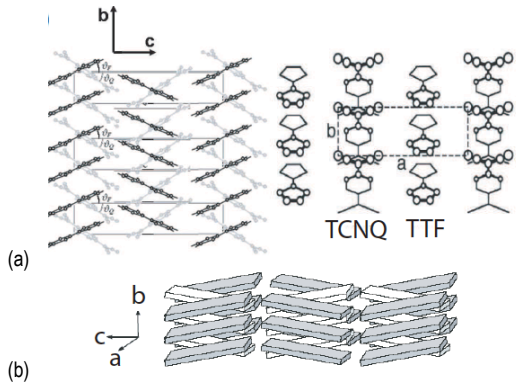

Figure 5.21: (a) Bulk structure of TTF-TCNQ and (b) 3-dimensonal scheme of the TTF-TCNQ structure (Source: T.J. Kistenmacher, T.E. Phillips and D. O. Cowan, Structural Crystallography and Crystal Chemistry 30 (3): 763-768, 1974)

The charge transfer between the donor and acceptor molecules accounts to 0.59 e^- [102,109]. This charge transfer in the crystal complex, takes us back to our study: charge transfer between the moieties of the TTF-TCNQ complex and with a metallic substrate. The transition from bulk TTF-TCNQ to thin films (SAMs) deposited on a metal surface is expected to introduce new phenomenology related to the organic-inorganic interface.

We have already seen along sections 5.3 and 5.4 the role played by each counterpart of the charge transfer complex and the properties emerging upon interaction of each molecule with the Ag(111) surface. In this section, we focus on the TCNQ+TTF/Ag(111) interface. We present possible patterns for the SAM depending on the TCNQ:TTF stoichiometry, adsorption energies, electronic structure, and the beauty of the whole discussion: the charge transfer, and how its differences with the charge transfer taking place in the crystal bulk TTF-TCNQ, makes TCNQ+TTF/Ag(111) a top of mind device for nanoelectronics.

5.5.1 Experimental structure (STM) *vs.* Theoretical models for TCNQ+TTF/Ag(111)

STM experiments found three different patterns for the charge transfer complex TCNQ+TTF adsorbed on Ag(111), depending on the stoichiometry (i.e. TCNQ:TTF ratio). Figure 5.22 shows the three possibilities here considered (2TCNQ:1TTF, 1TCNQ:1TTF and 1TCNQ:2TTF).

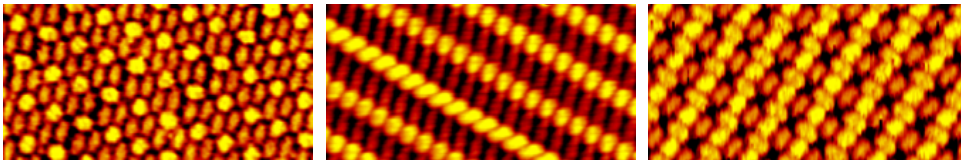

TCNQ+TTF/Ag(111) 2TCNQ:1TTF | TCNQ+TTF/Ag(111) 1TCNQ:1TTF | TCNQ+TTF/Ag(111) 1TCNQ:2TTF

Figure 5.22: Experimental STM images for TCNQ+TTF/Ag(111), for a 2:1, 1:1 and a 1:2, TCNQ:TTF ratio. Lighter molecules are TTF and darker ones, TCNQ. (Obtained by the experimental group at the IMDEA-Nanoscience Institute).

In this figure, lighter and darker yellow molecules correspond to TTF and TCNQ, respectively. For the 2TCNQ:1TTF pattern, the unit cell resembles a flower, where the corolla is a TTF molecule and the petals around it are TCNQ ones. The 1TCNQ:1TTF pattern is formed by a lineal arrange of the molecules spattered by areas where the angle between the TCNQ and TTF molecules switches from 180^{o} to 45^{o}. Finally, the 1TCNQ:2TTF pattern is formed by to well-differentiated lines of TCNQ and TTF molecules. TTF molecules arranged in an alternate manner, where molecules form 90^{o} between them; while, TCNQ molecules are all in the same layout, in lines interspersed with the TTF ones.

Figures 5.23-5.25 show the theoretical models proposed for these three patterns. This theoretical unit cells sizes resemble exactly the experimental ones.

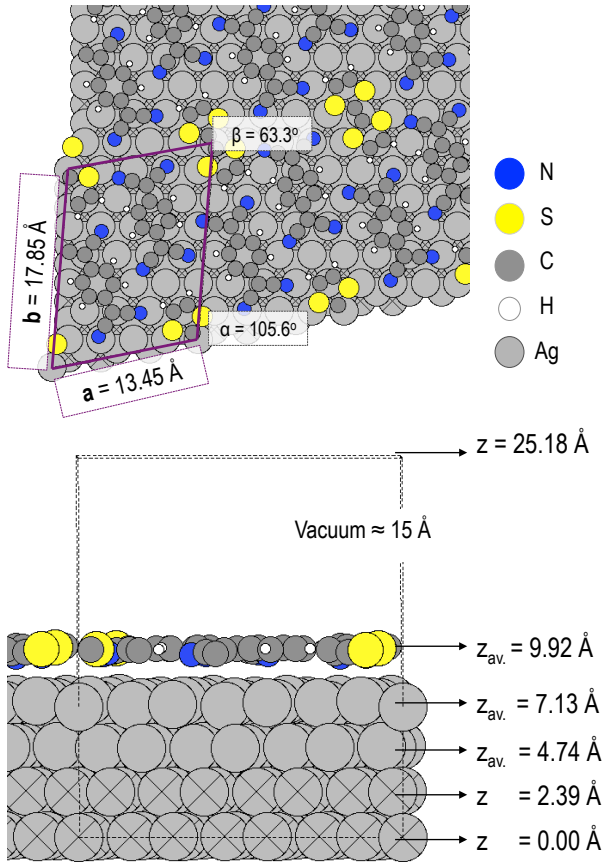

Figure 5.23: Top and side views of the 2TCNQ+1TTF/Ag(111) pattern. In the top view the unit cell has been delimited by purple solid lines and the axes (a and b) length is shown, as well as the α and β angles of the unit cell. In the side view the average location of each Ag layer is shown. Silver atoms that are crossed out are those that are not relax during the optimization. The unit cell contains 124 Ag atoms.

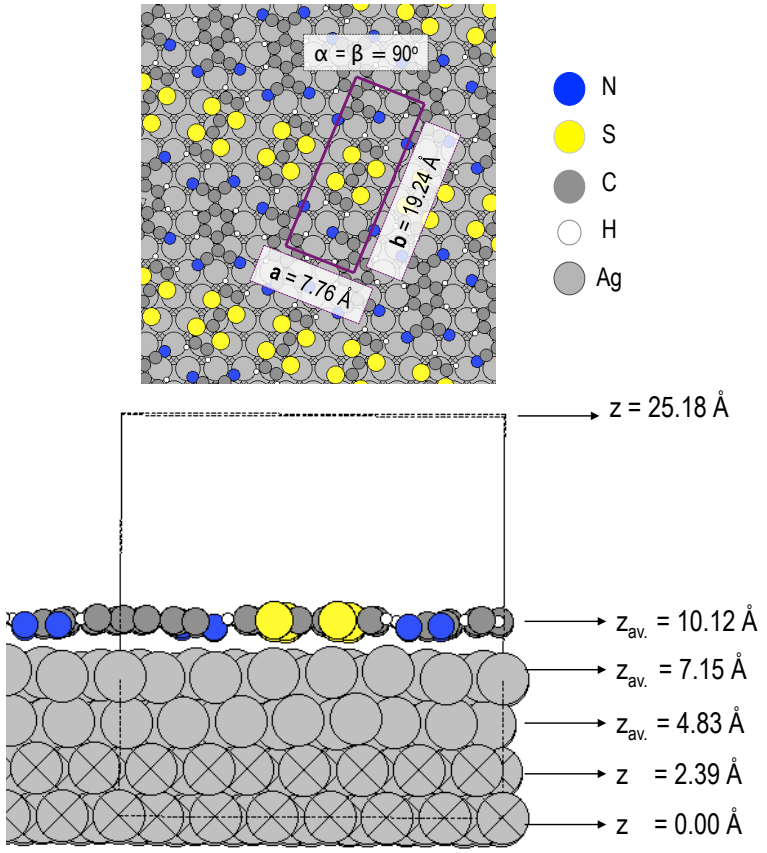

Figure 5.24: Top and side views of the 1TCNQ+1TTF/Ag(111) pattern. In the top view the unit cell has been delimited by purple solid lines and the axes (a and b) length is shown, as well as the α and β angles of the unit cell. In the side view the average location of each Ag layer is shown. Silver atoms that are crossed out are those that are not relax during the optimization. The unit cell contains 80 Ag atoms.

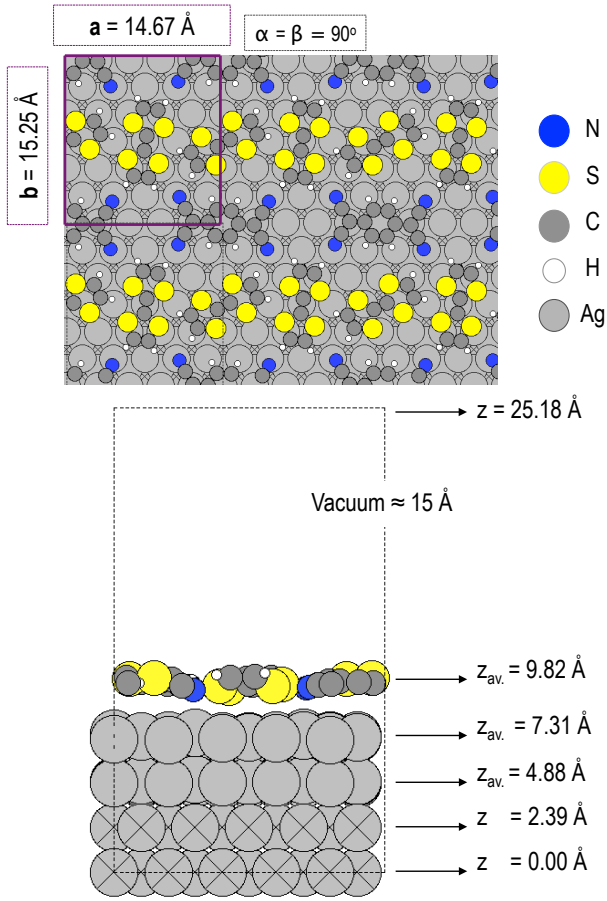

Figure 5.25: Top and side views of the 1TCNQ+2TTF/Ag(111) patterns. In the top view the unit cell has been delimited by purple solid lines and the axes (a and b) length is shown, as well as the α and β angles of the unit cell. In the side view the average location of each Ag layer is shown. Silver atoms that are crossed out are those that are not relax during the optimization. The unit cell contains 120 Ag atoms.

5.5.2 Structure and adsorption properties of TCNQ+TTF/Ag(111)

The 2TCNQ:1TTF/Ag(111) pattern contains two TCNQ molecules inside the unit cell, while one single TTF molecule is placed at the edges. One of the TCNQ molecules is on a top site, oriented following one of the high symmetry axes of the Ag(111) surface, which leads to a direct contact between the nitrogen atoms of the organic molecule and the silver ones beneath them. The average bond distance between the nitrogen atoms and the silver surface is 2.38 Å, while the carbon atoms of the central ring stand at an average distance of 2.96 Å, leading to a bent molecule. The other TCNQ molecule is adsorbed on a hollow site, slightly rotated with respect to the high symmetry axes of the Ag(111) surface. Its nitrogen atoms stand at 2.56 Å from the surface and the central carbon ring at 2.88 Å; thus, this TCNQ molecule is less folded on the surface, due to the smaller contact between the nitrogen atoms and the silver ones, which hinders the bent of the molecule. On the other hand, the TTF molecule has its sulphur atoms at 2.94 Å from the Ag surface and its central C=C bond at 3.06 Å, which makes the organic molecule to stand almost parallel to the surface plane. The average distance between the whole SAM of organic molecules and the first metallic surface layer is 2.79 Å. Furthermore, there is a slight compression of the Ag surface upon adsorption: the first layer of silver atoms, in direct contact with the SAM, compresses by 0.06 Å and the second metallic by 0.02 Å, upon adsorption.

For the 1TCNQ:1TTF/Ag(111) pattern, both molecules are adsorbed on a top site of the (111) metallic surface. The TTF molecule is oriented following one of the high symmetry axes of the silver surface, while the TCNQ one is rotated 45^{o} with respect to the former. The TCNQ molecule presents all of its nitrogen atoms in direct contact with silver ones and at an average bond distance of 2.66 Å, while the central carbon ring stands at 3.26 Å from the surface, showing a bent molecule. The TTF molecule has all sulphur atoms in direct contact with silver ones as well, and at an average distance of 2.85 Å, while the central C=C bond is placed a bit further, at 3.10 Å; however, the overall appearance of the TTF molecule is that it stands planar on the surface. Furthermore, the average adsorption distance between the SAM of organic molecules and the metallic surface is slightly larger than in the 2TCNQ:1TTF pattern, 2.97 Å; this fact leads to a smaller surface reconstruction, compared to the previous pattern. Thus, the first Ag shifts down 0.02 Å, while the second one shifts up 0.03 Å.

Finally, the 1TCNQ:2TTF pattern presents two TTF molecules per unit cell, one of them is adsorbed on the edge of the cell and the other one at the center of it. The layout

of both molecules is such that the S···H bonds between them are maximized. Thus, the TTF molecule on the edge is rotated 45° with respect to the **b** unit cell axes, while the TTF molecule in the center of the cell also rotates approximately 5°, in order to form two H···S···H bonds. This odd structure not only is the most energetically favorable, but it is also confirmed by the high-resolution STM images and the theoretical simulation of the STM images as it is shown in figure 5.26.

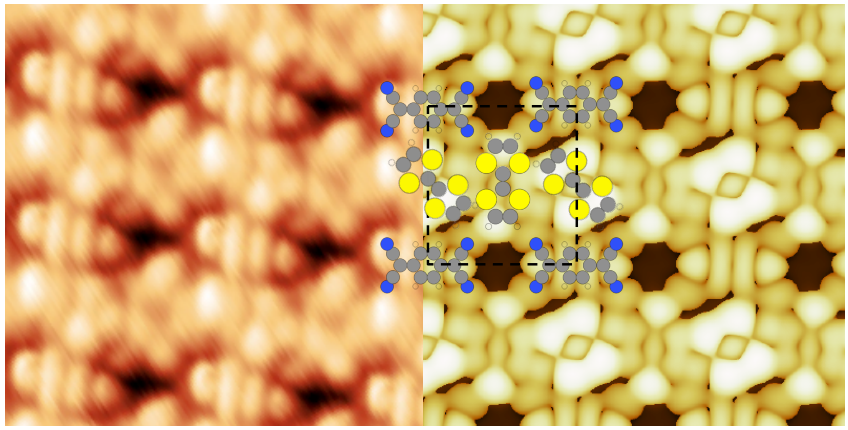

Figure 5.26: Left side, high resolution STM images, performed at -1.0 V bias voltage and at 80 K. Right side, theoretical STM image and unit cell, showing the perfect agreement between theory and experiment, confirming therefore the H···S bond between the TTF molecules.

On the other hand, the TCNQ molecule is adsorbed on the corner of the unit cell, on a top site, with all of its nitrogen atoms in direct contact with the silver ones beneath. It is, as expected, bent over the surface with its nitrogen atoms at 2.28 Å and its central carbon ring at 2.92 Å from the metal surface.

The TTF molecule adsorbed in the center of the unit cell presents an average distance between its sulphur atoms and the first Ag monolayer of 2.25 Å, while the central C=C bond is at 2.90 Å from the metallic surface. Thus, this TTF molecule is oddly bent over the surface. However, it is remarkable that its carbon atoms at the end of the molecule are slightly tilted up, at 3.00 Å, making the molecule resemble as a boat. On the other hand, the sulphur atoms of the TTF adsorbed on the edges are at an average distance from the surface of 2.08 Å and the central C=C bond at 2.94 Å, leading as well to a bent TTF molecule, though the carbon atoms at the end are also bent toward the surface and at the same distance from it as the central C=C bond, 2.94 Å. The surface

reconstruction for this pattern follows a different trend compared to the former two: the Ag surface is not pushed towards the bulk, but slightly lifted up: the first Ag monolayer by 0.13 Å and the second one by 0.09 Å. The average distance between the SAM of organic molecules and the first Ag layer is 2.51 Å, which is the closest of all three studied patterns.

The adsorption energy per molecule, for the three patterns, has been computed as shown in equation 3.10.

$$E_{Ad} = \frac{E_{nTCNQ:mTTF/Ag(111)} - [E_{Ag} + (n * E_{TCNQ\ "flat"} + m * E_{TTF\ "flat"})]}{(n+m)} \quad (3.10)$$

where $E_{nTCNQ:mTTF/Ag(111)}$ is the energy of the complete adsorbed system, E_{Ag} is the energy of the bulk Ag, $E_{TCNQ\ "flat"}$ and $E_{TTF\ "flat"}$ are the energy of the TCNQ and the TTF molecules in gas phase (where they acquire a planar configuration), respectively, and n and m are the number of TCNQ and TTF molecules per unit cell, respectively. Please note that this way to define E_{Ad} includes the interaction of the organic layer with the metal and the interaction among molecules in the organic layer. Adsorption energies for the 2TCNQ:1TTF, 1TCNQ:1TTF and the 1TCNQ:2TTF patterns are -3.05, -2.27 and -2.49 eV/molecule, respectively. Thus, a significant decrease is observed when we move from the 2TCNQ:1TTF pattern to the 1TCNQ:1TTF one, due to the lack of one TCNQ molecule, which enhances the adsorption energy thanks to its nitrogen atoms and the covalent N-Ag bonds. However, some of this adsorption energy is recovered when we move from the 1TCNQ:1TTF pattern to the 1TCNQ:2TTF one. Though there is still just one TCNQ molecule per unit cell, the presence of two TTF molecules, the odd layout of the formers and the interaction between them (i.e. H···S bonds) enhanced again the adsorption energy.

At sight of all the former results on the equilibrium geometry features for the TCNQ+TTF/Ag(111) systems, several questions may come to our minds: Why do the TCNQ and TTF molecules rearrange always in a 1:1 pattern for the crystal bulk? Why do they present several patterns and stoichiometry when a metallic substrate as Ag(111) is beneath them? First of all, we must remember that in the crystal bulk the only interaction is that taking place between the molecules themselves (hydrogen bonds, π-interactions, etc.). Thus, molecules rearrange in such a way that they favor those kinds of interactions. Furthermore, several layers of molecules must be achieved in order to build up a 3-D material, and that kind of structure can only be made by a

linear arrangement of the two molecules where π stacks interactions are advantaged.
Our situation is however completely different. First of all we have different stoichiometry, which have been forced in the experiment (i.e. they dump double the volume of one substance compared to the other) and second of all we have added a metallic substrate. Taking these two aspects into account, conclusions are drawn straightforward: molecules come into the sample in different proportions finding a metallic substrate. Interactions with the silver surface predominate over the intramolecular ones; therefore, molecules will first spread over the surface, giving rise to one single monolayer, and in a second step they will interact between them, giving rise to the showy patterns we have already discussed. These patterns do not support the formation of a second monolayer, which is why they are not observed on the crystal bulk material.
Charge transfer has been computed, for all patterns, from a quantitative (Bader analysis) and a qualitative perspective (induced charge density difference). Charge transfer is in fact the most relevant process taking place at these systems. The values, depending on the pattern, vary significantly, not only referred to the total amount of charge donated from the surface to the molecules, but also the amount of charge that each TCNQ or TTF molecules are able to accept or donate, respectively.

	Work function (eV)		Charge (Δq_{Bader})			E_{ad} (eV)
	ϕ	$\Delta\phi$	Ag	TCNQ	TTF	
Ag(111)	4.543	---	---	---	---	---
TCNQ/Ag(111)	4.985	0.442	+3.46	-1.15	---	-3.39
2TCNQ:1TTF/Ag(111)	4.604	0.061	+2.20	-1.30/-1.27	+0.37	-3.05
1TCNQ:1TTF/Ag(111)	4.287	-0.256	+1.12	-1.42	+0.30	-2.27
1TCNQ:2TTF/Ag(111)	4.168	-0.375	+1.06	-1.44	+0.14/+0.24	-2.49
TTF/Ag(111)	3.757	-0.786	-0.13	---	+0.07/+0.06	-1.75

Table 5.1: Work function, ϕ in eV, change in the work function with respect to the bare metal surface, $\Delta\phi$ in eV, charge given by the Ag surface, taken by the TCNQ molecules and given by the TTF ones, Δq_{Bader} in e^-, and E_{ad} per molecule, E_{ad} in eV for the TCNQ/Ag(111) Zipper phase, the 2TCNQ:1TTF/Ag(111), 1TCNQ:1TTF/Ag(111) and the 1TCNQ:2TTF/Ag(111) patterns and the TTF/Ag(111) 53^o model, per unit cell. Negative values of Δq_{Bader} mean gain of electrons and vice versa.

Table 5.1 shows the amount of charge donated from the Ag surface to each molecule for the three TCNQ+TTF/Ag(111) systems, together with a reminder of the charge

transfer taking place at the most stable structures of TCNQ/Ag(111) and TTF/Ag(111). Values of the work function, for all the former systems, are also shown. The relation between charge transfer and changes in the work function will be discussed later on.

Our first analysis begins with the values of charge transferred from the Ag surface to the whole SAM of organic molecules, starting with a pure TCNQ SAM adsorbed on the metal and ending at the TTF/Ag(111) adsorbed system. At first glance, the amount of charge transferred from the surface significantly decreases with the amount of TCNQ molecules in SAM. The values vary from 3.46 e^- at the TCNQ/Ag(111) Zipper phase to almost no electrons at the TTF/Ag(111) 53^o model (where it seems that Ag surface is taking some charge from the TTF molecules).

If we now analyze the behavior of the molecules themselves, we observe that TCNQ's take an average of 1.20 e^- when we have pure TCNQ monolayer and when the stoichiometry of the mix is 2TCNQ:1TTF. This quantity increases when the amount of TCNQ and TTF is the same (1TCNQ:1TTF/Ag(111)) and even when the amount of TTF is greater than TCNQ per unit cell (1TCNQ:2TTF/Ag(111)). Concerning the charge donated by the TTF molecules, we saw in section 5.4.2 that it is almost zero for the TTF/Ag(111) adsorbed systems (+0.06 e^-); however, this amount of charge notably increases when TCNQ molecules start to appear to a greater or lesser extent. Thus, the charge transfer from the TTF molecules is +0.14/+0.24 e^-, +0.30 e^- and +0.37 e^- in the 1TCNQ:2TTF, 1TCNQ:1TTF and in the 2TCNQ:1TTF patterns, respectively. Therefore, the presence of the TCNQ molecules is forcing the TTF ones to donate them charge, and this transfer of electrons is being mediated by the Ag surface. This is an exciting and new finding, which has not been observed previously, and that implies that, when TCNQ and TTF molecules are adsorbed on Ag forming SAMs, the charge transfer is much higher than when it is forming the crystal bulk structure. In fact, previous studies have seen a total amount of charge transferred of +0.59 e^- [110] and +0.53/+0.56 e^- [111] for the TCNQ+TTF single crystals and our studies show a total amount of charge of ≈1.2 e^-, which is twice the previous quantity.

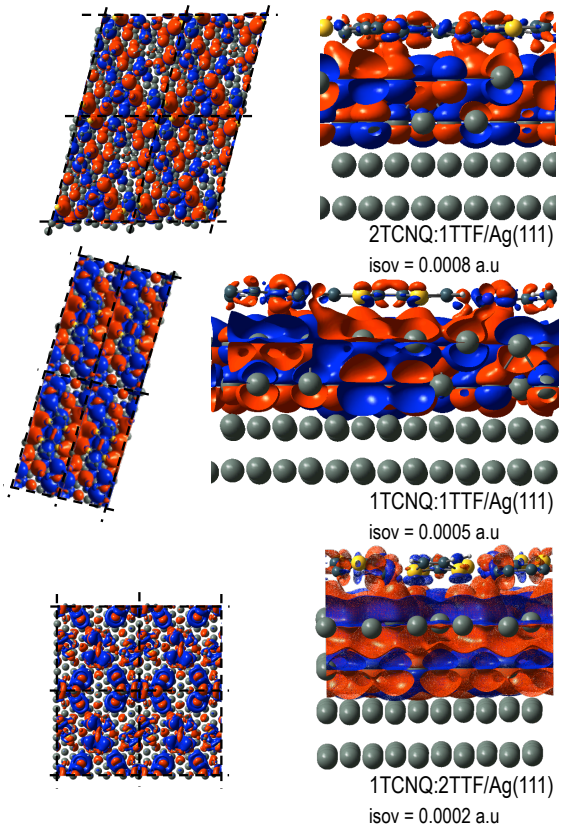

Figure 5.27: Induced charge density difference for 2TCNQ:1TTF/Ag(111), 1TCNQ:1TTF/Ag(111) and 1TCNQ:1TTF/Ag(111). Red and blue lobes represent charge accumulation and depletion, respectively. Different isovalues (indicated for each pattern, in the figure) have been used in order to properly visualize the charge for each model.

Induced charge density difference for the three studied patterns is shown in figure 5.27 from top and side views. These images show charge accumulation in between the nitrogen atoms of the TCNQ molecules and the silver atoms lying beneath, as well as underneath the TTF molecules. These red lobes are accompanied together with blue lobes right below them, which indicate charge depletion. This interweaved blue and red lobes show polarization of the interface and the involvement of the Ag surface in the charge transfer process.

The electronic structure has been studied through the Partial DOS and the change in the

work function upon adsorption of the SAM; the results for both can be seen in figure 5.28 and table 5.1, respectively.

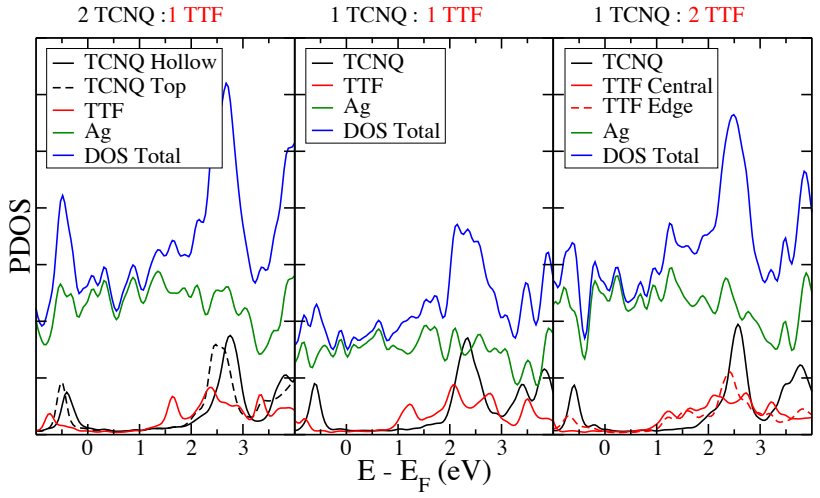

Figure 5.28: Partial density of States (Arbitrary Units) as a function of the energy, in eV, for the 2TCNQ:1TTF/Ag(111), 1TCNQ:1TTF/Ag(111) and the 1TCNQ:2TTF/Ag(111) systems. TCNQ and TTF molecules are shown in black and red solid and dotted lines, respectively. The metal surface is shown in solid green and the complete adsorbed system is depicted in blue solid lines.

Table 5.1 shows how the work function increases when a pure TCNQ SAM is adsorbed on the Ag substrate, compared to the bare metal surface. There is also an increase of the work function, though smaller, when the SAM is 2TCNQ:1TTF. However, the work function of the adsorbed system decreases whenever the proportion of TTF is larger or equal to the TCNQ one. In fact, the variation of the work function is related to the charge transferred between the SAM and the metallic substrate due to the dipole formation in the interface. Thus, for TCNQ/Ag(111), where the charge donated from the substrate to the SAM is maximum, the increase in the work function of the adsorbed system compared to the bare metal surface is the largest. As more TTF molecules are present in the organic layer, the work function starts to decrease; already for the 1TCNQ:1TTF/Ag(111) system is smaller than in the Ag(111) bare metal surface. We find the largest decrease of the work function at the TTF/Ag(111) system, where there is no charge transfer from the metallic substrate to the SAM. The PDOS depicted in figure 5.28 show the frontier orbitals of the TCNQ and TTF molecules

adsorbed on the Ag surface. For the 2TCNQ:1TTF pattern, two well differentiated LUMO's and HOMO's are observed around 2.5 and -0.5 eV, respectively; being the orbitals of the TCNQ on top slightly more stabilized than those of the TCNQ on the hollow site. The HOMO and LUMO for the TTF molecule are slightly left shifted with respect to the TCNQ ones.

For the 1TCNQ:1TTF pattern, we find a similar situation, i.e. the LUMO and HOMO orbitals of the TCNQ molecule appear at approximately 2.5 and -0.5 eV, respectively, while the HOMO and LUMO orbitals of the TTF, which are less pointed and more broadened, are stabilized with respect to the TCNQ one. Finally, for the 1TCNQ:2TTF PDOS, we find the same behavior for the TCNQ frontier orbitals, while for the TTF ones we observe now the differences between the two TTF molecules present at the unit cell of the SAM.

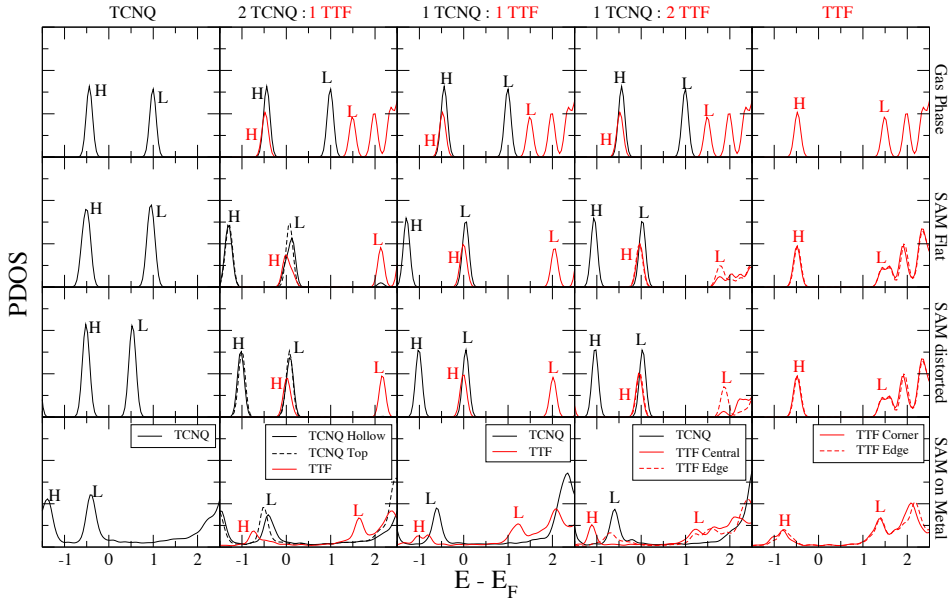

Figure 5.29: PDOS for TCNQ/Ag(111), 2TCNQ:1TTF/Ag(111), 1TCNQ:1TTF/Ag(111), 1TCNQ:2TTF/Ag(111) and TTF/Ag(111) systems. Columns of the matrix indicate the five different systems; rows show isolated molecules, SAM distort (molecules have the same adsorption geometry as in the complete adsorbed system) and SAM on metal (complete adsorbed system, i.e. including the metallic substrate). TCNQ molecules are represented by solid and dotted black lines, while TTF molecules are in solid and dotted red lines. H and L designate the HOMO and LUMO orbitals, respectively.

We have performed a deeper analysis of the PDOS by comparing all systems considered in this chapter, i.e. TCNQ/Ag(111), TCNQ+TTF/Ag(111) and TTF/Ag(111). We also compare it with the SAM in gas phase, considering it distorted as it is when adsorbed on the metal surface. This comparison is shown in figure 5.29, where we also include the isolated molecules in gas phase.

For pure TCNQ molecules (first column), the HOMO and LUMO orbitals appear almost at the same energy for an isolated molecule in gas phase and for the SAM in gas phase. This means that the intermolecular interactions, between the same kinds of molecules, do not stabilize the orbitals to lower energies. However, we observe a slight left shift of the LUMO at the distorted SAM in gas phase, thus the bent of the molecules stabilizes this orbital. Finally, both frontier orbitals (HOMO and LUMO) shift almost 1 eV to the left when the SAM is adsorbed on the metal substrate and the LUMO now appears below the Fermi level. This stabilization is the consequence of the charge transferred from the metal to the molecule. We also observe broadening of the peaks, associated to the interaction between the molecular orbitals with the substrate states.

For pure TTF molecules (last column), we observe a slight stabilization of the orbitals (there is not charge transfer) and broadening of the peaks due to the molecule-metal interaction.

For the mixed patterns, the picture is different: the frontier orbitals of the TCNQ molecules stabilize when they are in the SAM in gas phase together with the TTF molecules, compared to the isolated gas phase molecules; however, the HOMO and LUMO orbitals of the TTF shift to the right. In this way that the HOMO of the TTF and the LUMO of the TCNQ overlap at the Fermi level. This situation is repeated at the distorted SAM. It is the situation where 0.6 e^- are transferred from TTF to TCNQ; this is the reason why there is a destabilization of the HOMO in TTF and the stabilization of the LUMO in the TCNQ. I.e. when TTF and TCNQ are together they form an organic metal (as in the bulk material). Finally, at the adsorbed system (SAM on metal), the frontier orbitals for all molecules stabilize, though to a lesser extent for the TCNQ molecules, breaking the former overlap. I.e. the presence of the metal substrate changes drastically the electronic properties of the SAM with respect to the gas phase, in agreement with the charge transfer analysis: now most of the charge transferred to the TCNQ comes from the metal. Thus, the LUMO of TCNQ is stabilized and appears below the Fermi level, but the HOMO of the TTF remains at the same position than in the isolated molecule.

5.5.3 The Peierls transition in the TCNQ:TTF crystal bulk

In 1955, Peierls[112] showed that a 1-D metal is unstable against a periodic deformation of its lattice, with the period given by twice the Fermi wavevector ($\mathbf{k}_F$). The periodic lattice deformation is responsible for a lowering of the energies of the filled one-electron states of the conduction band, while empty states are raised in energy. The charge density of the conduction band exhibits a periodic variation with the same wave vector as the Periodic Lattice Distortion; this is called the charge-density wave (CDW). Peierls demonstrated that a linear chain of atoms is never stable for a unidimensional metal with a half-filled band (each atom containing a single electron). Distortions of this chain lead to formation of dimers and give rise to a discontinuity in the energy spectrum of electrons, i.e., to a forbidden gap. In this case, the spins of electrons in a pair are aligned antiparallel, and the lattice becomes antiferromagnetic. The gap is situated in such a way that all states below are filled, and those above, empty (see figure 5.30). Thus, there is a phase transition from the metallic state to an insulator one. In the 1970s, experimental studies revealed transitions of this kind first in unidimensional organometallic compounds, and then in quasi-2D compounds: $CuGeO_3$[113] and NaV_2O_5[114]. Later, similar properties were found in $Gd_2Ti_2O_7$[115].

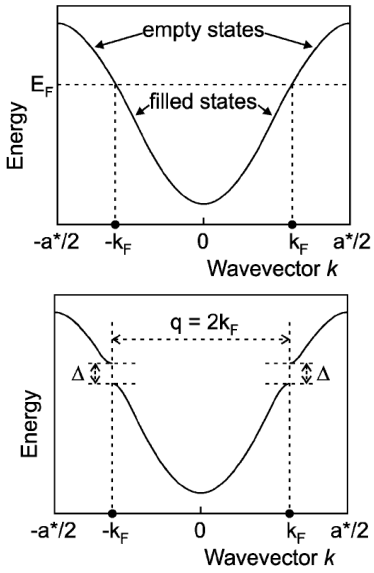

Figure 5.30: Left side, periodic crystal with $\pm a^*/2$ describing the boundary of the first Brillouin zone. Right side, 1D crystal with a periodic lattice distortion with period $\mathbf{q} = 2\mathbf{k}_F$, showing an energy gap (Δ) in the dispersion at $\mathbf{k} = \pm \mathbf{k}_F$. (Source: Sander van Smaalen, Acta Crystallographica (2005) A61, 51-61])

The results obtained made possible the determination of the general properties of substances experiencing a Peierls transition[116]:

I) A static distortion of the structure appearing as a result of the transition to the dimerized state.

II) The paramagnetic susceptibility sharply decreasing in an isotropic way.
III) A gap opening-up in the energy spectrum.

In 1973, a group from the Cavendish laboratory in Cambridge[117] and from the group of Pennsylvania[107] called attention to the giant superconductivity of TCNQ:TTF material. This molecular crystal comprises weakly coupled one-dimensional (1-D) molecular stacks and it was the first molecular crystal to show a conductivity approaching that of conventional metals at room temperature. Surprisingly, under cooling this material became an insulator rather than a superconductor. This was the first example of Peierls transition, a widespread phenomenon observed in quasi 1-D systems. In the crystal bulk material of TCNQ:TTF two Peierls transitions are observed: one corresponding to the formation of TCNQ-TCNQ dimers at 54 K[118] and another one, which takes place at lower temperature, 38 K[118], for the TTF-TTF dimerization.

However, this phase transition should not be observed when TCNQ and TTF molecules are adsorbed on the metallic substrate. The reason is that interactions between molecules and the metal substrate predominate over the intramolecular ones; thus, molecules will rather stick to the Ag substrate than to change their initial rearrangement in order to dimerized between them. For instance, the interaction energy between TCNQ molecules in a SAM following the Zipper pattern and in gas phase (i.e. flat configuration of the molecules) is -0.18 eV/molec. Moving well away from the adsorption energy of -3.39 eV/molec. That we obtained for the adsorbed system TCNQ/Ag(111) in Zipper pattern.
Since no symmetry of the periodic potential is broken due to the formation of dimers, no phase transitions of this kind would be observed. Therefore, the adsorbed system not only allows us to control the amount of charge transfer, but also enable us to avoid the Peierls transition.

5.6 Computational details for the TCNQ+TTF/Ag(111) systems

Calculations for the TCNQ/Ag(111), TTF/Ag(111) and TCNQ+TTF/Ag(111) systems were carried out using Density Functional Theory (DFT) including periodic boundary conditions (PBC) and using the Vienna Ab initio Simulation Package (VASP)[46–49]. The

exchange and correlation effects have been described using the Generalized Gradient Approximation, in particular employing the Perdew-Wang 91 functional (GGA-PW91)[50,51].The interaction of the electrons with the atoms has been taken into account within the projector augmented wave method (PAW pseudo-potentials)[52,53]. The electron density has been described employing a plane wave basis set expanded up to a kinetic energy cutoff of 400 eV.

The metal surfaces were modeled by a slab consisting of four atomic layers, separated by a vacuum space of 20 Å in the coordinate perpendicular to the surface, z. Geometries have been optimized sampling the Brillouin zone with a **Γ**–centered Monkhorst–Pack of 1x1x1 K-mesh. Final electronic energies have been computed employing the previously optimized geometries by single point energy calculations using a **Γ**–centered Monkhorst-Pack of 4x4x1 K-mesh. Both samplings of the Brillouin zone include a Methfessel–Paxton smearing of 0.2 eV. The geometries of the studied systems were optimized by relaxing all atoms of the adsorbate, TCNQ, TTF or both molecules, in the three spatial directions (xyz), and the Ag two first layers in the z direction. The layer spacing of the two lower Ag layers was taken from the optimized lattice constant parameter (a_o = 4.15 Å). All these coordinates were optimized until all forces were smaller than 0.001 eV $Å^{-1}$. The electronic self-consistent convergence was set in an energy difference of 10^{-5} eV with respect to the previous cycle.

References to chapters 3, 4 and 5

(1) Barth J. V.; Constantini G.; Kern K. *Nature* 2005, *437*, 671–679.

(2) Faraggi, M. N.; Jiang, N.; Gonzalez-Lakunza, N.; Langner, A.; Stepanow, S.; Kern, K.; Arnau, A. *J. Phys. Chem. C* 2012, *116*, 24558–24565.

(3) Fernández-Torrente, I.; Franke, K. J.; Pascual, J. I. *Phys. Rev. Lett.* 2008, *101*, 217203.

(4) Krause, B.; Dürr, A. C.; Ritley, K.; Schreiber, F.; Dosch, H.; Smilgies, D. *Phys. Rev. B* 2002, *66*, 235404.

(5) Schwalb, C. H.; Sachs, S.; Marks, M.; Schöll, A.; Reinert, F.; Umbach, E.; Höfer, U. *Phys. Rev. Lett.* 2008, *101*, 146801.

(6) Rohlfing, M.; Bredow, T. *Phys. Rev. Lett.* 2008, *101*, 266106.

(7) Kilian, L.; Hauschild, A.; Temirov, R.; Soubatch, S.; Schöll, A.; Bendounan, A.; Reinert, F.;Lee, T.-L.; Tautz, F. S.;Sokolowski, M.; Umbach, E. *Phys. Rev. Lett.* 2008, *100*, 136103.

(8) Ruiz, V. G.; Liu, W.; Zojer, E.; Scheffler, M.; Tkatchenko, A. *Phys. Rev. Lett.* 2012, *108*, 146103.

(9) Heimel G., et al. *Nat. Chem.* 2013, *5*, 187–194.

(10) Mercurio, G.; McNellis, E. R.; Martin, I.; Hagen, S.; Leyssner, F.; Soubatch, S.; Meyer, J.;Wolf, M.; Tegeder, P.; Tautz, F. S.; Reuter, K. *Phys. Rev. Lett.* 2010, *104*, 036102.

(11) Mercurio, G.; Maurer, R. J.; Liu, W.; Hagen, S.; Leyssner, F.; Tegeder, P.; Meyer, J.;Tkatchenko, A.; Soubatch, S.; Reuter, K.; Tautz, F. S. *Phys. Rev. B* 2013, *88*, 035421.

(12) Lauhon L. J.; Ho W. *J. Phys. Chem. A* 2000, *104(11)*, 2463–2467.

(13) Triguero L.; Patterson L. G. M.; Minaev B.; Agren H. *J. Chem. Phys.* 1998, *108*, 1193.

(14) Lorente N.; Hedouin M. F. G.; Palmer R. E.; Persson M. *Phys. Rev. B* 2003, *68*, 155401.

(15) Repp J.; Meyer G. *Phys. Rev. Lett.* 2005, *94*, 026803.

(16) Atodiresei N.; Cacinc V.; Lacić P.; Blügel S. *Phys. Rev. Lett.* 2009, *102*, 136809.

(17) Olsen T.; Yan J.; Mortensen J.J.; Thygesen K. S. *Phys. Rev. Lett.* 2011, *107*, 156401.

(18) Stradi D. et al. *Phys. Rev. Lett.* 2011, *106*, 186102.

(19) Grimme S. *J. Comput. Chem.* 2006, *27*, 1787–1799.

(20) Gigli G. et al. *Appl. Phys. Lett.* 2001, *78*, 1493.

(21) Kenji Toyoda, Yosuke Nakano, Yoshitada Morikawa, Kyuho Lee, Susumu Yanagisawa, Yoshitada Morikawa. *Surf. Sci.* 2009, *603*, 2912.

(22) Bader R. F. W. Atoms in Molecules: A Quantum Theory. *Oxf. Univ. Press USA* 1994.

(23) Bader R. F. W. *Chem. Rev.* 1991, *91*, 893–928.

(24) Olsson F. E.; Persson M.; Surface Science. 2003, *540*, 172–184.

(25) A.J.Mayne; G.Dujardin. Atomic and Molecular Manipulation. *Elsevier Amst. Neth.*

(26) Ma, J. C.; Dougherty, D. A. *Chem. Rev.* 1997, *97*, 1303–1324.

(27) Alkorta, I.; Rozas, I.; Elguero, J. *J. Am. Chem. Soc.* 2002, *124*, 8593–8598.

(28) Quiñonero, D.; Garau, C.; Rotger, C.; Frontera, A.; Ballester, P.; Costa, A.; Deya, P. M. *Angew. Chem. Int. Ed* 2002, *41*, 3389–3392.

(29) Garau, C.; Frontera, A.; Quiñonero, D.; Ballester, P.; Costa, A.; Deya, P. M. *Chem. Phys. Lett.* 2004, *392*, 85–89.

(30) Garau, C.; Frontera, A.; Quiñonero, D.; Ballester, P.; Costa, A.; Deya, P. M. *Chem. Phys. Lett.*

2004, *399*, 220–225.
(31) Rodriguez-Otero, J.; Cabaleiro-Lago, E. M.; Pena-Gallego, A. *Chem. Phys. Lett.* 2008, *452*.
(32) Wheeler, S. E.; Houk, K. N. *J. Am. Chem. Soc.* 2009, *131*, 3126–3127.
(33) Cubero, E.; Luque, F. J.; Orozco, M. *Proceeding Natl. Acad. Sci. USA* 1998, *95*, 5976–5980.
(34) Wheeler, S. E.; Houk, K. N. *J. Phys. Chem. A* 2010, *114*, 8658–8664.
(35) Prada, S.; Martinez, U.; Pacchioni, G. *Phys. Rev. B* 2008, *78*, 235423.
(36) Díaz-Tendero, S.; Borisov, A. G.; Gauyacq, J.-P. *Phys. Rev. B* 2011, *83*, 115453.
(37) Ploigt, H.-C.; Brun, C.; Pivetta, M.; Patthey, F. m. c.; Schneider, W.-D. *Phys. Rev. B* 2007, *76*, 195404.
(38) Cabailh, G.; Henry, C. R.; Barth, C. *New J. Phys.* 2012, *14*, 103037.
(39) Lauwaet, K.; Schouteden, K.; Janssens, E.; Van Haesendonck, C.; Lievens, P.; Trioni, M. I.;Giordano, L.; Pacchioni, G. *Phys. Rev. B* 2012, *85*, 245440.
(40) Avouris P. *Acc. Chem. Res.* 1995, *18*, 95.
(41) Ho W. *Acc. Chem. Res.* 1998, *31*, 567.
(42) Lee H.; Ho W. *Science* 1999, *286*, 1719.
(43) Bartels L.; Meyer G.; Rieder K.-H-. *Phys. Rev. Lett.* 1997, *79*, 697.
(44) Lesnard H.; Bocquet M.-L.; Lorente N. *J. Am. Chem. Soc.* 2007, *129*, 4298.
(45) Bocquet M.-L.; Lesnard H.; Lorente N. *Phys. Rev. Lett.* 2006, *96*, 096101.
(46) Kresse, G.; Furthmühller. *J. Phys. Rev. B* 1996, *54*, 11169.
(47) Kresse, G.; Furthmühller, J. *J. Comput. Mater. Sci.* 1996, *6*, 15.
(48) Kresse, G.; Hafner. *J. Phys. Rev. B* 1994, *49*, 14251–14269.
(49) Kresse, G.; Hafner, J. *J. Phys. Rev. B* 1993, *47*, 558–561.
(50) Perdew, J. P.; Chevary, J. A.; Vosko, S. H.; Jackson, K. A.; Pederson, M. R.; Singh, D. J.; Fiolhais, C. *Phys. Rev. B* 1992, *46*, 6671–6687.
(51) Perdew, J. P.; Chevary, J. A.; Vosko, S. H.; Jackson, K. A.; Pederson, M. R.; Singh, D. J.; Fiolhais, C. *Phys. Rev. B* 1993, *48*, 4978.
(52) Blöchl, P. E. *Phys. Rev. B* 1994, *50*, 17953–17979.
(53) Kresse, G.; Joubert, D. *Phys. Rev. B* 1999, *59*, 1758–1775.
(54) Soler J. M.; Artacho E.; Gale J. D.; García A.; Junquera J.; Ordejón P.; Sánchez-Portal D. *J. Phys. Condens. Matter* 2002, *14*, 2745.
(55) Perdew, J. P.; Burke K.; Ernzerhof M. *Phys. Rev. Lett.* 1996, *77*, 3865–3868.
(56) Perdew, J. P.; Burke K.; Ernzerhof M. *Phys. Rev. Lett.* 1997, *78*, 1396.
(57) Bamford C.H.; Eastmond G. C. Acrylonitrile Polymers. *Encycl. Polym. Sci. Technol. Wiley-Intersci.* 1964, *1*, 374–425.
(58) Olabisi O. *Handb. Thermoplast.*
(59) Irwin M. D.; Hains A. W.; Chang R. P. H. *Proceeding Natl. Acad. Sci. USA* 2008, *105*, 2783–2787.
(60) Kim H.; Horwitz J. S.; Kim W. H.; Mäkinen A. J.; Kafafi Z. H.; Chrisey D. B. *Thin Solid Films* 2002, *420*, 539–543.
(61) Geskin V. M.; Lazzaroni R.; Mertens M.; Jérôme R. *J. Chem. Phys.* 1996, *105*, 3278.
(62) Fredriksson C.; Lazzaroni R.; Brédas J. L.; Mertens M.; Jérôme R. *Chem. Phys. Lett. 258*, 356–362.
(63) Bureau C.; Defranceschi M.; Delhalle J.; Deniau G.; Tanguy J.; Lecayon G. *Surf. Sci.* 1994, *311*,

349–359.
(64) Schüle J.; Panas I.; Siegbahn P.; Wahlgren U. *Chem. Phys. Lett.* 1985, *83*, 2293.
(65) Morse M. D.; Geusic M. E.; Heath J. R. Smalley R. E. *J. Chem. Phys.* 1985, *83*, 2293.
(66) Díaz-Tendero S.; Alcamí M.; MArtín F. *Phys. Chem. Chem. Phys.* 2013, *15*, 1288.
(67) Tornero J.; Telle H. H.; García G.; Gonzalez Ureña A. *Phys. Chem. Chem. Phys.* 2011, *13*, 8475–8484.
(68) Zhi-Xin Hu; Haiping Lan; Wei Ji. *Sci. Rep.* 2014, *4*, 5036.
(69) Henkelman G.; Uberuaga B.P.; Jónsson H. *J. Chem. Phys.* 2000, *113*, 9901.
(70) Bussi, G; Donadio, D; Parrinello. *J. Chem. Phys.* 2007, *126*, 014101.
(71) Berendsen H. J. C.; Postma J. P. M.; van Gunsteren W. F.; DiNola A.; Haak J. R. *J. Chem. Phys.* 1984, *81*, 3684.
(72) Tang W.; Sanville E.; Henkelman G. *J. Phys. Condens. Matter* 2009, *21*, 084204.
(73) Sanville E.; Kenny S.D.; Smith R.; Henkelman G. *J. Comput. Chem.* 2007, *28*, 899.
(74) Henkelman G.; Arnaldsson A.; Jonsson H. *Comput. Mater. Sci.* 2006, *36*, 354.
(75) Krack M. *Theor. Chem. Acc.* 2005, *114*, 145–152.
(76) VandeVondele, J; Krack, M; Mohamed, F; Parrinello, M; Chassaing, T; Hutter, J. *J. Comput. Phys. Commun.* 2005, *167*, 103–128.
(77) VandeVondele, J; Hutter, J. *J. Chem. Phys.* 2003, *118*, 4365–4369.
(78) Hartwigsen, C; Goedecker, S; Hutter, J. *Phys. Rev. B* 1998, *58*, 3641–3662.
(79) Lippert, G; Hutter, J; Parrinello, M. *Mol. Phys.* 1997, *92*, 477–487.
(80) Goedecker, S; Teter, M; Hutter, J. *Phys. Rev. B* 1996, *54*, 1703–1710.
(81) Lowe J. C.; Estroff L. A.; Kriebel K.; Nuzzo R. G.; Whitesides G. M. *Chem. Rev.* 2005, *105*, 1103–1169.
(82) Bain C.D.; Troughton E. B.; TAo Y. T.; Evall J.; Whitesides G. M.; Nuzzo R. G. *J. Am. Chem. Soc.* 1989, *111*, 321–335.
(83) Hartgerink J. D.; Benieash E.; Stupp S. I. *Science* 2001, *294*, 1648–1688.
(84) Hartgerink J. D.; Benieash E.; Stupp S. I. *Proceeding Natl. Acad. Sci. USA* 2002, *99*, 5133–5138.
(85) Mirkin C. A.; Letsinger R. L.; Mucic R.C. Storhoff J. J. *Nature* 1996, *382*, 607–609.
(86) Yan M.; Zhang H. T.; Widjaja E. J.; CHang R.P.H. *J. Appl. Phys.* 2003, *94*, 5240–5246.
(87) Grzybowski B.A.; Wiles J.A.; Whitesides G.M. *Phys. Rev. Lett.* 2003, *90*, 083903.
(88) Grzybowski B.A.; Stones H.A.; Whitesides G.M. *Nature* 2000, *405*, 1033–1036.
(89) Sowaya M.R.; Guo S.Y.; Tabor S.; Richardson C.C.; Ellenberg T. *Cell* 1999, *99*, 167–177.
(90) Binning G.; Rohrer H.; Gerber Ch.; Weibel E. *Appl. Phys. Lett.* 1982, *40*, 178–180.
(91) Binning G.; Rohrer H.; Gerber Ch.; Weibel E. *Phys. Rev. Lett.* 1982, *49*, 57–61.
(92) Martínez J.I.; Abad E.; Flores F.; Ortega J.; *Phys. Status Solidi B* 2011, *248*, 2044–2049.
(93) Kaim W.; Moscherosch M. *Coord. Chem. Rev.* 1994, *129*, 157.
(94) Kahn A.; Koch N.; Gao W.Y. *J. Polym. Sci. Part B Polym. Phys.* 2003, *41*, 2529.
(95) Tzu-Chun Tseng et al. *Nat. Chem.* 2010, *2*, 374.
(96) Chelvayohan M.; Mee C.H.B. *J. Phys. C Solid State Phys.* 1982, *15*, 2305.
(97) Braun S.; Salaneck W.R.; Fahlman M. *Adv. Matter* 2009, *21*, 1450–1472.
(98) Wang Y. et al. *J. Phys. Chem. A* 2011, *115*, 13082–13087.
(99) Hofmann O.T.; Rangger G.; Zojer E. *J. Phys. Chem. C* 2008, *112*, 20357.

(100) Umbach T.R.; Fernández-Torrente I.; Ladenthin J.N.; Pascual J.I.; Franke K.J. *J. Phys. Condens. Matter* 2012, *24*, 354003.
(101) Crispin X.; Geskin V. M.; Crispin A.; Cornil J.; Lazzaroni R.; Salaneck W.R.; Brédas J.L. *J. Am. Chem. Soc.* 2002, *124*, 8132.
(102) Jérome D. *Chem. Rev.* 2004, *104*, 5565.
(103) Toyota N.; Lang M.; Müller J. *Low Dimens. Mol. Met. Springer* 2007.
(104) Fraxedas J.; Lee Y. J.; Jiménez I.; Gago R.; Nieminen R.M.; Ordejón P.; Canadelli E. *Phys. Rev. B* 2003, *68*, 195115.
(105) Ishibashi S.; Kohyama M.; *Phys. Rev. B* 2000, *62*, 7839–7844.
(106) Sing M.; Schwingenschlögl U.; Claessen R.; Blaha P.; Carmelo J.M.P. Martelo L.M.; Sacramento P.D.; Dressel M.; Jacobsen C.S. *Phys. Rev. B* 2003, *68*, 125111.
(107) Coleman L. *Solid State Commun.* 1973, *12*, 1125.
(108) Ara N.; Kawazu A.; Shigekawa H.; Yase K.; Yoshimura M. *Appl. Phys. Lett.* 1995, *66*, 3278.
(109) Khanna S.K.; Pouget J.P.; Comes R.; Garito A. F.; Heeger A.J. *Phys. Rev. B* 1977, *16*, 1468–1479.
(110) Comes R.; Shapiro S.M.; Shirane G.; Garito A.F.; Heeger J. *Phys. Rev. Lett.* 1975, *35*, 1518.
(111) Denoyer F.; Comes F.; Garito A.F.; Heeger J. *Phys. Rev. Lett.* 1975, *35*, 445.
(112) Peierls R.E. *Quantum Theory Solids Oxf. Clarendon Press* 1955.
(113) Hase M.; Terasaki I.; Uchinokura K.; *Phys. Rev. Lett.* 1993, *70*, 3651.
(114) Isode M.; Ueda Y.; *J. Phys. Soc. Jpn.* 1996, *65*, 1178.
(115) Ramirez A.P.; Shastry B.S.; Hayashi A. et al. *Phys. Rev. Lett.* 2002, *89*, 067202.
(116) A.N.Vasilyev Priroda. *J. Phys. Conf. Ser.* 2009, *150*, 042207.
(117) Anderson P.W.; Lee P.A. *Solid State Commun.* 1973, *13*, 595.
(118) Wang Z.Z.; Girard J.C.; Pasquier C.; Jérome D.; Bechgaard K. *Phys. Rev. B* 2003, *67*, 121401.

Chapter 6

Summary and Conclusions

At the beginning of this manuscript we have exposed the features of organic devices possessing electronic conductivity. We have divided them in three main groups, depending on their molecular characteristics and their different behavior against a metal surface: (I) Compounds with a number of delocalized electrons, (II) Intermolecular addition compounds and (III) Electron donor and acceptor molecules. Each group behaves in an entirely different way, but all of them share the promising fact of bringing new organic materials that may be useful in the nanoelectronics field.

6.1 Compounds with delocalized electrons: Benzene adsorbed on Cu(100) and the effect of an ultrathin insulating film

We have taken the first group as a chance to study a benchmark molecule: benzene; and we have studied its adsorption properties on a widely used metal as copper. In order to be able to visualize and embrace its individual molecular properties, we have included one, two and three monolayers of NaCl, an ultrathin insulating film. The study has been based in the analysis of several properties: (i) adsorption energies and equilibrium geometries, which gave us a picture of the soft potential energy surface that these systems represent; (ii) Charge transfer from a quantitative and a qualitative point of view, which provides complementary information on the adsorption properties; (iii) and finally, we have presented a thorough analysis of the electronic

structure of the system, which allowed us to make an insight on what it is going on with the molecular orbitals, and the insulating films and metal bands when the interaction between substrate and adsorbate takes place. All the exposed results are preceded by an extensive study of the van der Waals dispersion forces and the way they must be applied to the system. It has been stressed repeatedly along this manuscript how a correct implementation of these dispersion forces is mandatory in order to properly account for these weak interactions, which prevail in most of the systems presented here. However, the presence of a metallic substrate hinders the straightforward application of any method proposed to the date. The reason lies on the screening effect of the forces inside the metallic substrate. Therefore, we have used a simple method: strictly apply van der Waals dispersion forces just to those atoms that are undergoing this weak dispersion forces, and avoid including them to those that are far from experiencing them, i.e. only the atoms in the organic molecule, the insulating film layers and the first copper layer have been treated with van der Waals.

Furthermore, including the NaCl layers has not only given us a qualitative picture of the molecular decoupling, but also a quantitative one: we have observed how the computed adsorption energies decrease as more NaCl layers are added and how the charge transfer from the substrate to the adsorbate became negligible. On the other hand, we have also presented the abilities of a Scanning Tunneling Microscope (STM) to induce chemical reactivity of single molecules. Thereby, we have simulated two copper electrodes between which we have placed a benzene molecule. An increasing voltage between the two metallic leads has been then applied. This device may resemble the effect of a tunneling current when a STM tip is placed on a C_6H_6/Cu sample. The effect of the current on the molecule has been studied through the analysis of the atomic forces on each C-H pair of atoms, showing an increasing force that might be a hint of the bond breaking, as previous works pointed out. Not only atomic forces, but also transmission as a function of the applied voltage has been studied, showing us a remarkable hybridization between the benzene HOMO and the *d* band of the copper electrodes. However, and due to the large gap between the HOMO and the LUMO orbitals of benzene, no further big changes are observed in the molecule. Anyhow, this has shown that a larger voltage than the one applied is needed in order to observe bond breaking in the molecule.

The study of the benchmark system, benzene, adsorbed on Cu(100) and NaCl/Cu(100) has pointed out:

- The importance of including van der Waals dispersion forces in order to describe interactions between organic molecules and metallic substrates and to apply them in the proper manner, i.e. not including them in the whole system, but to those atoms that are strictly interacting through weak dispersion forces.
- The different behavior in the interaction with metal substrates and metal surfaces covered with ultrathin insulating films: lowering the adsorption energy, decreasing the charge transfer and changing the work function. This points out the important role of 2D ionic materials in modulating molecule/metal substrate interactions.
- The possibility of inducing a chemical reaction through an electric current; thus, the ability of control the processes taking place on an adsorbed system at the molecular scale.

6.2 Intermolecular addition compounds: AIMD as a tool for studying the PES of acrylonitrile on Cu(100) and on NaCl/Cu(100)

In this part of the thesis we have presented the second subgroup of organic compounds with conductivity properties. These are those formed from an intramolecular addition of other smaller molecules, the so-called polymers. As a first approach we have studied the acrylonitrile monomer adsorbed on a metallic Cu(100) surface and on this surface covered with an insulating ultrathin film of NaCl.

In this study, we have not only performed a similar analysis as the one carried out for C_6H_6/n NaCl/Cu(100), but we have also presented a new computational strategy: the combination of static and dynamic simulations to explore the potential energy surface and to analyze the stability of complex systems. Thus, in the static study we have first evaluated several adsorption sites of the acrylonitrile molecule on the different surfaces considered: Cu(100) and Cu(100) covered with 1, 2 or 3 NaCl monolayers. From this point, two different configurations have been chosen for each adsorbed system: the most stable adsorption site and a second configuration that stands apart from the other one for its completely different rearrangement on the substrate. This choice enabled us to compare different properties of two well-differentiated adsorption geometries of the molecule on a same substrate: adsorption energies, equilibrium geometries, charge

transfer and electronic structure have been evaluated. In this framework, we found how adsorption energies and charge transfer from the substrate to the adsorbate are highly influenced by the presence of the insulating film: adsorption energies and charge transfer decrease as more NaCl monolayers are added to the structure.

An interesting behavior in the charge transfer for the ACN/*n* NaCl/Cu(100) systems was established: the charge accumulation depends on the position of the N atom upon adsorption (on top of a Na^+ ion or on top of a Cl^- one), since it determines the orientation of the molecule itself (upwards or towards the surface) and therefore the orientation of the molecular dipole. Depending on its direction, the ACN molecule will present charge accumulation or charge depletion in between itself and the surface. The electronic structure analysis has shown how the work function of the system decreases when the ACN molecule is adsorbed on it due to the dipole formation in the interface and the charge accumulation/depletion taking place between the molecule and the surface. Once again the orientation of the molecular dipole highly influences the behavior of the work function. Beyond the static analysis, the dynamic study of this system has given us an overall picture of the stability of the ACN monomer on the different substrates. We have evaluated several situations considering different temperatures and the effect of the surface reconstruction. We have observed that the temperature highly influences the desorption time of the molecule: higher the temperature, lower the desorption time. On the other hand, the surface reconstruction, due to thermal excitation, completely controls the path followed by the molecule along the dynamics simulation.

To sum up, this second part of the work has shown us that:

- Clarifying the adsorption behavior of the polymer precursors is mandatory if we wish to understand and control the coating of a metallic substrate with it, since its stability on the substrate might be unlikely.
- The different behavior of the ACN/2NaCl/Cu(100) adsorbed system can be ascribed to the different orientation of the molecule upon adsorption. The results depend on the molecular dipole pointing towards the surface or pointing to vacuum. However, the molecule orientation is a consequence of the singularity of the system: in the case of 2ML, each Na^+/Cl^- couple is accompanied by the opposite couple (Cl^-/Na^+) in the perpendicular direction. Thus, the interaction between the molecule and the surface is different than in the cases of 1ML and 3ML, since in these two former cases there is an odd number of insulating film rows between the ACN and the Cu(100) substrate. In addition, the corrugation of

the ionic layers adsorbed on a metal surface tends to be smaller with the thick of the layer. Therefore, we can expect an even-odd effect that might disappear with the ionic layer thickness.

- The combination of static and dynamic simulations presents a new interesting computational strategy for the study of the interaction of small molecules on different surfaces as metals, oxides, salts, etc.

6.3 Electron donor and acceptor molecules: the promising combination of TCNQ and TTF on a metallic substrate

Finally, we have presented a set of donor-acceptor organic molecules with semiconductive properties. We have first studied tetracyanoquinodimethane (TCNQ) and tetrathiafulvalene (TTF) molecules individually adsorbed on a Ag(111) surface (i.e. low coverage regime of the surface), which has given us a broad idea of the interaction with the substrate, mainly adsorption energies, as well as the orientation and bending of the molecules when they interact with the metallic surface. Hereafter, we have studied the features of the Self-assembled monolayers (SAMs) of either TCNQ or TTF; and finally, we have presented three different SAMs made by the combination of both molecules in different proportions. These theoretical studies have been combined with experimental ones based on the use of the STM as a tool for visualizing the molecules, their orientation on the surface and, at its best, for visualizing a high resolution image of the molecular orbitals. Thus, we have studied adsorption energies and equilibrium geometries, charge transfer and electronic structure of different SAM on the Ag(111) surface, from a complete TCNQ coverage to a complete TTF one, running across the mixing of both molecules in 2TCNQ:1TTF, 1TCNQ:1TTF and 1TCNQ:2TTF proportions. This study gives rise to several conclusions:

- The interaction between the TCNQ and the Ag(111) surface produces a large distortion of the molecule, which bends over the surface due to the $-\mathrm{C} \equiv \mathrm{N} \rightarrow$ Ag bonds. The interaction also implies large adsorption energies and charge transfer from the surface to the molecule.
- The interaction between the TTF and the Ag(111) surface, although weaker, also involves the distortion of each molecule, mainly in the SAMs due to the

proximity to neighbor molecules that provoke cambering of the SAM. However, we have observed negligible charge transfer in the TTF/Ag(111) systems.

- The mixing of both molecules has given us remarkable results on the charge transfer process. Thus, while in the crystal bulk material the charge transfer between the acceptor-donor couple is just 0.6 e^-, we observe 1.2 e^- when the Ag surface stands beneath the molecules. This fact points out the important role of a composite organic-metal material and the promising benefits that can be drawn from them.
- From the electronic structure analysis of the systems with only one type of molecule (TCNQ SAM in gas phase and TTF SAM in gas phase), we can conclude that intermolecular interactions between the same kind of molecule, in the gas phase (i.e. flat configuration of the molecules) do not stabilize the orbitals to lower energies; however, the bending of the molecules produces a slight left shift of the HOMO. On the other hand, when they are adsorbed on the metallic surface (TCNQ/Ag(111) and TTF/Ag(111)), there is a broadening of the peaks, due to the molecule-metal interaction and a shift in energy when charge transfer takes place. For the mixed patterns, we conclude that when TTF and TCNQ are together, they form an organic metal: the TCNQ orbitals stabilize, while the HOMO and LUMO orbitals of the TTF shift to the right, giving rise to the overlap of the TTF's HOMO and the TCNQ's LUMO at the Fermi level. For the complete adsorbed system, though frontier orbitals do stabilize as well, they do it to a lesser extent, breaking the former overlap.
- We have as well immersed in the study of phase transition, via the Peierls transition given in the TCNQ:TTF crystal bulk material. This transition would not be observed in the TCNQ+TTF/Ag(111) adsorbed system due to the presence of the metallic substrate. The metal-molecule interaction is much stronger than the intramolecular one; therefore TCNQ and TTF molecules will rather be adsorbed on the surface than interact between them giving rise to the dimers that provoke the Peierls transition. Furthermore, the rearrangement of the molecules on the surface, driven by the stoichiometry and the molecule-metal interactions, does not allow the pattern to dimerize and to keep any symmetry at the same time. Thus, this process is not likely to take place.

6.4 Electronic nanodevices based on a combination of organic molecules and metal substrates: Summing-up

To conclude, I would like to synthetize in a few paragraphs what it has been the purpose of this Doctoral Thesis:

From the beginning we aimed to achieved a thorough study of different, but still sharing common properties, organic molecules, which were either benchmark ones (as benzene), highly used molecules in the industry (as acrylonitrile), or hot topic ones (as TCNQ and TTF); and of course, to evaluate their interaction with common and widely available metals as copper and silver.

We have not only centered our attention on the features resulting from the interaction between the organic molecule and the metal substrate, but we have also focused on the variation of several properties wheng an ultrathin insulating film is introduced between both, breaking thus the initial properties of the organic molecule/metal interface. To our knowledge, the addition of an insulating film as NaCl, has not been previously studied, from a theoretical perspective. But the case is that this combination gives us the possibility of decoupling the organic molecule from the metal substrate and thus, visualizing the individual and inherent properties of the adsorbed molecules. A complete opposite perspective has been presented via the study of self-assembled monolayers of organic molecules on metallic substrates. Self-assembly of organic molecules at surfaces is one of the nowadays most exciting and studied fields in he framework of Surface science. It presents us with a series of possibilities as different pattern formation over long scale substrates or the tunability of electronic structure, transport properties and the inducement of new chemical reactions. In addition, charge transfer processes in these kinds of systems can be very useful and one of the main motivations for the construction of 2D organic materials, in the framework of nano-devices and nano-electronic fields.

Beyond the specific results obtained along the whole study, it is important to highlight how we have got to them by combining well-differentiated tools. Thus, all the systems we have presented, have been studied applying periodic boundary conditions, using plane waves, and obtaining equilibrium geometries, adsorption energies, charge transfer and electronic structures. Ab initio molecular dynamics has been applied from a completely different perspective: using a combination of plane waves and Gaussian basis functions, thereby generating a completely different set of results that helped us achieve a deeper understanding of the organic molecule/metal substrate system.

Last but not least, we have applied the Landauer formula and the Green's functions, framed in the Transmission theory to picture the behavior of one of our organic molecules in between two metallic leads when an electric current was applied.

In a nutshell, all the work presented in this manuscript, aims to provide a useful guide for future studies on the interactions between organic molecule/metal substrate, organic molecule/insulating film and organic molecule/insulating film/metal substrate systems.

Capítulo 7

Resumen y Conclusiones

Al comienzo de este trabajo hemos expuesto las características de aquellos dispositivos orgánicos que presentan conductividad eléctrica. Para ello, los hemos dividido en tres subgrupos: (I) Compuestos con electrones deslocalizados, (II) Compuestos formados a partir de adición intermolecular y (III) moléculas dadoras y aceptoras de electrones. Cada grupo se comportará de una manera totalmente distinta, pero todos ellos comparten el hecho de que son materiales nuevos y prometedores para su uso en el capo de la nano-electrónica.

6.1 Compuestos con electrones deslocalizados: Benceno adsorbido sobre Cu(100) y el efecto de una fina capa de aislante

Hemos considerado este primer grupo como una oportunidad para estudiar un sistema de referencia: el benceno; y hemos estudiado sus propiedades de adsorción en un metal ampliamente utilizado como es el cobre. Para ser capaces de visualizar y abarcar sus propiedades moleculares individuales, hemos incluido una, dos y tres monocapas de NaCl, una película aislante. El estudio se ha basado en el análisis de distintas propiedades: (i) energías de adsorción y geometrías de equilibrio, que nos han proporcionado una idea de lo débil que es la superficie de energía potencial para estos sistemas, (ii) Transferencia de carga desde un punto cuantitativo y cualitativo, lo cual nos ha proporcionado información complementaria sobre las propiedades de adsorción;

(iii) y finalmente, hemos presentado un estudio en detalle de la estructura electrónica del sistema, lo cual nos ha permitido comprender qué ocurría con los orbitales moleculares y las bandas de la capa aislante y el metal cuando sucedía la interacción entre el sustrato y la molécula. Todos los resultados que se han presentado están precedidos de un estudio intenso de las fuerzas dispersivas de tipo van der Waals y la manera cómo deben aplicarse al sistema. Se ha remarcado en repetidas ocasiones a lo largo de este manuscrito que es muy necesario una correcta utilización de estas fuerzas si se quiere describir apropiadamente las interacciones débiles, que son mayoritarias en la mayoría de los sistemas que hemos presentado. Sin embargo, la presencia de un sustrato metálico entorpece la aplicación de cualquiera de los métodos conocidos hasta la fecha. El motivo recae en el efecto apantallante de las fuerzas en el interior del sustrato metálico. Por tanto, hemos utilizado un método sencillo: hemos aplicado las fuerzas van der Waals estrictamente solo a aquellos átomos que están experimentando estas fuerzas débiles y hemos evitado incluirlas a aquellos que están lejos de experimentarlas; esto es, solo a la molécula orgánica, a la capa de aislante y a la primera capa de átomos metálicos.

Además, el hecho de incluir las capas de NaCl no solo nos ha dado una imagen cualitativa de la molécula desacoplada, si o también una imagen cuantitativa: hemos observado como las energías de adsorción decrecen según aumenta el número de capas de NaCl y como la transferencia de carga del sustrato a la molécula pasa a ser despreciable. Por otro lado, hemos presentado también las capacidades de un microscopio de efecto túnel a la hora de inducir la reactividad química de moléculas aisladas. Así, hemos simulado dos electrodos de cobre entre los cuales hemos situado una molécula de benceno. A continuación se ha aplicado un voltaje creciente entre las dos capas metálicas. Este dispositivo simula el efecto de la corriente túnel cuando una punta del microscopio se sitúa sobre la muestra de C_6H_6/Cu. El efecto de la corriente sobre la molécula se ha estudiado mediante el análisis de las fuerzas atómicas en cada par de átomos C-H, mostrándose una fuerza creciente que puede ser indicativo de la ruptura del enlace, como ya indicaban trabajos anteriores. No solo hemos estudiado las fuerzas atómicas, si no que también hemos evaluado la transmisión en función del voltaje aplicado, lo cual nos ha mostrado una hibridación muy marcada entre el HOMO del benceno y la banda *d* de los electrodos de cobre. Sin embargo, y debido a la gran distancia entre los orbitales HOMO y LUMO del benceno, no se observa ningún otro gran cambio en la molécula. Sea como sea, esto nos ha mostrado que se necesita un voltaje mayor, si queremos observar cambios en la naturaleza del enlace.

El estudio de este sistema de referencia, benceno, adsorbido sobre Cu(100) y NaCl/Cu(100) nos ha mostrado:

- La importancia de incluir fuerzas dispersivas de tipo van der Waals, para poder describir de una manera adecuada las interacciones entre moléculas orgánicas y los substratos metálicos, así como la importancia de incluir estas fuerzas de una manera correcta, es decir, no incluirlas en todo el sistema, si no solo en aquellos átomos que están interaccionando mediante fuerzas débiles de van der Waals.
- Las diferencias que se presentan cuando existe una interacción con un sustrato metálico o con un sustrato metálico previamente recubierto con una capa aislante: disminuye la energía de adsorción, decrece la transferencia de carga y cambia la función de trabajo del sistema. Estos factores destacan el importante papel que juegan los materiales iónicos bidimensionales a la hora de modular las interacciones molécula/metal.
- La posibilidad de inducir una reacción química mediante una corriente eléctrica; así como la habilidad de controlar los procesos que tienen lugar en un sistema a escala molecular.

6.2 Compuestos a partir de adición intermolecular: AIMD como herramienta para el estudio de la superficie de energía potencial del acrilonitrilo sobre Cu(100) y sobre NaCl/Cu(100)

En esta parte de la tesis hemos presentado un segundo subgrupo de compuestos orgánicos con propiedades semiconductoras. Estos son aquellos formados a partir de la adición intramolecular de otras moléculas pequeñas, los llamados polímeros. Como primera aproximación hemos estudiado el monómero de acrilonitrilo adsorbido sobre una superficie metálica de Cu(100) y sobre esta superficie cubierta con una capa fina de aislante, NaCl. En este estudio, no solo hemos llevado a cabo un análisis similar al efectuado previamente para el sistema C_6H_6/n NaCl/Cu(100), si no que también presentamos una nueva estrategia computacional: la combinación de simulaciones estáticas y dinámicas para explorar la superficie de energía potencial y analizar la estabilidad de sistemas complejos. Así, en el estudio estático hemos evaluado primero

distintas posiciones de adsorción de la molécula de acrilonitrilo sobre las distintas superficies que se han considerado: Cu(100) y Cu(100) recubierto con 1, 2 y 3 Capas de NaCl. A partir de aquí, se han elegido dos conformaciones para cada uno de los sistemas: la posición más estable y una segunda conformación que se diferencia de la primera por la reorganización, completamente distinta, de la molécula- Esta decisión nos ha dado la posibilidad de comparar propiedades de dos geometrías de adsorción bien diferenciadas: energías de adsorción, geometrías de equilibrio, transferencia de carga y la estructura electrónica. Así, encontramos que las energías de adsorción y la transferencia de carga están altamente influenciadas por la presencia de la capa aislante: decrecen cuantas más monocapas de NaCl se añaden a la estructura.

Además encontramos un comportamiento interesante en cuanto a la transferencia de carga para los sistemas ACN/*n* NaCl/Cu(100): la acumulación de carga dependerá de la posición del átomo de N tras la adsorción (sobre un ión Na^+ o sobre uno de Cl^-), ya que determina la orientación de la propia molécula (hacia la superficie o hacia el vacío) y por tanto la orientación del dipolo molecular. Dependiendo de su dirección, la molécula de ACN presentará una acumulación de carga o una disminución de la misma. El estudio de la estructura electrónica muestra cómo la función trabajo del sistema decrece cuando la molécula de ACN se adsorbe debido al dipolo formado en la interfase y debido a la acumulación/disminución de carga que tiene lugar entre la molécula y la superficie. Una vez más, observamos que la orientación del dipolo afectará a una de las propiedades, en este caso a la función trabajo. Más allá del estudio estático, el estudio dinámico nos ha dado una visión global de la estabilidad del monómero ACN en cada uno de los distintos sustratos. Hemos evaluado distintas situaciones considerando temperaturas diferentes y la reconstrucción del sustrato. Así hemos observado que la temperatura influencia en gran medida el tiempo de desorción de la molécula: a mayor temperatura, menores tiempos de desorción. Por otro lado, la reconstrucción de la superficie, debida a la temperatura, controla por completo el camino a seguir por la molécula durante toda la simulación.

Para concluir, esta segunda parte del trabajo nos ha mostrado que::

- Es imprescindible entender correctamente el comportamiento de un precursor de polímeros cuando esta adsorbido sobre una superficie, si queremos controlar el recubrimiento de dicha superficie metálica, ya que la estabilidad del monómero sobre el metal puede ser poco favorable.
- El comportamiento distinto del sistema ACN/2NaCl/Cu(100) puede deberse a la distinta orientación de la molécula. Los resultados dependen de que el dipolo

molecular apunte o no a la superficie. Sin embargo, la orientación de la molécula es ya de por sí una consecuencia de este sistema singular: en el caso de 2ML, cada pareja de iones Na^+/Cl^- esta acompañado de su pareja opuesta (Cl^-/Na^+) en el plano perpendicular. De manera que, la interacción entre la molécula y la superficie es diferente que para el caso de 1ML y/o 3ML, ya que en estas dos hay un número impar de capas de aislante entre el ACN y el Cu(100). Además, la ondulación de las capas iónicas tiende a ser menor según aumenta el espesor de la propia capa. Así pues, podemos esperar que este efecto par-impar vaya desapareciendo con el espesor de la capa iónica.

- La combinación de simulaciones estáticas y dinámicas presentan una estrategia computacional nueva e interesante para el estudio de moléculas pequeñas sobre distintas superficies como metales, sales, óxidos, etc.

6.3 Moléculas dadoras y aceptoras de electrones: la combinación prometedora de TCNQ y TTF sobre un substrato metálico.

Finalmente, hemos presentado un conjunto de moléculas orgánicas dadoras-aceptoras con propiedades semiconductoras. Primero hemos estudiado la adsorción individual del tetracianoquinodimetano y del tetratiofulvaleno sobre la superficie de Ag(111) (es decir, en un régimen de bajo recubrimiento), lo cual nos ha dado una amplia idea del tipo de interacción con el substrato, sobre todo, de las energías de adsorción, así como de la orientación y el doblamiento de las moléculas cuando interaccionan con el substrato metálico. A partir de aquí, hemos estudiado las características de monocapas auto-ensambladas de TCNQ o de TTF; y finalmente, hemos presentado tres patrones distintos de monocapas auto-ensambladas, hechas a partir de la combinación de ambas moléculas en distintas proporciones. Estos estudios teóricos se combinan con otros experimentales basados en un microscopio de efecto túnel, como herramienta para la visualización de moléculas, su orientación sobre la superficie y, en el mejor de los casos, para visualizar una imagen de alta resolución de los orbitales moleculares. Así, hemos estudiado energías de adsorción y geometrías de equilibrio, transferencia de carga y estructura electrónica de las diferentes monocapas sobre Ag(111), desde un recubrimiento completo de TCNQ hasta un recubrimiento completo de TTF, pasando por la mezcla de ambas moléculas en proporciones 2TCNQ:1TTF, 1TCNQ:1TTF y 1TCNQ:2TTF. Este estudio nos lleva a varias conclusiones:

- La interacción entre la monocapa auto-ensamblada de TCNQ y la Ag(111) produce una distorsión grande en las moléculas de TCNQ, que se doblan sobre la superficie debido a la interacción $-C \equiv N \rightarrow Ag$. La interacción también implica energías de adsorción grandes y transferencia de carga desde el substrato a las moléculas.
- La interacción entre la monocapa auto-ensamblada de TTF y la superficie de Ag(111), aunque es menor que la anterior, también implica la distorsión de cada molécula de TTF, sobre todo debido a la proximidad de moléculas vecinas de TTF, que provocan la combadura de la monocapa. Sin embargo, hemos observado una transferencia de carga casi despreciable en los sistemas de TTF/Ag(111), debido al carácter dador de electrones de esta molécula.
- La mezcla de ambas moléculas nos ha proporcionado resultados llamativos en cuanto al proceso de transferencia de carga. Así, mientras que en el material cristalino la transferencia de carga entre la molécula aceptora y la dadora es tan solo 0.6 e-, nosotros observamos una transferencia de carga de 1.2 e- cuando la superficie de Ag esta por debajo de las moléculas. Este hecho destaca el importante papel que juegan los materiales compuestos, donde se juega con la interacción de distintos sustratos como metales y moléculas orgánicas y los beneficios tan prometedores que pueden sacarse de estos materiales.
- Del análisis de la estructura electrónica de los sistemas TCNQ/Ag(111) y TTF/Ag(111), podemos concluir que las interacciones intermoleculares entre el mismo tipo de moléculas, en fase gas (en la cual las moléculas están planas) no estabilizan los orbitales a más bajas energías; si embargo, la flexión de las moléculas produce un ligero desplazamiento hacia la izquierda del HOMO. Por otro lado, cuando las moléculas están adsorbidas sobre la superficie metálica, los picos se ensanchan debido a la interacción molécula-metal. Para los patrones en los que existe una mezcla, concluimos que cundo el TTF y el TCNQ se encuentran juntos formarán un metal orgánico: los orbitales del TCNQ se estabilizan, mientras que los orbitales HOMO y LUMO del TTF se desplazan a la derecha, dando lugar al solapamiento del HOMO del TTF y el LUMO del TCNQ en el nivel de Fermi. Para el sistema adsorbido completo, aunque los orbitales frontera también se estabilizan, lo hacen en menor medida, rompiendo el anterior solapamiento.
- También nos hemos adentrado en el estudio de una transición de fase, mediante la transición de Peierls que se observa en el cristal de TCNQ:TTF. Esta

transición no se observará en el sistema de TCNQ+TTF/Ag(111) debido a la presencia de un sustrato metálico. La interacción meta-molécula es mucho más fuerte que la intramolecular, de manera que las moléculas de TCNQ y de TTF preferirán estar adsorbidas sobre la superficie antes que interaccionar entre ellas dando lugar a los dímero que provocan la transición de Peierls. Es más, la reorganización de las moléculas sobre la superficie esta conducida por la estequiometria y las interacciones molécula-metal, de manera que no permitirán la dimerización y mantener al mismo tiempo una simetría. De manera que es poco probable que este proceso tenga lugar.

6.4 Nano-dispositivos electrónicos basados en la combinación de moléculas orgánicas y sustratos metálicos: recapitulación

Para concluir, me gustaría sintetizar en unos cuantos párrafos cual ha sido la intención de esta tesis doctoral:

Desde el principio hemos deseado conseguir un estudio de diferentes moléculas orgánicas, que aun así compartían propiedades comunes, que o bien eran sistemas de referencia (como el benceno), o bien moléculas que se utilizan ampliamente en la industria (como el acrilonitrilo) o bien que son temas candentes (como el TCNQ y el TTF); y por supuesto, su interacción con metales comunes y ampliamente utilizados como el cobre y la plata.

No solo nos hemos centrado en las características que resultan de la interacción entre la molécula orgánica y el metal, si no que también nos hemos fijado en las propiedades individuales de cada moléculas mediante la introducción de una capa fina de aislante entre el metal y la propia molécula. Hasta donde sabemos, la adición de una película aislante como el NaCl, no se ha estudiado previamente desde un punto de vista teórico. Pero el caso es que esta combinación nos proporciona la posibilidad de desacoplar la molécula orgánica del sustrato metálico y así, visualizar las propiedades inherentes e individuales de la propia molécula. Hemos presentado también una perspectiva completamente distinta mediante el estudio de monocapas de moléculas orgánicas auto-ensambladas sobre sustratos metálicos. El auto-ensamblaje de moléculas sobre distintas superficie es hoy en día uno de los campos más llamativos y estudiados en el marco de la ciencia de superficies. Nos brinda una serie de posibilidades como por

ejemplo la formación de distintos patrones sobre sustratos a gran escala o la posibilidad de ajustar y controlar la estructura electrónica, las propiedades de transporte e inducir reacciones químicas. Además, los procesos de transferencia de carga en este tipo de sistemas puede ser de gran utilidad y una de las mayores motivaciones para la construcción de materiales orgánicos 2D, en el marco de nos nano-dispositivos y el campo de la nano-electrónica.
Más allá de los resultados concretos obtenidos a lo largo de este estudio, es importante remarcar como hemos llegado a ellos mediante la combinación de herramientas muy distintas. Así, todos los sistemas han sido estudiados aplicando condiciones de periodicidad y de contorno, mediante el uso de ondas planas, obteniendo así geometrías de equilibrio, energías de adsorción, transferencia de carga y estructuras electrónicas. Pero también hemos aplicado dinámica molecular ab initio desde un punto de vista completamente distinto: utilizando ondas planas y funciones de base Gaussianas, generando así un conjunto de resultados completamente distinto que nos ha ayudado a conseguir una mayor comprensión de los sistemas molécula/sustrato metálico.
Por último, pero no por ello menos importante, hemos utilizado la fórmula de Landauer, y las funciones de Green, enmarcadas en la teoría de Transmisión para hacernos una idea del comportamiento de nuestras moléculas orgánicas entre dos placas metálicas cuando se aplica una corriente eléctrica.

En conclusión, el trabajo presentado en este manuscrito, pretende proveer una guía útil para estudios futuros sobre la interacción en sistemas formados por moléculas orgánicas/sustratos metálicos, moléculas orgánicas/aislantes y moléculas orgánicas/aislantes/sustratos metálicos.

Publications

List of publications related to this thesis

1. Adsorption of Benzene on Cu(100) and on Cu(100) covered with an ultrathin insulating ionic film: molecule-substrate interaction and decoupling.
   M. Robledo, G. Pacchioni, F. Martín, M. Alcamí and S. Díaz-Tendero.
   The Journal of Physical Chemistry C (2015) 119, 4062-4071; DOI: 10.1021/jp5106604

2. Acrylonitrile adsorbed on Cu(100) and Cu(100) previously coated with NaCl: a DFT static and dynamic study.
   M. Robledo, S. Díaz-Tendero
   The Journal of Physical Chemistry C (Submitted)

3. Surface mediated charge transfer in TCNQ+TTF/Ag(111)
   K. Lauwaet, M. Robledo, J. Rodriguez-Fernández, S. Díaz-Tendero, J. M. Gallego, M. Alcamí, R. Otero, F. Martín, R. Miranda
   (In preparation)

4. Theoretical aspects of the charge transfer processes in TCNQ+TTF/Ag(111)
   M. Robledo, S. Díaz-Tendero, M. Alcamí, F. Martín
   (In preparation)

5. Benzene dehydrogenation in between two copper leads
   M.Robledo, P. Abufager, N. Lorente
   (In preparation)

List of publications not related to this thesis

1. Exohedral interactions in cathionic lithium metallofullerenes.
   M. Robledo, F. Martín, M. Alcamí, S. Díaz-Tendero.

Theoretical Chemistry Accounts (2013) 132:1346; DOI: 10.1007/s00214-013-1346-8

2. Bonding in exohedral metal-fullerene cationic complexes.
M. Robledo, N. Aguirre, S. Díaz-Tendero, F. Martín, M. Alcamí.
RSC Advances (2014), 4, 53010; DOI: 10.1039/c4ra10776d

3. Hydrogen storage in metal-fullerene cationic complexes
M. Robledo, S. Díaz-Tendero, M. Alcamí
(In preparation)